Particle Tracking with Micro-Pattern Gaseous Detectors

Bernhard Matthias Flierl

München 2018

Particle Tracking with Micro-Pattern Gaseous Detectors

Bernhard Matthias Flierl

Dissertation
an der Fakultät für Physik
der Ludwig–Maximilians–Universität
München

vorgelegt von
Bernhard Matthias Flierl
aus Bobingen

München, den 6. März 2018

Erstgutachter: Prof. Dr. Otmar Biebel
Zweitgutachter: Prof. Dr. Wolfgang Dünnweber
Tag der mündlichen Prüfung: 19. April 2018

Zusammenfassung

GEM und Micromegas zählen zu den mikrostrukturierten Gasdetektoren (MPGDs). Sie zeichnen sich durch intrinsisch hohe Ratenfestigkeit und Ortsauflösung aus, welches durch kurze Driftwege und einen hohen Grad an Segmentierung erreicht wird. Großflächige Micromegas-Detektoren werden deshalb auch Teile des Myonspektrometers des ATLAS-Detektors ersetzen, da diese die nötige Spurauflösung auch unter hoher Untergrundbestrahlung erhalten. Dies wird mit einer geplanten Erhöhung der Luminosität des Large Hadron Colliders über die aktuelle Luminosität von $2 \times 10^{34} \, \mathrm{cm}^{-2} \, \mathrm{s}^{-1}$ hinaus ab dem Jahr 2020 erforderlich sein.

Mit standardmäßigen Auslese- und Analysemethoden kann das volle Potential zur Spurrekonstruktion dieser Detektoren nicht ausgenutzt werden. In dieser Arbeit werden neue alternative Techniken untersucht und vorgestellt, die es erlauben, die volle Spurinformation eines Teilchens im Detektor zur Ortsbestimmung auszunutzen. Die Spurbestimmung in GEM- und Micromegas-Detektoren erfolgt dabei für verschiedene Anwendungen unter Zuhilfenahme von Rekonstruktionsmethoden ähnlich einer Spurendriftkammer (TPC).

Die Anwendung dieser Technik erlaubt den hochaufgelösten Nachweis von thermischen Neutronen. Dies geschieht, indem die Spuren von Ionen vermessen werden, die von einem Neutroneneinfangprozess in einer dünnen ^{10}B-Konversionsschicht stammen. Die Methode wird in einem $10 \, \mathrm{cm} \times 10 \, \mathrm{cm}$ GEM-Detektor mit einem Strahl thermischer Neutronen (3.7 meV) getestet. Mit einer Dicke der Konversionsschicht von 2 µm wird dabei eine Rekonstruktionseffizienz von 5 % und eine Ortsauflösung von (100 ± 10) µm erreicht.

Eine Abwandlung derselben Rekonstruktionsmethode erlaubt auch eine deutlich verbesserte Ortsrekonstruktion in Thick-GEM-Detektoren (TGEM). Für Messungen mit 5 MeV alpha-Teilchen kann durch Rekonstruktion ihrer Spur die Position im Driftbereich mit einer Ortsauflösung von (360 ± 30) µm bestimmt werden.

Unter Ausnutzung ähnlicher Herangehensweise lässt sich auch die Rekonstruktion von minimal ionisierenden Teilchen in MPGDs deutlich verbessern. Eine Methode, die eine Ortsrekonstruktion basierend auf dem Energieverlust entlang von Myonspuren in einem Strahl von 10–150 GeV ausnutzt, erlaubt dabei Ortsauflösungen von unter 150 µm unabhängig von der Spursteigung in einem $10 \, \mathrm{cm} \times 10 \, \mathrm{cm}$ GEM Detektor. Durch die Modellierung und Kompensation von Signalkopplung auf benachbarten Auslesestrukturen kann außerdem die Spurrekonstruktion in einer einzelnen Detektorlage verbessert werden.

In der Arbeit wird auch die Konstruktion der Micromegas-Detektoren für das ATLAS Muonspektrometer beschrieben und Resultate von ersten Tests mit einem vierlagigen Prototyp von $2 \, \mathrm{m}^2$ Fläche werden vorgestellt. In einem Myonteststrahl werden die Pulshöhe, Rekonstruktionseffizienz sowie die Orts- und Zeitauflösung bestimmt. Myonen, die den Detektor senkrecht zu seiner Ausleseebene treffen, können dabei mit einer Ortsauflösung von unter 100 µm nachgewiesen werden. Hierbei liegt die Nachweiswahrscheinlichkeit bei über 95 %. Für Myonen, die unter Winkeln von $20°$ und $30°$ auftreffen, kann durch Rekonstruktion ihrer Spur eine deutlich verbesserte Auflösung von 200 µm bei hoher Effizienz von 97 % erreicht werden.

In einem Kohlenstoff-Ionenstrahl mit einer Rate im Bereich von 2 MHz bis 50 MHz wird die Eignung von GEM-Detektoren unter sehr hohen Raten für Anwendungen wie Strahlüberwachung oder Ionenradiographie getestet. Einzelne Ionen können dabei auch bei der höchsten Rate noch mit guter Auflösung nachgewiesen werden, obwohl im Durchschnitt bis zu acht Teilchen zeitgleich den Detektor passieren.

Abstract

GEM and micromegas detectors are Micro-Pattern Gaseous Detectors (MPGDs). They are intrinsically high-rate capable and show excellent spatial resolution due to small drift lengths and high read-out granularity. Large micromegas detectors will replace parts of the forward high-precision muon tracking system of the ATLAS detector, which will be able to cope with the increased background when the Large Hadron Collider will exceed its current luminosity of $2 \times 10^{34}\,\mathrm{cm^{-2}\,s^{-1}}$ after 2020.

The full tracking potential of these detectors cannot be reached by standard read-out and reconstruction techniques. In this thesis different novel approaches are discussed and introduced, which allow a distinct enhancement in position information. This is achieved by employing methods that take into account the full track information of a charged particle in the detector. In thin planar GEM and micromegas detectors particle tracking is performed by utilization of a time resolving read-out, which allows a Time-Projection-Chamber-like (TPC) track reconstruction for several applications.

Thermal neutrons are detected with high precision by reconstructing the tracks of ions emerging from a neutron capture process in a thin ^{10}B conversion layer. The method is tested in a thermal neutron beam of 3.7 meV with a 10 cm × 10 cm GEM detector. Thereby a reconstruction efficiency of 5 % in a 2 μm boron conversion layer and a spatial resolution of $(100 \pm 10)\,\mu\mathrm{m}$ is achieved.

From this a similar method is derived for the usage in Thick-GEM detectors (TGEM), which results in an enhanced spatial resolution as well. This is tested through the tracking of 5 MeV alpha particles. For these a spatial resolution of $(360 \pm 30)\,\mu\mathrm{m}$ is reached.

An alternative reconstruction method for tracking of minimal ionizing particles in multiple detector layers allows for a significantly enhanced position determination for small GEM-detectors. For muons of 10–150 GeV a spatial resolution below 150 μm is obtained independent of the track inclination. A model for strip cross-talk is developed and a compensating method is applied, which allows improved track inclination reconstruction in a single detector layer.

In this thesis the construction of micromegas detectors for the ATLAS muon spectrometer upgrade is described. Furthermore a $2\,\mathrm{m}^2$ prototype with four layers is tested in a 10–150 GeV muon beam. The pulse height, efficiency and spatial and timing resolution of the quadruplet are determined and the general suitability for triggering on this type of detector is studied. Perpendicularly incident muons are reconstructed with a spatial resolution below 100 μm and an efficiency above 95 %. With a modified tracking technique and by application of a timing compensation a considerably improved spatial resolution of 200 μm is obtained for inclinations of 20° and 30° at high reconstruction efficiency of 97 %.

The capability of GEM-detectors for beam monitoring or ion radiography under very high rates is evaluated in a carbon ion beam with particle fluxes between 2–50 MHz. The separation of single particles and the spatial resolution depending on the particle flux is studied. Single particles are resolved with good spatial resolution even at the highest rates, when in average eight particles are traversing the detector simultaneously.

Contents

Chapter 1

Micro-Pattern Gaseous Detectors

Gas filled systems are among the widest and most commonly used technologies for detecting and measuring the properties of elementary particles. Albeit these systems, which utilize ionization in a counting gas, belong conceptionally to the oldest detectors, their development is far from finished. Modern detectors offer the possibility to combine high spatial resolution, high rate capability and also very high scalability like no other available technology.

1.1 Micromegas and GEM Detectors

Micro-Pattern-Gaseous-Detectors (MPGDs) are a relatively recent development in gaseous detectors. They emerged in the 1990s from the miniaturizing and progression of wire chambers, which were already developed in 1968 by Charpak [Charpak, 1969]. This type of detectors owe their name to the size of the structures, which are used to amplify the signal of charged particles inside an active gas volume. The size of these structures is usually below 100 µm. The first type of this new family of detectors was invented in 1992 by Giomataris and Charpak [Giomataris et al., 1996], the **Microme**sh **gas**eous detector (micromegas). This detector uses a gas volume to detect particles, which is divided in two different sections by a mircomesh and is shown schematically in figure 1.1. The mesh is typically woven from steel wires with a diameter of less than 50 µm and a pitch of less than 100 µm. It divides a drift from an amplification region. In the typical around 5 mm wide drift region charged particles can create electron-ion pairs, which are guided by electric fields towards the mesh. In the drift region an intermediate electric field $E_{drift} \sim 600 \, \text{V} \, \text{cm}^{-1}$ is used to separate and guide ions and electrons. In the amplification region below the mesh on the other hand the electrons are accelerated by a much higher electric field of around $40 \, \text{kV} \, \text{cm}^{-1}$, which allows the electrons to ionize further gas atoms. The typical distance of the micromesh to the anode of around 100 µm is ensured by a regular structure of small insulating distance pieces, the so called pillars.

The second famous representative of this generation of detectors, the **G**aseous-**E**lectron-**M**ultiplier, was invented by Sauli in 1997 [Sauli, 1997] with a very similar concept. The collection of charge is still managed by a drift region, but the electron amplification is done in a high electric field in the order of $50 \, \text{kV} \, \text{cm}^{-1}$, which is produced inside a copper clad thin film made from Kapton, FR4, glass or ceramic [Breskin et al., 2003, Takahashi et al., 2013]. The thickness of this basic material varies in the range from 0.05–2 mm and the amplification itself happens in holes which are drilled or etched through the foil. To ensure homogeneous amplification these holes are usually distributed in a triangular pattern over the whole area of the GEM. This pattern can be seen in figure 1.2, where a laser-microscopic image of a standard Kapton GEM is shown with a thickness of 50 µm and a copper cladding of two times 5 µm. There the holes were etched from both sides of the foil, leading to a double cone shape, with an outer diameter of 60 µm an inner diameter of 50 µm and a pitch of the holes of 140 µm. In this type of GEM the gas amplification can reach up to 10000. For reasons of discharge protection and charge handling in the detector often multiple GEM foils are stacked, mostly three times, and the amplification is limited to a factor of about 20 in each of them. This is also shown in a schematic in figure 1.3. The advantage of both
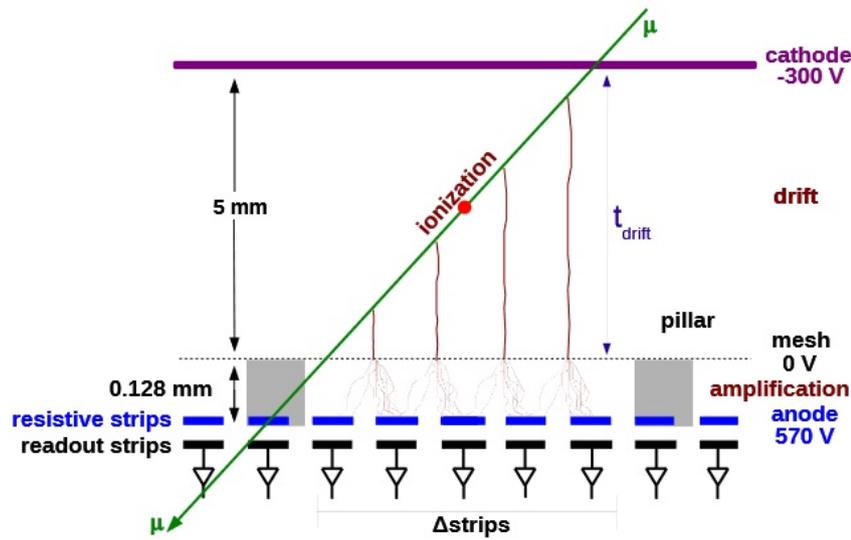
Figure 1.1: Schematic of a resistive strip micromegas detector (taken from [Lösel, 2017]). The fundamental design incorporates three planes, the cathode, the mesh and the read-out anode, which form two electric fields. The field in the drift region of usually around 50–1000 V cm^{-1} is used to separate the electrons and ions and to guide the electrons towards the amplification region between the micromesh and the anode with an electric field in the order of typically around 40 kV cm^{-1}.

detector types is that they are by construction capable to deal with very high particle rates of more than 7 MHz mm^{-2} [Bortfeldt, 2014], show an intrinsic high time resolution below 10 ns and have an excellent spatial resolution below 100 μm.
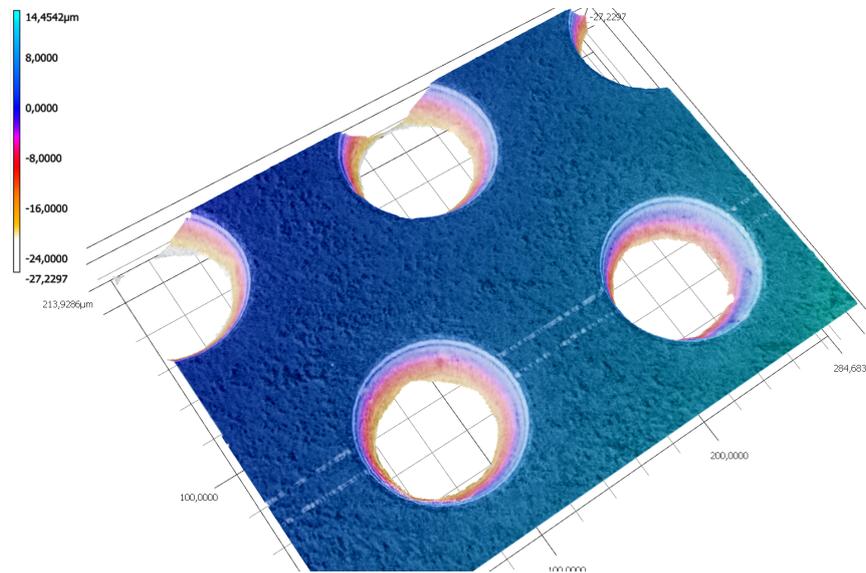
Figure 1.2: Laser microscopic image of a standard GEM foil. The upper half of the double-conic structure of the 60 μm holes in the 50 μm thick film and the triangular arrangement are shown
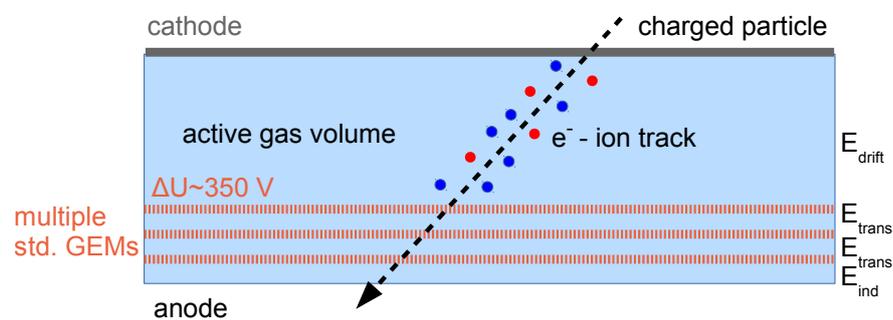
Figure 1.3: Schematic of a GEM detector with 3 GEM foils with a traversing charged particle, which leaves a track of electron-ion pairs. The electrons are guided and amplified by electric fields towards a read-out anode and the ions are collected by the cathode.

1.2   GEM Detector Set-up

Apart from chapter 6 in this thesis various techniques for particle tracking by GEM detectors will be discussed. The different GEM detectors, which are described here shared their principle design. Inside an aluminium housing, which acted as a Faraday-cage and pressure vessel, one or three GEMs were stacked in a distance of 2 mm above a read-out anode and also 2 mm apart from each other[1]. The drift region was then confined by the last GEM and a cathode. The active area of the GEM detectors was defined by the size of the GEM-foils of 100 mm × 100 mm. An example of the inner part of a detector equipped with three standard GEM foils is shown in figure 1.4.
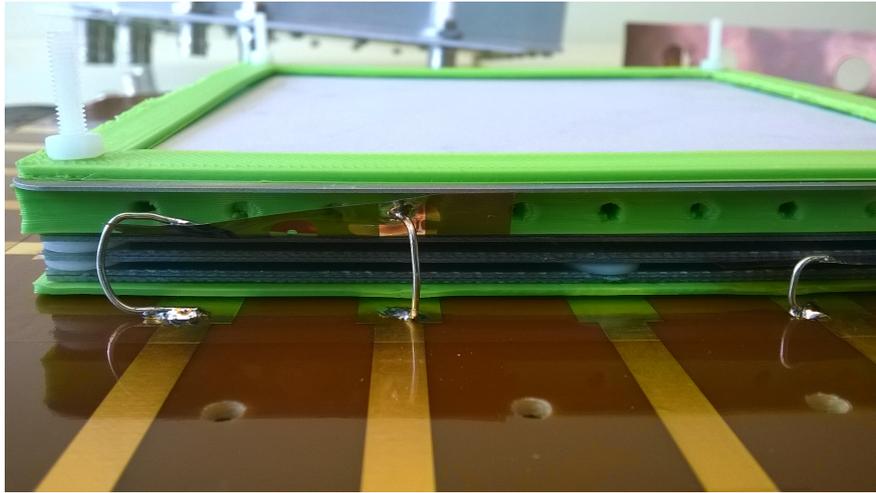

Figure 1.4: Disassembled triple GEM detector with standard GEM foils and an aluminium cathode

The necessary electric fields were applied in a cascade on both sides of the GEM-foils and the cathode, with increasing negative high voltage from bottom to top and a grounded read-out anode. For convenience the electric fields, necessary for the transport of the electron, will be abbreviated the same way, as it is shown in the schematic 1.3. The electric field in the drift region between the cathode and uppermost GEM will be called E_{drift} and the intermediate fields in between the GEM-foils, which ensured the transport of the electrons, will be called E_{trans}. The electric field between the last GEM and the anode, which was necessary to induce a signal on the read-out segments, will be called E_{ind}

The read-out anodes featured a 2D-copper strip segmentation with two layers of strips separated by a 25 μm thin etched Kapton layer. The two strip layers were perpendicularly oriented for the best spatial resolution in both read-out directions. The strip pitch of both layers was 400 μm, with 80 μm wide strips in the upper layer and 320 μm wide strips in the lower layer, which ensured an even charge distribution on both layers.

The charge amplification was performed by two different types of GEMs: Standard GEMs with a thickness of 50 μm as described before, which were always used in stack of three and on the other hand a single so called Thick-GEM (TGEM). The TGEM was made from standard printed-circuit-board material with a thickness of 0.5 mm with drilled holes in the same configuration as in the standard GEMs but with a diameter of 0.5 mm and a pitch of 0.8 mm. Both different designs are shown in figures 1.5(a) and 1.5(b).

---

[1]The anodes as well as the GEMs used here were produced at the CERN PCB workshop (see `https://ep-dep-dt.web.cern.ch/micro-pattern-technologies`)
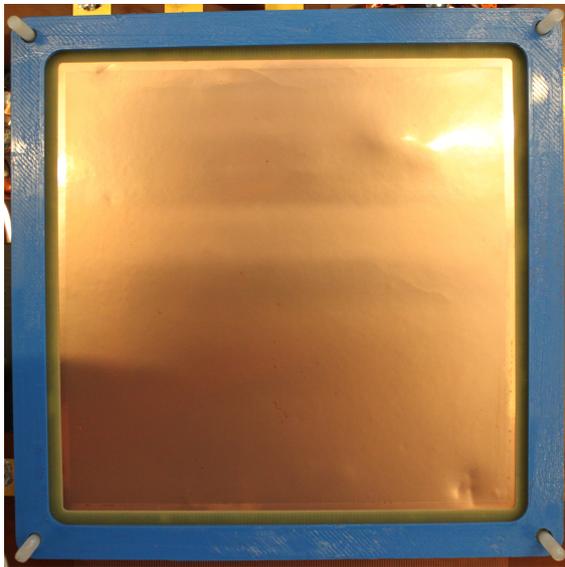
(a) Standard GEM foil made from copper clad Kapton of 50 μm thickness with an active size of 100 mm × 100 mm
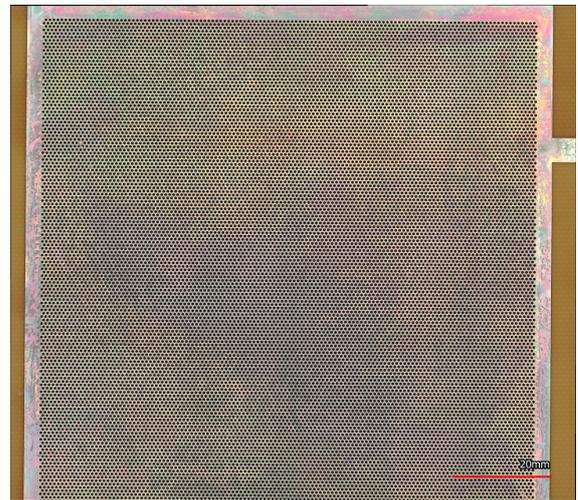
(b) TGEM made from 0.5 mm printed circuit board with 0.5 mm drilled holes with a pitch of 0.8 mm

Figure 1.5

Chapter 2

Particle Detection and Signal Processing

In this chapter the physical processes and the technical concepts, which allow particle detection and tracking by gaseous detectors, will be discussed. Based on the characteristic interactions of different particles this allows to reconstruct the passage of these particles with extremely high precision.

2.1 Energy loss of Charged Particles in Matter

The particle detection in gaseous detectors is directly or indirectly always connected to ionization of the counting gas atoms and the collection of the resulting free electrons. For electrically charged particles this is mitigated by the energy transfer of a traversing particle to the gas atoms via the electro-magnetic force. The probability of the interaction of the particle can be described by the mean free path:

$$\lambda = \frac{1}{N\sigma} \tag{2.1}$$

Where N is the electron density of the medium and σ the cross-section for an ionizing interaction with a gas atom. This free path describes the mean distance between two ionizing hits of the traversing particle in the medium. As hits with the gas atoms are purely random the probability of n hits in a given path length x can be described by Poisson statistics in the following way:

$$P(x/\lambda, n) = \frac{\left(\frac{x}{\lambda}\right)^n}{n!} \exp\left(-\frac{x}{\lambda}\right) \tag{2.2}$$

The ionization process itself is separated in two parts: Primary ionization, which describes the direct production of free electrons by an interaction of the traversing particle or secondary ionization, which is caused by interaction of primary electrons or ions with the gas or by intermediate exited states. The latter being actually responsible for most of the ionization [Penning, 1927]. The mean energy transfer from a charged particle, with the explicit exception of electrons (see section 2.2), to a medium is described by the so called Bethe-Bloch equation [Olive et al., 2014]:

$$-\left\langle \frac{dE}{dx} \right\rangle = Kz^2 \frac{Z}{A} \frac{1}{\beta^2} \left[\frac{1}{2} \ln \frac{2m_e \gamma^2 \beta^2 c^2 T_{max}}{I^2} - \beta^2 - \frac{\delta(\beta\gamma)}{2} \right], \tag{2.3}$$

where $K=4\pi N_A r_e^2 m_e c^2$, with N_a the Avogadro constant, m_e and r_e are the mass and the classical radius of the electron of $2.818 \cdot 10^{-15} m$. Z and A are the atomic number and mass of the medium, $\beta = \frac{v}{c}$ is the relativistic velocity of the incoming particle , z is the charge of this particle, δ the Fermi density correction (see [Fermi, 1940]), T_{max} the maximum energy transfer and I the mean ionization potential of the material.

Non-charged particles like photons and neutrons can indirectly be detected in a similar way, by charged particles they leave after interaction in the detector. Photons for example interact as well with the electron-shell of atoms and can either by absorption or scattering produce free primary electrons with enough energy to ionize further atoms. A third interaction of photons with matter

is the production of electron-positron pairs in the electric field of an atom. This occurs either in the nuclear field or the field of the shell electrons. The probability of these interaction is strongly depending on the energy of the photons and typically a single process is dominant in a given energy region. In low energy regions the photoelectric absorption is dominant. The interaction cross-section is depending on the photon's energy E_γ and the density of electrons in the material the photon is traversing. It can be approximated by [Kleinknecht, 1998]:

$$\sigma \propto Z^5 E_\gamma^{-3.5} \tag{2.4}$$

Here the shell structure of the electron hull of the medium with atomic number Z the photon passes is neglected. The photon can only ionize electrons, which have a binding energy $E_b < E_\gamma$, therefore the number of possible interaction increases in steps with the photon energy every time a new shell of the atom is reached. This results in characteristic absorption edges for different materials based on their electron configuration. The photo-electric absorption is the dominant photon attenuation process in the energy range up to $\mathcal{O}(100\,\text{keV})$.

In the intermediate energy range of 0.1–10 MeV the main interaction of photons with matter is mediated by Compton-scattering. Here a photon with an initial energy E_γ scatters off a single electron, which absorbs a fraction of the photon's energy and is ejected under an angle θ from the initial direction of the photon. The energy of the photon after the process E'_γ depends on this angle and can be parametrized by:

$$\frac{E'_\gamma}{E_\gamma} = \frac{1}{1 + \frac{E_\gamma}{m}(1 - \cos\theta)} \tag{2.5}$$

The differential cross-section for this process is described by the Klein-Nishina formula [Klein and Nishina, 1929]:

$$\frac{\mathrm{d}\sigma}{\mathrm{d}\Omega} = \frac{1}{2}\frac{\alpha^2}{m_e^2}\left(\frac{E'_\gamma}{E_\gamma}\right)^2\left[\frac{E'_\gamma}{E_\gamma} + \frac{E_\gamma}{E'_\gamma} - \sin^2\theta\right] \tag{2.6}$$

Here $\mathrm{d}\Omega$ is an infinitesimal solid angle, α is the fine structure constant and m_e is the electron mass. For energies higher than two times the rest energy of an electron $E_e = 511\,\text{keV}$ a photon can annihilate and produce an electron-positron pair, which is the dominant process for photon energies above 10 MeV. Exemplarily the interaction of photons depending on their energy is shown in figure 2.1 as the attenuation coefficients for the different processes in argon. The mass attenuation coefficient μ here is a measure for the absorption power of a material with density ρ and thickness d:

$$I = I_0 e^{(-\mu\rho d)} \tag{2.7}$$

The detection of photons in a gaseous detector is always through the detection of electrons produced in one of the above conversion processes. The detection of neutrons, which follows the same pattern, but originates from different interactions, will be discussed in chapter 3.
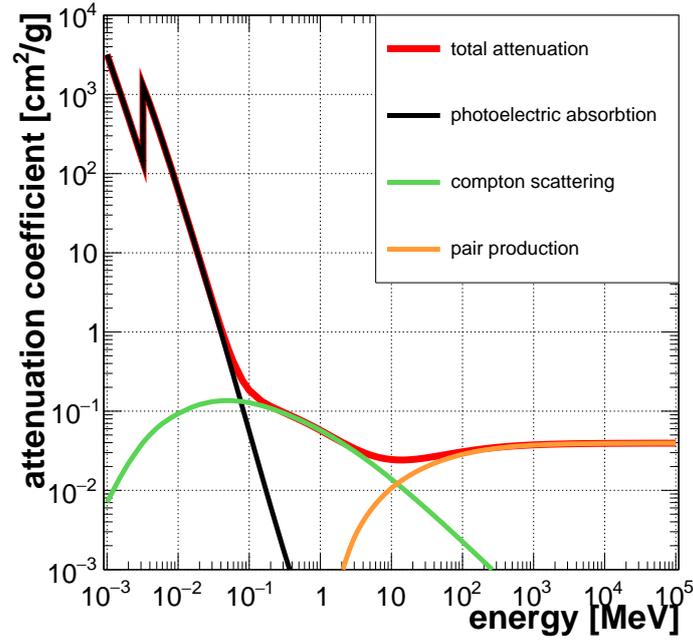
Figure 2.1: Total mass absorption coefficient and its components for photons in argon. At about 3 keV a distinct absorption edge is visible (data taken from [Berger et al., 2010])

2.2   Ionization and Charge Clustering along Particle Tracks

Depending on the energy loss of a charged particle in a gas a trace of electron-ion pairs along its trajectory can be formed, but as the charge deposition in the gas is never completely homogeneous the track is formed by locally separated clusters of electrons along the path. Following [Blum et al., 2008] the differential cross section for the energy transfer E, which is much higher than the highest binding energy in the medium E_K, on a single electron from a fast particle can be parametrized in this limit by:

$$\frac{d\sigma}{dE} = \frac{2\pi r_e^2}{\beta^2} \frac{mc^2}{E^2} \tag{2.8}$$

Here r_e is the classical electron radius, which is equal to e^2/mc^2, with e and m being charge and mass of an electron, and β is the relativistic velocity of the particle. For the electron density N, the energy-normalized differential cross-section then reads:

$$P(E) = \frac{N\left(\frac{d\sigma}{dE}\right)}{\int N\left(\frac{d\sigma}{dE}\right) dE'} \tag{2.9}$$

And in the limit of $E_K \ll E$ this would lead to a probability of a specific energy transfer to a single electron, which is schematically shown in figure 2.2. This shows that, although low energy transfer to single electrons is favoured also primary electrons with very high kinetic energy can be produced. These electrons might have a considerable range in the medium and will also leave a track of secondary electrons in the process, which is the reason for the charge clustering. For electrons with a kinetic energy E the energy loss $\hbar\omega$ per unit distance is given by [Thompson and Vaughan, 2001]:

$$P(E, \hbar\omega) = \frac{1}{\pi a_0 E} \int_{k_-}^{k_+} \frac{dk}{k} \Im\left[\frac{-1}{\epsilon(k,\omega)}\right], \tag{2.10}$$

where $a_0 = \frac{4\pi\varepsilon_0\hbar^2}{m_e e^2}$ is the Bohr-radius, $\hbar k_{\pm} = \sqrt{2m_e}\left(\sqrt{E} \pm \sqrt{E - \hbar\omega}\right)$ and $\epsilon(k,\omega)$ is the dielectric constant of the medium. Integration of $P(E, \hbar\omega)$ over all allowed energy transfers yields the
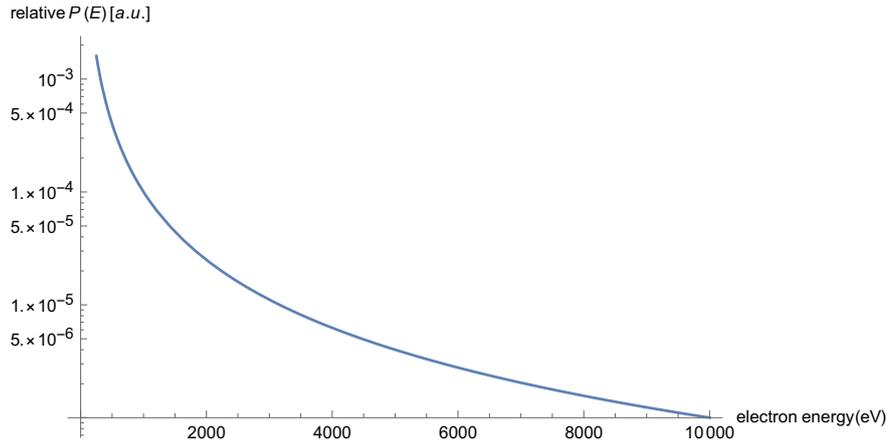
Figure 2.2: Calculated primary electron energy spectrum for a muon of 2 GeV after equations (2.9) and (2.8).

stopping power $S(E)$, which is the energy loss per unit length. The range of an electron down to a final kinetic energy, which is usually assumed to be 10 eV can then be calculated by:

$$r_{CSDA}(E) = \int_{10eV}^{E} \frac{dE'}{S(E')} \tag{2.11}$$

As in this calculation incessant energy loss is assumed. This is called the continuous slowing down approximation range (CSDA). The range of 1 keV electrons in Argon is in the order of 60 µm and increases to above 1 mm for 10 keV as can be seen in figure 2.3, where the ranges of electrons are plotted at different energies for Argon and Helium at standard conditions.
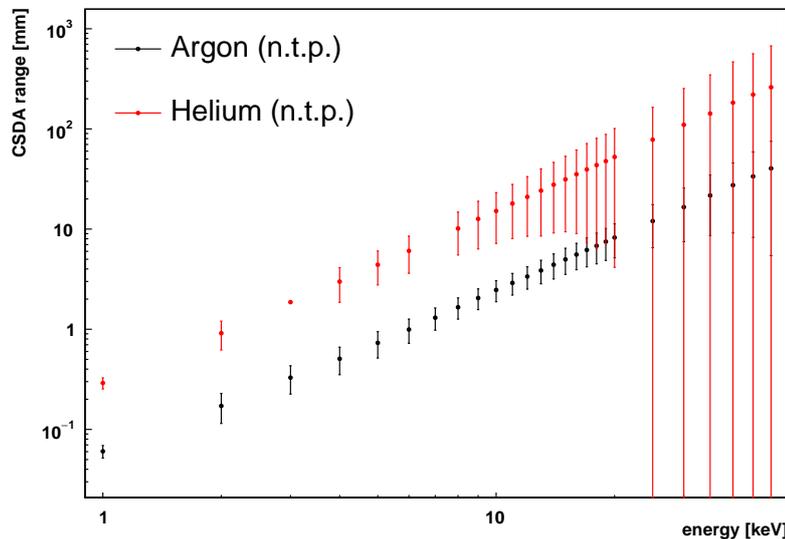
Figure 2.3: Simulated CSDA range in He and Ar at normal temperature and pressure (n.t.p.) for electrons plotted against the initial energy of the electron (Simulation based on [Berger, 1992] with data from [Perkins and Seltzer, 1991])

The distribution of cluster sizes on the other hand can be described by:

$$P(k) = \int_{0}^{\infty} P(E)p(E,k)dE \tag{2.12}$$

Here k is the number of ionization electrons and $p(E,k)$ is the probability of producing k electrons. An example for the cluster size distributions in different gases, which were experimentally determined, is shown in appendix A. The number of electrons and the mean energy loss together
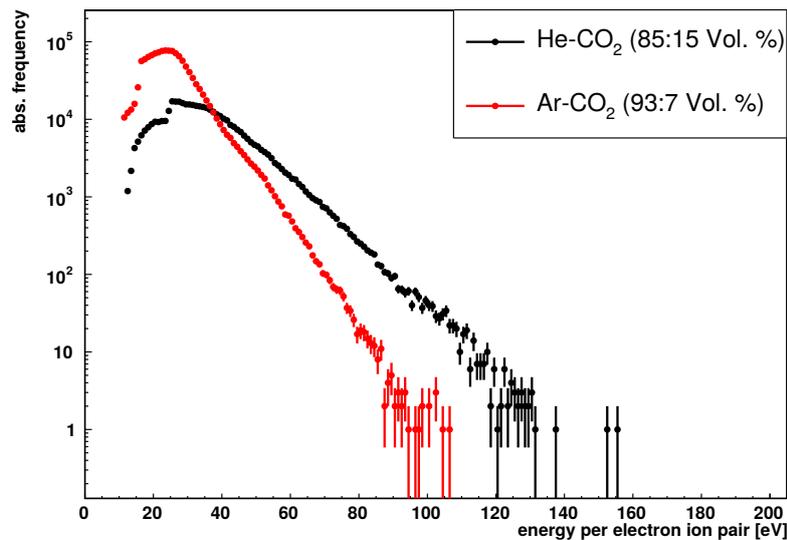
Figure 2.4: Simulated distribution of energy necessary for the creation of a single electron-ion pair for muons of 2 GeV for two gas mixtures at n.t.p. For the argon based mixture this results in a mean energy necessary for the production of an electron-ion pair of 26.4 eV and for the helium based mixture in average 39.8 eV are necessary. The underlying simulation is described in section 2.4.

allow to calculate the mean energy necessary for the creation of a single electron-ion pair, which in gaseous detectors is typically in the range between 10–50 eV, but there are indeed some fluctuations in the amount of energy an initial particle has to lose in order to create a single electron-ion pair. This can be seen for the example of two commonly used gas mixtures in figure 2.4, which shows the simulated spectrum of necessary energy loss per produced electron-ion pair. Depending on the energy-loss of the traversing particle and the medium this leads to a trace of electrons in the gas, which consists of agglomerations of small electron clouds. For example for muons of 120 GeV in Argon this yields an average of 35 clusters per cm track length of the traversing particle with an average of 2 electrons per cluster [Blum et al., 2008]. For the reconstruction of the track additionally the extent of every cluster is of great importance, as primary electrons with high energy impair significantly the reconstruction of a track in the detector (compare 2.7.7).
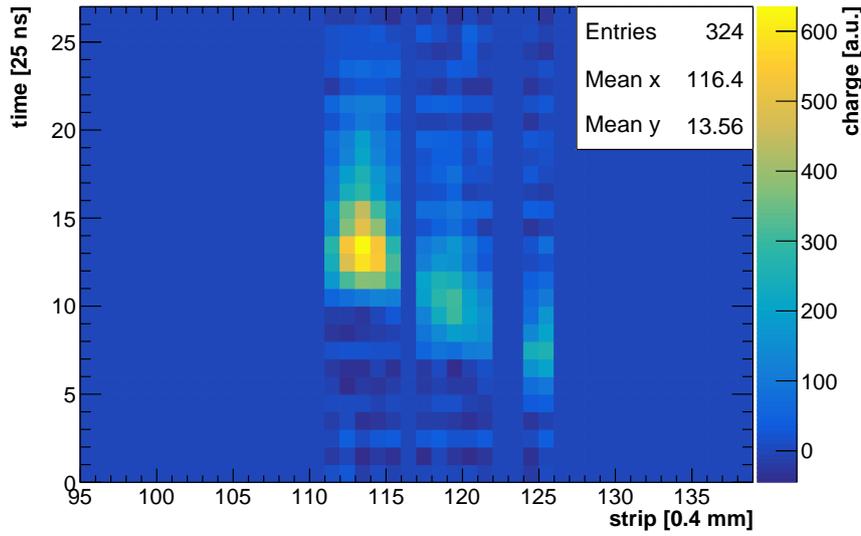
Figure 2.5: Event display of a clustered track recorded from a cosmic muon

2.3   Charge Transport and Amplification

In order to be measured the electrons from the charged track have to be guided to some read-out pattern, which is done by electric fields. By the electrostatic force originating from these fields it is ensured that the electrons do not instantaneously recombine with the ions in their vicinity and additionally the electrons are pulled towards an anode.

2.3.1   Electron Transport in a Gaseous Medium

The electrons move along the field lines of the electric field and gain kinetic energy in this process, but as they are very light they lose their initial direction constantly by scattering on the much heavier gas atoms. This scattering is practically isotropic and therefore the resulting velocity of the electron is described by the acceleration it experiences between two collisions v and its immediate randomly oriented velocity w. Following [Blum et al., 2008] the velocity v between two encounters with the gas atoms can then be described by the acceleration due to the electric field E and the mean time between two impacts t.

$$v = \frac{eEt}{m_e} \tag{2.13}$$

This drift velocity is lost on average again in the next inelastic collision by recoil or excitation, which leads to a balance of gained energy from the electric field and losses due to collisions with an equilibrium energy H_0 and an energy loss of a fraction ϵ with every collision:

$$\frac{x}{vt}\epsilon H_0 = eEx \tag{2.14}$$

As the thermal energy here can be neglected[2] the equilibrium energy is defined by:

$$H_0 = \frac{1}{2}m_e w^2 \tag{2.15}$$

The time between two collisions can be calculated in the limit of much higher energy of the electron due to the electric field than from thermal motion by:

$$t = \frac{1}{N\sigma w}, \tag{2.16}$$

---

[2]For electrons at room temperature and this energy is $\frac{3}{2}k_B T \simeq 0.04\,\text{eV}$ with the Boltzmann constant k_B and the temperature T
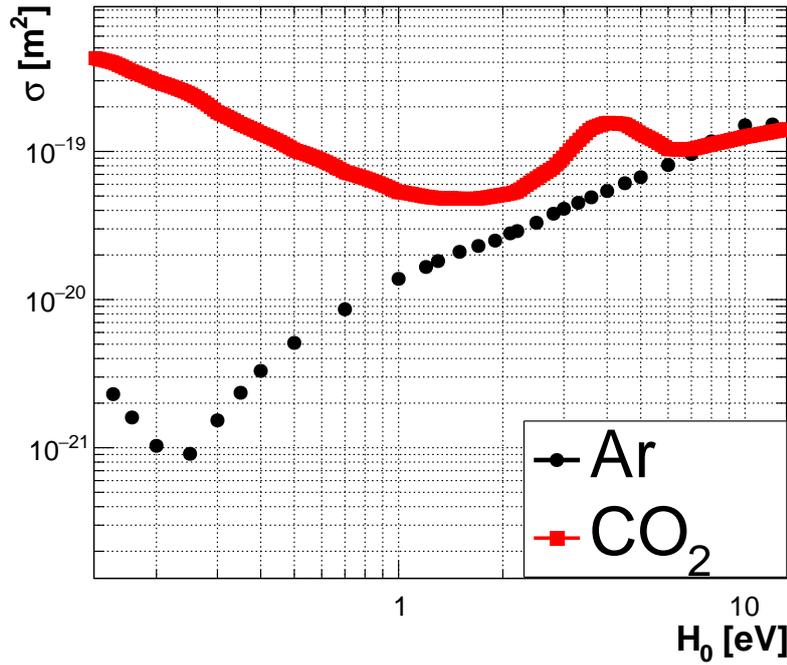
Figure 2.6: Momentum transfer cross-section for Ar and CO_2 as a function of the equilibrium energy. The data is taken from [Hagelaar and Pitchford, 2005] and [Alves, 2014] for CO_2 and [Phelps, 2017] for Ar.

where σ is the cross-section for a collision and N the particle density. Both equilibrium velocities than can be written as follows:

$$v^2 = \frac{eE}{m_e N\sigma}\sqrt{\frac{\epsilon}{2}} \tag{2.17}$$

$$w^2 = \frac{eE}{m_e N\sigma}\sqrt{\frac{2}{\epsilon}} \tag{2.18}$$

The exact drift velocity in a gas mixture is not only depending on the electric field, but also on the specific mixing proportion. Here it has to be considered that the fractional energy loss ϵ and the cross-section σ are not independent of H_0 as it can be seen in figure 2.6 for the two gases Ar and CO_2. The effective cross-section of Ar shows a clear minimum at $H_0 \simeq 0.2$ eV the so called Ramsauer minimum (see [Ramsauer, 1921]). The reason for this behavior is described by [Allis and Morse, 1931] by quantum mechanical processes in the scattering of the electrons with the gas molecules. This behavior however is not always shown in other gases.

In the additional presence of a magnetic field $\vec{B}$ the drifting electrons also experience the magnetic force:

$$\vec{F}_b = e|\vec{v}_D \times \vec{B}| \tag{2.19}$$

Balancing the electric force $\vec{F}_E = e\vec{E}$ and the magnetic force the resulting drift direction can be calculated by:

$$eE\sin\alpha = ev_D B$$

$$\sin\alpha = \frac{B}{E}v_D, \tag{2.20}$$

which allows to describe the resulting electron trajectory by the so called Lorentz angle α, which is the deviation from the drift direction with respect to the electric field. With the motion in the magnetic field also the drift velocity is slightly altered, which unfortunately cannot be calculated easily, as here the microscopic interaction of the electron with the drift gas has to be considered.

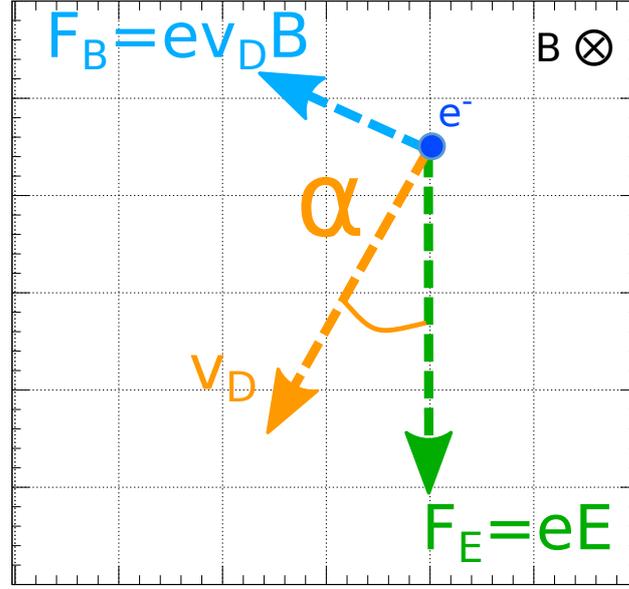Figure 2.7: Resulting deflection of the electron drift in an electric field under the influence of a magnetic field $\vec{B}$. The deviation from the electric field E is described by the Lorentz angle α.

In the absence of an electric field, free electrons start to diffuse from their initial point of creation. Their quick energy loss in form of collisions with the gas atoms evokes a fast thermalization of the electrons and from the kinetic gas theory their velocity can be described by:

$$v = \sqrt{\frac{8k_B T}{\pi m_e}}, \tag{2.21}$$

which is depending on Boltzmann constant k_B and the temperature of the gas T. Under the assumption of an arbitrary direction change with every collision the distribution of N_0 electrons from the origin in a distance r after a time t can be described after [Leo, 2012] by:

$$\frac{dN}{dr} = \frac{N_0}{\sqrt{4\pi Dt}} e^{-\frac{r^2}{4Dt}}, \tag{2.22}$$

where D is the diffusion coefficient which is a measure for the standard deviation of the distribution:

$$\sigma(r) = \sqrt{6Dt} \tag{2.23}$$

In the presence of an electric field the diffusion can be split into two components, the longitudinal diffusion along the direction of the electric field and the transverse diffusion perpendicular to the drift of the electrons.

The requirements for a gas used in a detector are a sufficiently high electron lifetime, which means that electrons can be guided through the detector at least several millimeters before they are captured or get attached, and that a stable avalanche amplification is possible. The two examples of Ar and CO_2 are actually a very common combination for gaseous detectors, whereby counting gases are mostly mixtures of a noble gas with a molecular organic gas (see e.g. [Nakhostin, 2017]). Besides the possibility to fine-tune the electron motion by selection of a suited gas mixture the purpose of the organic gas, often also referred to as quencher gas, is to absorb photons produced in the gas amplification process. These photons could produce unwanted de-localized charge all over the detector. Organic gases, due to their high amount of rotational and oscillatory degrees of freedom, have a high absorption capability for the complementary UV-light produced in the amplification stages ([Blum et al., 2008]). All measurements, which are shown in this thesis have been performed with an admixture of argon and carbon-dioxide with relative composition of 93:7 Vol%.
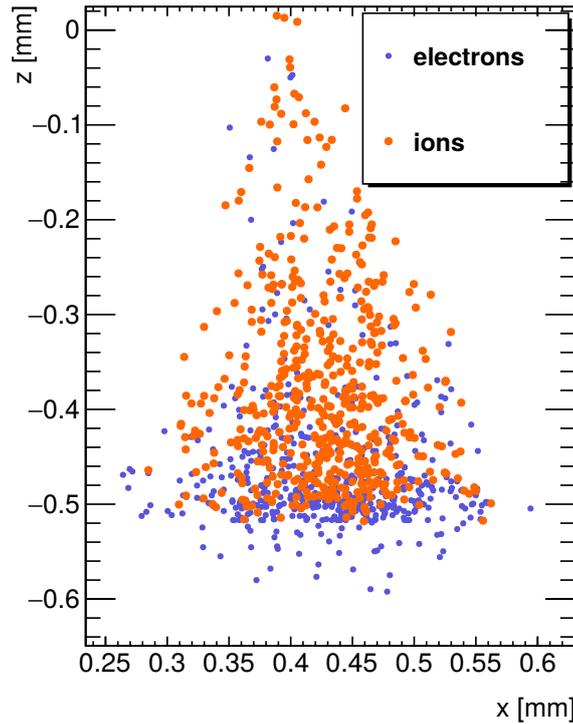
Figure 2.8: Garfield Simulation (see section 2.4) of a Townsend-avalanche in a single GEM-hole

2.3.2 Amplification Process

As mentioned earlier the amount of electrons in a gaseous detector is usually too low to be directly measured, which is overcome by multiplying them with a high electric field. Due to this field the energy transfer on a single electron between two collisions is sufficient for it to reaches an energy, which allows the ionization of another atom. This leads to a subsequent increase of free electrons, a process which is called Townsend-multiplication. As every electron itself can be accelerated and ionize further atoms this causes a Townsend-avalanche of electrons an ions. The multiplication itself on a path from r_1 to r_2 can be described by (see [Kleinknecht, 1998]):

$$G = e^{\left[\int_{r_1}^{r_2} \alpha(x)dx\right]},$$ (2.24)

where α is the first Townsend-coefficient, which is a function of the electric field and the gas. This dependence has been parameterized by Rose and Korff [Rose and Korff, 1941] and can be used to describe the gain also in a GEM-detector.

$$\frac{\alpha}{n} = A_0 e^{-\left(\frac{B_0 n}{E}\right)},$$ (2.25)

where A_0 and B_0 are gas constants, E is the applied electric field and n is the particle density in the gas. This avalanche like amplification with exponential growth of the amount of electron-ion pairs leads to a rain drop like shaped cloud in the amplification area. A simulation of this is shown in figure 2.8.

The detectors used here were always operated at voltages where an increase in the amplification voltage ensured an exponential increase in the pulse height. Depending on the absolute value of the electric field this is not necessarily true for all gaseous detectors. The range of voltages covered so far is called the proportional counting region. Here the number of electrons reaching the anode is proportional to the number of primary electrons and therefore to the energy loss in the drift region. Increasing the voltage further would lead to a Geiger–Müller counter, where an incoming particle produces a vast amount of avalanches in the whole detector, which are also driven by ultra violet radiation produced by the avalanche amplification. These avalanches are
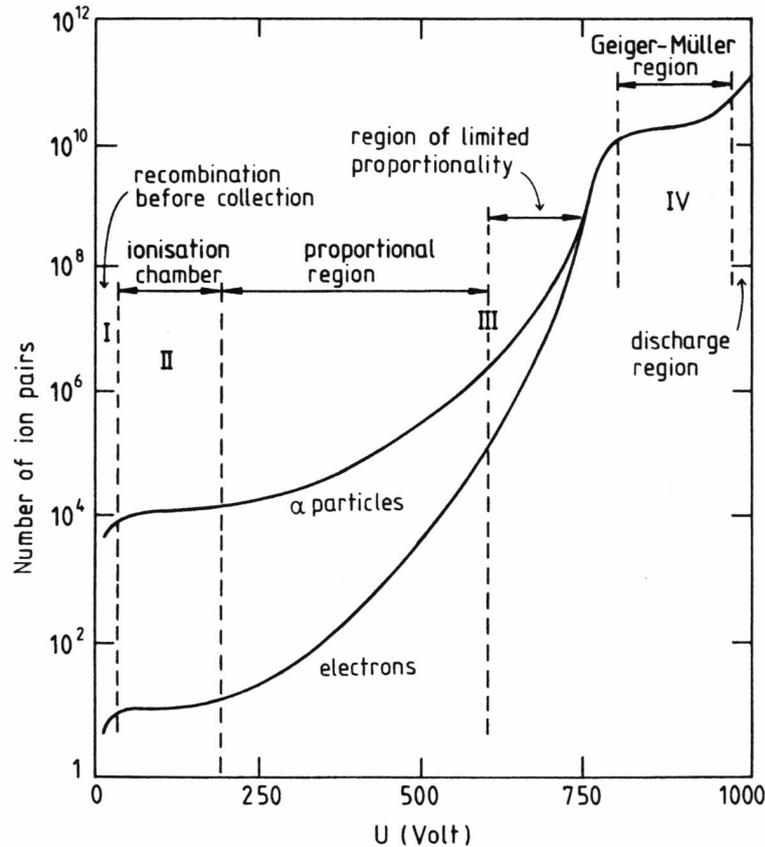
Figure 2.9: Different operation regions of gaseous detectors in dependence of applied electric field (taken from [Melissinos, 1966]).

terminated eventually by a breakdown of the amplification voltage, which is slowly recharged by a quenching resistor. As here every incoming particle leads to a similar response, detectors of this type are mostly used for counting particles. Further increasing the voltage can lead to self triggered continuous discharges. On the other hand decreasing the voltage too much would lead to no amplification at all, which is used in ionization chambers were only the primary charge is collected and measured. Even further decreasing the voltage would lead to an increasing fraction of the ions and electrons, which recombine before they can be detected at an electrode. A schematic of the different regions depending on the applied voltage can be seen in figure 2.9.

2.4   Garfield Simulation of the Signal Creation at the Read-out Anode

The simulations previously described in the course of this thesis, were carried out by a combination of the three tool-kits: Garfield++, MAGBOLTZ and Geant4. In this section the general structure of the simulations will be defined, whereas predictions and comparison with measurements follow in the subsequent chapters.

A quantitative simulation of the signal, the motion of the electrons and the creation of the primary electrons from charged particles can only be achieved by a full simulation of the detector, which was done with Garfield++ [Veenhof, 1998]. Garfield++ is a software tool-kit with the aim to simulate gas filled detectors. It allows to simulate a whole detector and events from the energy-loss of charged particles in the counting gas [Smirnov, 1997], to the transport of the ions and electrons in the electric field, the subsequent simulation of gas amplification and the generation of Townsend avalanches and finally the calculation of the expected signal in the read-out electronics. In Garfield++ the MAGBOLTZ [Biagi, 2000] software is used to calculate the transport of electrons in the gas or gas mixtures, which also directly allows to calculate gas parameters like the electron drift velocity or diffusion coefficients depending on the electric field. In Garfield a full geometric
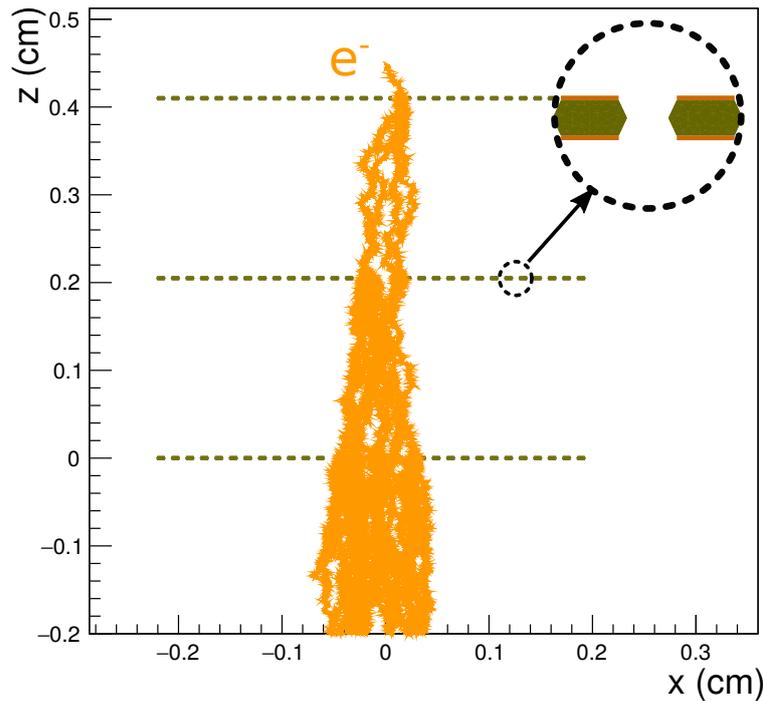
Figure 2.10: Sectional drawing of a standard triple GEM with the simulated motion and amplification of a single primary electron for E_{Drift}=300 V cm^{-1}, E$_{Trans1/2}$=1 kV cm^{-1}, E$_{ind}$=2 kV cm^{-1} and ΔU=350 V. This lead to a total simulated amplification in this example of about 10000.

model of the three layer GEM-detector has been imported in order to directly compare simulation results with a real detector.

Garfield itself can analytically calculate simple electric field geometries, but is not capable to compute the complex electric field inside the complicated structures of a full detector itself, therefore the finite element solver Elmer [Lyly et al., 1999] was used to calculate the electric fields at specific nodes, which Garfield could use to extrapolate the fields in the whole detector. An example of the full simulation of an event for this detector is shown in figure 2.10, where the path of electrons emerging from a single primary electron through the three amplification stages to the anode is shown. These simulations allowed to predict the amplification for different field configurations, the spread of the electron cloud due to diffusion at the anode, the drift velocity of the electrons and also the expected signal shape. Here and in the following the coordinate system used will be oriented in a way, that the X- and Y-axis are equivalent to the direction of the read-out strips and the Z-axis points towards the cathode.

The underlying primary interaction of particles in the detector, the production of primary electrons, straggling of the particle or conversions however are only rudimentarily implemented in Garfield. The Geant4 [Agostinelli et al., 2003] tool-kit on the other side allows to calculate the interaction of particles in matter with high precision and was used to simulate all relevant interactions in the detector, which lead to primary electrons in the drift region of the detector. Here again a full description of the detector was necessary, but instead of the electric field configuration the focus lied on the correct description of the materials used in the detector. This allowed to calculate the position of primary electron production in the drift region for different production processes and also the motion of particles before their entering into the detector, for example the scattering of thermal neutrons in a collimator system in chapter 3.

2.4.1 Electron Drift Velocity and Diffusion in Ar-CO$_2$

A crucial role in the course of this thesis will be assigned to the electron drift velocity in the gas. One key aspect of the position reconstruction later will be the use of the detectors in a Time-Projection-chamber (TPC) like mode. The basic idea of a TPC, which was first described by [Nygren, 1974],

is to use the timing information of the drifting electrons in order to reconstruct their origin. As previously described, the drift velocity of the electrons is depending on the electric (and magnetic) fields they are moving in. With known field configuration and drift velocity the time of arrival of the electrons relative to the passage of a particle through the detector can directly be translated to a distance from the read-out along the electric field lines where the electrons were produced. In the absence of a magnetic field for planar Micro Pattern Gaseous Detectors (MPGD) this simplifies to a position measurement in the Z-position by a drift time measurement. This information can be used for full particle tracking in a single detector layer. As the drift gap in the detectors used here is large compared to the structures of the MPGDs the electric field in the drift region is nearly homogeneous, as it can be seen in figure 2.11 from an electrostatic simulation for a single GEM-detector.
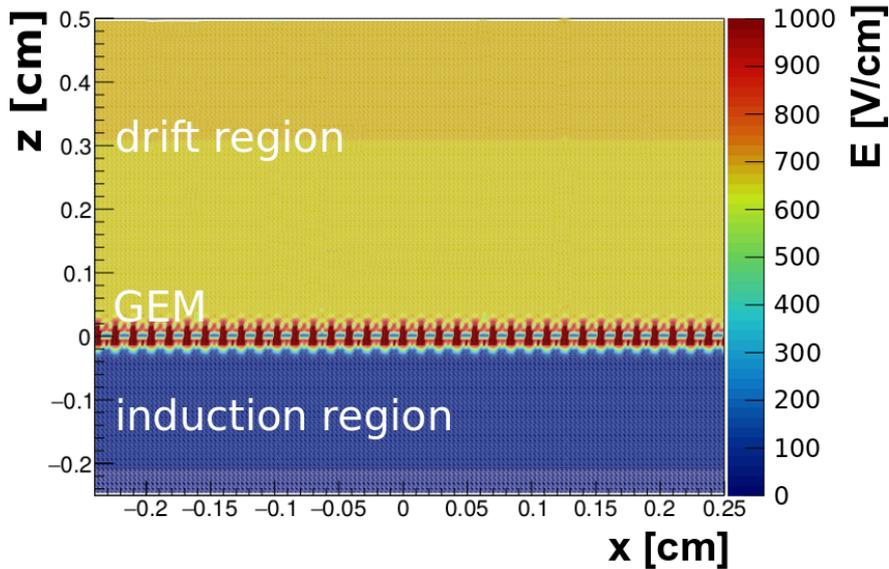
Figure 2.11: Simulation of the electric field components E_z normal to the read-out plane for a single GEM-detector. Distortions of the electric field above and below the GEM are limited to a range of <0.25 mm, which leads to a nearly uniform electric field in the drift region.

The assumption of an uniform electric field in the drift seems therefore well justified and leads to an electron drift velocity dependence on the electric field as shown in figure 2.12(a) for the gas mixture of Ar-CO_2 93:7 Vol% at standard conditions. The simulations used here are described in section 2.4. This gas mixture has a characteristic fast rise of the drift velocity at low electric fields
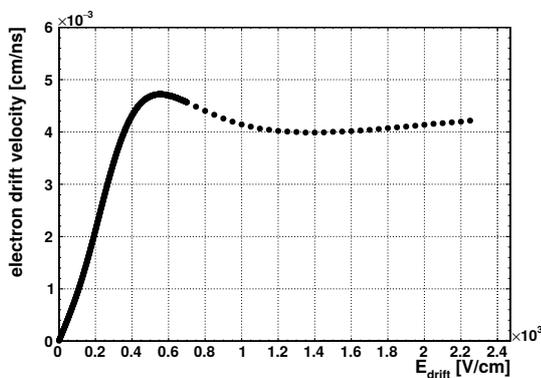
(a) Simulated mean electron drift velocity in the direction of the electric field for a mixture of Ar and CO_2 at standard conditions
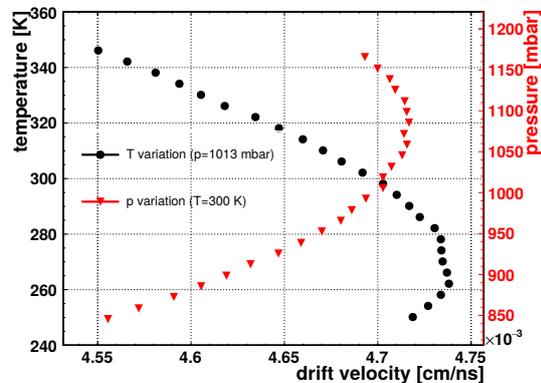
(b) Electron drift velocity for a gas mixture of Ar-CO_2 93:7 Vol% at an $E_{drift} = 600\,\text{V}\,\text{cm}^{-1}$ plotted as function of temperature and pressure

Figure 2.12
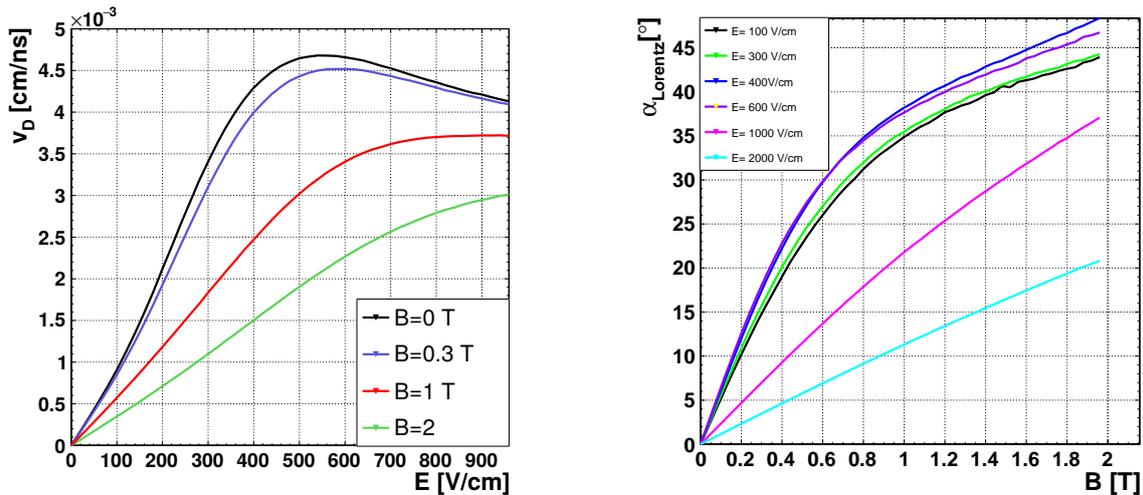
(a) Simulated electron drift velocity in the presence of an additional magnetic field perpendicular to the electric field.

(b) Simulated Lorentz angle in dependence of the magnetic field for different combinations of electric fields.

Figure 2.13

and a local maximum of the drift velocity around an $E_{drift} \simeq 600\,\mathrm{V\,cm^{-1}}$ followed by a plateau, meaning that only in the low field regions slight changes in the electric field have a strong influence on the drift velocity. The drift velocities of the gas mixture used here are in the range between 10–50 µm ns^{-1}, which means for the typical size of the active regions, which will be used in this thesis, relative time differences in the order of 100 ns between the first and last electrons reaching the read-out anode.

For a strip read-out this also has the direct implication that the maximum rate capability of the detector is limited by the drift velocity. The limit here would be reached if two particles hit the same or an adjacent group of strips within the time window defined by the drift velocity. Signals from more particles in the same area and timing become indistinguishable then (see also chapter 7). One big advantage of MPGDs is that they can be used with gases at standard conditions, i.e. atmospheric pressure and room temperature, which means they can be built with low material budget. Fluctuations in the ambient temperature and pressure have only minor influence regarding the electron drift velocity as it can be seen in figure 2.12(b) for an $E_{drift} = 600\,\mathrm{V\,cm^{-1}}$. Here the simulations with a variation of the temperature at fixed pressure of 1013 mbar (black scale and data points) and the variation of the pressure at fixed temperature of 300 K (red scale and data points) are shown. Over the whole range of these variations the electron drift velocity changes by about 4 % only.

The presence of a magnetic field has not only direct influence on the direction of the electron drift, but also alters the drift velocity (see section 6.6). The influence on the relative direction of the drift strongly depends on the actual drift velocity as it can be seen in the figures 2.13(a) and 2.13(b). For mixtures of Ar and CO_2 simulations show a general decrease in the longitudinal electron diffusion with the electric field due to the increased drift velocity in the range between 200–600 V cm^{-1}. This can be seen for an effective diffusion coefficient D_{eff}, which describes the diffusion after one cm of drift in figure 2.14. In the same region for this gas the transverse diffusion increases due to the decrease in the mean free path length with the on average increased electron energy in CO_2 [Binnie, 1985].

2.4.2 Signal Calculation and Charge-Sharing

The signal on a read-out structure is caused by motion of charge carriers between electrodes. These charge carriers cause a current onto the electrodes, supplied by a reservoir originating in the electric
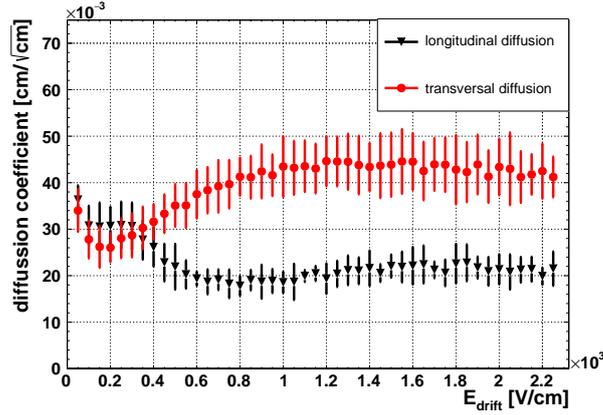
Figure 2.14: Simulation of effective transverse and longitudinal diffusion coefficients for Ar:CO$_2$

potential the electrode is connected to. This in general leads to two contributions to the measurable signal, which emerge from the two different types of charge carriers. For a set of electrodes A_n the current signal due to the motion can be calculated from the mirror charges Q_n on these electrodes. Assuming a slow movement of the electrons and ions in the gas - as it was done by [Ramo, 1939]- this signal can be calculated electrostatically by the Ramo Theorem:

$$I_n^{ind}(t) = -\frac{dQ_n(t)}{dt} = \frac{q}{V_w}\nabla\psi_n[x(t)]\frac{dx(t)}{dt} = -\frac{q}{V_w}E_n[x(t)]v(t) \tag{2.26}$$

Here the motion of the charge q is described by $\frac{dx(t)}{dt}$ towards an electrode set to voltage V_w. The so called weighting field E_n of the electrode can be calculated iteratively by adding a potential ψ_n to the electrode and grounding the rest of the electrodes in the system.

In the case of a GEM-detector the signal component due to the ions is negligible, because the ions are produced far away from the read-out in the holes of the GEM-foils and the read-out is shielded from the influence of the ions by the complementary electron cloud. The signal therefore consists mainly of the drifting of the electron cloud towards the anode and the shape of the signal is dominated by the drift velocity of the electrons in the induction region. The induced charge on the read-out shows a timing behavior as shown in figure 2.15(a), where a typical signal has been calculated for a distance of a GEM to the read-out anode of 2 mm with an E$_{ind}$=400 V resulting in an electron drift velocity in Ar-CO$_2$ 93:7 Vol% of $(41 \pm 2)\,\mu m\,ns^{-1}$. The motion of the electrons and ions was calculated by a Garfield simulation and the weighting field of a single read-out anode was calculated by Elmer.

In the case of the micromegas, discussed in chapter 6, the two components of the signal are more clearly separated as shown in figure 2.15(b). A fast negative component comes from the drift of the electrons in the amplification region, as this zone typically is around 100 μm wide this signal in the order of 2 ns. After the electrons reached the read-out structure the signal is dominated by the slow drift of the remaining ions towards the micromesh. The ions are about a factor of 100 slower than the electrons and the signal component due to the induced current in the read-out is much slower with a corresponding duration of more than 100 ns.

So far only an unsegmented read-out anode has been considered. For a segmented read-out, which allows position reconstruction, some correlations between the signals on adjacent structures occur close to the actual electron or ion cloud, which forms the signal. This will be discussed here for the example of a copper-strip read-out identical to the design of the GEM-detectors used in the following chapters. In the case of a typical GEM-detector, where the induction region is large compared to the distance of the read-out strips the weighting fields of neighboring strips have a considerable overlap. Even for a point like electron cloud located directly above a strip this leads to very similar signals on adjacent strips, which can be seen in figures 2.16 and 2.17(a). Figure 2.16 shows the calculated charge signal for a signal consisting of 15 electrons drifting towards the center of 20 consecutive strips and figure 2.17(a) shows the fraction of the full signal on the
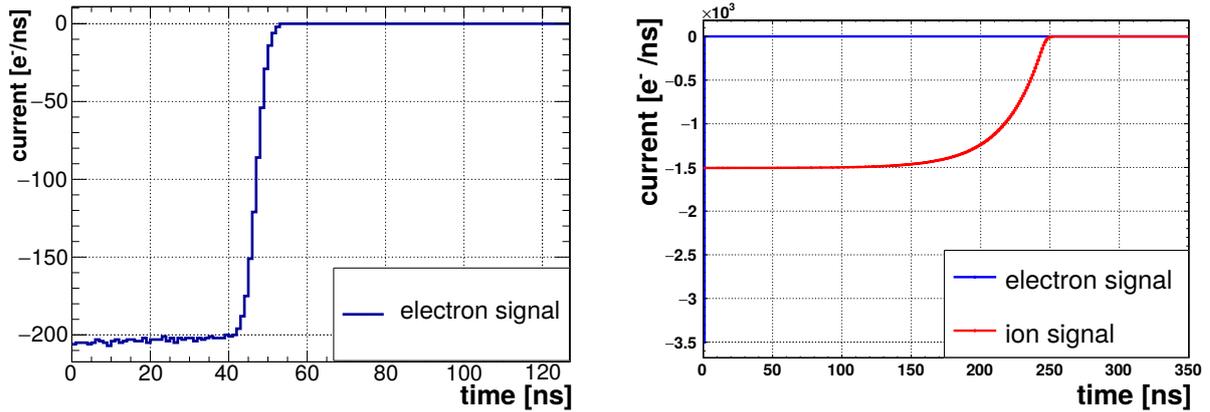
(a) Calculated signal of a single anode segment in a GEM-detector caused by the drift of an electron cloud towards the read-out structure. The influence of the ions on the signal on this scale would not be visible and is therefore not shown.

(b) Calculated signal components for a micromegas detector. The much higher velocity of the electrons and their relative low distance to the read-out structure causes a fast peaking signal in the first 5 ns. The ions, which are slower and have to travel through the whole amplification region to reach the micro-mesh add a slower component of $\mathcal{O}(100\text{ns})$ with the same polarity

Figure 2.15

neighboring strips. The simulation was based on a strip pitch of 400 μm, a strip width of 80 μm, a strip thickness[3] of 35 μm, a width of the induction gap of 2 mm and an $E_{ind} = 2\,\text{kV cm}^{-1}$. Here the charge signal, i.e. the integrated current, is shown.

As long as the electrons are far away the neighboring strips see a signal similar to the central strip, with 80 % of the pulse-height for the next neighbors and still 20 % for the fifth neighbor. As the electrons drift towards the anode, the fraction of charge the other strips see decreases continuously until the electrons reach the anode. In this specific case the charge sharing for the first neighbor reaches a final coupling of 15 % of the cumulative charge on the central strip. The final coupling of the second neighbor is already as low as 0.8 %, because in the region close to the read-out the first neighbor shadows the signal on the following strips. For neighbors even further away the final charge sharing is completely negligible, as it can be seen in figure 2.17(a).

In the case of a strongly confined electron cloud this behavior helps to determine the position with higher accuracy, as the relative charge on the different strips allows to reconstruct the position of the initial charge cloud with an accuracy well below a strip pitch. For broad charge clouds, which also reach the read-out structure over a longer time interval, this cross-talk on the other hand influences the signal shape of strips, which are reached later by the electron cloud. This causes a systematic error in the timing measurements based on the actual signal shape.

Recording this shape and subtracting subsequently the influence of the first responding strips to the following strips allows to compensate the timing shifts introduced by this cross-talk. To test this in a simulation, 1000 electrons were placed in a distance of 2 mm directly above the center of a strip and another 1000 electrons were placed in the same distance directly above the center of the next strip, but were released 5 ns later. This case is motivated by the similar signature of a particle, which traverses the active volume of the detector with a relative inclination of 30° with respect to the normal of the read-out plane. This simulation allowed to decouple the components of the signal due to both electron clouds on the second strip. In figure 2.18 both, the total signal and the signal component origin in the second electron cloud for this strip are shown. The timing of the total signal exhibited a clear shift and bulge emerging from the first electron cloud, which interferes with the timing measurement. Without the correction the timing of the second electron cloud in this example was shifted by 1.5 ns. The signal of the second electron cloud on the other hand could nearly perfectly be reconstructed by subtracting 15 % of the signal of the first strip, which allowed to reconstruct the correct timing of the second electron cloud.

---

[3]Which is a standard copper thickness on printed circuit boards and corresponds to 1 oz/ft^2
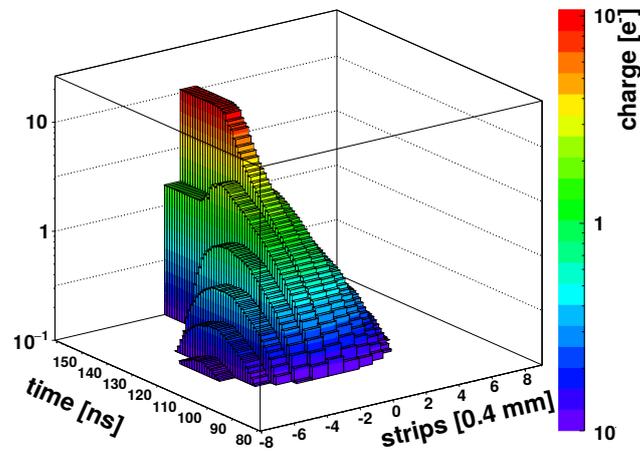
Figure 2.16: Calculated charge collected on neighboring strips for 15 electrons drifting through the weighting fields of the strips. The start timing of 100 ns is equivalent to an electron drift for five millimeters previous to the start of the amplification process.
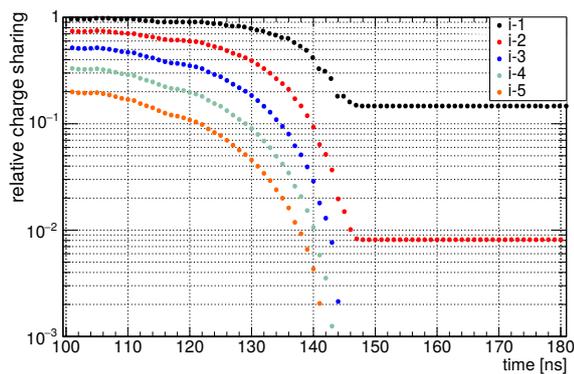
(a) Fraction of the signal the n-th neighboring strip sees if an electron drifts towards a single strip
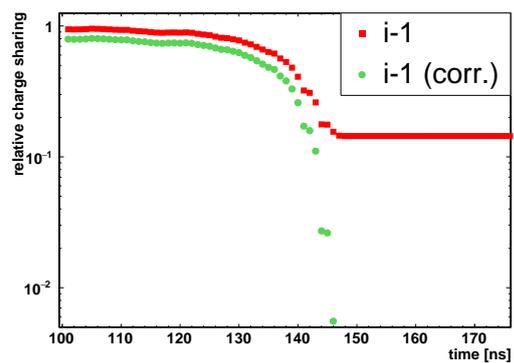
(b) Fraction of the signal on a neighboring strip before and after a correction of 0.15^i of the signal on the central strip

Figure 2.17
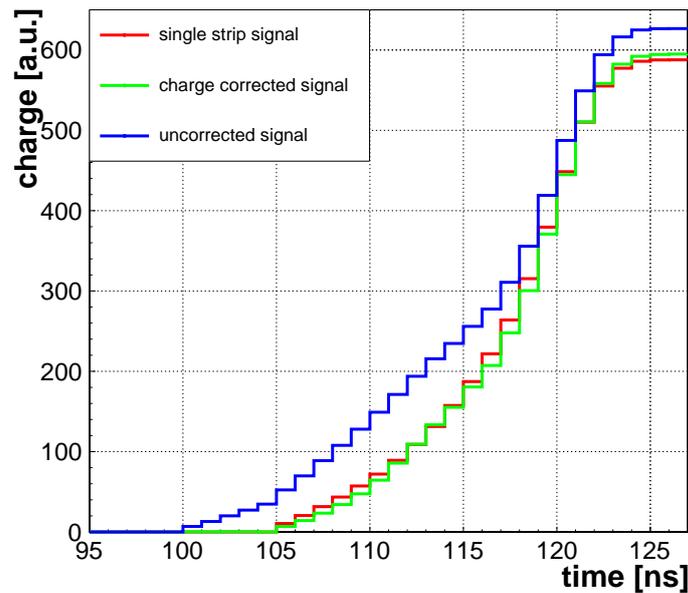
Figure 2.18: Calculated signal on a single strip for an event with two nearby electron avalanches located directly above adjacent strips and 5 ns earlier on the neighboring strip. The red signal corresponds to the strip signal of the electron avalanche directly above it. In blue the signal is shown, which contains the component of the other avalanche as well. Thus a bias and smearing is introduced, which would lead to a loss in timing accuracy in the reconstruction later. This bias is nearly completely removed by time wise subtraction of a fraction of the signal of the neighboring strip, which saw the full signal of the first avalanche, leading to the green signal.

2.5 Read-out Electronics - The Scalable Read-out System

The read-out of all detectors was based on different versions of the Scalable Read-out System (SRS) [Martoiu et al., 2013], which is a development of the RD51[4] collaboration. As the name suggests this system was developed in order to accommodate high scalability, but also to provide a read-out for a variety of read-out chips and detector technologies. The core components of this system are shown in figure 2.19.

One of the intends of this system was the usage within the LHC[5] read-out chain. Sampling is performed by default with the LHC bunch-crossing clock of 40.08 MHz and synchronization with this or any other clock is prepared (see [Zibell, 2014a]).

The connection to the detector is established by a front-end chip, which is usually an application specific chip (ASIC) and adapted to the detector system. An example of commonly used front-end chip for micromegas and GEM detectors is the APV25 [Raymond et al., 2000]. This ASIC, which was originally developed for the silicon tracker of the CMS experiment [French et al., 2001], contains 128 read-out channels, each of them equipped with a charge-sensitive pre-amplifier, shaper and analog pipeline memory. With every clock-cycle the signal for all channels are stored in this pipeline memory after amplification and shaping of the signals. The data from the APV25 chip can be read-out in up to 30 consecutive samples, allowing to reconstruct the pulse shape on every read-out segment of the detector in steps of 25 ns. The limit of the read-out rate is defined by the number of time-bins which are used, as the chip needs 140 clock cycles to send out the data on the analog line for every time-bin and therefore the maximum trigger rate for a clock of 40 MHz is

$285.7 \, \text{kHz} \cdot \dfrac{1}{\#\text{time-bins}} \simeq 11 \, \text{kHz}$ for 27 time-bins.

The APV25 chips in the context of the SRS are used on hybrid chip-carrier boards, which are

---

[4]`www.cern.ch/rd51-public`
[5]The Large Hadron Collider at CERN will be described in chapter 6
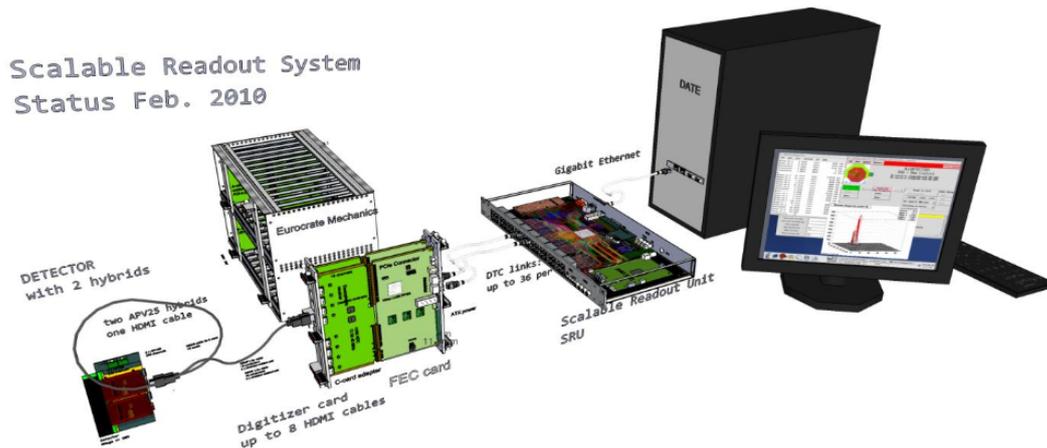
Figure 2.19: Schematic overview of the components of the Scalable Read-out Unit (SRS) (taken from [RD51-collaboration, 2010])
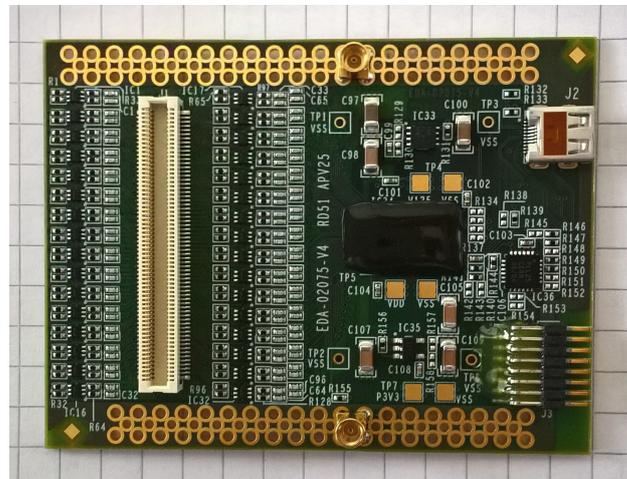
Figure 2.20: Master APV25-Hybrid board with protection circuits and connectors for connection with the detector (left) and mini-HDMI for the connection with the read-out system are visible. The actual APV25 chip is covered in black casting compound

shown in figure 2.20 and provide the necessary circuitry for direct connection to the detector and the rest of the SRS. On the detector side the board contains a network of protection circuits containing resistors and diodes to clip potentially high current signals, which occur due to rare discharges in the detector. The connection to the rest of the SRS is facilitated by HDMI cables, which supply the necessary power to the APV-boards and are also used for the bidirectional communication with the SRS. The hybrid-boards come in two different versions, master and slave, which are read-out in parallel by a single HDMI cable.

The hybrid-boards send their analog data to an Analog-to-Digital converter card (ADC), which is connected to a Front End Concentrator card (FEC). Up to eight pairs of hybrid-boards can be connected to a single FEC-card, thus allowing a total of 2048 read-out channels to be recorded. If a higher number of channels or additional pre-processing is needed one or multiple Scalable Read-out Units (SRU) can be added to the system. The SRU is based on a Virtex-5 Field-Programmable-Gate-Array (FPGA), which propagates a common clock and trigger to all connected FEC-cards and also handles the data coming from them. Single FEC-cards are connected to a SRU or directly to a data acquisition PC via 1 Gbit Ethernet connections. For the digital line the size of an event, which is dominated by the data samples for every strip and time-bin, is the limiting factor in the data acquisition rate. The size of an event from a fully equipped FEC-card with 16 APVs and 27 time-bins per strip is around 110 kB. This leads to a maximum digital read-out rate of $1100\,\mathrm{s}^{-1}$ over the Ethernet connection of the FEC-cards.

2.6   Software and Zero-Suppression

Depending on the number of FEC cards used, three different software versions were handling the data acquisition with the SRS system. In the case, where only a single FEC card was used like in chapter 3, the data stream coming from the FEC-card was recorded with the mmdaq software [Byszewski, 2012]. This software subtracts the specific baseline offset - the pedestal- from every strip, selects strips, which are considered as hit and saves the signal on those strips for every event. This selection is based on the sum of the signal on each strip. One way to read-out a higher number of FEC-cards was mitigated via a SRU, where a selection of the hit strips was done already on a hardware level directly by each FEC-card, which employed the same algorithm as the mmdaq-software. This set-up is described in [Lösel, 2017] and [Zibell, 2014b]. The on-line zero-suppression allowed data acquisition rates up to a few kHz. As the real occupancy by particles in the experiments described here was in the range between 1–3 % of all channels of a detector no loss in actual information was involved in this, as most channels contained only baseline noise. In the last case, see chapter 6, where the signal of 4 FEC-cards was recorded simultaneously, on-line zero-suppression has not been applied. Here an untested detector system was used for the first time, which additionally was prone to collect substantial noise on its read-out strips. Therefore a modified signal selection and noise canceling algorithm had to be applied off-line on the data in order to optimize the selection of hit strips. This was necessary because of common mode noise, which can be seen in figure 2.21(a). A clear signal on multiple strips is visible around the strip position 165. On all strips a sinusoidal structure is visible, which emerged by coupling of noise to the ground of the detector. This is called common-mode noise and led to non negligible distortions of the signal shape. Without adapted zero suppression it would culminate in an increased amount of falsely selected hit strips or even worse discarding strips, which actually were hit. This can be seen after application of the mmdaq intrinsic zero-suppression algorithm in figure 2.21(b), here most of the strips containing the signal survived the selection, but also false positive selected strips remained. The shape of the signal however still contains the ripples from the underlying noise.

As the amplitude of the noise on the non-hit strips is nearly identical for each time-bin this can be corrected by iteratively selecting hit strips and adding the baseline of the non-hit strips time-bin-wise to reduce the noise.

Selection of hit strips was done here in the following way: First the minimal value of each strip i was subtracted from all time-bins t at this strip $q_{it} = q_{0it} - q_{i_{min}}$, this corrects for the individual baseline of the respective electronics channel. The standard deviations of all time samples for every strip were then compared to the mean standard deviation for all strips. A strip was selected, if its standard deviation exceeded the mean standard deviation by a factor ZS=(1.5-2.5).

To compensate the common mode noise all strips, which were regarded to be not hit are then used to calculate the mean value for every time-bin, which was subtracted from the hit strips. As it can be seen in figure 2.21(c), this selection and correction reduced the influence of this specific kind of noise very well and led to an improved selection of strips with an actual signal on them.
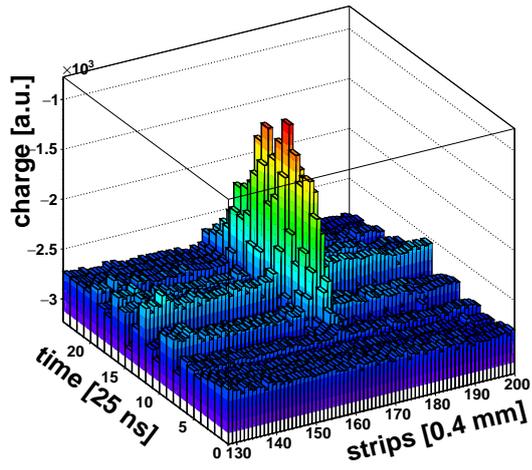
(a) Raw (inverted) output of the ADC with a clear signal signal around the strip position 165. Common mode noise on all channels is visible in the time-bin-wise wave structure. with
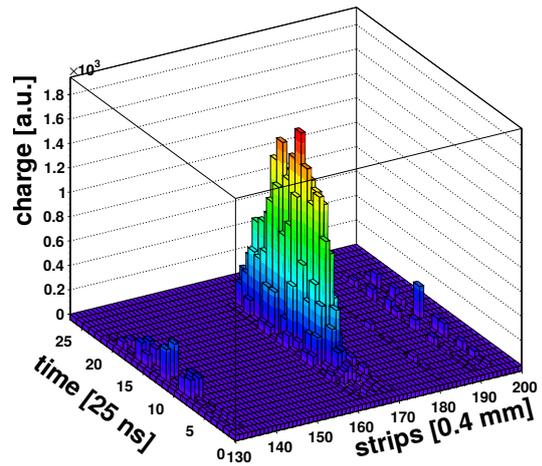
(b) Zero-suppressed and pedestal corrected version of the same signal, but the common mode noise is still visible
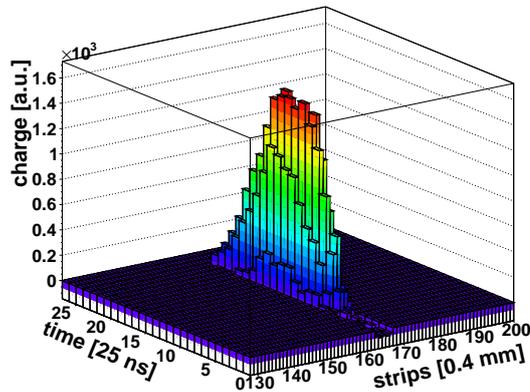
(c) Zero-suppressed, pedestal and common-mode noise corrected version of the same signal.

Figure 2.21

2.7 Signal Evaluation and Position Reconstruction

The position and the shape of the signals in the detector allow to reconstruct a wide range of the characteristics of the detected particle and its track in the detector. In this section the methods used in this thesis are described, which allowed to reconstruct the position and direction of a traversing particle from the response of the strip read-out with APV25-chips.

2.7.1 Evaluation of the Signal Shape

The different methods of the position reconstruction described later on depend all on the evaluation of the signal and its shape at the read-out strips. As it was described in section 2.4.2 the integrated signal on a single anode segment has a fast rising component, which is caused by the motion of the electron-ion avalanches in the gaseous volume. An additional slower component is the drain of the collected charge on the anode, which in the specific case of the APV25 is accomplished by a $1\,M\Omega$ resistor to ground in order to slowly discharge the anode again. A typical single strip signal with a fast rise-time and a slow drop recorded with a GEM-detector is shown in figure 2.22. The physically interesting part of this signal is mostly described by the rise of the signal, which was parametrized and evaluated by a fit using a Fermi function:

$$q\left(t\right) = \frac{Q}{1 + e^{\frac{t-t_0}{\sigma}}} + q_0,\tag{2.27}$$

where Q is the maximum of the charge distribution, t_0 is the point of inflection of the distribution, σ is a measure for the rise time and q_0 is the offset from the baseline to the zero value of the ADC. As the detectors used here are proportional counters, the total charge Q on all strips is proportional to the deposited energy in the drift region.

   The timing of a signal was determined by a linear extrapolation to the baseline from the values of the function, where it reaches 10 % and 90 % of its maximum.

$$t_{start} = t_0 - \frac{\log\left(81\right)}{2 \times 0.8}\sigma\tag{2.28}$$

This procedure allowed to reconstruct the start time of a signal with high precision and is nearly independent of the actual shape of the signal. This can be seen in the comparison of the extrapolated timing to the timing determined by the point of inflection of the fit, which is shown in figure 2.23. Here the timing of single strips are plotted for a measurement with high energy muons, which is described in chapter 5, against the strip charge. It would be expected, that the signal shape and the signal timing are independent of the charge collected at the read-out strips, which is actually the case in the range between 200-1000 ADC-channels. The two methods differ here only by a constant time offset. For higher charge deposition both methods exhibited a dent in the timing measurement, meaning that the timing for higher charge collection is biased towards earlier timings due to saturation of the APV's dynamic range. The extrapolated timing however is less affected by this, with a maximum drop of only 40 ns compared to 70 ns for the timing determined by the point of inflection.

   The rise time of a signal, which is depending on the detector geometry, electric field configuration and partly also on the shape of the track, can be described by the slope σ of the Fermi-function. From now on the rise-time will always be described by this parameter, as the determination of the full signal length is not well defined by this fit. Using equation (2.28) it can be seen that the time between any two percentages of the full signal are proportional to this parameter and for example the time t_{80} between 10–90 % of the signal is described by: $\sigma = t_{80}/5.5$

2.7.2 Charge Cluster Reconstruction

Due to the lateral diffusion, the amplification process and charge sharing it is highly unlikely that only a single strip of the read-out collects a signal from a traversing particle. On the other hand
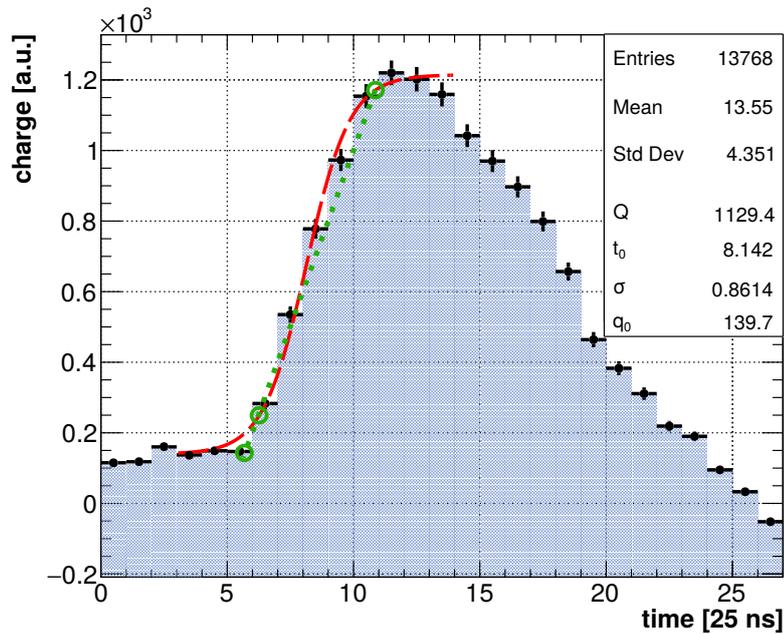
Figure 2.22: Single strip signal with a fit of equation (2.27) shown in red and the extrapolated from the fit start timing of the signal determined by equation (2.28) shown in green
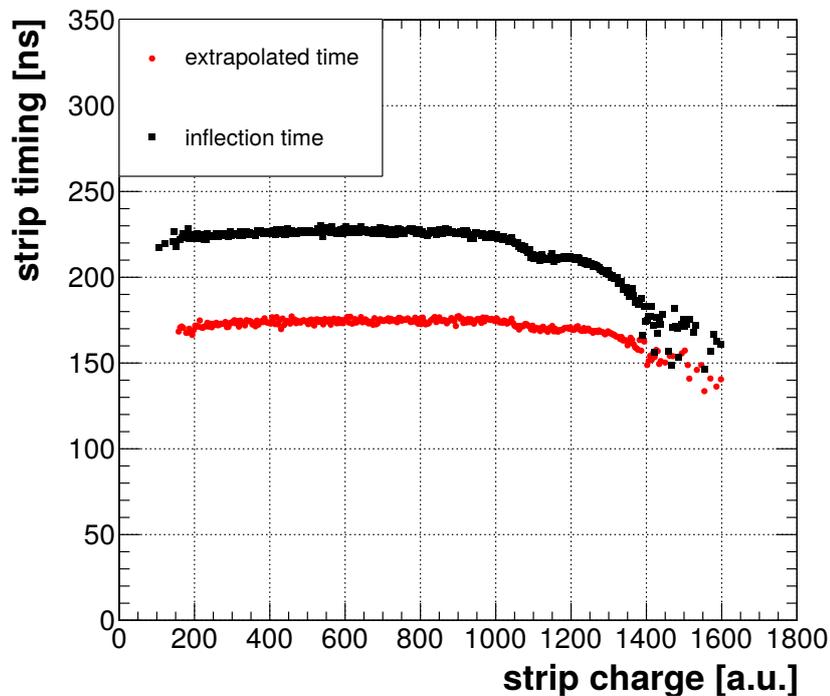
Figure 2.23: The comparison of the timing determined for the point of inflection and the extrapolated timing for every strip plotted against the charge of the strips shows a reduced distinct dependence of the reconstructed timing for high charges on a strip for the extrapolated time value.
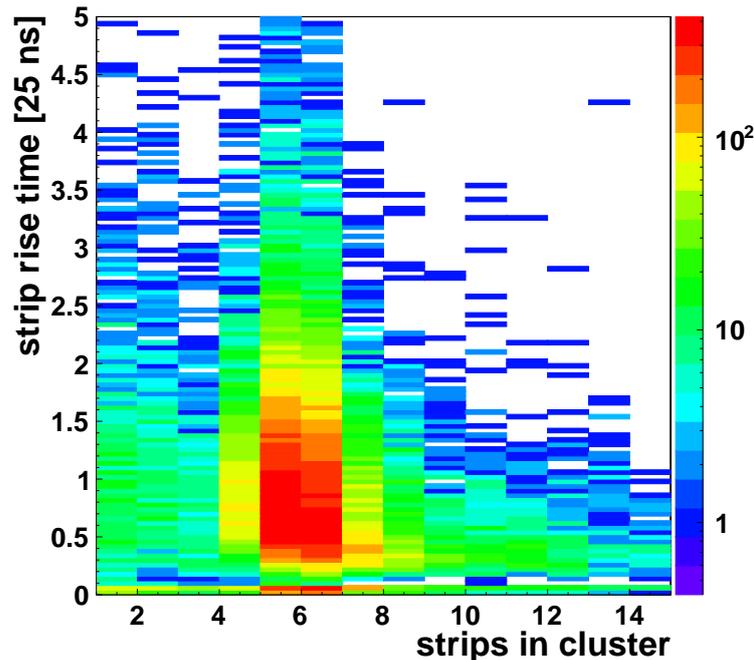
Figure 2.24: Rise-time from the Fermi-fit to all strips responding in a cluster plotted against the cluster size (i.e. number of consecutive strips hit) of the strip belonging to. As already described, rise-times below 3 ns are most likely caused by noise on a strip and indicate, that individual hit strips do not belong to real signals.

single strips with neighboring strips not hit, which survived the zero-suppression are very likely to be caused by noise. This can be seen from figure 2.24 for a measurement with a collimated muon beam, which hits a GEM-detector perpendicular to its read-out plane[6]. Here the rise-time of every strip is plotted against the number of consecutively neighboring strips exceeding the signal threshold (see section 2.6). The relative amount of strips with an unnatural short rise time of less than 3 ns for less than four adjacent strips is more than three times higher than for those with four or more strips, which means that agglomerations of less than 3 strips typically carry no particle signal. Full signals were constructed from single strips in the following way:

- At least three adjacent strips were hit

- Gaps of single strips in a group are allowed

- The sum of the charge of the strips is larger than 300 ADC counts

From now on a group of hit strips, which are assumed to contain all the information of a single particle, is called a charge cluster, which is not to be confused with electron clusters in the primary ionization process.

2.7.3 Centroid Position Reconstruction

One way to determine the position of a particles passing through the detector is to determine the center of charge or centroid which is defined as:

$$\vec{x}_c = \frac{\sum_{i=0}^{n} q_i \cdot \vec{x}_i}{\sum_{i=0}^{n} q_i} \tag{2.29}$$

Here $\vec{x}_i$ is the position vector of a read-out structure in the detector, here the strips, and q_i the charge collected at this structure. For a completely homogeneous track $\vec{x}_c$ is then the projected position of the center of the track on the read-out plane.

---

[6]The whole set-up is described in greater detail in chapter 5

Figure 2.25: Centroid and geometric mean position in this signal are identical. The centroid method delivers best results for a homogeneous charge distribution along the track.
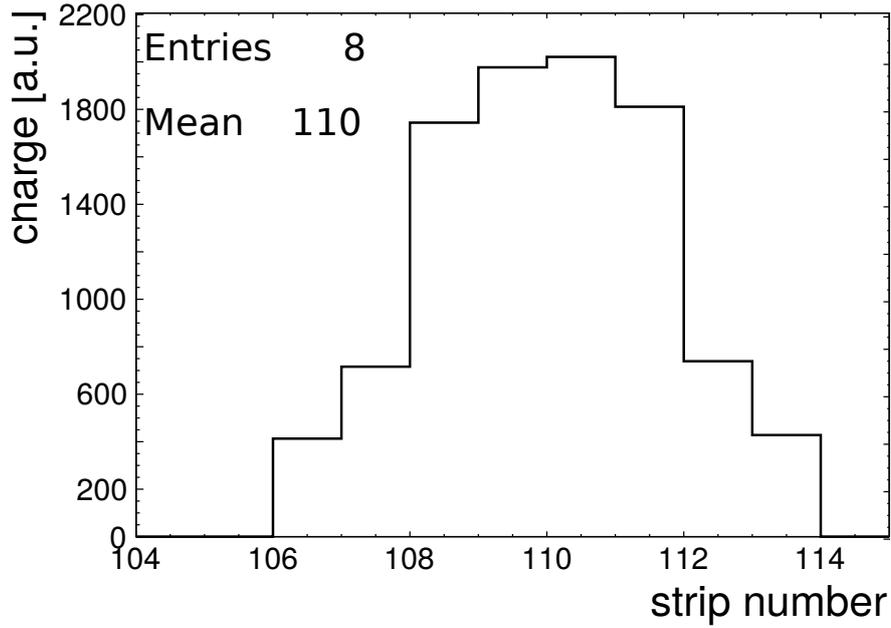
This well established method of determining the particle's transit position has the general advantage over the calculation of the geometric mean of a better substructure resolution, which is predefined by the detector granularity and the lower weight of signals caused by fewer electrons. The best results here are obtained if the charge distribution along the track is homogeneous. For inclined tracks one has to assume that the position of the centroid in fact is also in the geometric center of the track, for example shown in figure 2.25. For a very in-homogeneous charge distribution this leads to partly substantial deviations of the centroid from the true center of the track and therefore miss reconstructions.

2.7.4 µTPC Position Reconstruction

If a time resolving read-out is used the full track can be obtained by utilizing the uniform electron drift velocity in a homogeneous electric field. From the time of arrival of the collected electrons at the read-out structure the initial Z-position of the track can be restored. This concept is called Time-Projection-Chamber. They are often built in larger dimensions, especially with a large drift region. Fitting the position-timing distribution of the full track with a suitable function then allows to compute the position of the particle at every Z-position in the active volume. In particular this allows to calculate the track position at the center of the drift region. This concept in the context of MPGDs is called µTPC-method [Ntekas, 2016] and is shown in figure 2.26.

The position in z in the drift gap of thickness D for a particle, which traverses the detector under an angle θ can be described by slope $\tan\theta$ and intercept z_0 of a linear equation:

$$z = \tan\theta \cdot x + z_0 \tag{2.30}$$

From the edges of the track, which correspond to the minimal and maximal position in Z x_{min} and x_{max} the track inclination can be calculated approximately: $\tan\theta = \frac{x_{min}-x_{max}}{D}$ From this the position of the particle in the center of the drift region z_{mid} can be calculated by inversion of equation (2.30):

$$z_{mid} = \tan\theta \cdot x_{mid} + z_0$$

$$x_{mid} = \frac{z_{mid} - z_0}{\tan\theta} \tag{2.31}$$

In the detector z is not actually measured, but the time t the electrons for drifting from their initial point of creation in z-direction $z = v_D(t - t(z=0))$. $t(z=0)$ here corresponds to the timing
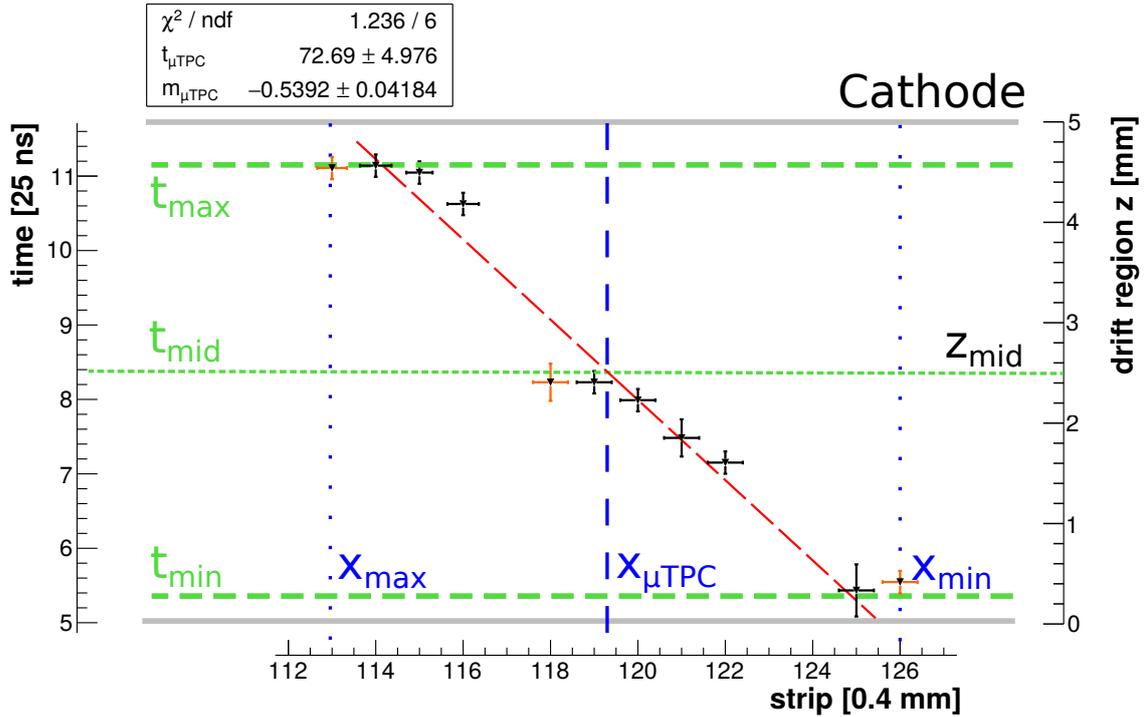
Figure 2.26: Extrapolated strip timing plotted versus the strip position and fitted with a linear function. The orange colored strips were discarded by the pre-selection and not used by the fit (the same event is show on figure 2.5)

of electrons, which are created at the lower end of the drift region at $z = 0$. This allows to rewrite equations (2.30) depending on the measured timing:

$$t = \frac{\tan\theta}{v_D}x - \frac{2\tan\theta \cdot sx_{z=0} - D}{2v_D} + t_{mid} \tag{2.32}$$

This again is a linear equation with slope $m_{\mu TPC} = \frac{\tan\theta}{v_D}$ and intercept $t_{\mu TPC} = t_{mid} - \frac{2\tan\theta x(z=0) - D}{v_D}$ and equation (2.31) becomes:

$$x_{\mu TPC} = \frac{t_{mid} - t_{\mu TPC}}{m_{\mu TPC}} \tag{2.33}$$

Together with the parameter t_{mid}, which has to be obtained from a calibration, this allows to calculate the position of the track at the center of the drift region z_{mid}. In an ideal case, where $t_{min} = t(z = 0)$, $t_{max} = t(z = D)$ and correspondingly $x_{min} = x(z = 0)$ and $x_{max} = x(z = D)$, this could also be parametrized by:

$$t = \frac{1}{v_D D}\left(x_{min} - x_{max}\right)\left(x - x_{min}\right) + t_{min}$$

$$x_{\mu TPC} = \frac{\left(2t_{min} + t_{max}\right) D v_D}{2\left(x_{min} - x_{max}\right)} + x_{min} \tag{2.34}$$

Since typically neither of these conditions are met, experimentally $m_{\mu TPC}$ and $t_{\mu TPC}$ are determined by a fit of a linear equation to the timing position distribution, which is exemplarily shown in figure 2.26. $x_{min/max}$ and $t_{min/max}$ typically are determined by strips with a low signal at the edge of charge clusters, therefore both position and time measurement can be biased by cross-talk and charge clustering.

The calibration parameter t_{mid} translates to the time between the trigger and the arrival of the electrons created in the center of the drift gap at the read-out electrode. This method in principle is more stable against charge fluctuations along the track, as the drift time of the electrons is hardly influenced by the number of electrons created and additionally allows to fully reconstruct the track of a particle.
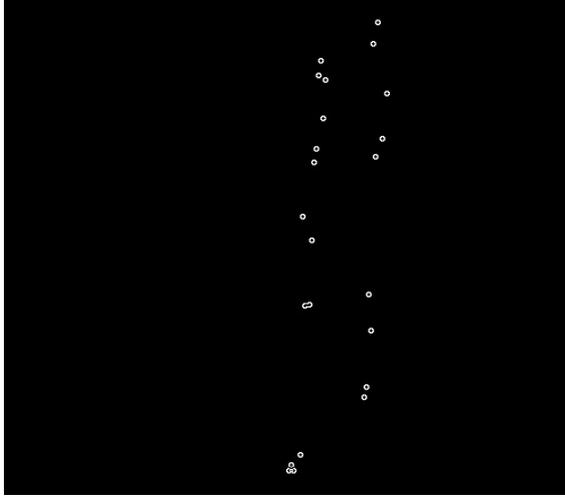
(a) Event display of an event with two nearby tracks with similar inclination, which could be misinterpreted as a single particle passing the detector.
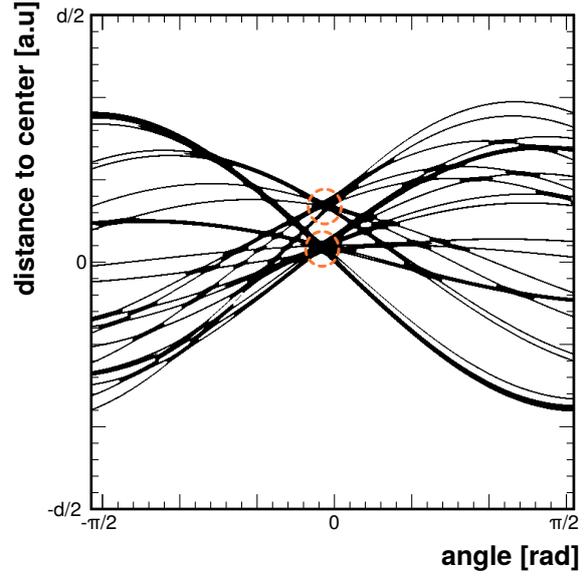
(b) Radon transform of the above event. Both tracks are clearly separated by different accumulation points, which represent straight tracks in the detector.

Figure 2.27

2.7.5 µTPC Strip Selection and Fit

As an accurate timing measurement of all selected strips is compulsory and the selection of strips in fact belonging to a track has a large impact on the quality of the reconstruction before the actual fit a pre-selection on the strips in a cluster was conducted by a pattern recognition algorithm. A pre-selection in the strips which are used for the fit is done in two different ways:

- A Radon transform on the time-position is performed in order to select timings which lie on a straight line

- A linear fit on the remaining timings is applied and all points which have a distance to this line larger than 0.6 mm are discarded

The Radon-transform [Radon, 1917] in two dimension is a special case of the Hough-transform [Hough, 1962]. The transform translates a function in the X-Y-space to a space of lines with parameters ρ and α. This leads to a sinusoidal curve $\gamma(\rho, \alpha)$ in the Radon-space[7] for every point in the X-Y-space p(x,y).

$$\rho = x \cos \alpha + y \sin \alpha \tag{2.35}$$

The corresponding curves of points, which lie on a straight line in the X-Y-space, intersect in the Radon-space at the position of ρ and α, which parametrized this line. Finding accumulations in the Radon space and determining the points in the X-Y-plane, which lie on the corresponding line allows to select straight tracks. A graphical example of this procedure can be seen in figure 2.27(a) and 2.27(b), where two tracks in close vicinity are shown. In the Radon transform, which here was implemented by the openCV-toolkit [Bradski, 2000], two clear agglomerations are visible, which correspond to the two tracks. By selecting all strips closer than $d < 0.85$ mm the tracks were formed. After this selection errors for the fit were assigned to the single strips in the way it is done in [Ntekas, 2016] described by equation (2.36). Here errors in the strip position σ_{x_i} are assigned to be the width of a strip pitch divided $\sqrt{12}$, which is then weighted by strip charge q_i in order to increase the weight of strips with higher charge:

$$\sigma_{x_i} = \frac{pitch}{\sqrt{12}} \sqrt{1 + \frac{q_{cl}}{n_{cl} q_i}} \tag{2.36}$$

---

[7]Technically the transform Rf is the set of line integrals $Rf(r, \alpha) = \int_{-\infty}^{\infty} f(r \cos \alpha + t \sin \alpha, r \sin \alpha - t \cos \alpha) \, dt$

Here n_{cl} and q_{cl} are the number of strips in the cluster and total charge in the cluster, whereas the error in the timing was determined from the fit-uncertainty of the Fermi-fit.

2.7.6 Determination of t_{mid}

The timing offset t_{mid} is a fixed value depending on the drift time of the electrons, the trigger and the read-out settings and has to be calibrated depending on the detector-settings.

Under the assumption that $t_{min} \simeq t_{mid} - \frac{D}{2v_D}$ and $t_{max} \simeq t_{mid} + \frac{D}{2v_D}$, t_{mid} can be obtained by calculation of the mean timing $t_{mid} = \frac{t_{min}+t_{max}}{2}$. As the values for single events can fluctuate significantly the mean value can be determined best by averaging over a large sample of events. A practical approach to this will be shown in chapter 5.

An alternative is to use a reference position and calculate the value t_{mid}. A possible reference value might be the centroid position x_c for a cluster and under the assumption $x_c \simeq x_{\mu TPC}$ equation (2.33) can be used for this calibration by:

$$t_{mid} = t_{\mu TPC} - x_c m_{\mu TPC} \tag{2.37}$$

This method in general is more robust as both fit parameters are determined after the selection of strips with good timing information.

### 2.7.7 Influence of Electron-Clustering on the Position Determination

The centroid method works best for short tracks or particles, which traverse the detector perpendicular to the read-out plane. A reason for this is the charge clustering along the tracks in the active drift region. The centroid position of particles, which traverse the detector under an angle and do not leave a homogeneous trace of electrons in the drift region is generally biased by the non-homogeneously clustered charge deposition in the drift area. The influence of the charge clustering on the position resolution was determined by means of a simulation. In a Geant4 simulation the production of electron-ion pairs was reproduced for muons of 120 GeV and alpha particles of 5 MeV, which were passing through a 5 mm wide drift gap filled with Ar-CO_2. The expected spatial resolution was then determined by calculation of the mean position of the electrons in one read-out direction for angles of $0°$, $10°$, $20°$, $30°$ and $45°$ and compared to the real position of the center of the track. In figure 2.28(a) this is exemplarily shown for the resulting distributions for 100000 muons of 120 GeV under an inclination of $20°$ and $40°$. The RMS of all distributions are shown in figure 2.28(b). The resolution here follows a trend, which depends on the slope of the track and was parametrized by:

$$\sigma(\theta) = \sqrt{\sigma_0^2 + (\sigma_{45} \tan \theta)^2} \tag{2.38}$$

With a minimal expected achievable resolution σ_0 for perpendicular tracks and σ_{45} the additional uncertainty coming from the inclination at $45°$.

For the muons this leads to a resolution in the range between 25 µm and 600 µm and for the alpha particles between 16 µm and 350 µm, which can be understood from the much lower free path length of the α particles and the much higher number of primary electrons. This leads to a much more homogeneous track.

By determining also the position in Z from the same simulation the limits of the performance for the µTPC-method could also be probed. Here a resolution of 25 µm for both particles and all angles, with the exception of $0°$ was observed. For perpendicular incident the spatial information only reached 1.2 mm. This in general suggests already, that for inclined tracks the µTPC method should have much less intrinsic limitations than the centroid method, albeit here neither timing resolution of a detector or read-out, nor the diffusion and amplification processes in the gas have been considered.
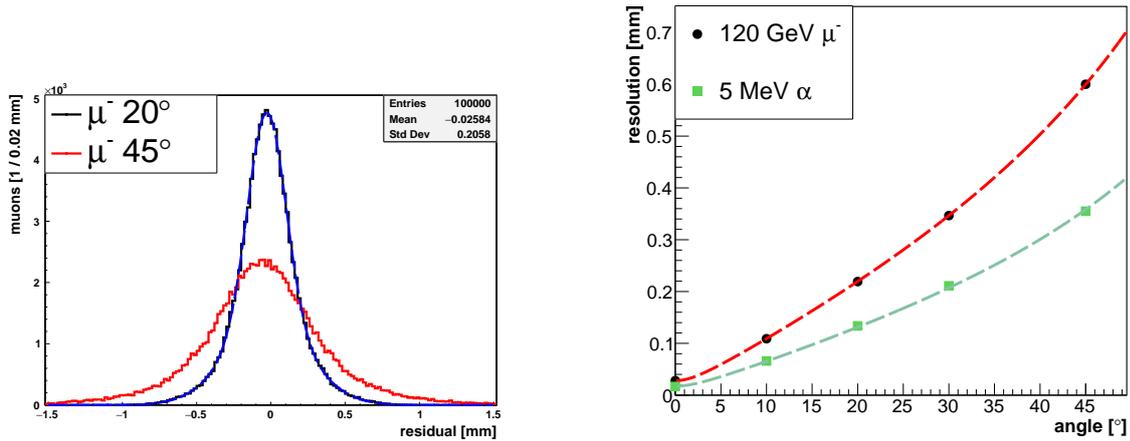
(a) Simulated residual distributions for muons of 120 GeV at inclinations of 20° and 45° with respect to the normal of the read-out plane.

(b) Simulated centroid resolution plotted against the inclination angle of 120 GeV muons and 5 MeV alpha particles in a 5 mm drift gap. The clear degradation visible for both particle types is caused by the non-homogeneous charge deposition along the tracks. As the alpha particles have a much higher average energy loss than the muons their charge distribution along the track is a lot more homogeneous and therefore the influence on the track reconstruction is less

Figure 2.28: Influence of the clustering along the tracks determined

2.8 Front-End-Concentrator-card (FEC) Time Jitter

The read-out system is designed for usage in a clock-synchronous environment in a collider experiment and allows triggers only every 25 ns. This leads to a 25 ns fluctuation in the absolute timing of the recorded signal with respect to the trigger, for continuously triggering particles like cosmic muons. The trigger signal is accepted from the FEC-card only at its next clock cycle. Therefore the recorded data had not only a fixed offset to the trigger signal, but also an additional jitter of 25 ns, which is schematically represented in figure 2.29. The reconstructed timing from the recorded events by the read-out system has to be corrected therefore with a value between 0–25 ns.

The FEC-card also provides a trigger output, which releases a NIM signal synchronous to its clock if a trigger has been accepted. This signal can be used to measure the jitter by means of an TDC, which measured the time between the real trigger signal and the response of the FEC-card, which can be seen in figure 2.30.

The µTPC-method is quite sensitive to this time-jitter, as the measurement of $t_{\mu TPC}$ is directly influenced by this. In order to examine this behavior calculations based on Garfield simulations have been done. Proceeding from the primary electrons, which a muon would leave in the drift region of 5 mm thickness by traversing it under an angle of 30° the response of the read-out was calculated. After simulation of the transport in $E_{drift} =600\,\mathrm{V\,cm^{-1}}$ and the amplification through a triple GEM the signal on a strip read-out with a pitch of 400 µm and a width of the strips of 80 µm was computed. The simulated signal on every strip was sampled in steps of 25 ns with offsets of the start value between 0–24 ns, which mimics the jitter. An example of this is shown in figure 2.31, where three different variations of sampling with 0 ns, 12 ns and 24 ns jitter for the same signal are shown together with a corresponding fit of a Fermi-function (see equation (2.27)). The obvious shift of the signal to earlier times is the direct consequence of the jitter on the signal. The more subtle difference between the shapes is due to the different sampling. The direct consequence of this is, that both the reconstructed inclination $m_{\mu TPC}$ and the reconstructed time $t_{\mu TPC}$ for the position reconstruction in the µTPC-method are directly influenced by the jitter. This can be seen in figure 2.32 for a simulated signal of an inclined track of 30° and a drift velocity of the electrons of
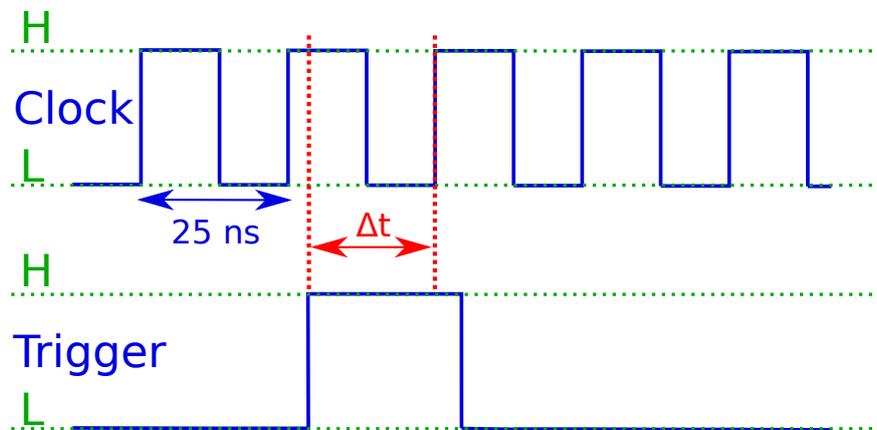
Figure 2.29: Schematic drawing of the time jitter in the recorded data relative to the trigger signal. The fast trigger signal from e.g. a cosmic muon is recognized by the FEC-card at the beginning of the next cycle of the 25 ns clock.
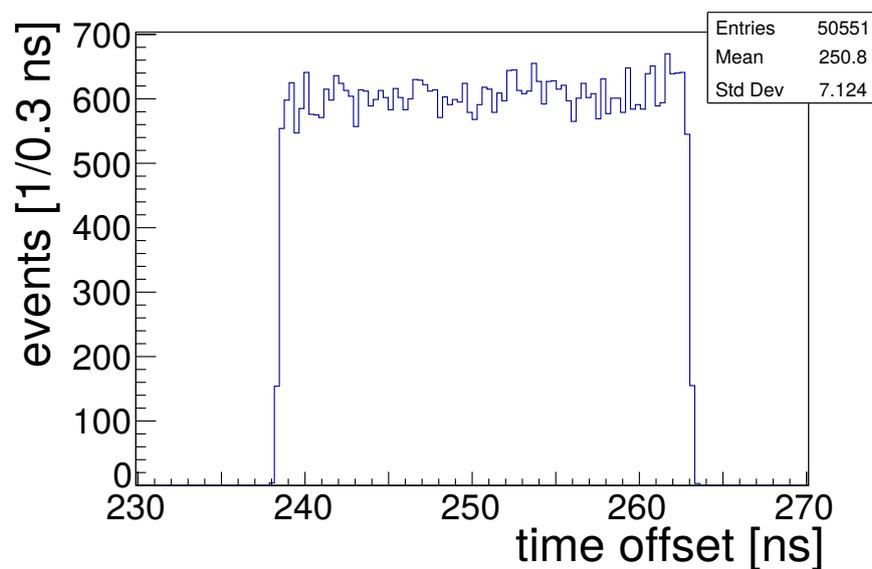
Figure 2.30: Measured offset between trigger signal and the corresponding answer from the FEC card. The precise width of 25 ns and the uniform distribution show the effect of the jitter due to the clocked acceptance of the trigger
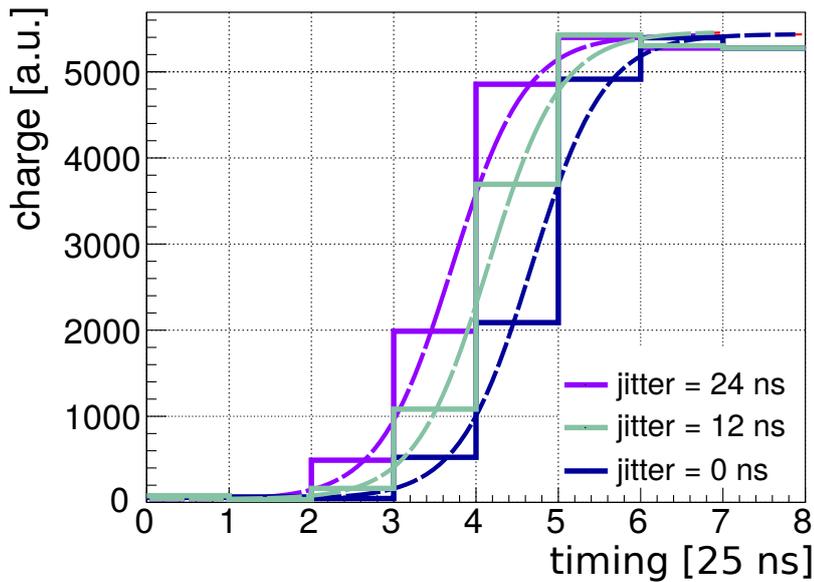
Figure 2.31: Shape of the same signal sampled with different relative starting time due to the time jitter fitted with a Fermi-function. Although the general shape of the different samples varies only marginally a clear difference in the seemingly timing is visible.

$30\,\mu m\,ns^{-1}$, where the parameters of the track fit are plotted against the jitter.

(a) Slope of the µTPC-fit

(b) Intercept of the µTPC-fit
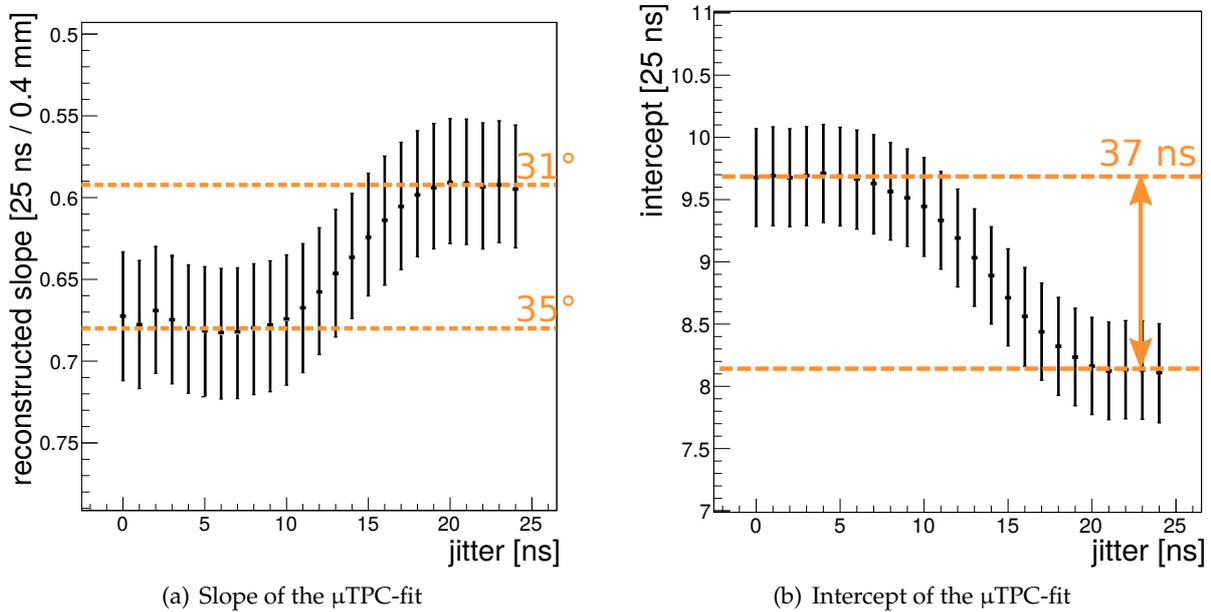
Figure 2.32: The simulation shows a distinct influence of the jitter on the parameters of the µTPC-fit.

This also leads to a dependence of the position reconstruction on the jitter, as it can be seen in figure 2.33. In the case where the timing information is strictly gained from the recorded strip data there is a quite drastic deviation in the reconstructed position of up to 1 mm. As the jitter always is positive this introduces a shift towards the end of the track. If the strip timings are corrected for the jitter previous to the µTPC-fit, this deviation nearly vanishes up to total deviations of less than 0.1 mm and the reconstructed values fluctuate only by a RMS of 50 µm around the true value.
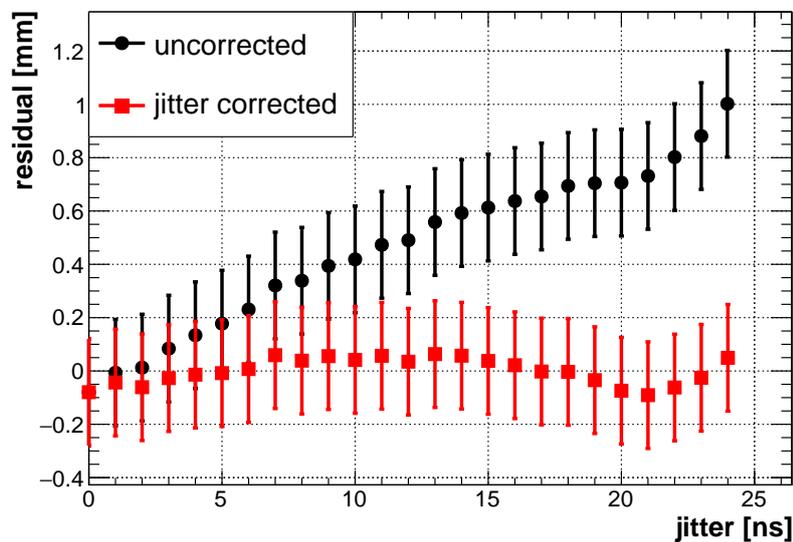
Figure 2.33: Calculated influence of the jitter on the position reconstructed by the µTPC-method at 30° with and without jitter-correction. The clear dependence of the residual on trigger fluctuations in the uncorrected case can nearly perfectly be compensated by subtraction of the recorded jitter from the strip timings.

Chapter 3

Thermal Neutron Detection

The need of high resolution and high rate capable neutron detectors is driven by the rather uncommon interaction of neutrons with matter. Neutrons interact mainly by the strong force with atomic nuclei and therefore allow to evaluate the atomic structure of materials for example in scattering or direct imaging applications. Both methods allow to observe complementary information to the same approaches traditionally achieved with X-rays. A vivid example of this is the difference of neutron and photon absorption, with photons being in general more likely to be absorbed in high-Z materials, as they interact mostly with the electrons. The absorption of neutrons on the other hand follows much more complex rules related to the configuration of the nuclei of the material, with large attenuation coefficients of low Z-materials (see for example [Lehmann et al., 2017] or [Banhart et al., 2010]). Exemplarily this can be seen in the different mass attenuation coefficient curves plotted in figure 3.1 for neutrons with an energy of 3 meV and 25 meV and photons with an energy of 125 keV. This allows non-destructive imaging of materials, which are non-transparent for X-rays, but transparent for neutrons like for example iron, silver or gold.
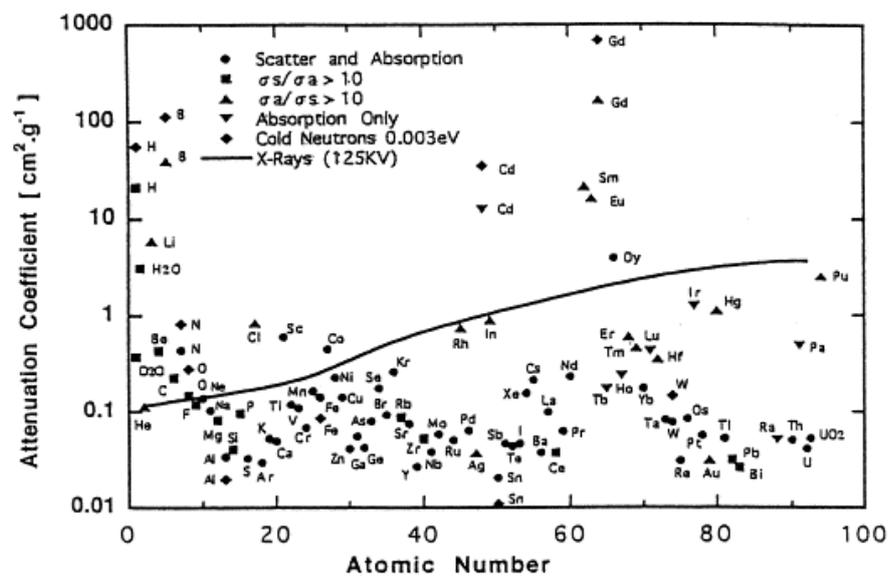
Figure 3.1: Mass-Attenuation coefficients for various materials for 3.25 meV neutrons and 125 keV photons plotted against the atomic number of the material (taken from [Mishima et al., 1999])

Gas detectors are widely used in the detection of neutrons. So far MWPCs or drift tubes are frequently used for this purpose (see e.g. [Stefanescu et al., 2017]), but also MPGDs are emerging to be utilized for neutron detection applications for example the CASCADE detector system based on multiple GEM-layers [Köhli et al., 2016]. As neutrons carry no electrical charge, they will not directly leave a track of electron-ion pairs and a gaseous detector as described before is nearly blind for neutrons. On the other hand MPGDs are very well suited for tracking of charged particles produced in a conversion process. This can be accomplished by the capture of neutrons in a

conversion layer and the subsequent emission of high energy charged particles. In this chapter a method of tracking the fission products of a neutron capture process with a triple GEM detector is described, which allowed position reconstruction of the point of interaction of the neutron with very high precision. Parts of the concept described here have been published in [Flierl et al., 2016b].

3.1 Detection Mechanisms and Reconstruction Concept

The interaction of neutrons strongly depends on the respective energy of the neutrons, which has a specific naming tradition owing to their production processes, see table 3.1. The literature here offers slightly varying ranges of energies, whereas the ones shown here are taken from [Beckurts et al., 1964].

Table 3.1: Naming convention of neutron energies, the limits are generally not definitive

Description	Energy	Temperature
High energetic neutrons	$> 20\,\mathrm{MeV}$	
Fission neutrons	$\sim 2\,\mathrm{MeV}$	
Fast/hot neutrons	40–1000 meV	2300 K
Thermal neutrons	3–150 meV	300 K
Cold neutrons	0.1–20 meV	25 K
Ultra cold neutrons	0.001–10 µeV	

In this thesis the detection of thermal neutrons will be discussed and for this energy range there are several materials, which have a high neutron capture cross-section and which emit at least one particle detectable in a gaseous detector. Some of the more common converters are listed in table 3.2. Here also the typical reaction products as well as the excess energy from these fission and excitation processes are stated. Detectors filled with ^{3}He for example are the gold-standard in detection efficiency for thermal neutrons with the ^{3}He being converter and counting gas simultaneously [Zeitelhack, 2012]. In the process a triton and proton are produced back-to-back, which both leave a track in the detector. Because of the slightly different energy and energy-loss of both particles a typical spatial resolution by determination of the center of charge in the resulting track is around 0.2–1 mm [Radeka et al., 1996]. High demand and limited supply of ^{3}He around 2010 peaking in the so called "^{3}He-crisis" led to extended searches for alternative converter materials [Shea and Morgan, 2010], which also might allow to push the limits of spatial resolution.

Table 3.2: Absorption cross sections for various isotopes for thermal neutrons with an energy of 25 meV (data taken from [Beckurts et al., 1964, Appendix I])

Isotopes	Reaction	σ_{th}[barn]	Q[MeV]
^3He	(t,p)	5330	0.764 MeV
^6Li	(^{3}He,α)	936±6	4.786 MeV
^{10}B	(^{7}Li,α)	3840±11	2.79 MeV
^{113}Cd	(^{114}Cd,γ)	20000±300	
^{149}Sm	(α,^{146}Nd)	40800±900	9.12 MeV
^{157}Gd	(^{158}Gd,γ)	242000±4000	

A very promising alternative, which will be used here, is the neutron capture and conversion by ^{10}B in the following processes:

$$^{10}B + n \rightarrow^7 Li +^4 He + \gamma + Q(2.31 MeV)(94\%)$$
$$^{10}B + n \rightarrow^7 Li +^4 He + Q(2.79 MeV)(6\%)$$
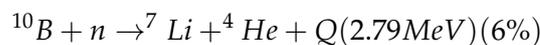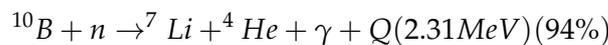
The capture of the neutron triggers instantaneous fission of the ^{11}B atom into an alpha particle and a lithium ion, which are emitted back-to-back. Due to the much higher excess energy of this

process compared to the kinetic energy of the thermal neutron the ions are emitted arbitrarily with respect to the direction of the neutron. The excess energy Q is shared unequally by the two products, because of momentum conservation, leading to $E_{He} = 1.47\,\text{MeV}$ and $E_{Li} = 0.84\,\text{MeV}$ in the case with additional photon and $E_{He} = 1.78\,\text{MeV}$ and $E_{Li} = 1.02\,\text{MeV}$ without additional photon [Beckurts et al., 1964]. With a relative abundance of 20 % in natural boron [Berglund and Wieser, 2011], ^{10}B is much more conveniently available than ^{3}He. Albeit also detectors with gaseous boron in the form of BF_3 exist, here the case of a solid conversion layer acting also as cathode for an triple GEM detector will be discussed. This approach was chosen in order to optimize the spatial reconstruction of the neutron interaction within the conversion layer. The interaction in a thin conversion layer leads to a case where always a single ion can be detected in the active gas volume, with its track pointing towards the point of interaction of the neutron, which can be reconstructed by tracking the ion. This is necessary because of the non-negligible range of the ions in the active volume of the detector of several millimeters (see section 3.3). The reconstruction of the centroid of the created charges position and thus the position of the neutron would lead to a systematic error in the reconstruction depending on the relative inclination of the ion track with respect to the read-out plane, which is schematically shown in figure 3.2, leading to a maximal spatial resolution of $\mathcal{O}(\text{mm})$.
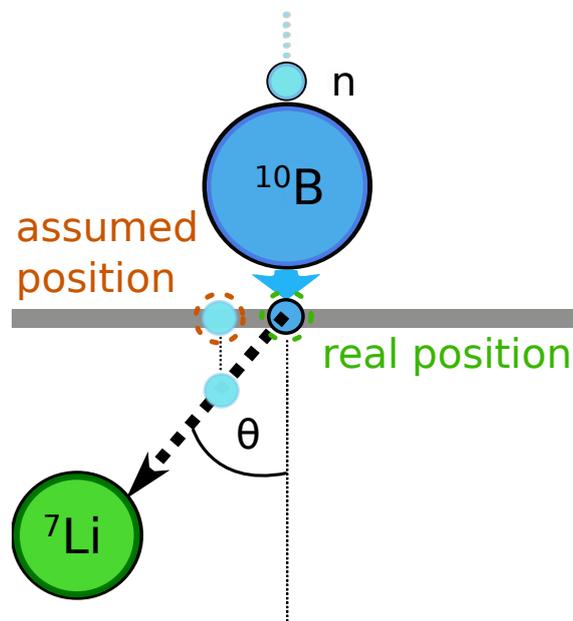
Figure 3.2: Schematic of the reconstruction concept: A thermal neutron is captured in a thin conversion layer of ^{10}B which leads to the back-to-back production of two high energy ions. One ion reaches the active volume of the detector and by tracking the path of the ion inside the active volume rather than just computing the charge centroid of the ion track the real position of the neutron interaction can be determined.

3.2 Detector and Beam-Line Set-up

In order to be sensitive to thermal neutrons a standard triple GEM detector described in section 1.2 was equipped with a converter cathode[8] made from an 0.5 mm aluminum sheet coated with 2 µm of ^{10}B in order to sustain an optimal conversion efficiency, which will be described in section 3.5. As external triggering after the conversion is impossible, a trigger signal for the time resolving read-out described in section 2.5 had to be generated from the detector itself. This was accomplished by collecting the signal of the last GEM-foil by a charge-sensitive pre-amplifier, which was then used to

---

[8]Which was provided by H. Takahashi (Tokyo University)

trigger the read-out. The lower-side of the last GEM-foil basically sees the same signal as the read-out strips, but with a different polarity, because the signal is generated from the electrons drifting away from the foil as in contrast to the read-out strips. Reconstruction of the neutron position by tracking the resulting ions was tested in a thermal neutron beam at the Heinz Maier-Leibnitz Zentrum (MLZ) [9] at the TREFF-beam line [Heinz Maier-Leibnitz Zentrum et al., 2017], which provided a monochromatic thermal neutron beam with an energy[10] of 3.7 meV. The beam was confined to a slit of $0.18\,\text{mm}^2 \times 4\,\text{mm}^2$ by a system of in total four boron and cadmium collimators, which were arranged as shown schematically in figure 3.3. This set-up provided a constant flux of about 1 kHz through the slit aperture on the converter cathode of the GEM detector. The large distance between the collimators allowed a very high parallelism of the neutron beam, which allowed to parameterize the expected beam-shape in the narrow direction of the slit by:

$$f(x) = A_0 \left(erf\left(\frac{a + (x - \mu)}{\sqrt{2}\sigma_0}\right) + erf\left(\frac{a - (x - \mu)}{\sqrt{2}\sigma_0}\right) \right) + A_1 \exp\left(\left(\frac{x - \mu}{\sqrt{2}\sigma_1}\right)^2\right) \quad (3.1)$$

Where the first two summands are the convolution of a box-car function of width a with a Gaussian smoothing function of width σ, which accounts for the remaining non parallelism of the neutron beam, which leads to the sum of two Gaussian error functions. The third term is a Gaussian distribution, which describes small angle scattering of the neutrons, either in the collimator, the detector housing or the cathode. This expected shape could be verified by a Geant4 simulation based on the full beam-line, which allowed to predict the neutron hit distribution on the converter cathode. The simulated distribution projected onto the narrow direction of the slit aperture is shown in figure 3.4. The main component of the hit distribution follows very well the expected box-car like shape of 180 μm width dictated for un-scattered neutrons by the slit collimator with only very little smoothing at the edges described by a negligible Gaussian component with a width of $\sigma_0 = 15$ μm. The additional contribution from scattered neutrons accounts for a non-negligible Gaussian distributed component with a width of $\sigma_1 = 140$ μm. From the difference between this expected and the measured beam-profile in the precision direction of the slit later in this chapter the detector resolution will be determined under the assumption of a Gaussian distributed resolution contribution from the detector. Neglecting the insignificant Gaussian smoothing contribution, equation (3.1) can then be used to determine the resolution by a fit to the measured distribution and is described by σ_0.
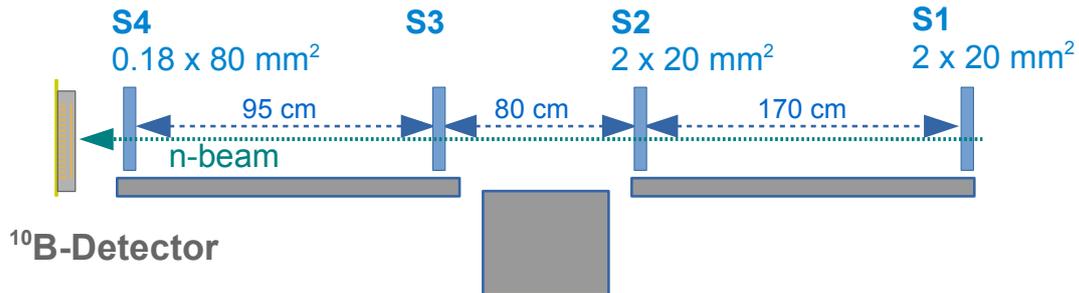
Figure 3.3: Schematic of the set-up at the TREFF beam-line. Shown are the four collimators S1-S4 leading to a narrow slit beam onto the converter cathode placed in the GEM detector behind the S4 aperture.

Utilizing the time-resolving read-out the actual track from an ion was reconstructed, by a time-bin wise reconstruction of the mean position in X and Y direction separately and thus reconstructing the particle's track in the projection onto the read-out plane, which led to a hit distribution as it is shown in figure 3.5. Although the slit is clearly visible the overlay from the full tracks smears the position information. From this picture is also obvious why the centroid method is not optimal in order to reconstruct the end-point of the neutron, as the projected track of the ions can reach several millimeters.

---

[9] https://www.frm2.tum.de/
[10] This corresponds to a De-Broglie wavelength of 4.7 Å

Mean	0.001085
Integral	1.622e+04
χ^2 / ndf	110.1 / 89
A_0	348.5 ± 5.0
σ_0	0.01447 ± 0.00063
A_1	165 ± 5.1
σ_1	0.1373 ± 0.0017
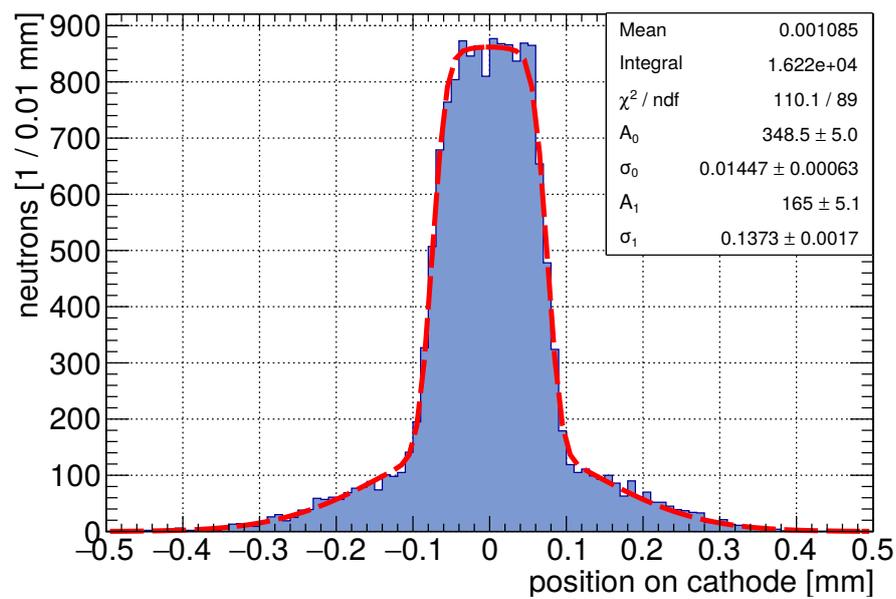
Figure 3.4: Simulated beam spot in the narrow direction of the slit on the cathode after the collimator system. A fit with equation (3.1) shows that a well defined boxcar like distribution with a width of 180 µm and a negligible Gaussian smearing of $\sigma_0 = 15$ µm of the slit sits on top of a broad Gaussian of scattered neutrons with a width of $\sigma_1 = 140$ µm.
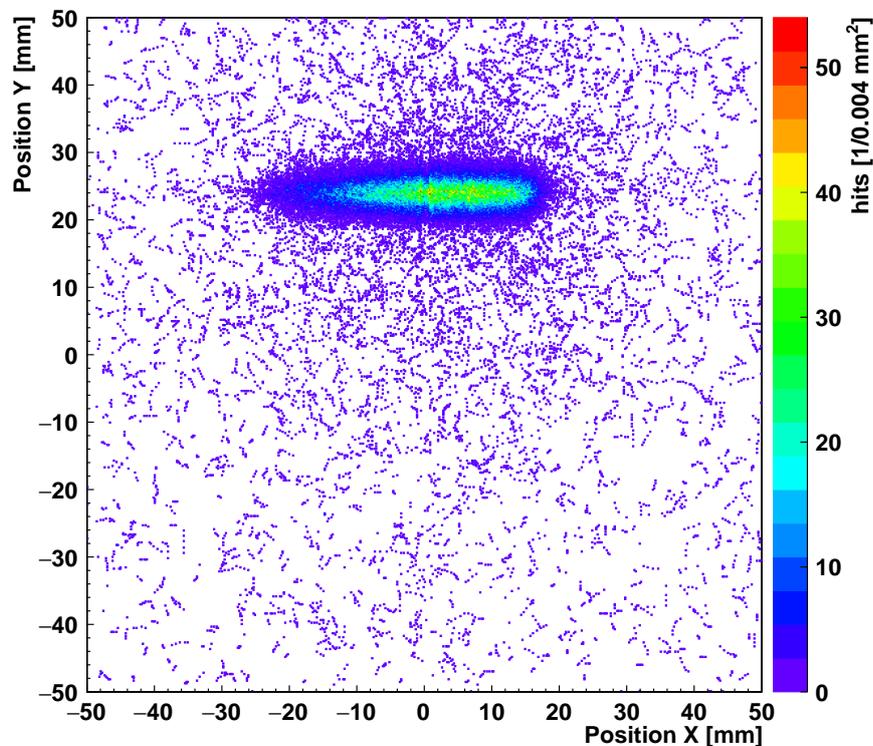
Figure 3.5: Projection of reconstructed ion tracks onto the read-out plane for a thermal neutron beam, which was shaped by a slit aperture.

3.3   μTPC-like Position Reconstruction

In order to determine the position of neutron conversion several approaches will be discussed in this chapter, which all utilize the reconstruction of the full ion track by the μTPC-method described in section 2.7.4. The direct application of the μTPC-method would deliver a point in the center of the ion track leading to similarly insufficient results as the centroid method. For a meaningful position reconstruction the μTPC calculation from equation (2.33) has to be modified slightly in order to obtain the start point of the track $x_{\mu TPC}$:

$$x_{\mu TPC} = \frac{t_{\mu TPC} - (t_{mid} + t_{\frac{1}{2}})}{m_{\mu TPC}} \tag{3.2}$$

Where $t_{\frac{1}{2}}$ is the time the electrons need to drift through half of the drift gap, which adds a small contribution to the total offset t_{mid}. The total offset could then be determined by the same method described in section 2.7.6. This method has some implicit assumptions on the shape and also the production of the electron-ion pair track the high energetic ion leaves in the active region of the detector. The two most important prerequisites are:

- The ion trajectory in the active gas volume can be described by a straight line

- All electron-ion pairs are produced virtually simultaneously

In equation (3.2) it is assumed that timing and z-position are proportional, which in the case discussed here not necessarily has to hold. The energy of both ions at the production is low enough, that they are already in the Bragg-peak of energy loss, as can be seen in figure 3.6 for the mean energy loss of alpha particles in argon. The fact that ions lose their velocity so fast might cause a significant deviation from the assumption of instantaneous creation of the primary electrons. Moreover a part of the ions is stopped inside the active gas volume. Fortunately the time difference between the neutron conversion and the production of the electron-ion pairs is still negligible compared to the drift times of the electrons and can be calculated from the Bethe-Bloch equation (2.3) and the resulting velocity of the ions. For alpha-particles with a start energy of 1.84 MeV this results in 95 % of the primary charge inside the drift gap being produced within 3 ns after the particle enters the drift region. This is also shown in figure 3.7 as time needed for a fraction of total energy loss, which in turns has been calculated from the data shown in figure 3.6. The range of the ions in the gas can be calculated in the same way, but has a much greater influence on the reconstruction. The range is depending on the type of the particle (^{4}He of ^{7}Li) and the distance it had to travel through the converter until it reached the gas volume hence depending on the energy left at this point. The range of the ions in the gas is generally limited to a few millimeters, with a maximum range for an alpha particle of energy 1.8 MeV in Ar-CO$_2$ of 8.6 mm, which was determined by [Ziegler et al., 2010]. Stopping the ion in the active volume of the detector however is not favorable, as the lower the energy of the ion is the more it gets scattered leading to a less straight trajectory. Therefore it is best to limit the drift gap to a width, where the ions with little inclination with respect to the read-out plane will traverse the whole gap. The drift gap therefore was set to a width of 6 mm, which limited the projected track length to around 3 mm, which can be seen in figure 3.8, where the projected track length in one read-out direction and also the predicted distribution from a Geant4 simulation is shown. The determination of the track length in the measurement follows equation (3.4) and will be explained later. The deviation of the measured track length from the simulated one is caused by a minimal cluster size due to lateral diffusion. By limiting the track-length of the ions in the active region it was ensured that both conditions stated earlier were met and the μTPC-method in general could be used. In practice arose a couple of problems there by this approach: Triggering on the signal of the ion at the last GEM-foil with a fixed threshold added a relative jitter to the recorded signal timing. Depending on pulse height and shape this led to an additional fluctuation in the timing of the recorded signal in the order of $\sigma_t \geq 50$ ns[11]. The effect of this can be seen in figure 3.9(a), where the timing calibration $t_{\mu TPC}/m_{\mu TPC}$

---

[11]This would lead to an additional uncertainty $\sigma \geq \dfrac{v_{drift}\sigma_t}{tan(\theta)}$
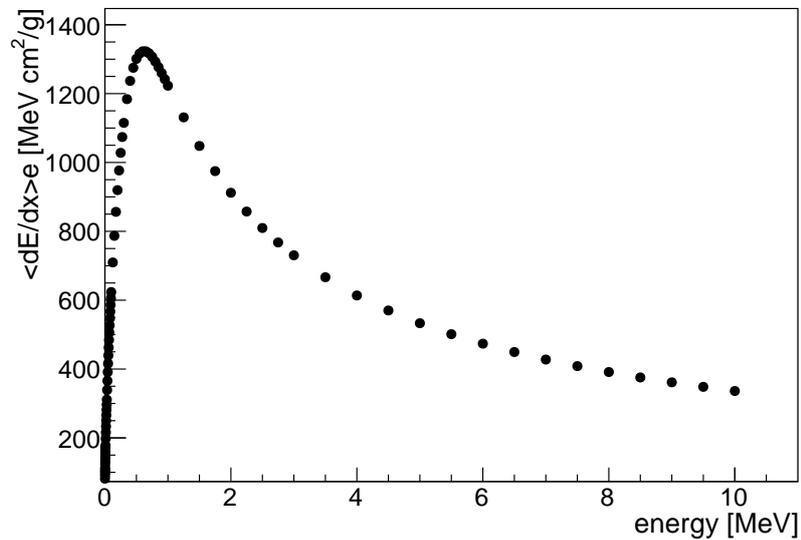
Figure 3.6: Mean energy loss depending on the energy of α-particles in argon (data taken from [Berger et al., 1998]).
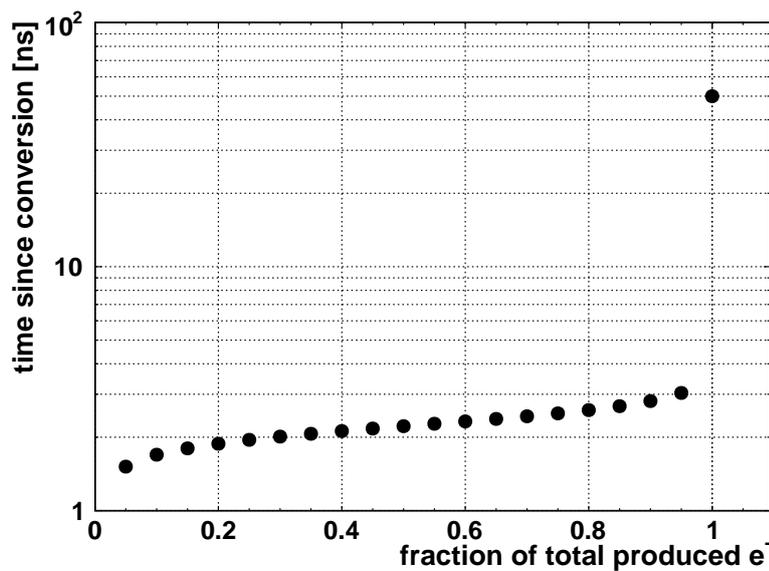

Figure 3.7: Time needed for a relative energy loss for an α-particle in argon with a start energy of 1.8 MeV.
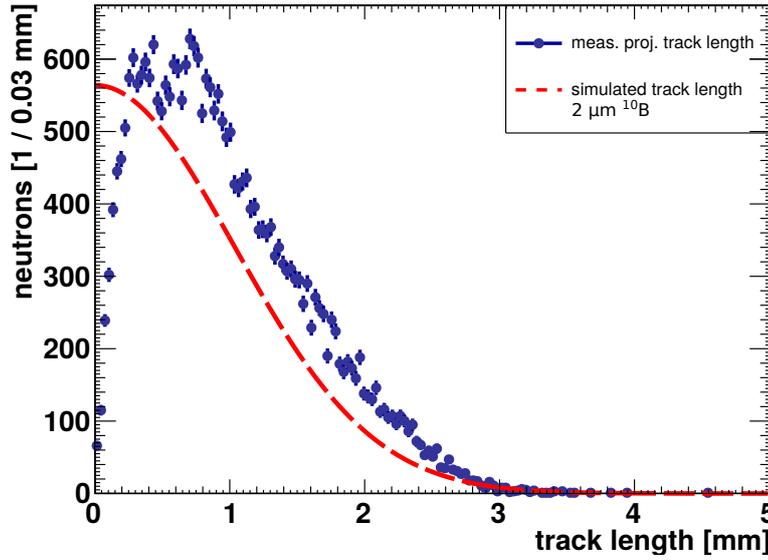
Figure 3.8: Measured and simulated projected track length of ions for a $2\,\mu m$ ^{10}B conversion layer. The measurement was done at $E_{drift} = 192\,V\,cm^{-1}$. The difference in simulation and measurement can be explained by the additional diffusion of the electron cloud leading to a minimal measured cluster size.

for $E_{drift} = 192\,V\,cm^{-1}$, the first part of equation (3.2), is plotted against $1/m_{\mu TPC}$ of the ion, here as projection corresponding to the direction of the narrow side of the slit. Since the timing t_{mid} is not well defined by the trigger the distribution is spread-out in Y-direction, which results in the previously mentioned loss in spatial information. This timing fluctuation can partially be removed by subtracting the timing of the last hit strip t_{last} for every event, which significantly improves the absolute timing information as it can be seen in figure 3.9(b), where $(t_{\mu TPC} - t_{last})/m_{\mu TPC}$ is plotted and $t_{mid} - t_{\frac{1}{2}}$ is determined by a linear fit. Using equation (3.2) the start point of every track could be calculated and compared to the position of the slit, which is plotted in figure 3.10 and the spatial resolution achievable by this method could be determined by a fit with function (3.1). Although the narrow part of the fit reaches a $\sigma_0 = (225 \pm 3)\,\mu m$ the broad Gaussian base has to be considered as a feature of the reconstruction algorithm rather than to be caused by the beam spreading, as it is with a width of $\sigma_1 = (720 \pm 20)\,\mu m$ significantly broader than the expected scattering of $140\,\mu m$. A total spatial resolution was determined by deconvolution of the scattering from the broad Gaussian and weighting the width of both parts of the fit with their respective integral. Altogether this lead to a spatial resolution of $\sigma_{weighted} = (590 \pm 20)\,\mu m$. This already quite good spatial resolution has to be taken with a grain of salt, as the reconstruction efficiency here is as small as $\eta \simeq 60\,\%$, because of the limitations of the μTPC fit for low inclination angles. The minimal cluster size in both read-out directions due to lateral diffusion is in the order of $1\,mm$, which means that inclination angles smaller than $10°$ are reconstructible in this set-up. For clusters with a smaller inclination angle the timing difference of the incoming electrons is suppressed by the first arriving electrons, as they already occupy the width of the full cluster and the signal on all strips appears simultaneous. This can be seen in the distribution of reconstructed track slopes in figure 3.11, here shown in units of time-bins per strip pitch. With a drift velocity of $20\,\mu m\,ns^{-1}$ for an $E_{drift} = 192\,V\,cm^{-1}$ inclination angles smaller than $10°$ would lead to a track slope larger than 4.5 time-bins/pitch, meaning that nearly all tracks with an inclination angle smaller than $10°$ are miss reconstructed. This resulted for the reconstruction shown before in figure 3.10 to $40\,\%$ of reconstructed start points laying outside of the active volume of the detector. For these events the position of the centroid would obviously deliver a better position information, hence it is useful to combine both methods.
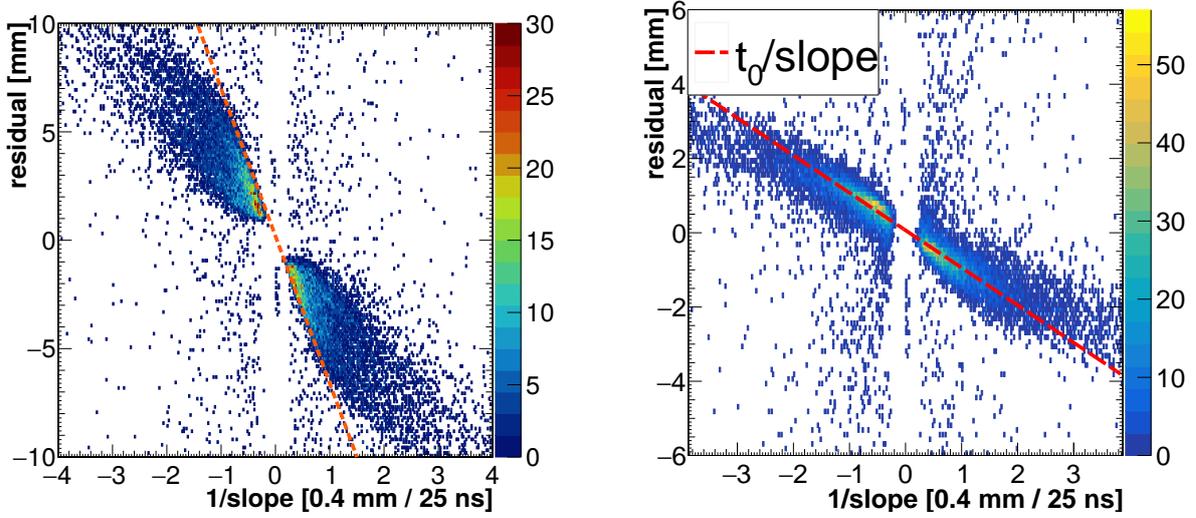
(a) Difference between slit position and μTPC-reconstructed position (only the first addend of equation (3.2)) plotted against 1/slope. Ions which would pass through the full drift gap correspond to the only fainted accumulation along the dashed line, which drawn for illustration. The fan like spreading of the distributions in both directions is caused by the time jitter of the trigger and ions which do no traverse the full drift gap.

(b) Residual distribution with the timing from the μTPC-fit corrected by the timing of the last hit strip plotted against 1/slope and fit with a linear function in order to obtain t_{mid}.

Figure 3.9: Determination of the start time of electron drift, exemplarily shown for $E_{drift} = 192\,\mathrm{V\,cm^{-1}}$.
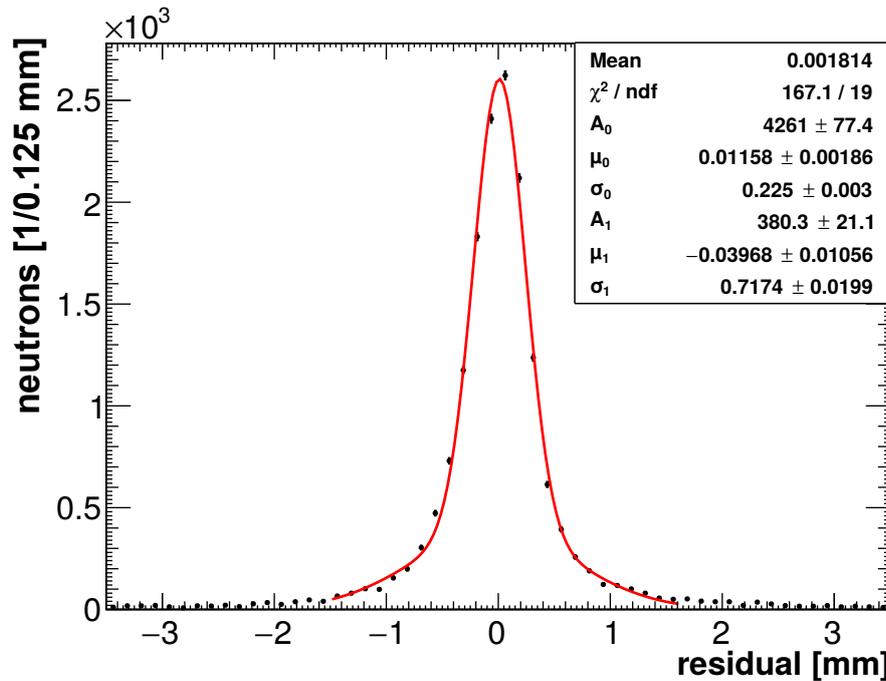

Figure 3.10: Difference of the slit position and the position determined by a μTPC fit, fit with function (3.1) for $E_{drift} = 192\,\mathrm{V\,cm^{-1}}$. The main contribution to the spatial resolution is $\sigma_0 = (225 \pm 3)\,\mathrm{\mu m}$, but the underlying broad Gaussian distribution $\sigma_1 = 720\,\mathrm{\mu m}$ is much wider than expected.
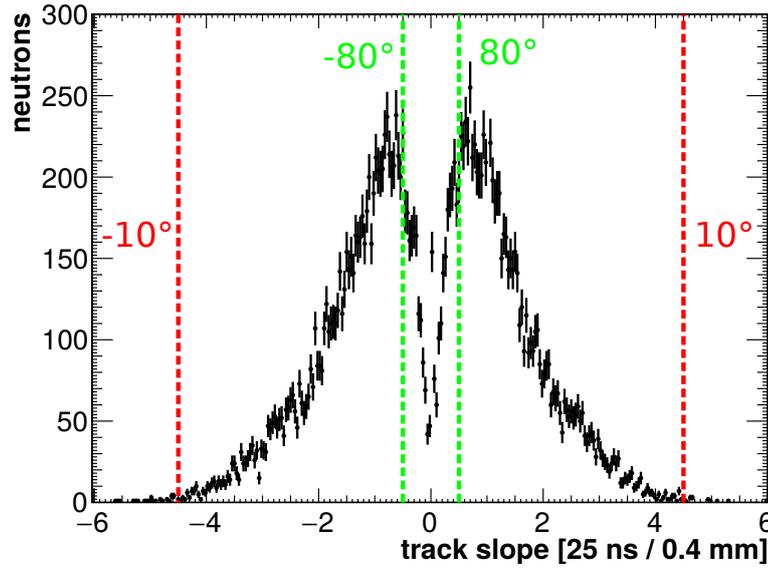
Figure 3.11: Track slope distribution $m_{\mu TPC}$ from the µTPC fit for $E_{drift} = 192\,\mathrm{V\,cm^{-1}}$. Inclination angles <10° and >80° could hardly be reconstructed, which implies that this method fails for very steep tracks.

3.4   Extrapolation of the Start Point

A very basic strategy towards a combination of centroid and µTPC-method would be to identify the strip in a cluster, which corresponds best to the electrons created closest to the cathode. In a first approach the position of the last strip in a cluster which was hit was used to determine this position. This resulted in a reconstructed distribution shown in figure 3.12, which was fit with a single Gaussian distribution in order to get a first impression of the start point of the track. This already increased the position accuracy below 0.5 mm, but is of course limited by the width of the strips. An additional problem arose from signals in strips purely attributable to charge sharing at the rim of a cluster, contributing a simultaneously shared signal on neighboring strips. Based on the considerations from section 2.4.2 this could lead to an overcompensation of 2 strips or 0.8 mm in this set-up[12].

A better reconstruction was achieved by exploiting the dense and regular ionization along the ion tracks, by extrapolation from the centroid position with the measured track inclination. In the projection of the track on the read-out anode this reduces to the determination of the track length and the asymmetry of the charge distribution along the track (skewness). Due to the high energy loss the charge distribution along the track can be described by:

$$q(x) = A \cdot \exp\left(-\left(\frac{x-\mu}{2 \cdot (\sigma + H(\mu)) \cdot \epsilon \cdot (x-\mu)}\right)^2\right) \tag{3.3}$$

This expression represents a piece-wise defined Gaussian function, with a most probable value μ, width σ and a skewness parameter ϵ. $H(\mu)$ describes a Heaviside function. The broad half of the function describes the dE/dx below the Bragg-peak, whose position is approximated by the mean of the Gaussian. The narrow part of the function mimics the following fast decline in dE/dx. This allowed to determine the projected track length by a fit to the distribution of the strip charges in every cluster around the highest responding strip, which is shown in figure 3.13. This function has been chosen because the smooth energy loss along the path of the ions is not expected to be homogeneous, due to the high energy loss of the ions with the highest value at the Bragg-peak.

---

[12]Assuming a threshold for a valid signal on a strip of 2.5 % of the ADC-range and a charge sharing of 15 % for neighboring strips (also determined in section 2.4.2)
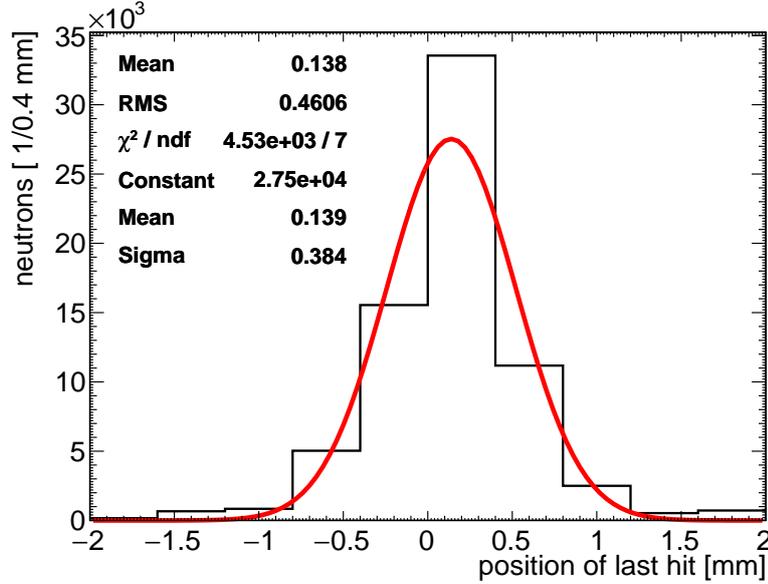
Figure 3.12: Position of the last hit strip in a cluster fit with a Gaussian

The skewness parameter ϵ describes where the centroid is located in the track between $-1 < \epsilon < 1$ with $\epsilon = -1$ meaning a centroid located at the far right of the track and $\epsilon = 1$ on the far left respectively. Together with the direction of the ion determined by $sign(\theta)$ from the µTPC-fit this allows to determine the position of the centroid in Z-direction. From this fit the projected track length can be parameterized by:

$$l_{proj} = p\,(2 - \epsilon)\,\sigma \qquad (3.4)$$

Here p is the factor which scales the width determined at $1/\sqrt{e}$ height of the charge distribution around the centroid in order to extrapolate the real track length. The exact parameter is depending on the charge distribution but here it is assumed to be constant and will later be determined as a calibration factor. For now assuming linear scaling, p will be fixed to be $\sqrt{e}$. This allows to recover also the full path length l_0 of the particle in the active volume by the determination of the projected track lengths in both read-out directions and the track inclination by:

$$l_{proj} = l_0 \cos \phi \sin \theta = l_0 sin\theta_{proj} \qquad (3.5)$$

Using the centroid position the start of the track can be extrapolated in the following way:

$$x_{ext} = x_{cent} + sign(\theta)\lambda l_{proj}$$

Where λ is a scaling parameter defined by the initial projected direction of the ion, determined by the µTPC-fit and the track length.

The transverse diffusion of the electron cloud due to the drift and amplification and also charge sharing of the read-out strips has not yet been considered so far, but has to be as it can be seen in figure 3.14. Here the projected track length determined by equation (3.4) is plotted against the difference from the expected position to the position of the centroid method. The difference increases as expected with the projected track length, but the minimal track length caused by both effects just described has a minimal value of $\approx 2 \cdot 0.4$ mm, which is significantly larger than 0. This additional contribution from the measurement has to be considered in the determination of the absolute projected track length. Assuming a fixed minimal width of the cluster d, but depending on electric fields, detector geometry and gas, the absolute track length can be written as:

$$l_{abs} = A\sqrt{l_{proj}^2 - d^2} \qquad (3.6)$$

Where A is a normalization factor, which usually should be 1, and here was used only as the track-length was determined in units of strip pitches of the read-out anode. This leads now to a set
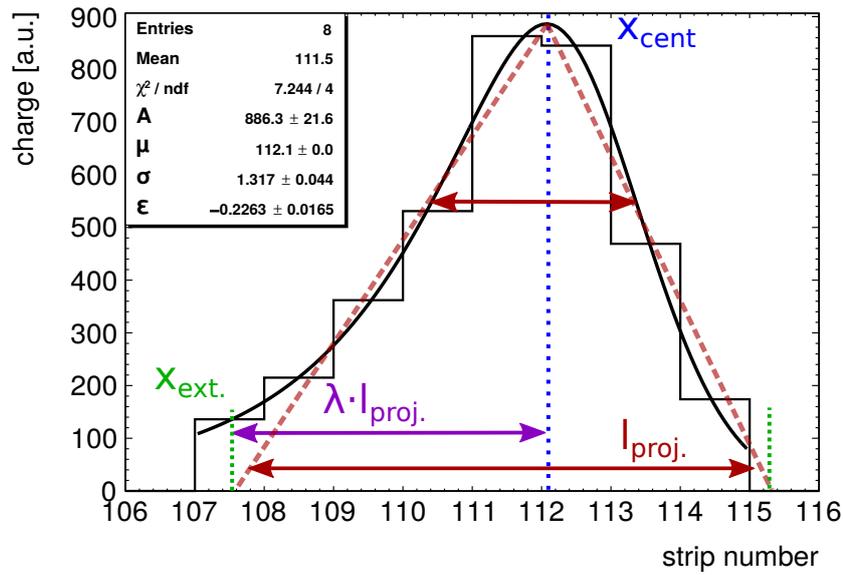
Figure 3.13: Schematic of the reconstruction concept by determining the projected track length $l_{proj.}$ from a fit of equation (3.3) to the distribution of charges along an ion track.
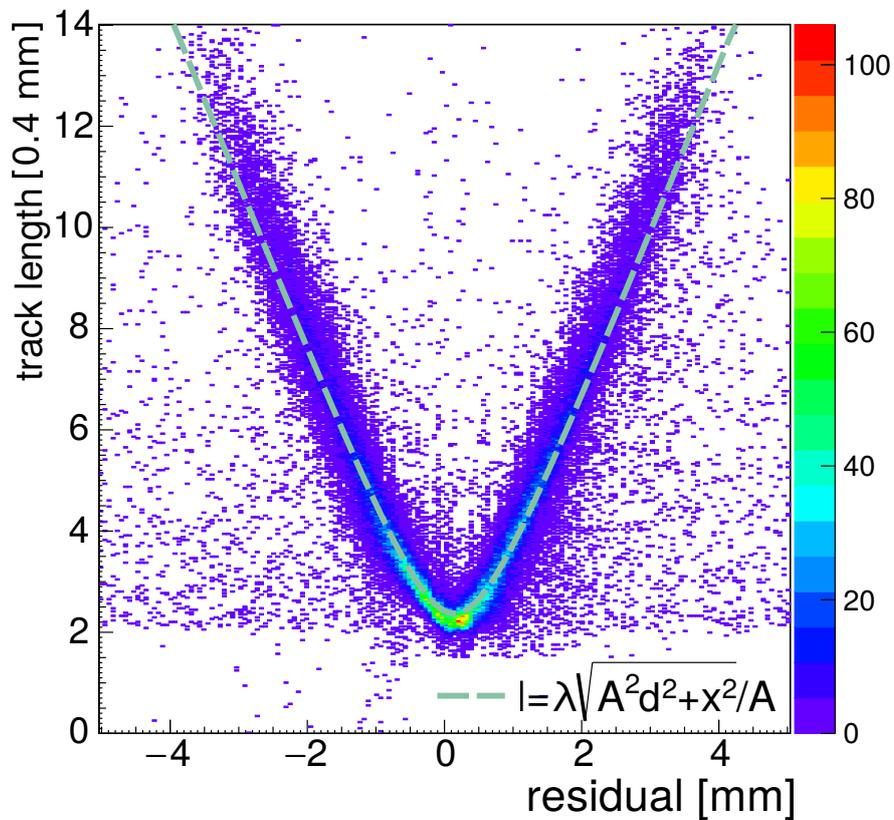

Figure 3.14: Reconstructed projected track length plotted versus the difference between the slit position and the position determined by the centroid. The distribution has been fit with equation (3.7).

of three calibration parameters A, λ and d, which all can be determined by a fit to the track length residual distribution shown in figure 3.14:

$$l_{proj.} = \frac{\lambda \sqrt{A^2 d^2 + (x - x_0)^2}}{A} \qquad (3.7)$$

This finally yields the extrapolated position by calculation of:

$$x_{ext.} = x_{cent} + \lambda A \cdot sign\,(\theta) \left(\sqrt{l^2_{proj} - d^2} \right) \qquad (3.8)$$

This extrapolation allows to reconstruct the origin of the track with high accuracy, as it it shown in figure 3.15 for $E_{drift} = 192\,\mathrm{V\,cm^{-1}}$, where the reconstructed position distribution is plotted and evaluated. Deconvolution of the beam shape by a fit with equation (3.1) resulted in an excellent spatial resolution of $\sigma_0 = (117 \pm 10)\,\mu m$ (or FWHM=$(280 \pm 30)\,\mu m$). Although the broad tail
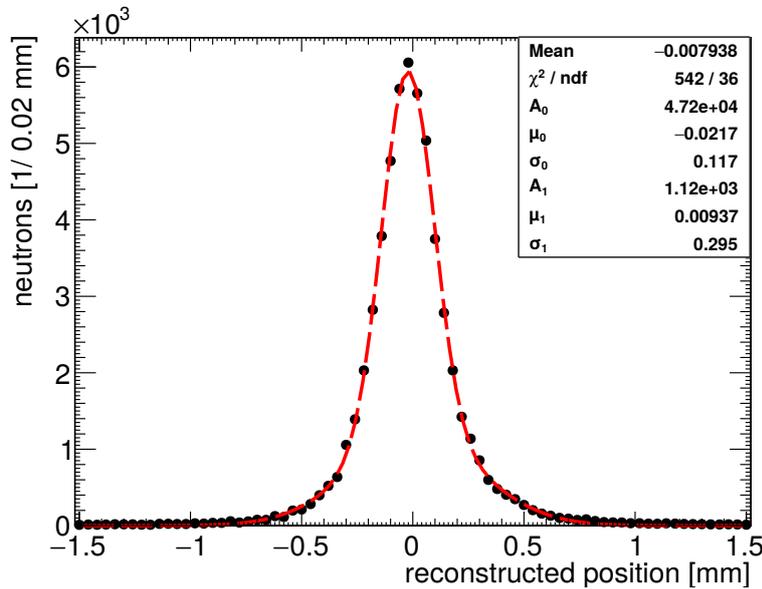

Figure 3.15: Reconstructed position of the slit collimator determined by extrapolation from the centroid position fit with function (3.1) for $E_{drift} = 192\,\mathrm{V\,cm^{-1}}$. Here a spatial resolution $\sigma_0 = (117 \pm 10)\,\mu m$ could be achieved.

distribution with a width $\sigma_1 = 295\,\mu m$ is larger than expected from the beam profile simulation the integral contribution of this distribution with $(34 \pm 2)\,\%$ of the total number of events is only marginally larger than the simulated contribution of 30 %. This suggests that the tails are caused by the real underlying beam profile. The outstanding performance of this extrapolation can be explicitly seen by the full reconstruction of the slit aperture in comparison to the hit distribution determined by the centroid method in figures 3.16(a) and 3.16(b). The spatial resolution for the centroid method in this case would be only $(1.5 \pm 0.1)\,mm$. Although this method also relies on the µTPC-fit it is much less depending on the quality of the actual reconstructed angle, as explicitly only the sign of the reconstructed inclination is used. This leads to a much higher reconstruction efficiency than for the pure µTPC-method, with more than 95 % of the actual triggered signals reconstructed in the active area. One reason for this is an erroneous assignment of the inclination direction $sign(\theta)$, which can be reduced by a cut on $|m_{\mu TPC}| \geq 32.5\,\mathrm{ns\,mm^{-1}}\,(\pm 80°)$, which allows to remove a region of events where the µTPC-fit frequently fails and has a high probability to reconstruct the opposite sign of the true track inclination. This allowed at the cost of a slightly decreased reconstruction efficiency even higher spatial resolutions as it can be seen in figure 3.17. Here a spatial resolution of $\sigma_0 = (100 \pm 10)\,\mu m$ could be achieved but the reconstruction efficiency decreased to 64 % of triggered events reconstructed within the active region. The detector used here
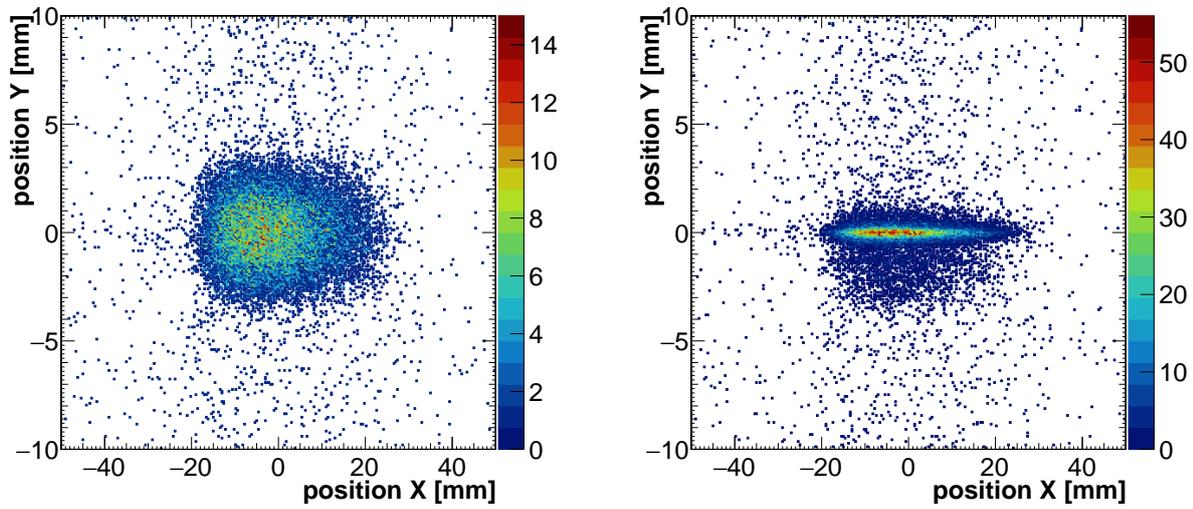
(a) Full hit distribution from the slit aperture determined by the centroid method, the slit width here seems to be exaggerated by several millimeters.

(b) Hit distribution extrapolated to the converter cathode, which allows to reconstruct the point of interaction of the neutron much better.

Figure 3.16: Hit distributions for the center and start point of the neutron track at $E_{drift} = 192\,\mathrm{V\,cm^{-1}}$.

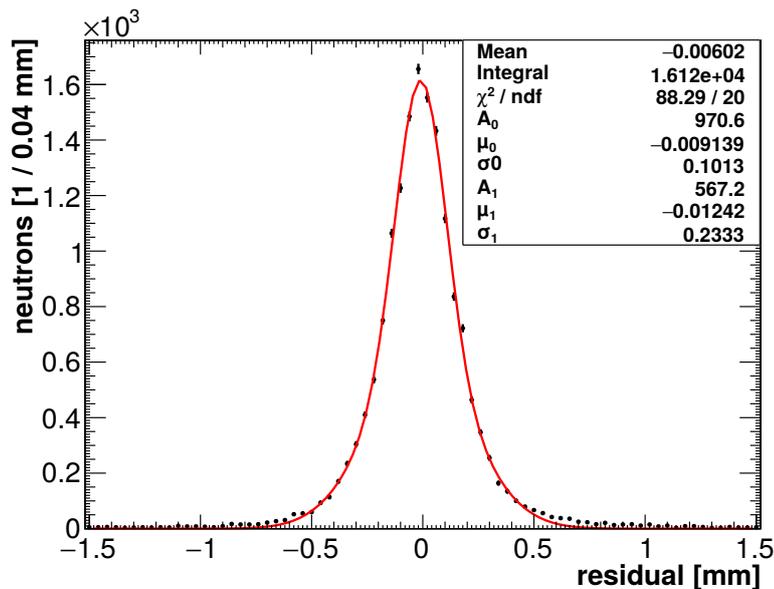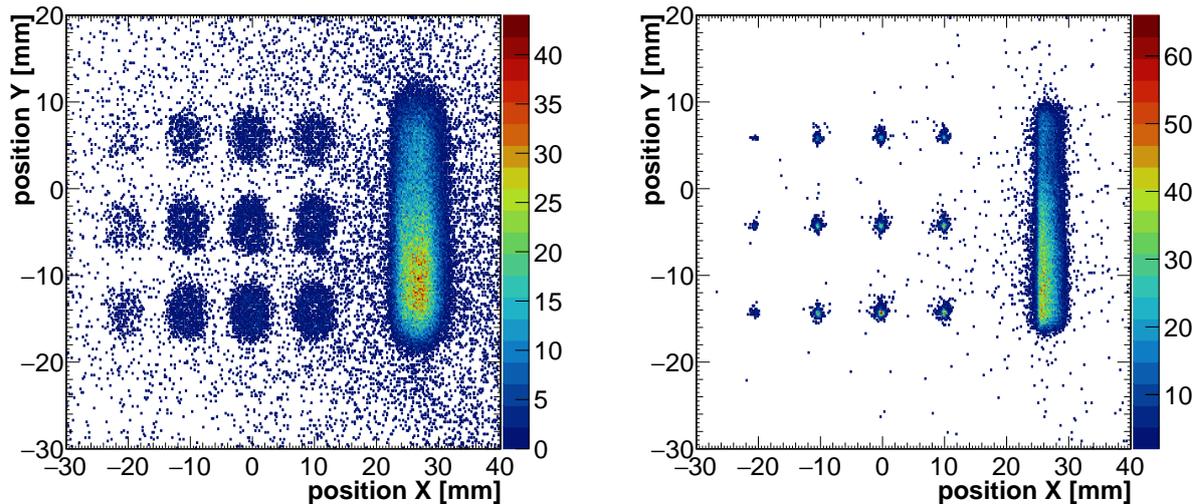|	
Mean	−0.00602
Integral	1.612e+04
χ^2 / ndf	88.29 / 20
A_0	970.6
μ_0	−0.009139
$\sigma 0$	0.1013
A_1	567.2
μ_1	−0.01242
σ_1	0.2333

Figure 3.17: Residual distribution after additional application of the skewness correction with a fit of function (3.1) with $E_{drift} = 192\,\mathrm{V\,cm^{-1}}$. The achievable resolution increases to $\sigma_0 = (100 \pm 10)\,\mu\mathrm{m}$.

(a) Hit distribution determined by the centroid method. The large agglomeration at the right side marks the edge of the boron-nitride block.

(b) Hit distribution reconstructed at the converter cathode by extrapolation of the ion start points, both the holes as well as the edge of the block are sharply visible.

Figure 3.18: Hit distributions determined by centroid and extrapolation for a hole mask made from a boron-nitride block of 5 mm thickness with 0.5 mm holes at $E_{drift} = 196 \, \mathrm{V \, cm^{-1}}$.

allowed to reconstruct the neutron position in both read-out directions with identical precision, which is exemplarily shown in figure 3.18. Here the collimator system was opened and a broad beam was used to light a 5 mm thick boron-nitride block with 0.5 mm diameter holes. Using the calibration parameters determined with the slit aperture and using the same method for both read-out directions individually again a clear enhancement relative to the centroid method start point extrapolation can be seen. The edges of the holes are sharply visible compared to the blurred image determined by the centroid method.

3.5 Reconstruction and Detection Efficiency

The detector concept shown and tested here cannot compete with ^{3}He detectors in terms of detection efficiency. For thermal neutrons ^{3}He based detectors can reach efficiencies of nearly 100 %. This is not possible for a single solid conversion layer of boron, as the range of the produced ions in the conversion layer is limited to about 2 µm, which can be seen from a Geant4 simulation shown in figure 3.19. Here the expected detection efficiency has been simulated for various neutron energies and different thicknesses of the conversion layer. The efficiency here was determined by the amount of ions leaving the conversion layer with an energy of more than 10 keV divided by the number of neutrons traversing the conversion layer.

The maximum detection efficiency follows roughly a $1/\sqrt{E}$ curve due to the same energy dependence of the capture cross-section [Beckurts et al., 1964].

The peak in the efficiency around 2 µm for the energies above 1 meV shown here can be explained by the average maximum range of the ions in this direction, which for sufficiently high cross-sections is overlayed with an exponential decrease in the efficiency due to the decreasing amount of neutrons left for conversion. This is also the reason for the slight shift towards a thinner conversion layer of the peak for the lowest neutron energy of 1 meV shown here.

For reasons of completeness here also two data points for layers of natural boron and boron-carbide are shown. Natural boron is nearly completely composed out of ^{11}B and ^{10}B, whereas ^{11}B has only a negligible neutron capture cross-section. The interaction probability and therefore also the detection efficiency scales therefore with the relative amount of ^{10}B atoms in the composition.
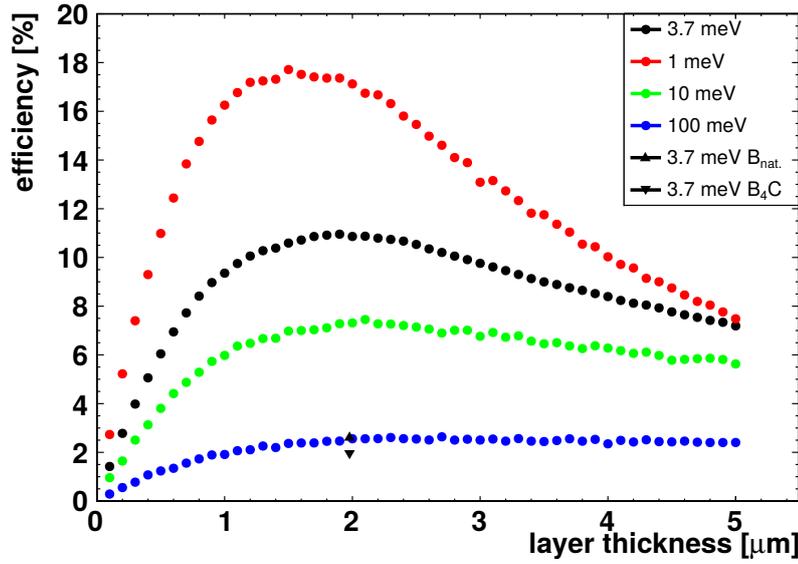
Figure 3.19: Simulation of detection efficiency with a single ^{10}B layer for different neutron energies plotted against the thickness of the conversion layer. Additionally the detection probability for natural boron and natural boron-carbide are shown for neutrons of 3.4 meV and a conversion layer thickness of 2 μm.

The detection efficiency was also measured in the beam-line by comparison with a ^{3}He counter leading to an efficiency of triggered events of (5.7 ± 0.1) %. Which is significantly lower than the conversion efficiency. This can be explained by a trigger threshold set to about 400 keV, which suppressed background in the detector caused by photons produced in the collimators, but also from the conversion layers.

3.6 Drift Field Dependence and Calibration Parameters

Since the parameter d of equation (3.6) as well as the quality of the result of the μTPC-fit are depending on the applied drift field, the resolution is also depending on the value of the drift field, which can be seen in figure 3.20(a). For low electric fields the resolution reaches its best values and steadily degrades to $\sigma \geq 180$ μm at electric fields above 700 V cm^{-1}. This behavior can nearly entirely be described by the absolute transverse diffusion in the drift region for a variation of E_{drift}, which is also shown and was determined by the simulations already discussed in section 2.4.1. The diffusion itself has also been measured by evaluating the parameter d from the fit with equation (3.6), which is shown in figure 3.20(b). The diffusion coefficients can be calculated from d in the following way:

$$D = \frac{d_{min}}{\sqrt{2}p} \simeq \frac{d_{min}}{\sqrt{2e}} \tag{3.9}$$

The values determined in this way are in good agreement with the simulated values. This can also be used to determine the calibration parameter d without a dedicated measurement with sufficient accuracy, which has so far been required dedicated calibration measurements. Using the simulated values for d and the approximated values for A and p a spatial resolution of $\sigma_0 = 140$ μm without efficiency loss was achieved. All together the application of a self consistent tracking method of the ions vastly improved the spatial resolution for the detection of thermal neutrons with a single ^{10}B-conversion layer. This allows for a position reconstruction of $\sigma \leq 120$ μm with a reconstruction efficiency of 95 %.
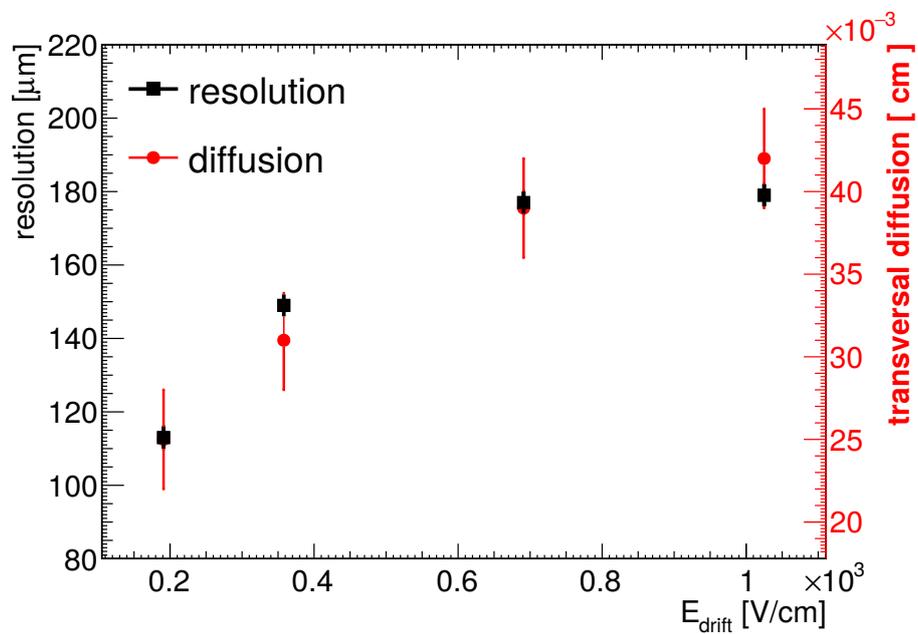
(a) Achieved resolution and simulated transverse diffusion of electrons drifting through 6 mm of $ArCO_2$ plotted against E_{drift}.
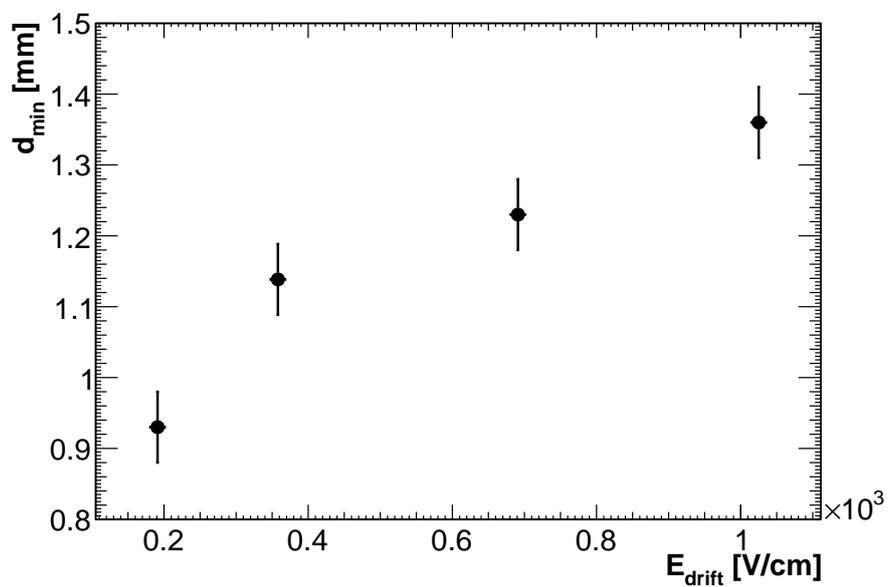
(b) Extracted minimal cluster size from fit to projected track length distribution.

Figure 3.20

Chapter 4

Particle Tracking using Thick-GEM (TGEM) Detectors

Of course the application of the methods described in the previous chapter is not limited to the usage of standard GEM detectors. In this chapter a similar extrapolation technique will be used, in order to optimize the spatial resolution of a single TGEM detector with identical read-out as before for the use with high energy alpha particles. TGEMs have the general advantage over standard GEMs to provide a higher amplification per layer, to be much cheaper and easier to produce and allow a more simple set-up with fewer high voltage channels. The major drawback of TGEMs compared to a standard GEM is the spatial resolution, which because of the much coarser granularity of the TGEM, suffers from a shadow mask like structuring. This leads to a much lower spatial resolution, which is typically in the order of the distance of the holes (see also [Breskin et al., 2009]). This behavior is shown in figure 4.1(a) for the hit distribution of a TGEM detector under homogeneous irradiation with alpha particles by a mixed nuclide alpha-source made from ^{239}Pu, ^{241}Am, and ^{244}Cm with the most dominant energies at 5.1 MeV, 5.5 MeV and 5.8 MeV [Firestone and Shirley, 1996]. The detector utilized a single TGEM as amplification stage with a thickness of 0.5 mm, a hole diameter of 0.5 mm and hole pitch of 0.8 mm together with a drift gap of 5 mm width. The energy of the particles corresponds to a range in Ar-CO_2 of about 30 mm, which was calculated by [Ziegler et al., 2010], and the source geometry allowed the particles to enter the active area of the detector with an inclination in the range between 0–70° with respect to the normal of the read-out plane under a $\cos\theta$-intensity distribution. The probability of the projection of the particle track onto the TGEM to cover only a single hole therefore was below 2 % and the mean number of holes covered was around 5.5. A high and nearly homogeneous energy-loss between 0.4–2 MeV was expected, which corresponds to 15000 to 75000 electron-ion pairs, depending on the track-length in the active volume. This value is in the same order as the energy-loss described in the chapter before, but the higher energy and range of the alpha-particles ensured that particles were actually not stopped in the drift region. Nonetheless the hole structure of the TGEM is clearly visible in the hit distribution determined by the centroid method. This is even more apparent, if only one slice of the hit distribution in the X-direction is considered, as it is shown in figure 4.1(b). The distance between the well pronounced peaks here precisely matches the distance between two holes in the TGEM of 0.8 mm and an additional (65 ± 5) % of the recorded events are reconstructed to be located directly beneath a hole. With an optical transparency of only 35 % it is apparent that this method is shifting reconstructed centers of the particle tracks to the holes in the structure, which is limiting its resolution.

Still straight tracks were reconstructed, whereas the hit position was only slightly distorted by the hole structure, as it can be seen for a set of fully reconstructed tracks for the same experimental set-up in figure 4.2(a). The points on the tracks here are determined by a time-bin wise fit to the charge distributions in both read-out directions leading to a full 3D-description of the track, which is visible in figure 4.2(b). The absolute Z-position of the electrons produced along the track leading to the signals shown here can be derived from the drift time with a drift velocity of 16 µm ns^{-1} for an $E_{drift} =150\,$V cm^{-1}, which has been chosen in order to spread the timing distribution for better
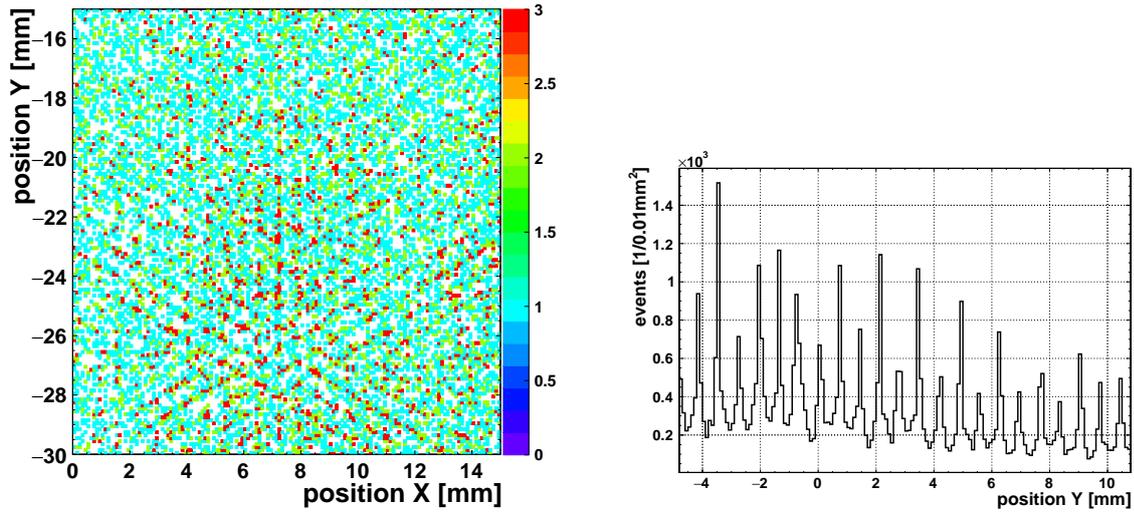
(a) Hit distribution in the read-out plane determined by the centroid method of an un-collimated alpha particle beam recurred with a TGEM. The hole structure of the TGEM with 0.5 mm holes with a relative distance of 0.8 mm is the reason for the typically lower spatial resolution achieved with TGEMs compared to standard GEMs.

(b) The cut through the left hit distribution recorded with higher statistics reveals the sharply peaked structure with a precise distance of 0.8 mm between two peaks corresponding to single holes in the detector.

Figure 4.1

track visibility here. For a direct conversion into the coordinate system of the detector here the timing offset and jitter coming from the trigger on the signal of the TGEM and the read-out would have to be considered, but this was not necessary here. Most of the tracks already directly pointed towards the common source of the particles at the cathode, which has been used to extrapolate the origin of the tracks in the drift region. In order to determine the tracking capabilities of this TGEM detector, the source was placed 3 mm above a $d = 1$ mm hole in an 0.5 mm aluminum collimator, which also served as cathode in this set-up [13]. This theoretically would have led to an in average decreased angular acceptance between 0–40°, but due to a slight asymmetry of the shape of the alpha particle source the overall angle distribution still was in the range between 0–70°. Application of the method described in chapter 3 allowed to reconstruct the collimator with high precision, as it can be seen in figures 4.3(a) and 4.3(b). Here a slight difference in the calculation of the projected track length arose from the specific hit pattern on the read-out anode due to the TGEM structure. The charge distribution along a track in contrast to the standard GEM detectors was neither smooth nor homogeneous and the charge asymmetry along the track ϵ, as it has been used before, could not be obtained from a fit to this charge distribution. Still the relative position of the centroid within the projected track could be used to calculate the charge skewness:

$$\epsilon = \frac{2 \cdot x_c - x_l - x_r}{x_r - x_l} + 1 \tag{4.1}$$

Here x_c is the centroid position and x_l and x_r are the position of the strips at the edges of the cluster, which also was used as measure for the projected track length $l_{proj.} = x_r - x_l$. Otherwise the same procedure was applied to both read-out directions separately to reconstruct the origin of the track in the drift region, i.e the hole in the cathode. From this the extrapolation to the origin by equation (3.8) could be applied leading to a reconstruction of the entrance hole in the cathode. The obvious increase in spatial information over the determination of the centroid position is visible in the direct comparison of figure 4.3(a) and 4.3(b). The long track length in the detector of up to 14 mm as expected afflicted the measurement with a washed out beam spot several millimeter in

---

[13]The size of the hole was sufficiently small not to disturb the drift field beneath
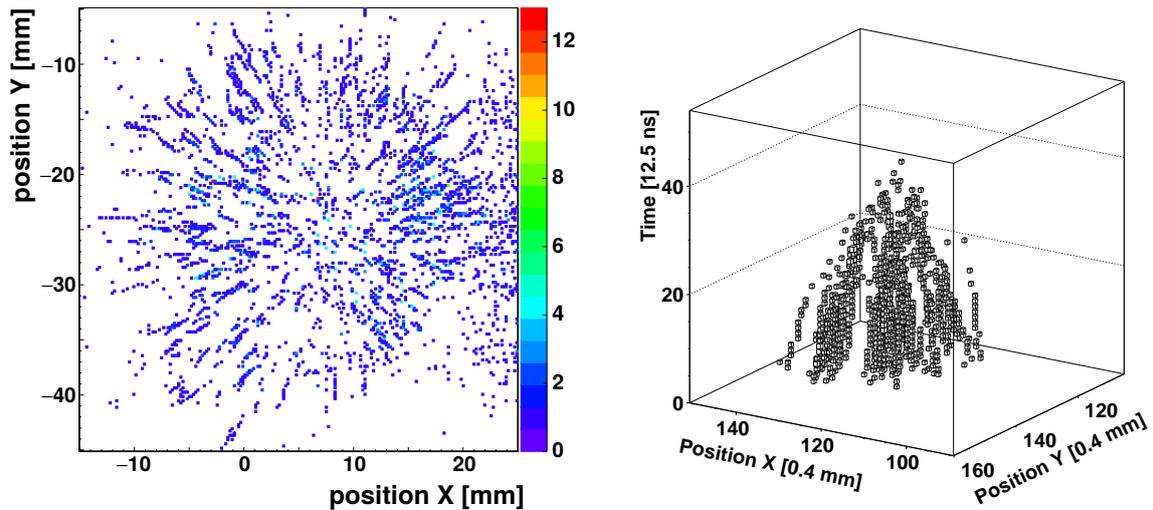
(a) Tracks of alpha particles projected onto the read-out plane. The star like structure reveals a common but spread source above the active region of the detector.

(b) 50 fully reconstructed alpha-particle tracks in the drift region. As the electric field in the drift region is constant and therefore also the electron drift velocity, the time given on the Z-axis can be converted in a relative Z-position in the detector

Figure 4.2

size. Extrapolation of the tracks on the contrary delivers a sharply defined image of the actual hole, which is only slightly exaggerated by a smooth blurring due to the intrinsic resolution of the TGEM. Notably is also that the slight elongation due to the asymmetry of the sources extend vanishes by reconstruction of the hole. In the reconstructed hit distribution also the position of some holes in the TGEM are marked by red circled for comparison, which shows that in fact a position was reconstructed between these holes and that a construction independent of the structure of the TGEM is possible. The achievable spatial resolution was calculated from the expected hit distribution compared to the measured distribution. From the angular intensity distribution and under the assumption of a circular source with radius R in a distance d to the hole the projected flux through the hole can be described by:

$$I(x) = H(x_0 + r)H(x_0 - r)A \cos\left(\pi \frac{(x - x_0)\,R}{2rd}\right)^2, \tag{4.2}$$

with a normalization parameter A and the radius of the hole r. In the specific case here this led to a distribution with a RMS of $\frac{r}{2}$. The convolution with an assumed Gaussian shaped response of the detector should then describe the hit distribution. Here the approximation by a convolution of two Gaussian distributions will be used, where the one resembling the underlying intensity distribution is assigned a standard deviation of the RMS of the real distribution $\sigma_0 = \frac{r}{2}$.

The real hit distribution is again best described by a fit of a double Gaussian distribution, with an underlying broad tail distribution. These broad tails can be attributed to suppressed, but still present, charge accumulations close to the holes of the TGEM. The result of this can be seen in figure 4.3(c) with a double Gaussian fit. Deconvolution of the hole size leads to a weighted spatial resolution of $(360 \pm 30)\,\mu\text{m}$, which could be achieved in both read-out directions independently with the same set of calibration parameters. This shows that for densely ionizing particles tracking with a single TGEM detectors is possible and exploitation of the fully reconstructed track can also offer a significant increase in the spatial resolution. This enhancement is independent of the inclination of the incoming particle and led to a position reconstruction well below the size and the pitch of the holes of the TGEM.
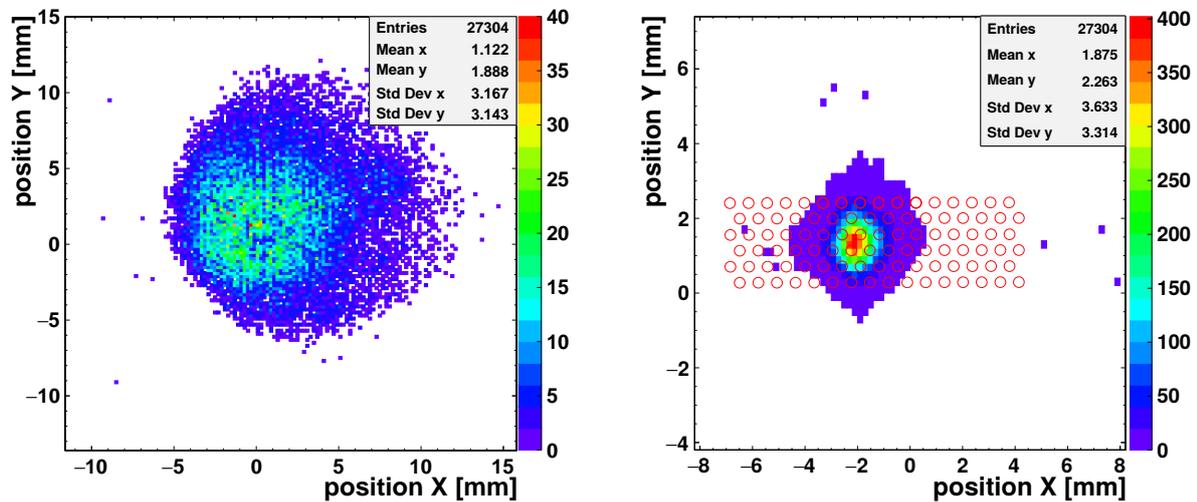
(a) Centroid hit distribution of TGEM by irradiation with alpha particles through a 1 mm pin hole in the cathode. An asymmetry in the shape of the source led to a slightly elongated hit distribution.

(b) Reconstructed shape of the collimator after extrapolation of the particle tracks to the start point in the drift region. N.B. the scales here strongly differ compared to the uncorrected case (a). For comparison here also the position of some of the holes in the TGEM are displayed by red circles.
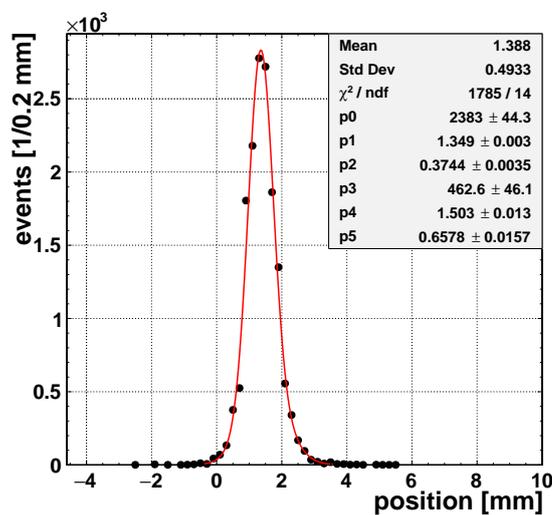
(c) Projection of the extrapolated hit distribution onto the Y-axis of the detector coordinate system. A fit with a double Gaussian distribution allowed to determine the spatial resolution to be $(360 \pm 30)\,\mu m$.

Figure 4.3

Chapter 5

High Energy Muon Tracking with a GEM Detector

Tracking in a single detector layer shown in the previous chapters strongly benefited from the dense ionizing particles used there. For minimum ionizing particles the same methods as described before cannot be applied directly, because of the much larger influence of charge clustering along a track in the detector formed by these particles[14]. In this chapter different methods applicable for tracking, also considering the characteristic timing features of the used read-out system, will be discussed at the example of a high energy muon beam.

5.1 Experimental Set-up at the SPS Accelerator

The tracking performance under the irradiation of a single triple GEM detector was investigated with a high intensity muon beam, which was provided by the Super Proton Synchrotron (SPS)[15] at CERN. The muons at the SPS are produced as the decay products of a 160 GeV pion beam with an energy in the range between 10–150 GeV. At this energy muons are still close to minimum ionizing and have an energy loss of $\langle dE/dx \rangle$=2–4 MeV cm^2 g^{-1} [Olive et al., 2014], which is about a factor of 1000 less than the energy loss of the ions in the previous chapters. It allowed tracking of the particles in a detector system consecutively built from five MPGDs with almost no contribution from multiple scattering[16]. A track reference was provided by four micromegas detectors sandwiching a rotatable mounted GEM detector, which is schematically shown in figure 5.1. The read-out system was triggered by the coincident signal of two plastic scintillators in front and behind the micromegas detectors with an active area of 9 cm × 10 cm. All gaseous detectors used here featured a 2D strip read-out with a total number of 3584 read-out channels[17]. This set-up allowed measurements with a read-out rate around 1 kHz at a real particle flux of about 4 kHz through the detectors. The construction of the GEM detector was based on a low material budget read-out anode, with a thickness of 300 μm of printed-circuit board equivalent, in order to minimize scattering of the muons. Otherwise it was identical to the ones described earlier, with a read-out based on crossed copper strips with 400 μm pitch. The cathode was made from aluminized Kapton of 25 μm thickness which enclosed the 8 mm drift gap. The mounting of the GEM allowed to rotate it with an accuracy of 0.1° in both directions perpendicular to the beam to angles of 15°, 20°, 30°, 36° and 40°, which allowed a dedicated study of the angular dependence of the signal formation in the detector and thus the spatial resolution under inclined tracks. As reference system micromegas chambers with resistive strip discharge protection [Byszewski and Wotschack, 2012] and a well

---

[14]Application of this method is possible, but the improvement in spatial resolution compared to the centroid method is much smaller. For measurements with cosmic muons this led for an Ar-CO_2 gas-mixture to an improvement of about 20 % [Flierl et al., 2016a]

[15]https://home.cern/about/accelerators/super-proton-synchrotron

[16]An estimation for this is shown in appendix B

[17]This made the use of 28 APV-hybrid boards and therefore two FEC-cards necessary, which were managed by one SRU (see section 2.5)

known spatial resolution of 60 μm in both read-out directions for perpendicularly incident muons of this energy were used [Lösel, 2013]. The active area of the reference detectors was with 9 cm × 9 cm and a drift gap of 5 mm slightly lower than that of the GEM.
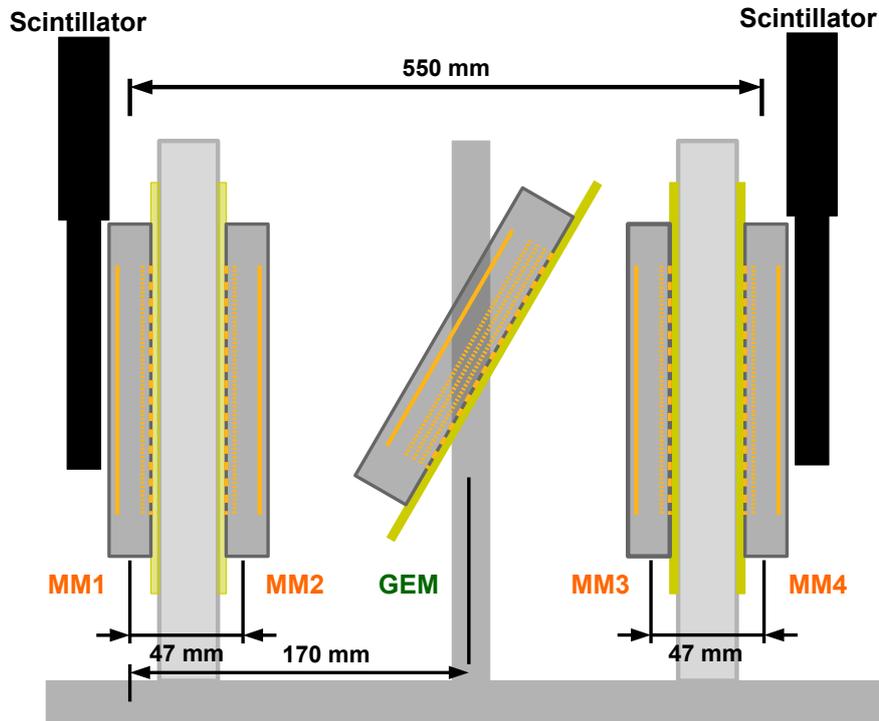
Figure 5.1: Schematic of the hodoscope set-up: Four micromegas detectors placed in front and behind the GEM detector form a reference system which was used to test the GEM detector in the middle. The GEM was rotatable in both directions perpendicular to the muon beam. A trigger was provided by the coincidence signal of two scintillators in front of and behind the hodoscope.

By determining the muon position in the fixed mounted reference detectors and by linear extrapolation, this set-up allowed a track prediction accuracy at the position of the GEM detector between 40 to 50 μm, depending on the inclination angle of the GEM Detector, as can be seen in figure 5.2. The calculation of the uncertainty can be found in appendix B.

The muons were produced by the decay of a pion beam upstream of the experimental area, leading to a broad beam profile, but very little beam divergence. This allowed large homogeneous coverage of the active area of the detector system and ensured well defined track inclination, which is shown in figures 5.3(a) and 5.3(b), where the beam profile in the GEM detector for perpendicular incident and the beam divergence measured by the reference system are shown. The divergence of the beam could be measured to be $\sigma_\theta = 0.1°$, see figure 5.3(a). This allowed for a very precise measurement of the inclination dependence of the position reconstruction.
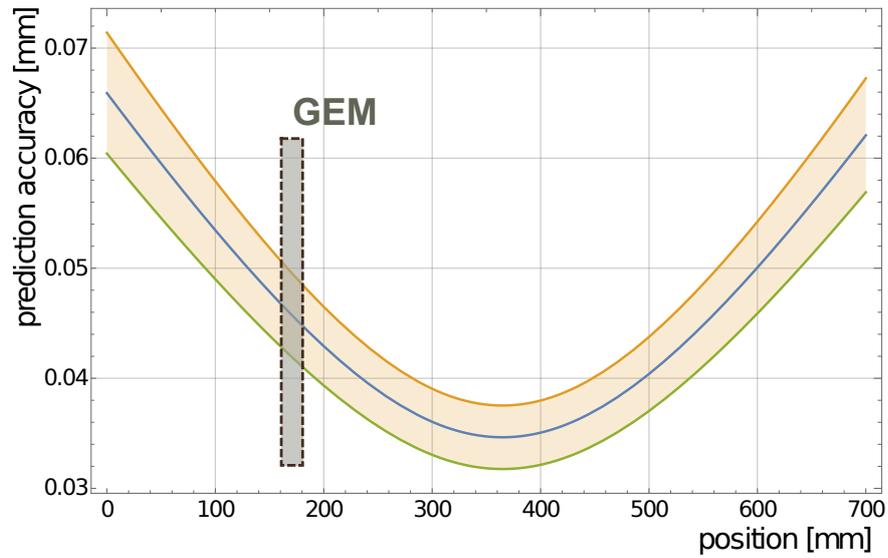
Figure 5.2: Calculated track prediction accuracy provided by the four reference micromegas detectors plotted against the position of a test detector in the direction of the beam.
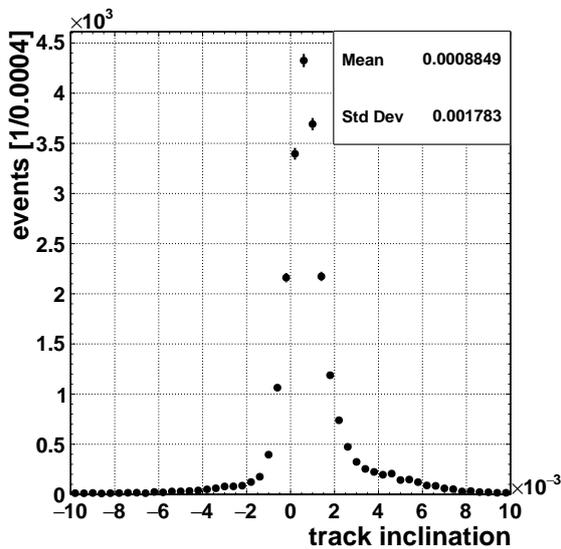
(a) Beam divergence in X-direction measured by the telescope relative to the Z-axis, the standard deviation of $\sigma_{incl.} = 1.8 \cdot 10^{-3}$ corresponds to a beam divergence of $\sigma_\theta < 0.1°$.
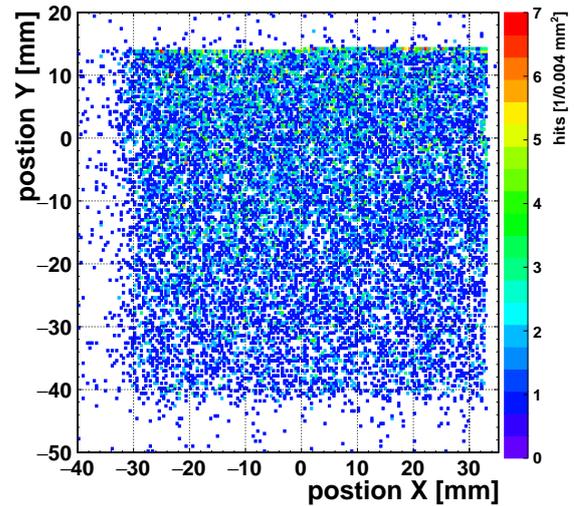
(b) Beam profile measured with the GEM detector. The sharp edges are due to the dimensions of the trigger scintillators. The size of the beam was actually much broader.

Figure 5.3

5.2 Centroid Position Determination: Spatial Resolution

The position measurement by the centroid method with the GEM detector for different track inclinations revealed the expected charge clustering dependence characterized by deceasing spatial resolution for inclined tracks. The determination of the spatial resolution in the following is implemented by deconvolution of the assumed Gaussian distributed track prediction accuracy of width σ_{track} from the residual distribution i.e. the difference between the predicted position and the reconstructed position in the GEM detector. The prediction of the position inside the GEM detector was done by a careful alignment of the detector coordinate system with respect to the coordinate system defined by the tracking telescope, which is illustrated in more detail in appendix B. A residual distribution for perpendicular incident muons in the X-Layer of the GEM detector is shown in figure 5.4, which has been fit with a double Gaussian distribution. This shape can be explained by a narrow core distribution of width σ_{core} containing the vast majority of events, which represents the intrinsic spatial resolution of the method applied. The underlying broader distribution of width σ_{tails} describes the more unlikely case, where the position reconstruction is impaired by features of the track like δ-electrons, which itself can have a considerable track in the gas region. Both contributions in the residual distribution are blurred by the track prediction accuracy, which also is assumed to be described by a Gaussian distribution:

$$f = \frac{1}{\sqrt{2\pi}\sigma_{track}} \cdot e^{\left(-\left(\frac{x}{\sqrt{2}\sigma_{track}}\right)^2\right)} \oplus \left[A_{core} \cdot e^{\left(-\left(\frac{x-\mu_0}{\sqrt{2}\sigma_{core}}\right)^2\right)} + A_{tails} \cdot e^{\left(-\left(\frac{x-\mu_1}{\sqrt{2}\sigma_{tails}}\right)^2\right)} \right] \tag{5.1}$$

$$f = A_0 \cdot e^{\left(-\left(\frac{x-\mu_0}{\sqrt{2}\sigma_0}\right)^2\right)} + A_1 \cdot e^{\left(-\left(\frac{x-\mu_1}{\sqrt{2}\sigma_1}\right)^2\right)} \tag{5.2}$$

Where $\sigma_0 = \sqrt{\sigma_{track}^2 + \sigma_{core}^2}$ and $\sigma_1 = \sqrt{\sigma_{track}^2 + \sigma_{tails}^2}$. Depending on the reconstruction method the relative contribution of both distributions to the full residual varies and therefore in the following spatial resolution will be defined by the weighted mean of both if not otherwise stated:

$$\sigma_{weighted} = \frac{A_0\sigma_0\sigma_{core} + A_1\sigma_1\sigma_{tails}}{A_0\sigma_0 + A_1\sigma_1} \tag{5.3}$$

For perpendicularly incident muons at an $E_{drift} =562.5\,\text{V cm}^{-1}$ this led after subtraction of the track prediction uncertainty of $(45 \pm 5)\,\mu\text{m}$ from the residual to a spatial resolution of $\sigma_{weighted}=(56 \pm 8)\,\mu\text{m}$ and $\sigma_{core} = \sqrt{\sigma_0^2 - \sigma_{track}^2}=(38 \pm 6)\,\mu\text{m}$ if only the narrow Gaussian in the residual distribution is considered.

For perpendicular incident muons this very good spatial resolution is not affected by variation of the drift field at all, as it can be seen in figure 5.5(b). Whereas the amplification had only little influence as long as the sum of the voltage difference ΔU of the GEMs is larger than 880 V, as it can be seen in figures 5.5(a). Although the amplification voltage does not directly influence the width of the electron cloud at the read-out anode, lower amplification also means a lower amount of strips exceeding the threshold is recognized as hits. This occurs typically at the edges of the charge distribution in every event and leads to fluctuations in the determination of the mean values. The spatial resolution is directly influenced by this. For the drift scan the amplification voltage was $\Delta U = 920\,\text{V}$ and the drift field for the amplification scan was $E_{drift} =562.5\,\text{V cm}^{-1}$. The amplification has been altered by modifying the voltage difference at the uppermost GEM. The rest of the voltages have been held constant and were chosen as it is shown in table 5.1.

For all further measurements the amplification and transfer fields were fixed and only the drift field was modified. In the next step the detector was tilted and as it was expected from the simulation shown in chapter 2 (see figure 2.28(b)) there is a drastic influence of the inclination angle on the spatial resolution, which is shown in figure 5.7. Here the spatial resolutions are plotted against the inclination angle for $E_{drift} =187.5\,\text{V cm}^{-1}$, which varies from $(56 \pm 8)\,\mu\text{m}$ to $(630 \pm 25)\,\mu\text{m}$ between $0°$ and $40°$. For angles below $15°$ the weighted resolution from a double

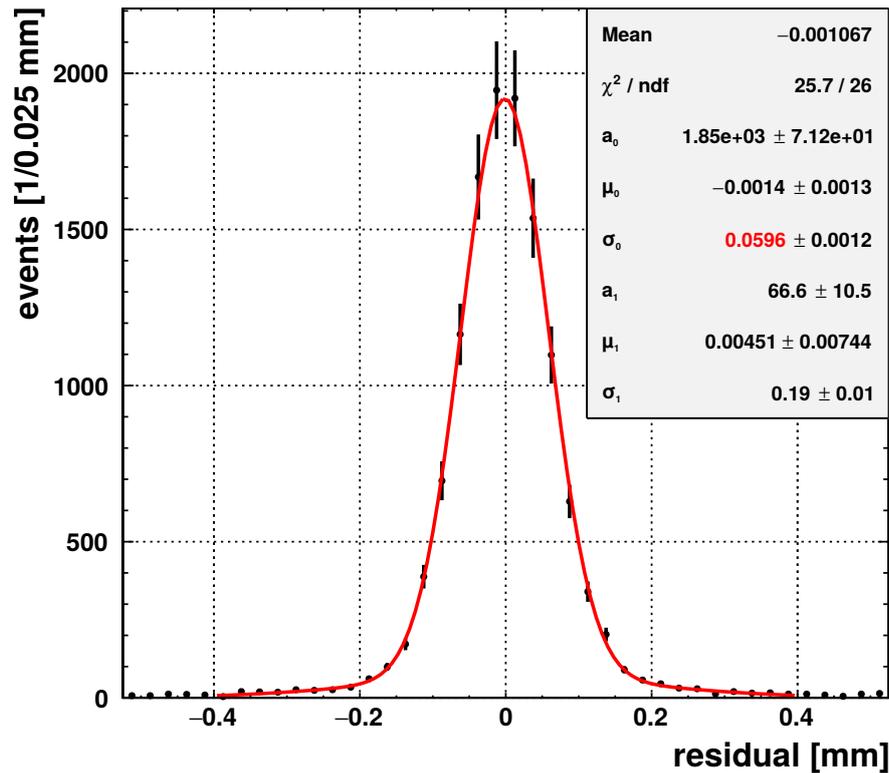|	
Mean	−0.001067
χ^2 / ndf	25.7 / 26
a_0	1.85e+03 ± 7.12e+01
μ_0	−0.0014 ± 0.0013
σ_0	0.0596 ± 0.0012
a_1	66.6 ± 10.5
μ_1	0.00451 ± 0.00744
σ_1	0.19 ± 0.01

Figure 5.4: Residual distribution of the GEM detector for perpendicularly incident muons fit with a double Gaussian function leading to a resolution of (38 ± 6) µm defined by the narrow Gaussian and a weighted resolution of $\sigma_{weighted} = (56 \pm 8)$ µm.

Table 5.1: Applied voltages and electric fields for the GEM detector (sorted from bottom to top)

	Voltages/Field strength
E_{ind}	2000 V cm^{-1}
ΔU_1	250 V
E_{Trans1}	2250 V cm^{-1}
ΔU_2	350 V
E_{Trans2}	1750 V cm^{-1}
ΔU_3	320 V

Gaussian fit is shown and for angles above $15°$ the width of a single Gaussian fit is plotted, which describes the residual distribution better and can be understood by the fact, that the range of δ-electrons in the gas is limited to about 1 mm (compare figure 2.3). The projected track length in the read-out direction on the other sides exceeds this value at around $15°$ and the effect of the δ-electrons is minimized. The residual distribution for an inclination angle of $36°$ at $E_{drift} = 562.5$ V cm^{-1} in figure 5.6 is in good agreement with the fit of a single Gaussian, translating to an already degraded spatial resolution of (575 ± 20) µm. The trend here is even slightly worse than predicted by the simulation for 120 GeV muons, but one has to consider that the muon spectrum of the beam also allowed muons with a significantly lower energy implicating even higher susceptibility for charge clustering and multiple scattering.
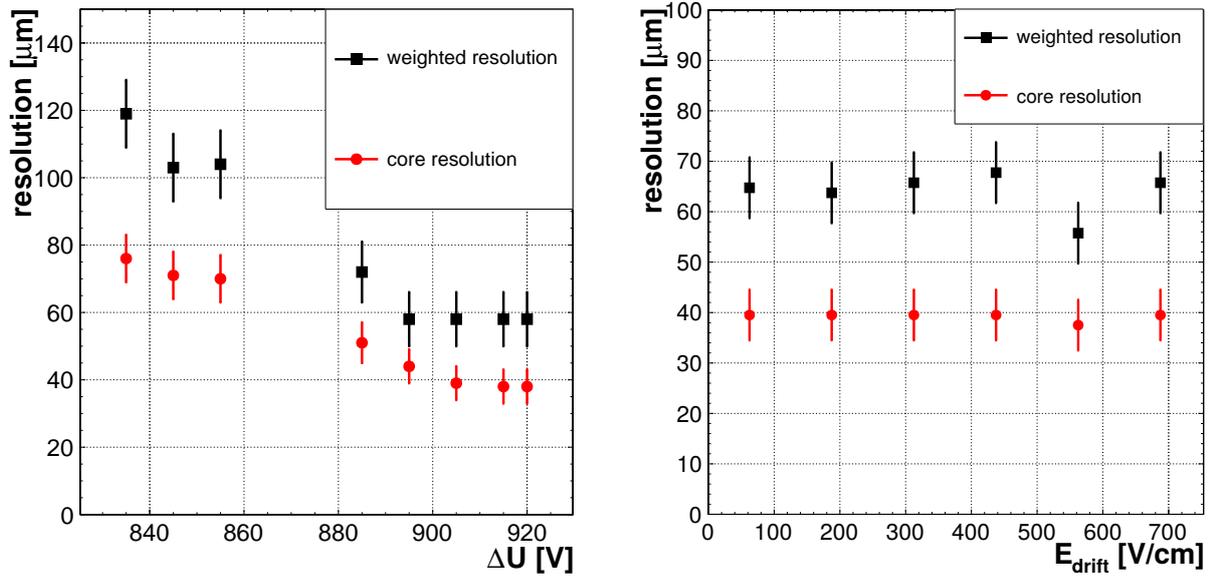
(a) Centroid resolution plotted against amplification voltage. The amplification was varied by tuning the voltage difference at the uppermost GEM.

(b) Weighted and core centroid resolution plotted against the drift field for perpendicularly incident muons, there is no significant effect on the resolution visible.

Figure 5.5
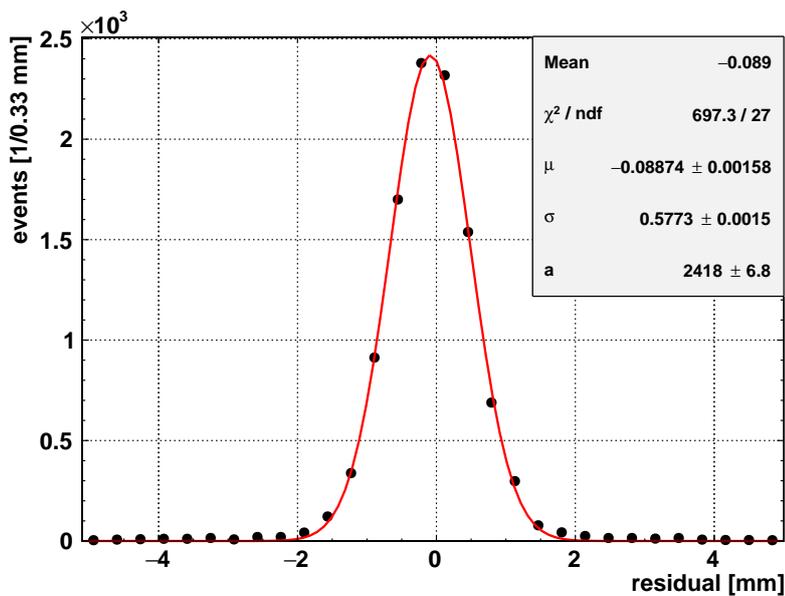
Figure 5.6: Residual distribution for an inclination angle of $36°$ and a drift field of $562.5\,\mathrm{V\,cm^{-1}}$ with fit of a single Gaussian.
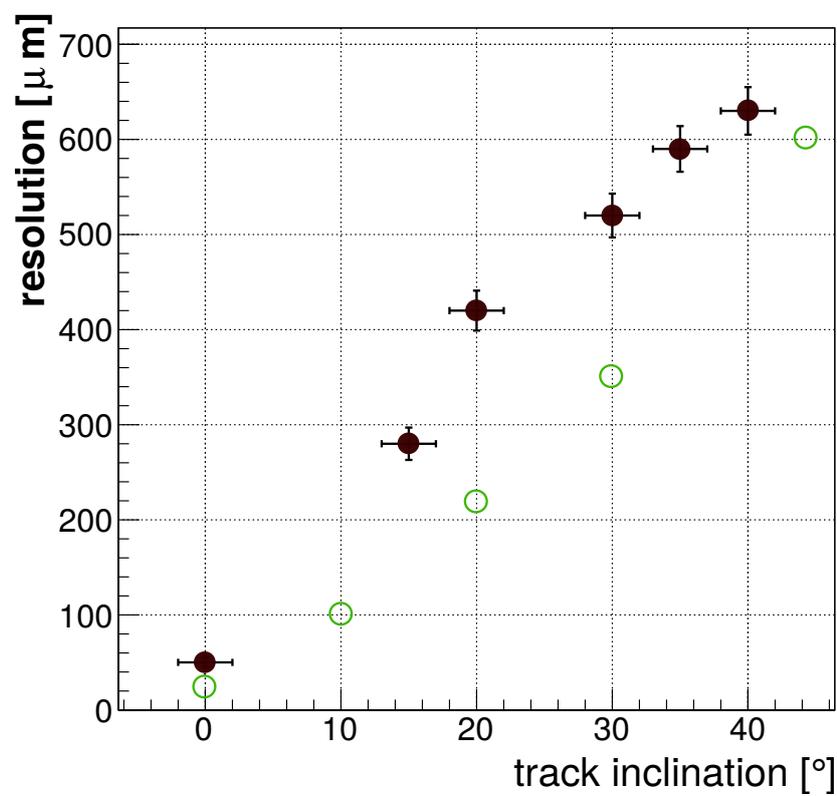
Figure 5.7: With increasing inclination angle a nearly linear decrease in the spatial resolution determined by the centroid method was observed. Here shown for an $E_{drift} =$562.5 V cm^{-1}. For reference also the simulated resolution from section 2.7.7 for 120 GeV muons are shown here as open circles.

5.3   μTPC Position Reconstruction and Tracking

The general deficit of position determination by the centroid method for inclined tracks should be overcome by the position determination using the μTPC method. The method itself is strongly depending as well on a precise absolute – with respect to the passage of the particle – as relative time measurement at all strips hit. The absolute timing measurement unfortunately suffers from the intrinsic time jitter inflicted by the APV-based read-out system, which directly influences the position resolution. On the other hand the relative time measurement, which is dominated by the actual signal shape dictated by the electron drift and the initial charge deposition in the drift region, is more influenced by the underlying physics and the detector geometry and can be optimized by the electron velocity and compensation of the charge dependence of the signal shape.

5.3.1   Determination of the Angle Resolution

In order to probe rather the detector and the method than the read-out system first the angle resolution of the detector was determined, which is almost independent of the absolute timing. The determination of the track inclination is relying on the quality of the measured timing for every strip in a cluster and therefore on the charge distribution on these strips. This translates into a strict dependence of the reconstructed angle on the slope of the μTPC-fit:

$$\theta = \arctan \frac{1}{m_{\mu TPC} v_{drift}} \tag{5.4}$$

The main contribution on this signal (see section 2.4.2) can be attributed to the electrons produced directly above the respective strip, but distortions due to coupling are possible, but this effect can be compensated by a charge-correction for every time-bin. Figure 5.8(a) shows an event where the timing determination and the linear fit in general worked for a by 36° tilted detector and $E_{drift} =$687.5 V cm^{-1}. Here an event display overlayed by the reconstructed strip timings is shown for a single muon. The reconstructed angle $(42 \pm 5)°$ was a bit too large which is equivalent to a too low slope in the fit. This slight mis-reconstruction is caused by the division of the track in three connected, but still clearly visible sub-clusters. Charge coupling of the dominant peak in the center of the track led to a step-like timing distribution and without charge-correction this led on average to larger reconstructed angles, which can be seen in figure 5.9 for the mean reconstructed angle plotted versus the set angle for $E_{drift} =$687.5 V cm^{-1}. An example for a case where this correction will not improve the reconstruction results is shown in figure 5.8(b), which was recorded with the same detector set-up as before. As mentioned before the influence of charge clustering is less critical for the μTPC position determination, but large charge agglomerations caused by high energy primary electrons, especially at the lower end of the drift gap can hide the time information for strips, which should have been hit later. In the example shown here the size of the charge cluster at the central hit position of the track is within the expectations for the tilt of the detector, but the large amount of strips with nearly equal timing and high charge disguise the real track shape and in this case even lead to an error in the angle reconstruction of more than 45°. Events like this later on distorted the position reconstruction considerably, but could be identified very well by the quality of the μTPC-fit and rejected effectively by requiring a χ^2/NDF < 5 of the fit.

The same effect also was responsible for a rather bad angle resolution especially for low inclination angles, which can be seen in figure 5.10 by the reconstructed angle distribution for an inclination of 15° at the same E_{drift}, which significantly differs from the set angle. Here a mean angle of $(18.89 \pm 0.09)°$ was reconstructed with a width of the distribution of $\sigma_w =(5.25 \pm 0.12)°$. The angle distributions were evaluated by a fit with the sum of a Landau- and a Gaussian-distribution with a single parameter for the most probable value of the Landau- distribution and the mean value of the Gaussian. The quality of the angle reconstruction from now on will be described by the value of this parameter and the width of the distribution defined as the widths of both functions
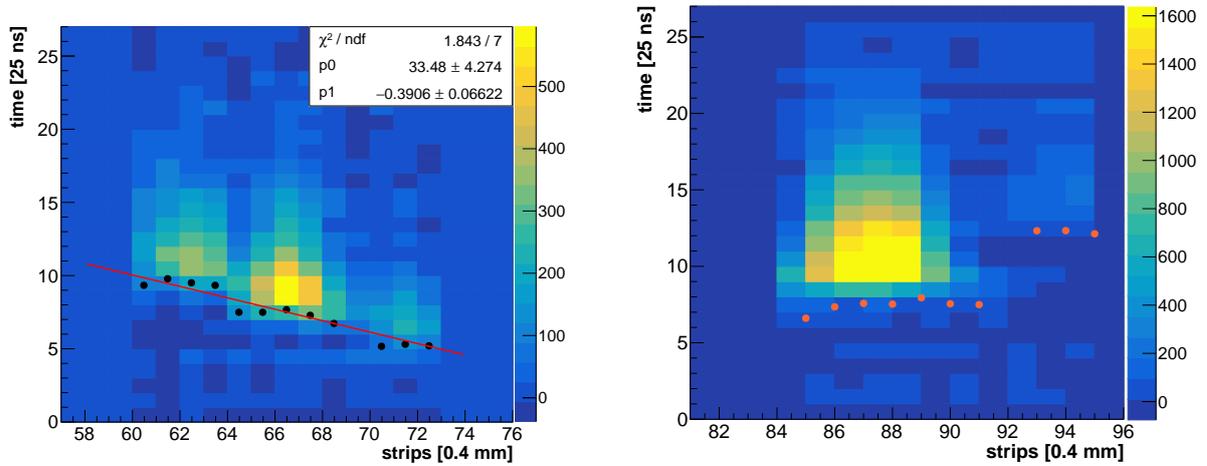
(a) Event display with overlayed strip timing for an event for 36° tilted detector at E_{drift} =687.5 V cm^{-1} with overlay of the reconstructed timing and µTPC-fit. For this angle a fit slope of -0.5 time-bins/strip is expected, the fit gives -0.391.

(b) Event display, where the µTPC-fit failed. Large charge agglomeration, most likely caused by a δ-electron overlays the charge distribution of most strips leading to an angle reconstruction, which is by 45° off the set 36° inclination.
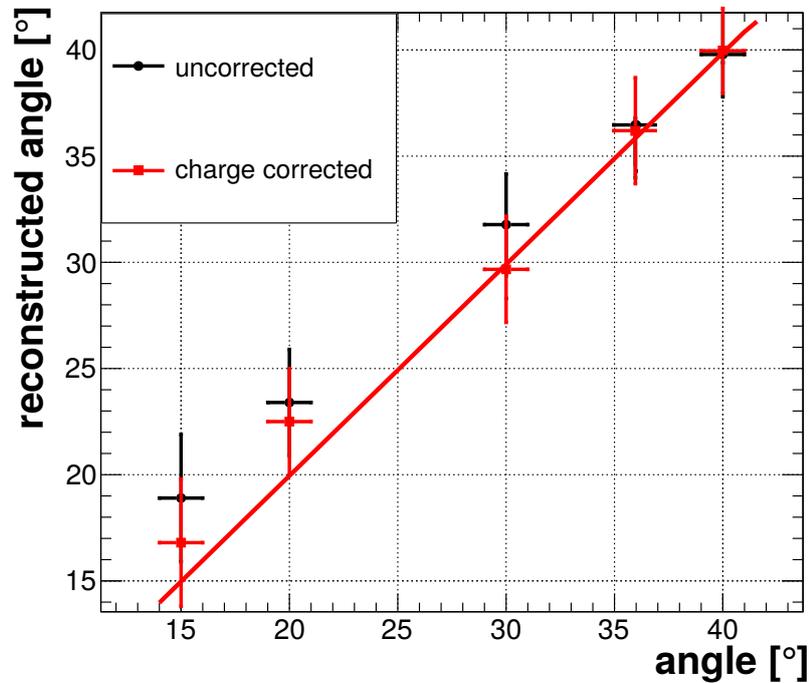
Figure 5.8

Figure 5.9: Mean value of the reconstructed angle for E_{drift} =687.5 V cm^{-1} with and without charge correction described in section 2.4.2 with the red line to guide the eye. The correction improves the reconstructed angle especially for low angles.
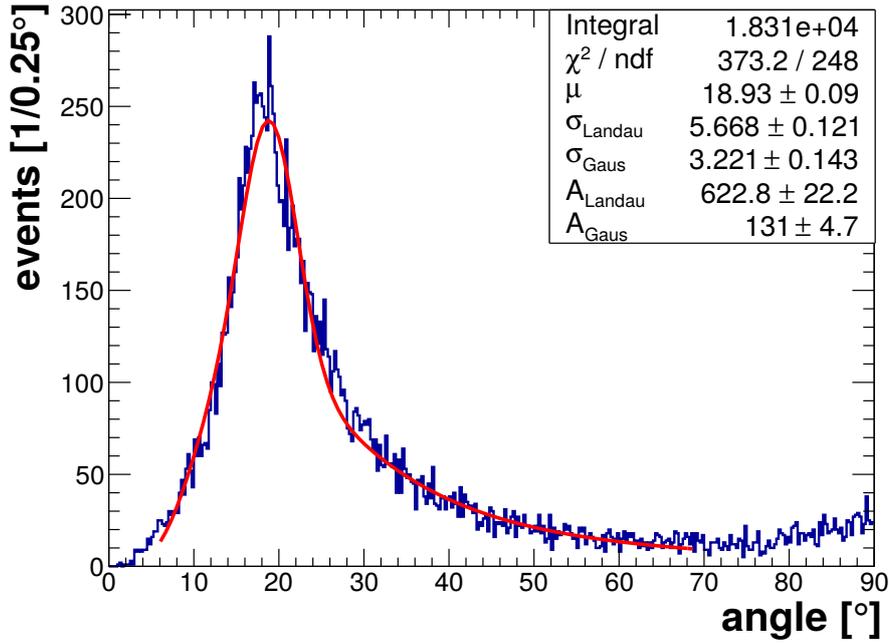
Figure 5.10: Distribution of uncorrected reconstructed angles for 15° tilted detector and E_{drift} =687.5 V cm^{-1}, fit with the sum of a Landau and a Gaussian distribution. The most probable value of the distribution is at 19°.

weighted with their relative integral[18]:

$$\sigma_w = \frac{N_{Gaus}\sigma_{Gaus} + (N_{total} - N_{Gaus})\sigma_{Landau}}{N_{total}} \tag{5.5}$$

Both, absolute value and width enhance with larger inclination angles, mostly because the number of hit strips increases and therefore the effect of the strips at the edge of a track minimizes, but still a significant deviation even at a set angle of 30° was observed, where the mean reconstructed angle was 32°. Application of the time-bin-wise charge-correction from section 2.4.2 to the pulse-height by a correction factor of 20 %[19] led to a much better angle resolution and reduced the systematic shift of the mean reconstructed angle considerably. At the example of 15° this is shown in figure 5.11, with an improved mean reconstructed value of $(16.99 \pm 0.04)°$ and a width of $\sigma_w = (2.70 \pm 0.04)°$. The direct comparison with the uncorrected reconstructed mean angles in figure 5.9 shows better agreement with the set angles over the whole range. Due to this obvious increase in the quality of the μTPC-fit, the correction will be used further on for all results presented in this chapter.

Two parameters, which directly influence the angle resolution are the electron drift velocity v_D and the electron diffusion. The influence of v_D on the angle reconstruction, which could be understood from the limited absolute timing resolution of the detector and the read-out, seems to be rather low as the angle resolution in fact seems to degrade slightly with lower E_{drift}. The longitudinal electron diffusion on the other hand in the same range of E_{drift} also decreases steadily and the best angle resolution here was obtained at a drift voltage where this diffusion was also minimal, as it is shown in figure 5.12(a), which has to be compared with the diffusion coefficients in figure 2.14. The general trend of a better angular reconstruction at larger angles was observed independently for all drift field variations and is exemplarily shown for an E_{drift}=562.5 V cm^{-1} in figure 5.12(b) for the reconstructed angle distributions of 15°, 30° and 40°.

---

[18]The integral of the Landau-distribution has been determined by subtraction of the integral of the Gaussian-distribution from the total number of events.

[19]Which was empirically found to deliver the best angle resolution, rather than the 15 % simulated before, this might be afflicted by additional capacitive coupling of the strips (see e.g. [Lösel, 2017]) which has not been considered in the simulation.

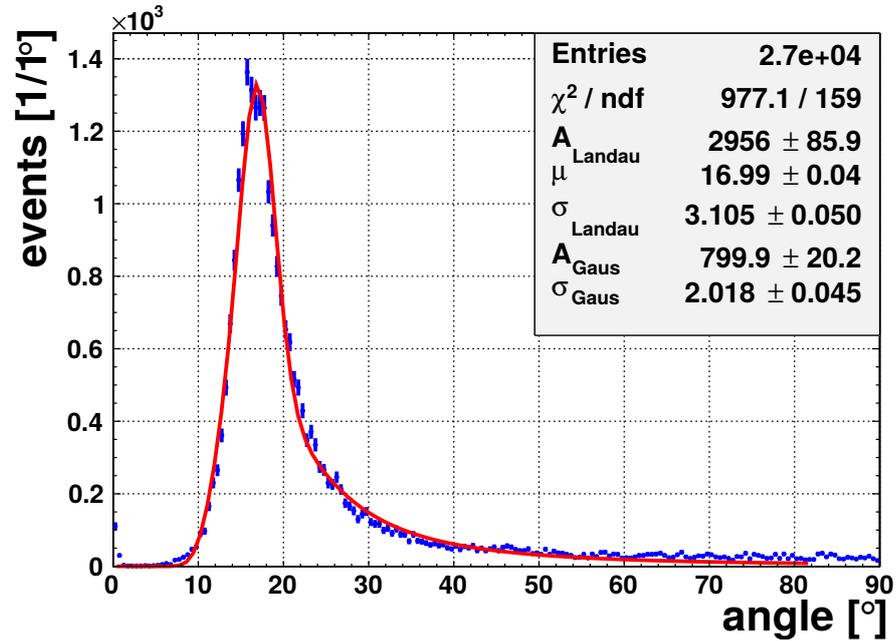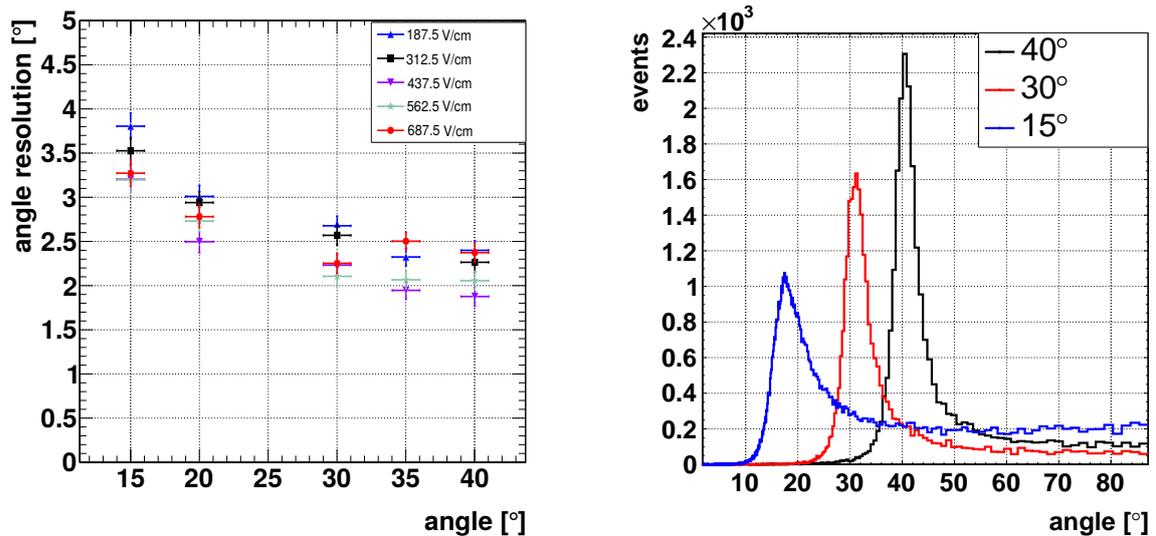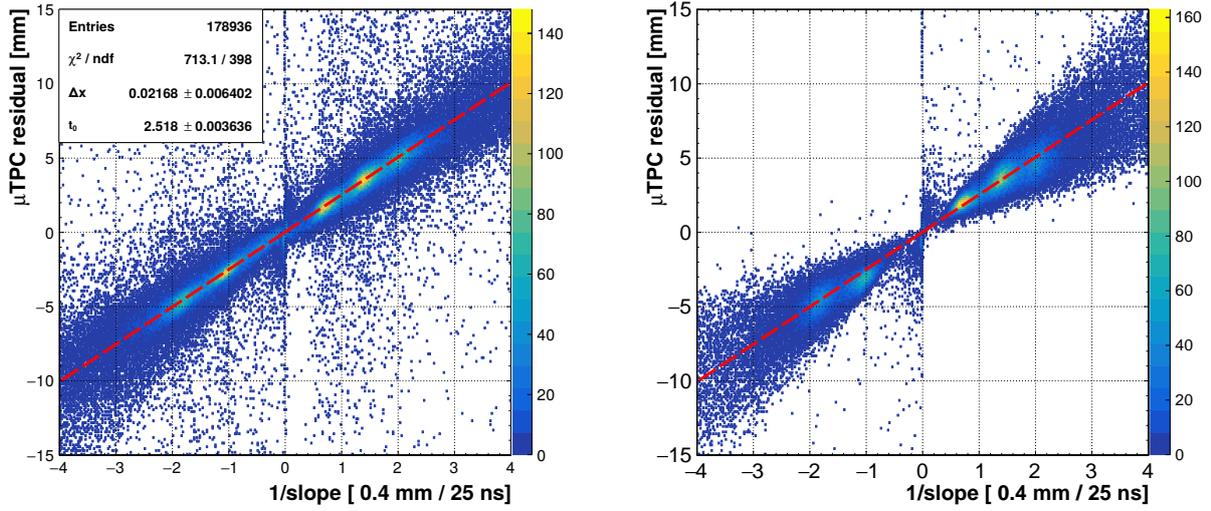Figure 5.11: Distribution of charge-corrected reconstructed angles for a detector tilted by 15° and $E_{drift} =$ 687.5 V cm^{-1}, fit with the sum of a Landau and a Gaussian distribution.

(a) Angle resolution for different angles and combinations of E_{drift}

(b) Direct comparison of reconstructed angular distributions for different angles at an E_{drift}=562.5 V cm^{-1}.

Figure 5.12

(a) Determination of t_{mid} by fit of a linear function to the µTPC -residual determined with the first term of equation (2.33) plotted versus $1/m_{µTPC}$ (see equation (2.37)). Here the distribution is plotted for the angles $15°$, $20°$, $30°$, $36°$ and $40°$ and $E_{drift} = 437.5 \, \text{V cm}^{-1}$.

(b) Determination of t_{mid} determined from the µTPC -residuals with respect to the centroid position plotted versus $1/m_{µTPC}$. The line is drawn with the parameters taken from the fit shown in 5.13(a).

Figure 5.13

On the other hand this shows, that the angle reconstruction works very well with an angular resolution below $3°$ and an absolute error of the reconstructed angle of less than $3°$ for all tested combinations of drift fields and angles $\theta \geq 20°$.

5.3.2   Determination of t_{mid}

Similar as in chapter 3 the calibration of the timing offset t_{mid} for the position determination by the µTPC-method was determined by a slight modification of equation (2.37). This was done by a fit of a linear function to the difference between the track prediction and the position determined by $(t_{µTPC}/m_{µTPC}) - x_{track}$ plotted versus $1/m_{µTPC}$ for all sets of measured angles recorded with a given E_{drift} simultaneously. For $E_{drift} = 437.5 \, \text{V cm}^{-1}$ this led to a distribution like it is shown in figure 5.13(a). This calibration not necessarily needs the input of a track prediction from other detectors, but also the centroid position in this detector can be used as reference. This is shown in figure 5.13(b) for the same E_{drift} with an overlay of the fit from figure 5.13(a). The value of the parameter t_{mid} corresponds geometrically to the middle of the drift region and depends on the drift velocity v_D there, the drift gap width Δz and an absolute time offset from the read-out electronics $t_{el.}$.

$$t_{mid} = \frac{\Delta z}{2 \cdot v_D} + t_{el.} \tag{5.6}$$

This allows alternatively to obtain this value by the drift-time spectrum, i.e. the distribution of all recorded strip timings. Under the assumption of on average equally distributed ionization within the drift gap, the spectrum should in general have a box-car like distribution of the strip timings. This distribution would be blurred by the time jitter and timing resolution of the read-out electronics as well as the timing fluctuations for the single electrons due to longitudinal diffusion. Assuming Gaussian shape of all uncertainties the drift time spectrum can be parametrized in the following way, by convolution of a Gaussian with a box-car function:

$$F(t, t_{mid}, \sigma_t) = A \cdot \left(erf\left(\frac{0.5 \cdot \Delta t + (t - t_{mid})}{(\sqrt{2}\sigma_t)} \right) + erf\left(\frac{0.5 \cdot \Delta t - (t - t_{mid})}{(\sqrt{2}\sigma_t)} \right) \right) \tag{5.7}$$
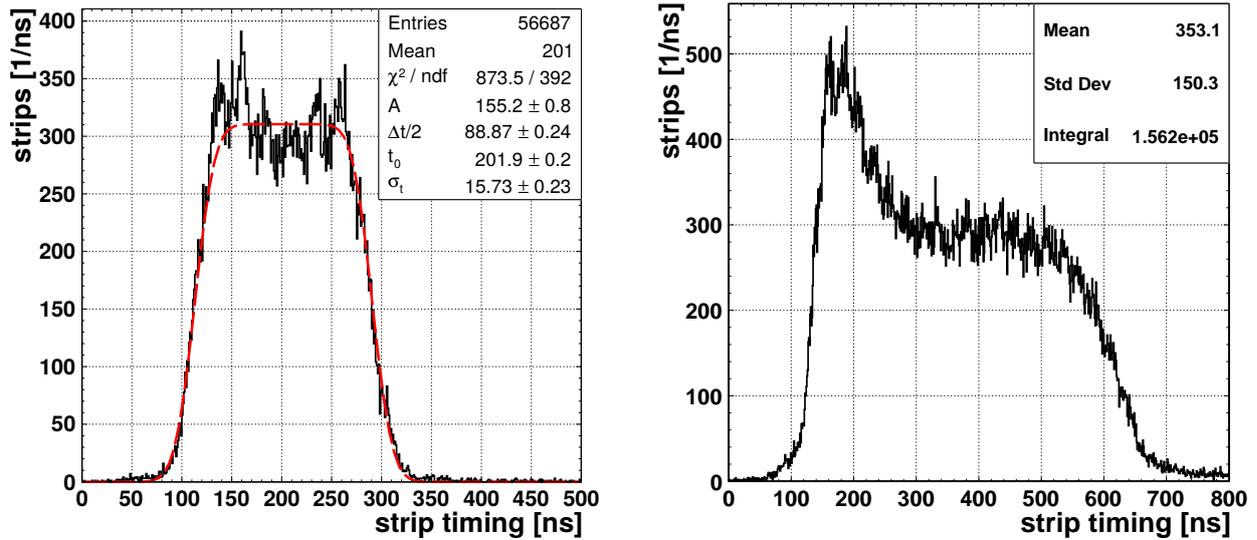
(a) Determination of t_{mid} from the distributions of all strip timings for an inclination angle of $20°$ and $E_{drift} =687.5\,\mathrm{V\,cm^{-1}}$.

(b) Distorted drift-time spectrum for low $E_{drift} = 187.5\,\mathrm{V\,cm^{-1}}$. Due to a slightly decreased electron transparency of the first GEM electrons produced closer to the GEM have a higher probability of being transmitted, leading to a pronounced peak in the spectrum at the fastest timings.

Figure 5.14

Here Δt is the mean time difference between the first and last electron reaching the read-out anode, which is equivalent with the thickness of the drift gap $\Delta z = v_D \cdot \Delta t$ and the parameter σ_t describes all effects, which limit the timing resolution. The drift-time spectrum in figure 5.14(a) actually is described quite well by this, which is here shown for an inclination angle of $20°$ and $E_{drift} =687.5\,\mathrm{V\,cm^{-1}}$. The absolute value of t_{mid} here additionally has to be corrected for the time jitter, which shifts the mean of the strip timing by half a time-bin, as described in section 2.8. By this method a value of $t_{mid} =(189.4 \pm 0.2)$ ns was determined here, which is in agreement with $t_{mid} =(175 \pm 18)$ ns determined by the method discussed before. The timing resolution by fitting to the drift-time spectrum however drastically declined for lower drift fields. This can be seen in figure 5.14(b) for an inclination of $20°$, but for $E_{drift} =187.5\,\mathrm{V\,cm^{-1}}$. The asymmetrical shape with early timings dominating is caused by the limited electron transparency of the drift gap. Electrons produced at the lower end of the drift region therefore have a higher probability of actually reaching the read-out, electrons produced at the upper have an increased risk of recombining, which can also be seen in section 5.5. This leads to a higher uncertainty in the determination of t_{mid} and therefore this method is not used in the following in order to allow direct comparison of results for different drift field configurations.

5.3.3   Spatial Resolution by the µTPC-method

Using again equation (2.33) the position information was obtained from the µTPC-fit, and an example for a resulting residual distribution is shown in figure 5.15 for $187.5\,\mathrm{V\,cm^{-1}}$ and an inclination of $36°$. A performance increase over the determination by the centroid position was achieved here with a resolution of $\sigma_{weighted} =(250 \pm 20)\,\mu m$. Over the full range of tested track inclinations the determination of the position by this method delivered a good spatial resolution below 300 µm, which is shown for $E_{drift} =187.5\,\mathrm{V\,cm^{-1}}$ in figure 5.16. The position information determined by the µTPC-method outperformed the pure centroid position determination for all examined angles, whereas the spatial resolution is best for angles between 20–$30°$. The distinct difference between the core resolution σ_{core} and the weighted resolution $\sigma_{weighted}$ implies that the contribution from the underlying broad distribution is rather large.
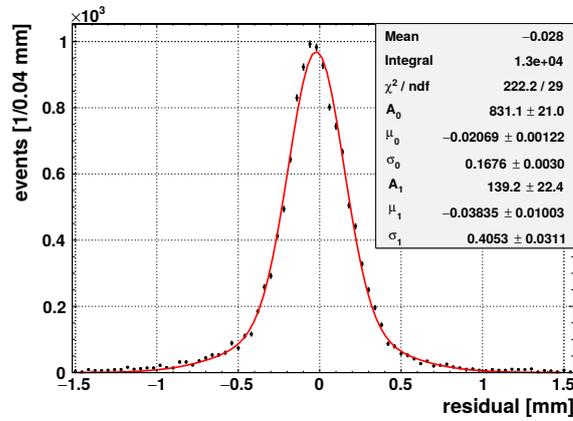
Figure 5.15: Residual determined by μTPC method for $E_{drift} = 187.5\,\mathrm{V\,cm^{-1}}$ and a detector tilt of $\theta = 36°$. The distribution has been fit with a double Gaussian function leading to a spatial resolution of $\sigma_{weighted} = (250 \pm 20)\,\mathrm{\mu m}$ ($\sigma_{core} = (170 \pm 20)\,\mathrm{\mu m}$).
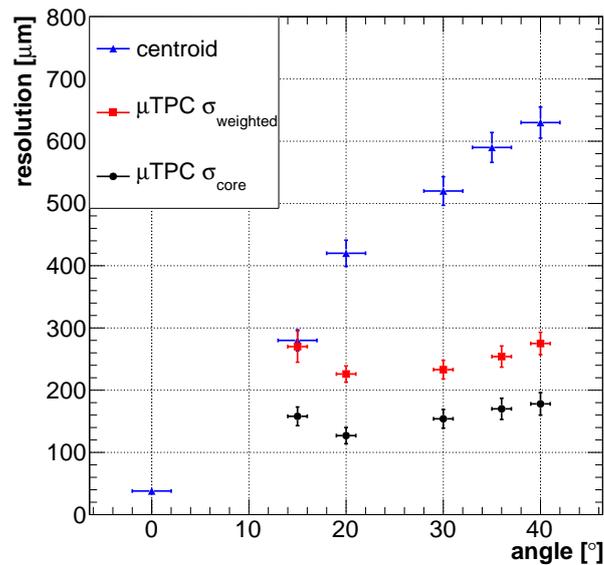
Figure 5.16: Resolution by centroid and μTPC-method plotted against the inclination angle for $E_{drift} = 187.5\,\mathrm{V\,cm^{-1}}$. For the μTPC-method weighted and core resolution are stated.
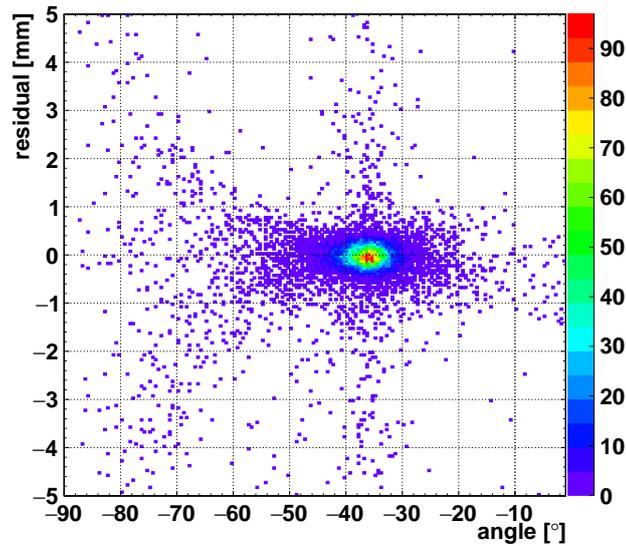
Figure 5.17: Dependence of the position determination on the reconstructed angle, shown for a nominal inclination of $36°$ and $E_{drift} = 187.5 \, \text{V cm}^{-1}$

In the example shown in figure 5.15 the Gaussian tails account for about $(29 \pm 2) \, \%$ of all events, whereas for reference at perpendicularly incident and reconstruction by the centroid in figure 5.4 the tails contributed only $(10.2 \pm 1.4) \, \%$ to the total number of events. This effect is promoted by possible failures in the reconstruction of the inclination angle, which can be seen at the same example data-point in figure 5.17, where the residual is plotted against the reconstructed angle. The fish-tail shaped structure for angles which are reconstructed too large causes this broad base in the residual distribution, but on the other hand the position reconstruction actually works still well even if the reconstructed angle is only correct up to $\sim \pm 15°$. Assuming an application where also a second coarse track inclination prediction would be in place, as it will be the case in the experiment described in chapter 6, which would allow to identify erroneously reconstructed angles and cut on them can lead to an improved weighted spatial resolution. In the example shown here a cut on the angle to be reconstructed within $\pm 15°$ of the nominal angle improves the spatial resolution to $\sigma_{weighted} = (220 \pm 20) \, \mu\text{m}$ compared to $(250 \pm 20) \, \mu\text{m}$ without the cut[20]. The decreased but still noticeable dependence of the spatial resolution on the inclination angle can be understood again by limitations in the timing resolution and absolute timing measurement. Assuming an error in the timing determination of Δt an error in the position measurement would be depending on the measured slope $m_{\mu TPC}$ in the following way:

$$\Delta x = \frac{\Delta t}{m_{\mu TPC}} = \Delta t v_D \tan \theta \tag{5.8}$$

By v_D this error is connected to E_{drift} and bearing in mind the absolute timing measurement fluctuation of width σ_t (see section 2.8) the actual spatial resolution $\sigma_{\mu TPC}$ should be even better:

$$\sigma_{\mu TPC} = \sqrt{\left(\sigma_{weighted}\right)^2 - \left(\sigma_t v_D \tan \theta\right)^2} \tag{5.9}$$

The influence of the read-out on the position determination will be discussed in more detail in the next section, but the direct implication on the position reconstruction can be seen in figure 5.18. Here the spatial resolution is shown for three different drift fields in the range between 187.5–$437.5 \, \text{V cm}^{-1}$, where the electron drift velocity scales nearly linearly with the electric field (see also figure 2.12(a)). For all fields the best resolution is achieved at an inclination angle of $20°$, with a within the errors identical mean resolution of $(240 \pm 40) \, \mu\text{m}$. This shows that, apart from

---

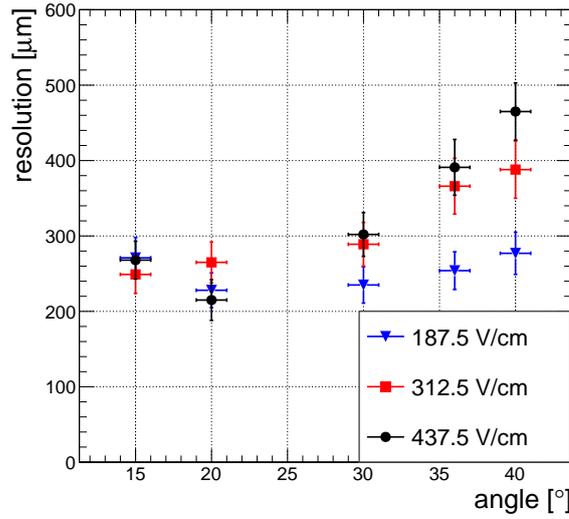[20]All other results in this chapter are shown without this cut

Figure 5.18: Fluctuation in the absolute timing leads to a dependence of the spatial resolution on the inclination angle and the applied E_{drift}. This leads to a better spatial resolution for lower v_D, here achieved by lowering E_{drift}.

the timing information, in fact very good spatial resolution with this technique can be achieved. However a drawback remains in the robustness of the μTPC fit, which leads to a separation in events where the fit works well with high spatial resolution and much lower spatial information if the fit fails.

5.4   Timing Correction of the Centroid Position

A more robust way of determining the position in the detector was found by further analysis of the position uncertainties of both methods shown so far. The poor resolution for inclined tracks for the centroid method can be understood as a mis-estimation of the position in Z-direction, perpendicular to the read-out plane. The centroid implicitly was assumed to lie on the same plane in Z at the center of the drift gap. This does not necessarily hold, because of charge clustering and in-homogeneous energy loss the centroid position of a track fluctuates in Z between the lower and upper edge of the drift gap. Using a similar method as in the chapters 3 and 4, this can be measured by comparing the centroid position with the geometric mean of the track with the skewness parameter ϵ defined in equation (4.1), which is a measure of the relative position of a centroid along the track and in this case therefore a measure of Z. The deviation from 0 of this parameter shows, whether the centroid position is higher or lower than the center of the drift gap. A value of 1 denotes that the centroid is at the upper edge of the drift gap and, respectively, a value of -1 for the lower edge. Plotting the residual of the centroid position versus the skewness, as it is done in figure 5.19(a), shows that there is a considerable fluctuation of the Z-position and the clear linear dependence of the residual position can be used to refine the centroid position in a very similar fashion as already shown in chapter 4. Alternatively, in a nearly equivalent approach, the homogeneous drift velocity in the drift gap is utilized. The position in Z-direction can also be determined by the charge weighted timing of the centroid position $t_{coc.}$:

$$t_{coc.} = \frac{\sum_{i=0}^{n} q_i \cdot t_i}{\sum_{i=0}^{n} q_i} \tag{5.10}$$

Where q_i and t_i are the charge and timing for all the strips in a cluster. A timing offset from the mean signal timing $\Delta t = t_{mid} - t_{coc.}$, translates in a shift of the centroid position in Z-direction and the corresponding shift in the read-out direction Δx can be described by:

$$\Delta x = \Delta t \cdot v_D \cdot \tan \theta_{proj.} \tag{5.11}$$

(a) Centroid residual plotted against the skewness of the cluster (defined by equation (4.1))

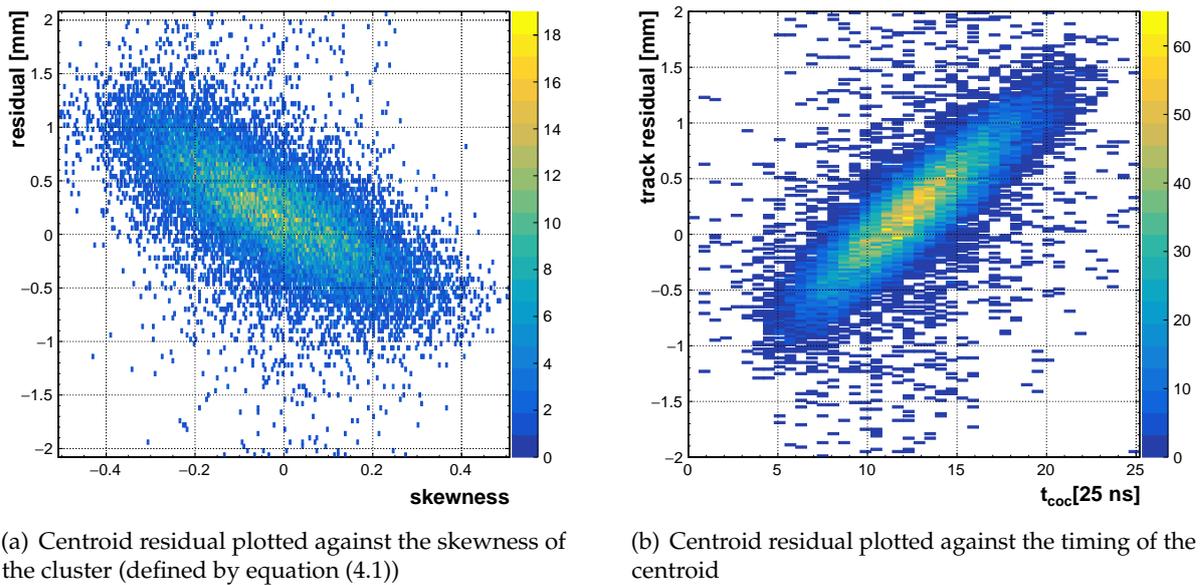(b) Centroid residual plotted against the timing of the centroid

Figure 5.19

Exemplarily the influence of the timing is shown in figure 5.19(b), where the residual determined by the centroid from the predicted position is plotted against $t_{coc.}$ for an inclination angle of 36° and E_{drift} =187.5 V cm^{-1}. The position-time distribution shown can be evaluated by a linear fit, where the slope should be purely defined by the track inclination and the electron drift velocity. This is in fact the case and was studied for various drift fields, which is shown in figure 5.20(a), where also fits of the form $s(\theta) = p_0 \tan \theta$ were applied. The fit parameter p_0 was found to be in good agreement with the expected drift velocity for every applied electric field, which is shown in figure 5.20(b), where the values of p_0 are plotted together with the simulated electron drift velocity from section 2.4.1.

Given a known track inclination[21] this allowed the correction of Δx of the centroid position described by equation (5.11), which led to a much sharpened spatial resolution for inclined tracks, as it is shown in figure 5.21 for E_{drift} =187.5 V cm^{-1} and an angle of 36° resulting in a $\sigma_{weighted}$ =(189 ± 6) µm. For this E_{drift} a spatial resolution improvement to below 200 µm was achieved over the full range of tested angles, as it is shown in figure 5.22. Notably the much steeper angular dependence in figure 5.22 was decreased down to (120 ± 20) µm for 15° and (180 ± 22) µm for 40°, compared to values between (280 ± 20) µm and (630 ± 30) µm for the uncorrected centroid method.

This correction obviously is depending on the intrinsic timing resolution of the detector, which in turns is depending on the actual amount of strips hit in an event. Additionally the usage of an absolute timing determined by the SRS read-out is prone to the 25 ns time jitter, which is depending on the drift velocity and track inclination and thus also influences the spatial resolution. This allowed, under the assumption of a Gaussian shaped total timing uncertainty σ_t, to calculate the limit of the spatial resolution σ_{x_0} by this method from the actual achieved resolution σ_x:

$$\sigma_x = \sqrt{\sigma_{x_0}^2 + (v_D \sigma_t \tan \theta)^2} \tag{5.12}$$

The total timing resolution can be described by two components: The intrinsic timing resolution of the detector and the timing resolution of the read-out, which will be described with a single parameter $\sigma_{t_{Det.}}$ and the shift in the absolute timing caused by the time jitter of the read-out

---

[21]In practice even a course prediction is sufficient, which can be achieved by using a second detector layer (compare section 6.6).
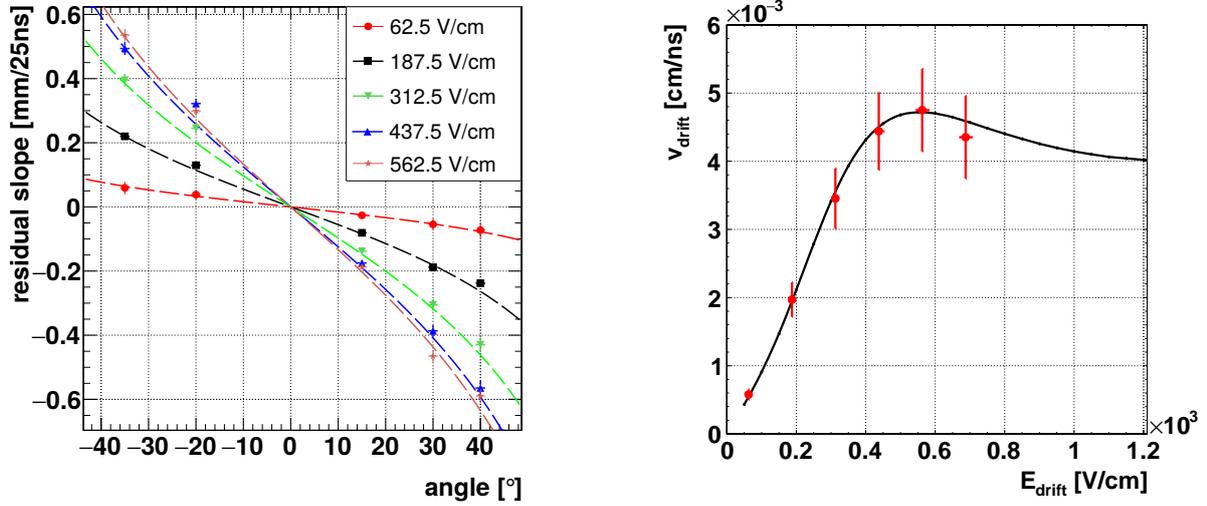
(a) Slope of timing dependence of the centroid position as in figure 5.19(b) plotted for different drift voltages and inclination angles and fit with function (5.11).

(b) Measured drift voltage determined from the fit of equation (5.11) to the data shown in figure 5.20(a) for different drift voltages compared with results from a MAGBOLTZ simulation.
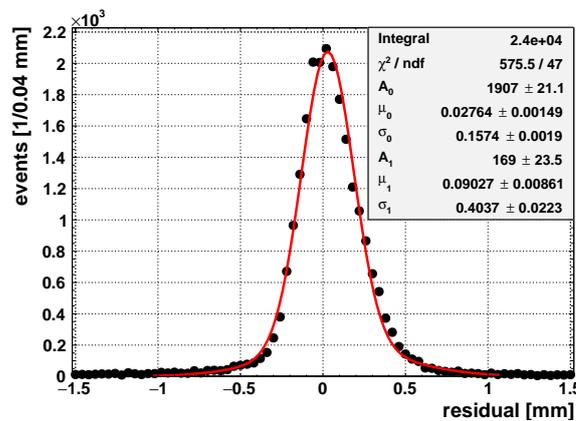
Figure 5.20

Figure 5.21: Residual distribution by correction of the centroid position by the centroid timing $t_{coc.}$ as described by equation (5.11). For a muon track inclination of $36°$ and $E_{drift} = 187.5\,\mathrm{V\,cm^{-1}}$ this results in a spatial resolution of $\sigma_{weighted} = (189 \pm 6)\,\mu m$.
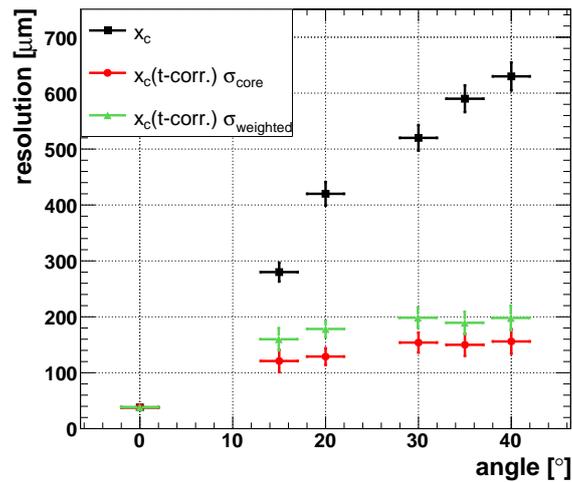
Figure 5.22: Time correction of the centroid position allows a spatial resolution below 200 μm up to an inclination angle of 40°, which is shown in direct comparison to the uncorrected centroid spatial resolution for $E_{drift} =187.5\,\mathrm{V\,cm^{-1}}$.

electronics:

$$\sigma_t = \sqrt{\sigma_{t_{Det.}}^2 + \sigma_{jitter}^2} \tag{5.13}$$

This separation is motivated as the time jitter of the read-out system actually can be measured and corrected, but the other two components cannot be disentangled. This actually describes the timing measurement dependence quite well, as can be seen in figure 5.23(a). Here the achieved resolution for different E_{drift} is plotted against the respective drift velocity for a track inclination of 40°, which is compatible with a fit of function (5.12). This allowed to determine the combined timing resolution at this angle to be $\sigma_t =(8.7 \pm 0.5)\,\mathrm{ns}$ and a minimal spatial resolution of $\sigma_{x_0} =(103 \pm 11)\,\mathrm{\mu m}$, which is a strong indicator that the decline in spatial resolution with increased v_{drift} is mainly caused by the time jitter of the read-out electronics. Considering the RMS of the time jitter of $25\,\mathrm{ns}/\sqrt{12} \simeq 7.22\,\mathrm{ns}$ and deconvoluting this distribution from the combined timing resolution left an intrinsic timing resolution of the detector of $\sigma_{t_{Det.}} =(4.8 \pm 0.7)\,\mathrm{ns}$ at this angle. Repeating the same procedure for all studied angles, revealed as expected a decline of the timing resolution with steeper inclination angles, which is shown in figure 5.23(b). Proceeding from a fixed time resolution $\sigma_{t_{strip}}$ for a single strip the timing resolution for a track should enhance with the number of strips in a cluster by $1/\sqrt{n}$. The number of strips on the other hand increases with the inclination angle by $\tan\theta$, but has a minimal size of $n_0 \simeq 3$ strips[22]. The combined detector and read-out timing resolution could be parametrized by:

$$\sigma_{t_{Det.}} = \left(\frac{\sigma_{t_{strip}}}{\sqrt{n - n_0}}\right) \tag{5.14}$$

Application of a fit with a combination of equations (5.14) and (5.13) with a fixed minimal cluster size $n_0 = 3$ to the σ_t distribution in figure 5.23(b) indicated a timing resolution per strip of $(19 \pm 3)\,\mathrm{ns}$ and on the other hand delivered a measurement of $\sigma_{jitter} =(7.1 \pm 0.9)\,\mathrm{ns}$, which is in good agreement with the expected value of $7.22\,\mathrm{ns}$.

Altogether this showed that the main contribution of the residual for inclined tracks can be attributed to the effect of the time jitter. Subtracting this effect, by equation (5.12) with $\sigma_t = \sigma_{t_{Det}}$ as determined before, the combined method shows excellent spatial resolution over all track angles, which is shown on figure 5.24, which has to be understood as the limit of this method for this detector and read-out given a possibility to measure and correct for the time jitter. A possible solution and its application for this will be described in chapter 6. This shows that with the correct

[22]Depending on the drift field and therefore the lateral diffusion (compare figure 3.20(b) with a mean value of 1.15 mm or 2.85 strips)
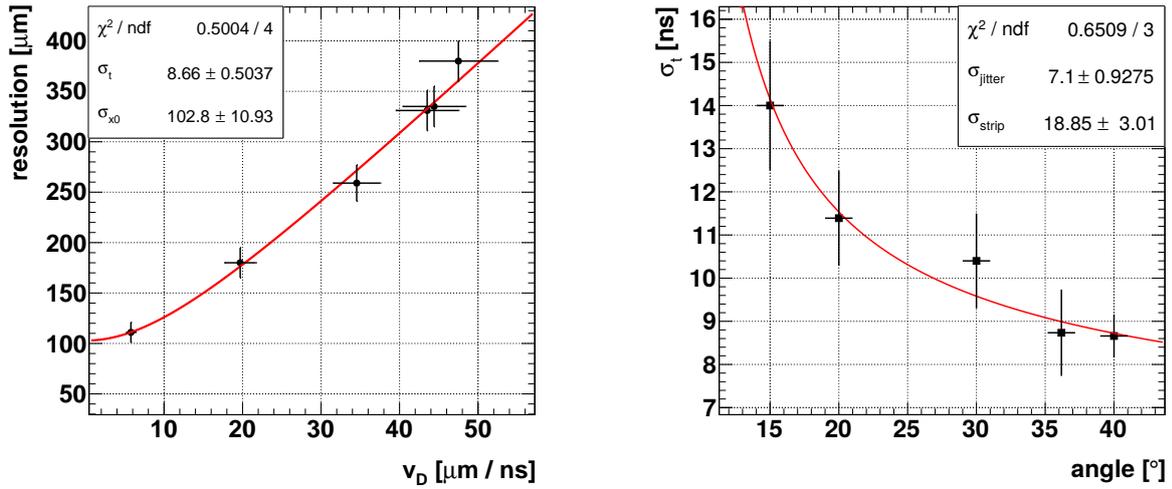
(a) Resolution determined by the combined method plotted for different drift velocities at 40° wit a fit according to equation (5.12)

(b) Timing resolution determined by the spatial resolution for different inclination angles for all drift fields plotted against the inclination angle and fit with equation (5.13)

Figure 5.23

choice of E_{drift} this method allows a spatial resolution below $\sigma_{weighted} = 140\,\mu\text{m}$ over the full tested range of track inclinations. Also the performance for an even lower $E_{drift} = 62.5\,\text{V}\,\text{cm}^{-1}$ is shown, which would even allow a spatial resolution below $100\,\mu\text{m}$ for all angles because of the even lower v_D. Unfortunately this low drift fields have a strong influence on the electron transparency from the drift gap through the GEMs and therefore the detection and reconstruction efficiency is seriously decreased in this case, which will be discussed in the following section. Both described methods, the μTPC-method and the timing-correction to the centroid, suffer from the same shortcoming of the read-out electronics and the residuals determined by both methods are strongly correlated, which is shown in figure 5.25 for an inclination angle of 36° and $E_{drift} = 187.5\,\text{V}\,\text{cm}^{-1}$. Further combination of both methods is therefore not possible to achieve even higher spatial resolutions for inclined tracks, as systematic effects are dominating.
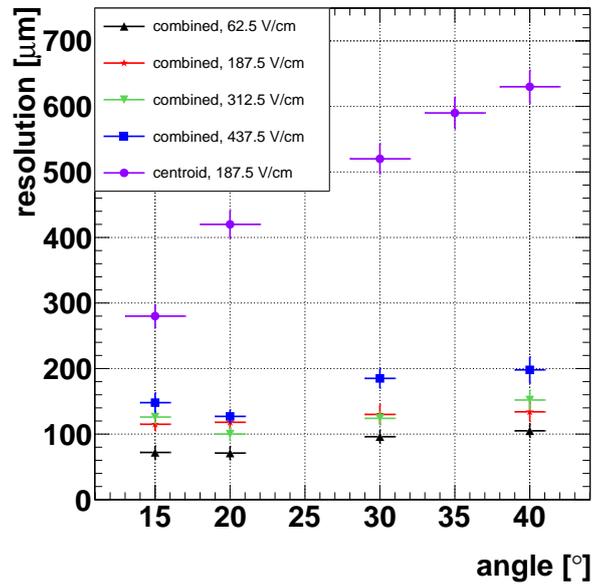
Figure 5.24: Achievable detector resolution $\sigma_{weighted}$ after deconvolution of the contribution from the time jitter inflicted by the SRS read-out system.
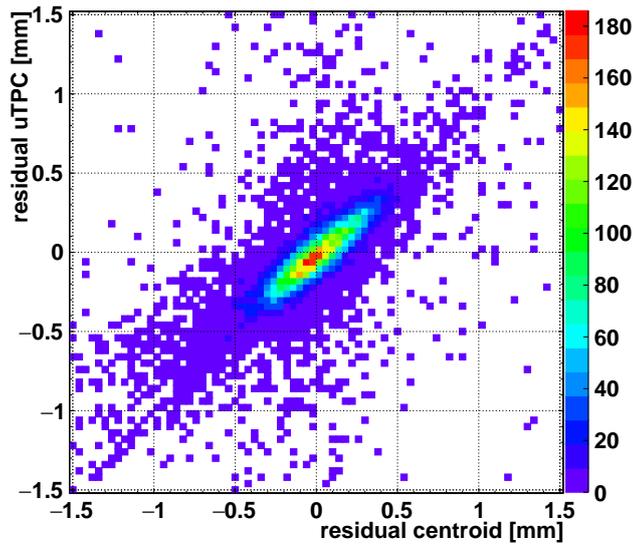

Figure 5.25: µTPC residual plotted against the timing corrected centroid residual for an inclination angle of $36°$ and $E_{drift} = 187.5\,\mathrm{V\,cm^{-1}}$. The residual distributions are strongly correlated.

5.5   Influence of E_{drift} on the Detection and Reconstruction Efficiency

One major advantage of the position determination by a timing-corrected centroid measurement over the μTPC-method is the much higher reconstruction efficiency. A failed μTPC-fit for example does not even ensure to reconstruct a position inside of the detector. This could be minimized by the previously mentioned χ^2/NDF cut on the result of this fit, but at the cost of reduced reconstruction efficiency. In order to determine the reconstruction efficiency, the fraction of events was determined, where a particle was found in the detector with a distance from the track prediction of less than $3 \cdot \sigma_{weighted}$, compared to all events, where a track was found by the tracking system.

$$\epsilon = \frac{N_{r < 3\sigma_{weighted}}}{N_{total}} \tag{5.15}$$

In figure 5.26 an efficiency map of the whole area which was covered by the trigger scintillators as well as the hodoscope is shown for the tested GEM detector as well as for one of the micromegas detectors from the tracking system for comparison. This is shown exemplarily for perpendicularly incident muons and E_{drift} =437.5 V cm^{-1} for the GEM detector and E_{drift} =600 V cm^{-1} for the micromegas. Both detectors show overall a quite homogeneous and high efficiency of more than 94 %.
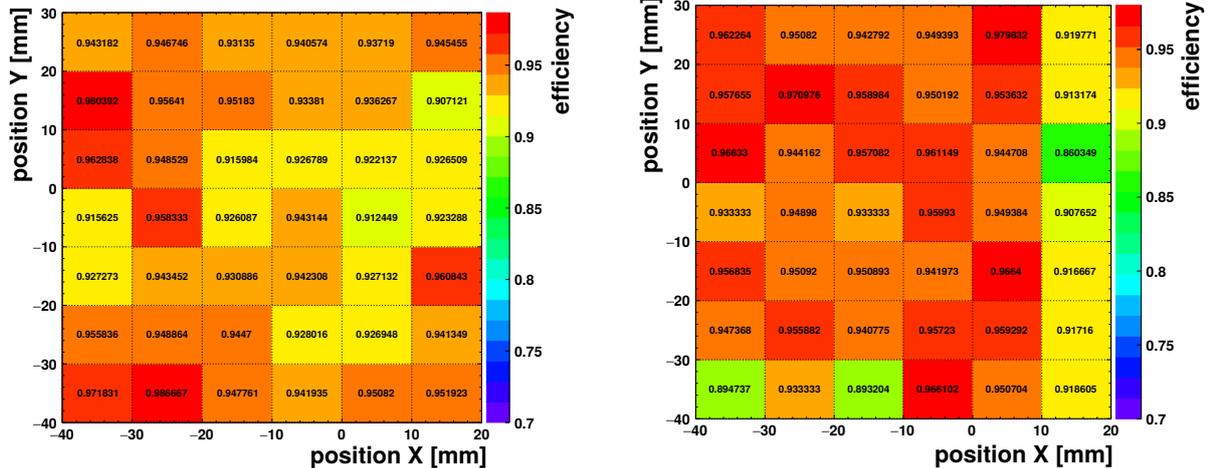
(a) Map of the detection efficiency for the GEM detector limited to the area of the detector, where tracks could be reconstructed due to the size of the hodoscope and the trigger scintillators. The overall efficiency was 94.1 %, which was determined for the X-layer of the detector.

(b) Detection Efficiency for the first micromegas of the hodoscope for comparison. An overall efficiency of 94.3 % was achieved, which was also determined for the X-layer.

Figure 5.26

The reconstruction efficiency of course is depending on the amount of charge, which reaches the anode, which in turn is depending on the amount of charge, which is transmitted by the uppermost GEM. This electron transparency of the first GEM-foil is depending on the ratio of E_{drift} to the electric field in the GEM, which can be seen in figure 5.27(a) by the mean charge collected at the anode in dependence to E_{drift}, which is shown for perpendicularly incident muons. Over a large range the pulse-height stays constant down to about 300 V cm^{-1}, but drops steeply for lower E_{drift}. This behavior also influences the reconstruction efficiency, which is shown in figure 5.27(b) for the centroid method. Albeit the plateau of (94 ± 2) % reconstruction efficiency extends at least down to $E_{drift} \geq 187.5$ V cm^{-1}, still a steep decrease down to 70 % efficiency was observed. The much steeper turn-on curve compared to the pulse-height can be explained by the cut on the minimum cluster size applied here (see section 2.7.2).

Taking into account also inclined tracks the real advantage of the timing-corrected centroid reconstruction over the position determination by the μTPC-method can be seen in figure 5.27(c).
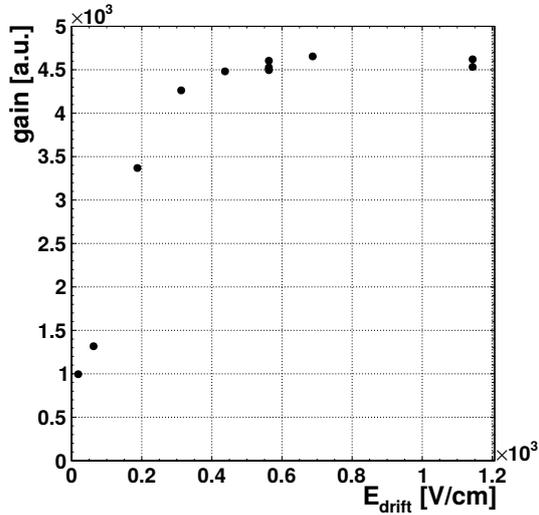
(a) Gain determined from the measured mean signal pulse height for perpendicularly incident muons as a function of E_{drift}.
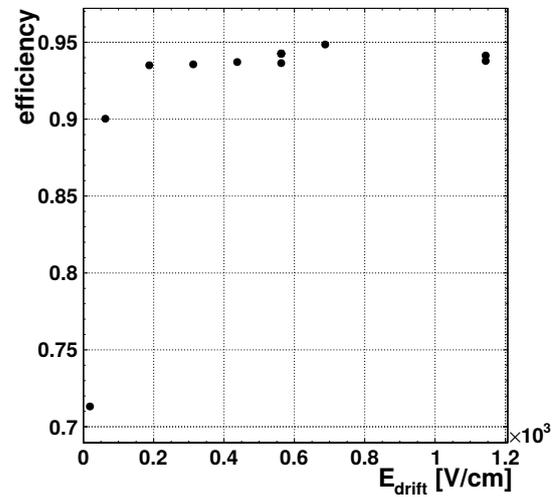
(b) Over a large range of E_{drift} the efficiency maintains at a high plateau around (94 ± 2) %.
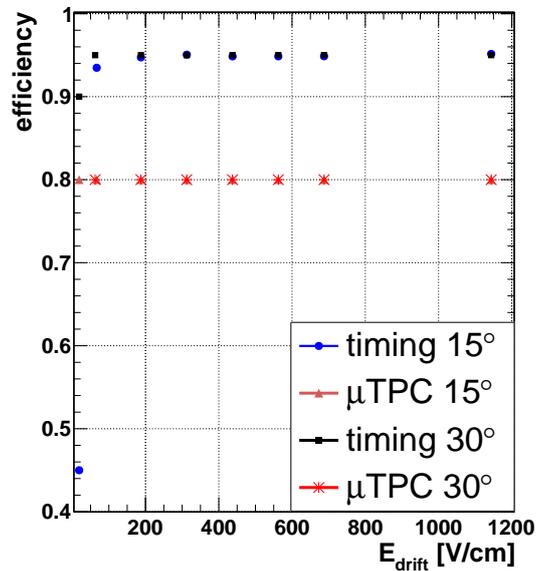
(c) The reconstruction efficiency for angles of 15° and 30° for the timing corrected centroid method stays over a wide range of E_{drift} at a plateau around 95 %. For both angles shown, it is significantly higher than the reconstruction efficiency determined by the µTPC method, which reaches a plateau of only 80 % .

Figure 5.27

The reconstruction efficiency is plotted for 15° and 30° for both methods. Compared to the case of non-inclined tracks no change in the reconstruction efficiency in the plateau region above the data point at $E_{drift} = 187.5 \, \text{V} \, \text{cm}^{-1}$ is observed for the corrected centroid method. A considerable drop of the efficiency plateau down to 80 % can be seen for both angles when using the μTPC-method. In both cases the rapid decrease of the reconstruction efficiency for $E_{drift} < 187.5 \, \text{V} \, \text{cm}^{-1}$ is the limiting factor for any further increase in spatial resolution by reduction of E_{drift}.

Chapter 6

Construction and Performance of Large Scale Micromegas Detectors

The ATLAS[23] detector is one of the four main experiments at the Large Hadron Collider (LHC), the currently largest and most powerful particle accelerator. The LHC is built as a storage ring collider with a circumference of 26.7 km and allows to accelerate and collide protons up to an energy of 6.5 TeV with a center of mass energy of 13 TeV in two counter-rotating beams and has reached recently a peak luminosity of more than 2×10^{34} cm^{-2} s^{-1} ([Atlas Collaboration, 2018]).
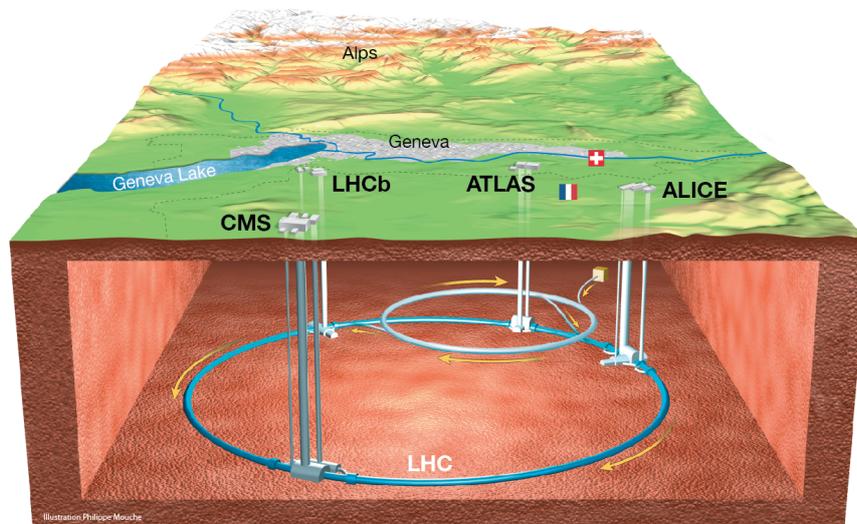
Figure 6.1: Position of the four main experiments in the Large Hadron Collider [Mouche, 2014]

The unprecedented high collision energy allowed so far the discovery of the long predicted Higgs-Boson in 2012 [ATLAS Collaboration, 2012] and is currently used to probe the standard model of particle physics with higher precision, but also to examine possible physics, which is not covered by this theory by reproducing an environment shortly after the big bang. Further investigation for example by the search for supersymmetry or dark matter aim for extensions of this model, which are mainly investigated by the two largest detectors: The Compact Muon Solenoid (CMS) and the previously mentioned ATLAS detector. So far no new particle was found, which could not be explained by the standard model, but many theories predict, that at least the lightest supersymmetric particles should be in the mass range of few TeV [Martin, 1998], which is only just available at the LHC, but will be better accessible with future upgrades as well in collision energy and luminosity (see for example [Rossi, 2011]). In this chapter a necessary upgrade of the ATLAS

---

[23]Short for: **A T**oroidal **L**HC **A**paratu**S**

detector, which will incorporate for the very first time $\mathcal{O}(\mathrm{m}^2)$ sized micromegas detectors for muon tracking, will be discussed and the production and performance of a first working prototype detector is shown.

6.1   The ATLAS Detector and the New Small Wheel Project

The ATLAS detector is the largest of all experiments at LHC with a length of 44 m and a diameter of 25 m. As most large multi purpose particle detectors it has a cylindrical shape. The detector is built symmetrically around the interaction point (IP), where the two particle beams collide. In order to fully reconstruct the collision processes multiple different detector layers enclose the IP. The first layers together form the so called inner detector, which consists of three different tracker systems and allows to reconstruct the path of charged particles with extreme high precision as well as to some extent to identify particles. The next logical unit is the electromagnetic calorimeter, which allows to measure the energy of electron, positrons and photons by totally absorbing them. Similarly the energy of hadronic jets is measured in the following layer, the hadronic calorimeter. The whole detector is surrounded by the muon spectrometer system, which measures the momentum of muons, which cannot be stopped in the whole detector, by the curvature of their trajectories due to a high magnetic field B of around 0.5 T in the name giving toroid magnets:

$$p = qBR \tag{6.1}$$

A sectional drawing of the whole ATLAS detector is shown in figure 6.2, which displays the most important systems of the whole detector. For a complete description of the detector the reader is referred e.g. to [Airapetian et al., 1999].

The muon system consists of three layers, which are located in each of the so called barrel and end cap regions. The part of the muon system closest to the interaction point in the direction of the beams are the two so called Small-Wheels, which have a distance to the interaction point of 7 m. The detectors located there face the highest particle flux of the whole muon system and the planned further increase in energy and luminosity will have negative influence on the operation of the currently used detector technologies. As part of a general upgrade and revision of the ATLAS detector in 2019 parts of the muon spectrometer will be exchanged and upgraded with detectors, which can withstand much higher particle rates. The Small-Wheel at the moment is composed of Resistive Plate Chambers (RPC) and Monitored Drift Tubes (MDT) and Cathode Strip Chambers (CSC) and the current maximal particle flux in the Small-Wheel is in the order of 1 kHz cm^{-2}, which is partly composed of muons but also has a significant contribution from photon and neutron background. A constant background at this level already leads for example at the MDTs to a significant efficiency loss of single drift tubes, as it can be seen in figure 6.3. This is partly compensated, because the MDTs consist of multiple layers of drift tubes, which are combined to chambers consisting of two times three or four layers of tubes, which together ensure a slower degradation in the reconstruction efficiency. Considering an expected hit rate of 15 kHz cm^{-2} closest to the interaction point, which for the case shown here would translate roughly to a rate of 750 kHz/Tube, it is obvious that the current technology will not be capable of providing sufficiently efficient track information.

An additional problem when dealing with increased hit rates is the limited bandwidth of the data-acquisition system. In 2015 the average proton collision rate was around 40 MHz, whereas by a hardware-based fast trigger a pre-selection of interesting events down to 100 kHz was applied which is the rate the following software-based high-level trigger (HLT) can cope with. It reduces the rate of actual recorded events down to 1 kHz [Martínez et al., 2016]. The current fast hardware trigger, the so called Level-1 (L1) trigger, in the forward region of the muon spectrometer relies on track information from the next end-cap system, the Big-Wheels. L1 triggers from the end-cap muon system unfortunately are also due to high background dominated by fake hits, which are caused by low energy particles which hit the muon system under angles which are similar to the ones expected of muons with high momentum coming from the IP. For a common trigger setting
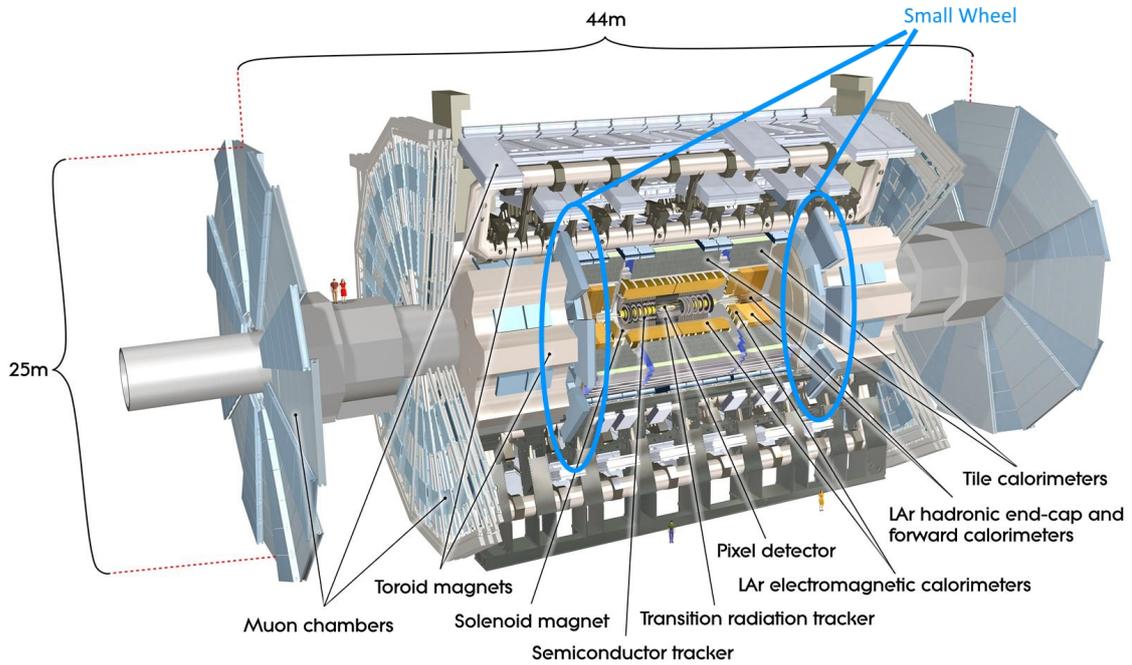
Figure 6.2: Sectional drawing of the ATLAS detector (modified and taken from [Pequenao, 2008])
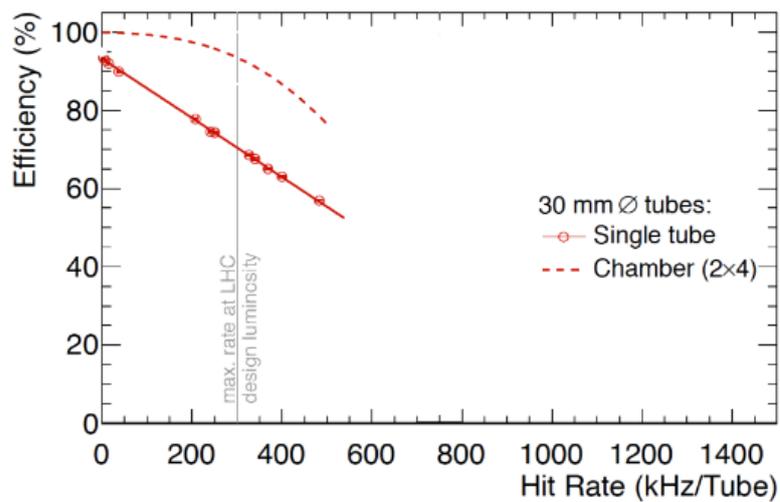

Figure 6.3: Measured efficiency loss of single drift tubes and whole MDT chambers in the Small-Wheel under high rates (taken from [ATLAS Collaboration, 2013]). The Design Luminosity here corresponds to $10^{34}\,\mathrm{cm^{-2}\,s^{-1}}$.
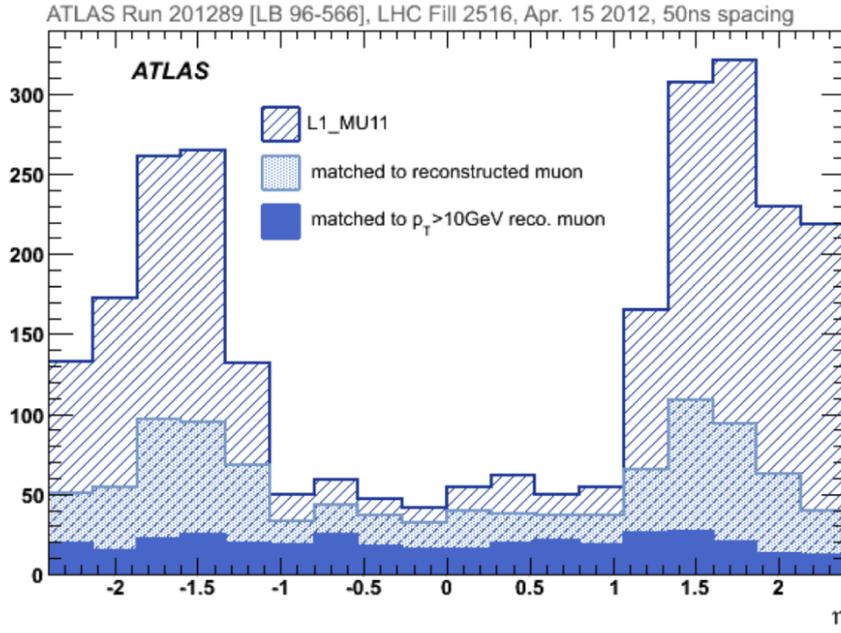
Figure 6.4: About 90 % of the total amount of muon triggers with an on-line reconstructed momentum p_T >10 GeV are reconstructed in the end-cap regions $|\eta| > 1$, shown by the distribution filled with solid lines (L1_MU11). Due to the high amount of fake-triggers, caused by background, most of these L1 triggers cannot be matched to muon tracks. In less than 10 % of the triggered events a muon exceeding the trigger threshold of 10 GeV can be reconstructed off-line (taken from [ATLAS Collaboration, 2013]).

(L1_MU11), which is equivalent to muons with a transverse momentum of p_T >10 GeV this can be seen in figure 6.4. This trigger in the forward region is already very inefficient, here the total amount of L1 triggered events with this setting is shown together with the number of events, where an off-line reconstruction actually confirmed the presence of a muon coming from the interaction point. Additionally the amount of events is shown, where this muon actually exceeded a momentum of 10 GeV. On the X-axis the angular distance of the detector from the beam axis is shown in units of pseudo-rapidity, which is defined as:

$$\eta = -\ln \tan \frac{\Theta}{2} \qquad (6.2)$$

The region covered by the end-caps is $|\eta| \geq 1$. From this distribution it is quite obvious that the largest amount of triggers produced in this region is not caused by events originating in the IP and even worse, about 90 % of all muon triggers are created by the very inefficient end-cap region. A solution for this fake-trigger rate will be the additional exploitation of muon track information from the Small-Wheel for the L1-trigger, which covers the area between 1.3< $|\eta|$ <2.7. The concept of this is depicted in figure 6.5, where different tracks are shown, which in the present triggering scheme would be identified by the Big-Wheel as valid track coming from the IP. The tracks A, B and C all point towards the IP if only the segments in the Big-Wheel are considered, but tracks B and C really are produced elsewhere and are only deflected by either straggling in the toroid (C) or bending of low momentum particles in the magnetic field (B). Considering now also additional track information from the Small-Wheel these cases could be sorted out, if only tracks are triggered, which in both Wheels point towards the IP. To achieve this a combination of detectors, which allow fast triggering and an on-line angle resolution of better than 1 mrad and an off-line spatial resolution of 100 µm will be needed. A combination of micromegas detectors, primarily for high off-line position resolution but also in principle usable for fast triggering, and small-strip Thin Gap Chambers (sTGC), which provide fast trigger information, but also good spatial resolution, will be used for this. Both detector systems can also cope with the much increased background and hit
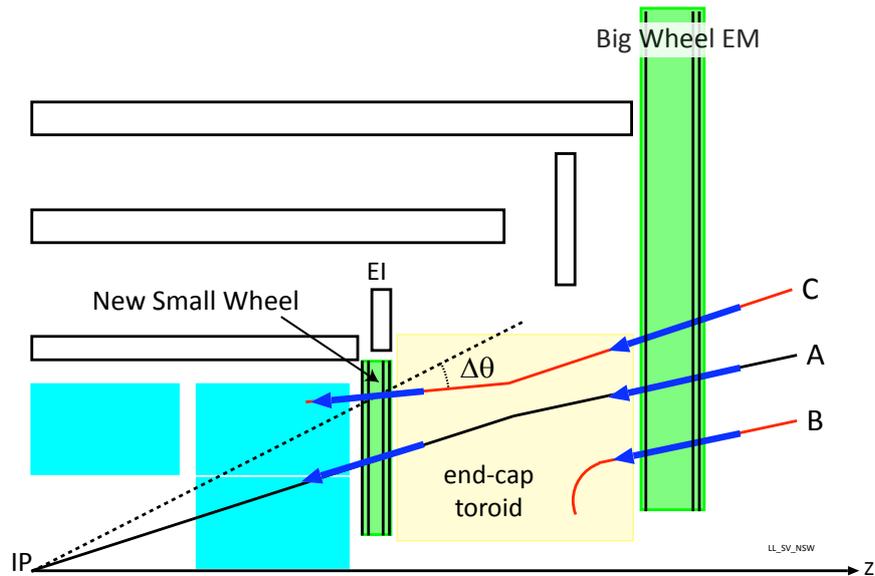
Figure 6.5: In the current triggering scheme only the Big Wheels are used for trigger information, which can lead to fake triggers, if a particle track is reconstructed there, which points towards the interaction point, but in reality is created elsewhere. This can be e.g. a particle coming from the beam-pipe (case B) or a particle, which is produced elsewhere in the detector and straggled in the massive end-cap toroid in a way where it mimics a particle coming from the IP (case C). Triggering additionally on the Small Wheel would discard these cases and allow much more efficient triggering on particles emerging from an actual collision (case A) (taken from [ATLAS Collaboration, 2013]).

rates.

The design of this so called New Small Wheel features two wheels with a total of sixteen detector layers each. Every wheel will consist of eight layers of micromegas and sTGC detectors each, which are subdivided in modules, four for the micromegas and six for the sTGCs. Each module consists of four detector layers and the modules will be assembled in wedges to a fan-like structure to cover the full wheel, as it is schematically shown in figure 6.6. In the wedges two multilayers of sTGCs will sandwich two multilayers of micromegas and a sector is built from two wedges mounted on a spacer-frame.

This chapter focuses on the construction and mainly the performance of a first full-size micromegas quadruplet prototype.
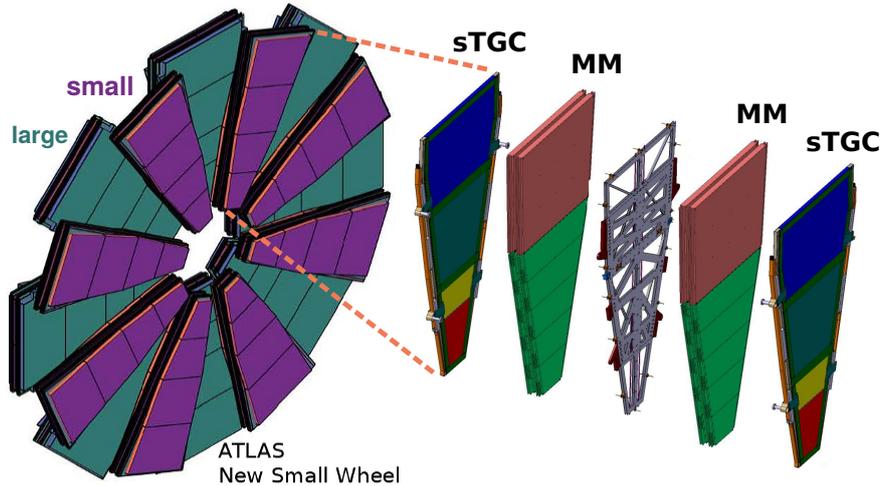
Figure 6.6: The New Small Wheels will consist of 16 detector layers made from two different detector technologies. Four different modules of micromegas detectors and six different small strip Thin-Gap-Chambers will be mounted together on a fan-like structure in order to cover the full area. For alignment purposes small and large sectors have small overlap regions (taken from [Schune, 2015]).

6.2   Design and Construction of the NSW-Micromegas

The wedges in the NSW will incorporate two different sizes of detectors, with smaller micromegas modules of (2m^2) SM1 and SM2 closer to the IP and larger modules LM1 and LM2 (3m^2) slightly overlapping behind as it is shown in figure 6.6. Although the shape and dimensions of the different detector modules varies somewhat, as it can be seen in figure 6.7, the overall construction is virtually identical for all four module types, therefore the construction will be explained at the example of the SM2-modules, which are built by a cooperation from the Johannes Gutenberg-Universität (Mainz), Julius-Maximilians-Universität (Würzburg) and the Ludwig-Maximilians-Universität (München).

The four micromegas layers are built from a total of five different panels, which consist out of a sandwich structure made from printed circuit boards, lightweight aluminum honeycomb and aluminum bars. Each module consists of two read-out panels with copper strips for one dimensional spatial information and a resistive discharge protection on both sides[24]. The drift regions are formed by three drift panels, one of them double sided, with a copper cathode and a steel micromesh 5 mm apart from the cathode. The distance between the mesh and the read-out structure of 128 μm when finally assembled is ensured by 128 μm high 1.2 mm × 0.2 mm insulating pillars, which are laminated on the read-out structures in a triangular shape with an equilateral distance of 7 mm. The sectional drawing of the whole stack of layers is shown in figure 6.8.

The production of printed-circuit boards in industry is limited to a width of at maximum 50 cm. Thus every side of each panel is made from three (SM2, LM2) or five (SM1, LM1) separate boards, which have to be carefully aligned relative to each other by better than 30 μm in order to meet the high requirements for the spatial resolution. For the same reason all panels have to be extremely planar with an allowed overall deviation from a plane of ±110 μm and a root mean square of the planarity of below 37 μm (see [ATLAS Collaboration, 2013]).

Two different schemes for the read-out layers have been chosen, which ensure high spatial resolution in pseudo rapidity direction and a coarser resolution in the azimuthal direction, which is

---

[24]Discharges in micromegas can occur between the micromesh and the read-out structure and effectively short both electrodes. Although this usually is non-destructive this introduces a dead-time as the amplification field breaks down and has to be recharged. A possible way to limit the effect of these discharges is an additional layer of resistive material above the grounded read-out strips, which quenches discharges and drastically reduces the following dead-time [Alexopoulos et al., 2011]
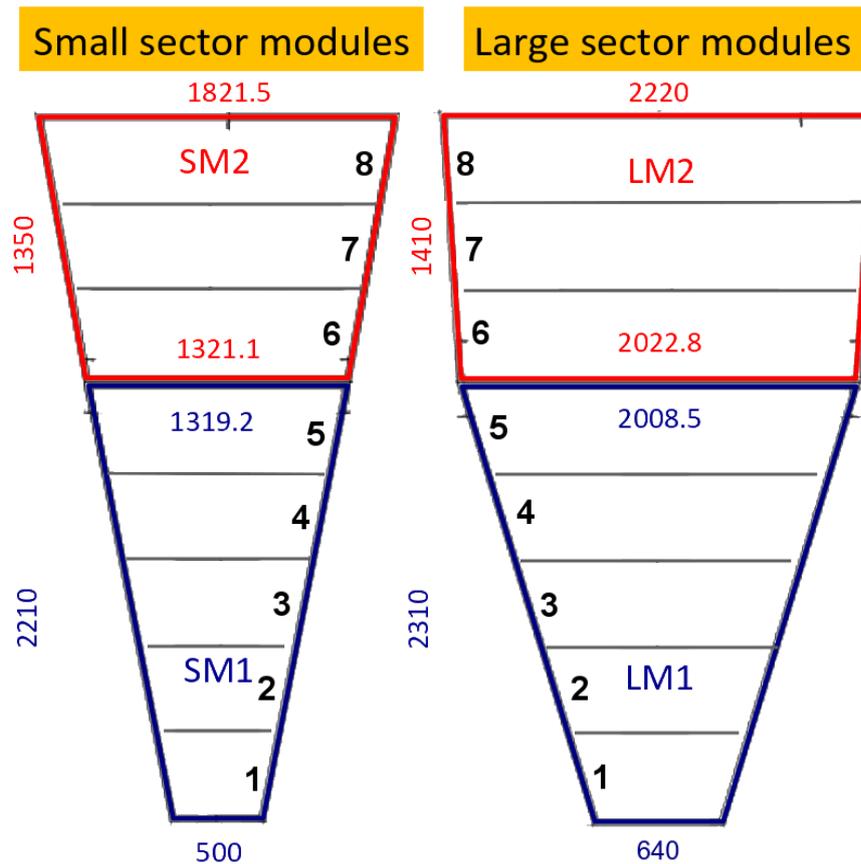
Figure 6.7: Envelope and dimensions of the four different micromegas modules (Taken from [Lösel and Müller, 2015])
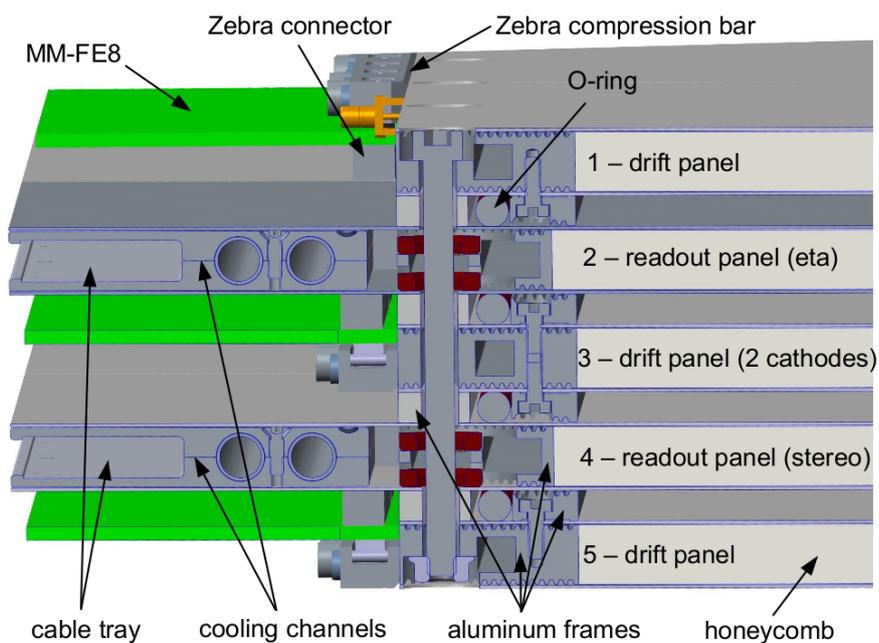

Figure 6.8: Sectional view of a micromegas quadruplet with the five different panels, which enclose four detector-layers. The eta- and stereo-layers pairwise share the same read-out panel and are separated and enclosed by drift panels, which carry the micromeshes and ensure a homogeneous drift gap (taken from [Iodice, 2015]).

driven by the configuration of the magnetic fields, which bend the muons in the plane of the beam axis. The accuracy in spatial information for both directions is achieved by using different types of double layers with strip read-out: The so called eta-layers are built mirror-symmetric on both sides, which means the strips are parallel to their counterpart at the other side of the board. These boards independently of each other deliver high spatial resolution in the direction perpendicular to the strips and no spatial resolution in the direction along the strips. On the so called stereo-panels the strips are tilted from the direction of the strips of the eta-layers by $\varphi = \pm 1.5°$. This rotation slightly reduces the spatial resolution in the η direction, but by combining the position in both stereo-layers also sufficient spatial information in the direction parallel to the eta-strips can be achieved, which is outlined in the scheme in figure 6.9. Assuming a Cartesian coordinate system with X being the direction perpendicular to eta-strips and Y along them, then the position in this system can be obtained by the stereo layers from the positions perpendicular to their respective read-out direction described by the coordinates u and v in the following way:

$$x = \frac{u + v}{2\cos\varphi} \tag{6.3}$$

$$y = \frac{u - v}{2\sin\varphi} \tag{6.4}$$

And in the same way, this allows to determine the spatial resolution in both directions by:

$$\sigma_x = \frac{\sigma_{u_{1/2}}}{\sqrt{2}\cos\varphi} \tag{6.5}$$

$$\sigma_y = \frac{\sigma_x}{\tan\varphi} = \frac{\sigma_{u1/2}}{\sqrt{2}\sin\varphi} \tag{6.6}$$

Here the simplifying approximation of a vanishing distance between the u- and v-layer has been used. The read-out planes in the NSW-quadruplets will be $\Delta Z = 16.8$ mm apart from each other, which implies that the position determination from the two stereo-layers will be depending on the track inclination in the following way:

$$x = \frac{u_1 + v_2}{2\cos\varphi} - \frac{\tan\theta\Delta Z\cos\Phi\tan\varphi}{2} \tag{6.7}$$

$$y = \frac{u_1 - v_2}{2\sin\varphi} - \frac{\tan\theta\Delta Z\sin\Phi}{2\tan\varphi} \tag{6.8}$$

Where θ and Φ are the polar and azimuthal angle with $\Phi = 0$ being the direction parallel to the Y-axis of this coordinate system. The spatial resolution in this case is modified in a similar fashion and depending on the variations in ΔZ ($\sigma_{\Delta Z}$) and the knowledge of θ and Φ[25]:

$$\sigma_x = \frac{\sigma_{u_{1/2}}}{\sqrt{2}\cos\varphi} \oplus \sigma_{\Delta Z}\frac{\tan\theta\cos\Phi\tan\varphi}{2} \oplus \sigma\left(\tan\theta\cos\Phi\tan\varphi\right)\frac{\Delta Z}{2} \tag{6.9}$$

$$\sigma_y = \frac{\sigma_x}{\tan\varphi} \oplus \sigma_{\Delta Z}\frac{\tan\theta\sin\Phi}{2\tan\varphi} \oplus \sigma\left(\frac{\tan\theta\sin\Phi}{\tan\varphi}\right)\frac{\Delta Z}{2} \tag{6.10}$$

A more complete description of the construction and building of these detectors for the general design of the NSW micromegas detectors can be found in [Iodice, 2015] and for the SM2 modules in particular in [Lösel, 2017] and [Müller, 2017].

The specifications defined in [ATLAS Collaboration, 2013] foresee a couple of key parameters, which in order to suffice the expectations on the New Small Wheel, have to be fulfilled by every micromegas module. In this chapter some of the main aspects will be examined at a first prototype of a SM2 module. The primary purpose of the micromegas detectors will be high precision muon tracking hence one of the core specifications is a single layer position resolution of below 100 μm

---

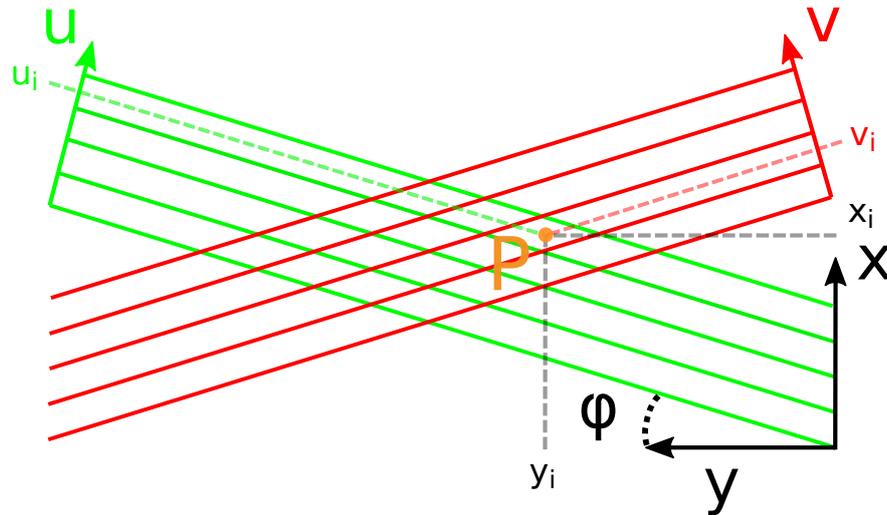[25]A complete treatment of the calculation can be found in [Alexopoulos et al., 2015] and in appendix D

Figure 6.9: Schematic drawing of the stereo-strip layout, the position of the Point P in the Cartesian coordinate system X-Y can also be described by the two coordinates (u_i,v_i) in the non-perpendicular coordinate system U-V.

independent of the track inclination in the eta direction. This spatial resolution requirement, which is equivalent to an accuracy of the track element in every module of 50 µm, will be necessary in order preserve the spatial momentum resolution of $\Delta p_T / p_T =$15 % at 1 TeV of the old Small Wheel [Amelung et al., 2015]. A second main aspect of the quality of the detectors is defined by the reconstruction efficiency, where several criteria have to be met: The overall efficiency should be higher than 98 %. The efficiency here is defined as the number of reconstructed tracks within 5 mm to the track position divided by the number of particles traversing the detector. Related to this, no more than 5 % of the events may have localized peaks in the hit distribution for homogeneous irradiation, which is a measure for noisy strips. Localized peaks are defined to contain more than five times the average event-count at homogeneous irradiation. On the other extreme less than 1 % of strips are allowed to be dead, defined as having less than 10 % of the average event count at homogeneous irradiation.

The emphasis of this chapter is on the position reconstruction capabilities of this detector under irradiation with a high energy muon beam.

6.3 Test Beam Performance

The first quadruplet of SM2 has been thoroughly tested at a test beam campaign in August 2017 with high energy muons and pions of 10–150 GeV [Chauchaix et al., 2000] at the SPS accelerator at CERN, which provided particles with an energy in similar range to be measured by the detectors in the NSW. Very similar to the set-up described in chapter 5, the quality of the module was evaluated by a reference measurement of the beam with a telescope built from 4 small detectors, which consisted of two triple GEM-detectors and two resistive micromegas, all of them equipped with two-dimensional strip read-out[26]. The read-out was triggered by the coincident signal of two plastic scintillators mounted in front and behind the telescope with an active area of 9 cm × 10 cm each. The large detector was placed in front of the telescope and mounted rotatable in order to determine its performance also for inclined tracks. The whole set-up is shown in figure 6.10 and schematically described in figure 6.11. The rotation point of the SM2-module was 5 cm below its lower edge therefore the position in Z for different angles and positions of the quadruplet changed by up to about 40 cm. Based on a spatial resolution of 60 µm for all detectors in the telescope a track prediction accuracy depending on the inclination of the quadruplet in the range between

---

[26]The set-up contained actually two additional GEM-detectors, which were not used for the analysis as they hardly improved the track prediction accuracy

65–100 µm could be achieved with the best prediction accuracy for an un-tilted module, which can be seen from the calculated track prediction accuracy plotted against the distance from the telescope in beam direction in figure 6.12. In beam direction the quadruplet was mounted in a way, that both eta-layers were in the front and the naming convention in this direction for the single layers in this thesis will be eta_{out}, eta_{in}, $\text{stereo}_{\text{in}}$ and $\text{stereo}_{\text{out}}$. The SM2-prototype was also mounted
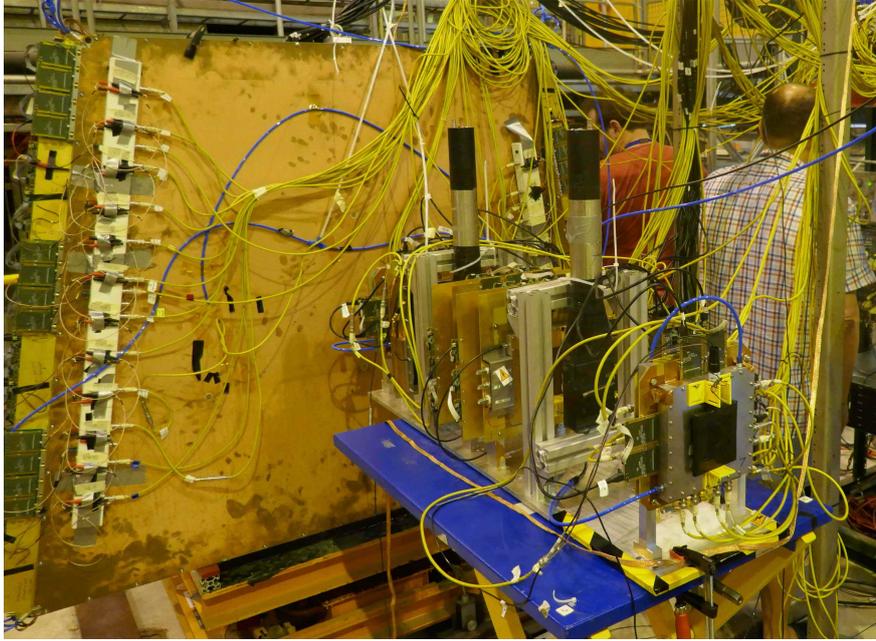

Figure 6.10: The experimental set-up at the H8 beam-line, the large prototype quadruplet is shown in upright position with the tracking telescope behind it in beam direction.

on a movable table, which allowed movement perpendicular to the beam-axis and therefore to scan the whole area of the large detector, despite that the active area of the telescope was $80\,\text{cm}^2$, which is $\approx 1/200$ of SM2. A constant small overpressure in all detectors was assured by a flux of $5\,\text{ln h}^{-1}$ of Ar-CO_2 (93:7 Vol.%) through the whole detector system.

6.3.1   Data acquisition and Jitter Recording

The time jitter of the read-out has been identified as one of the main sources for the degradation of the spatial resolution for the µTPC method and the combined centroid method for inclined tracks in chapter 5. In order to minimize the influence of this the time difference between the actual trigger signal and the trigger acceptance by the FEC-card was recorded. This was possible, because the clock synchronous trigger-output signal from a FEC-card, which is generated with a fixed offset to the acceptance of the trigger can be tapped as a NIM-signal. This signal then was compared to the raw trigger signal from the scintillators by a TDC, which yielded the time jitter with a fixed offset. This offset originates in the signal processing time of the FEC-card and also the signal propagation time in the cables connecting FEC-card with the trigger and the TDC. Recording this jitter event-wise allowed later-on to subtract it from the absolute timing of the strip signals.

In the set-up used, a total of 7536 channels from the gaseous-detectors had to be read-out, which required 60 APVs and four FEC-cards. As the TDC was not part of the SRS read-out chain the data-streams of the TDC and the four FEC cards needed to be synchronized, which ensured an event-by-event correct assignment of both systems, which was facilitated by an external counter. The whole read-out scheme is shown in figure 6.13 and was built up in the following way: The coincident signal of two trigger scintillators was used to trigger all FEC-cards separately, but also
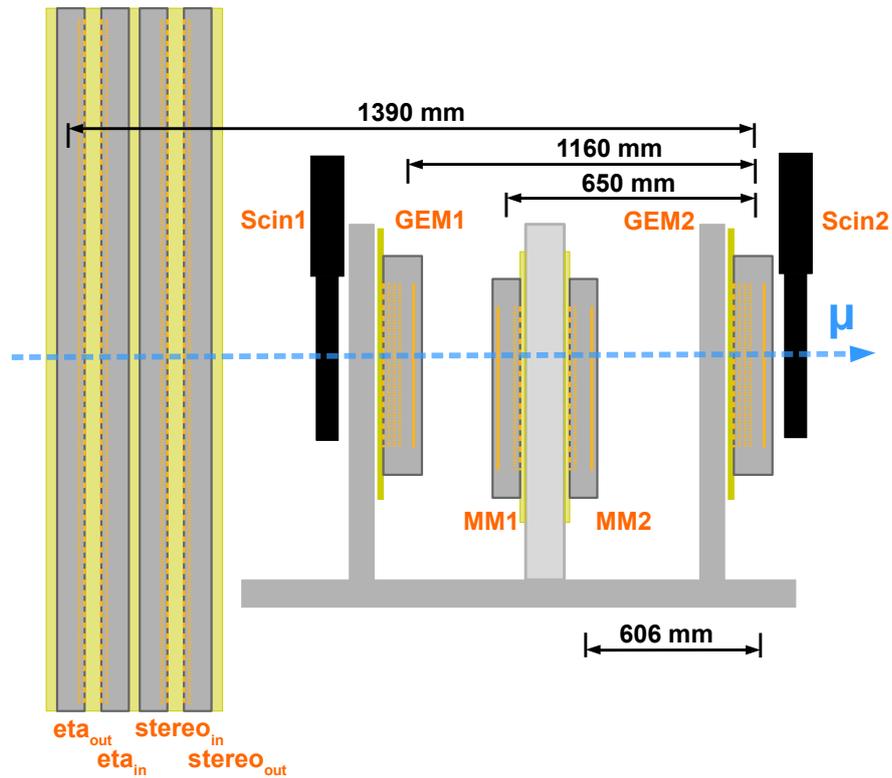
Figure 6.11: Schematic of the detectors used in the H8 (CERN) measurements (not to scale). The SM2-quadruplet was placed in front of a beam-telescope consisting of two GEM- and two micromegas-detectors with 2D-strip read-out. The whole system was triggered by scintillators placed in front and behind the telescope.
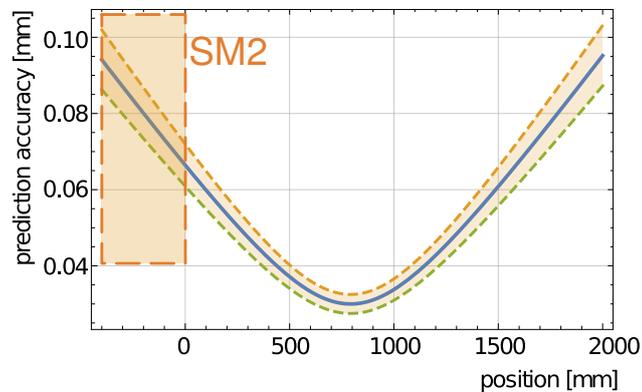
Figure 6.12: Calculated track prediction accuracy from the tracking telescope with 1-σ error bands and schematic positioning of the quadruplet at $0°$ and $30°$ inclination. 0 mm corresponds to the position of the un-tilted SM2 module.
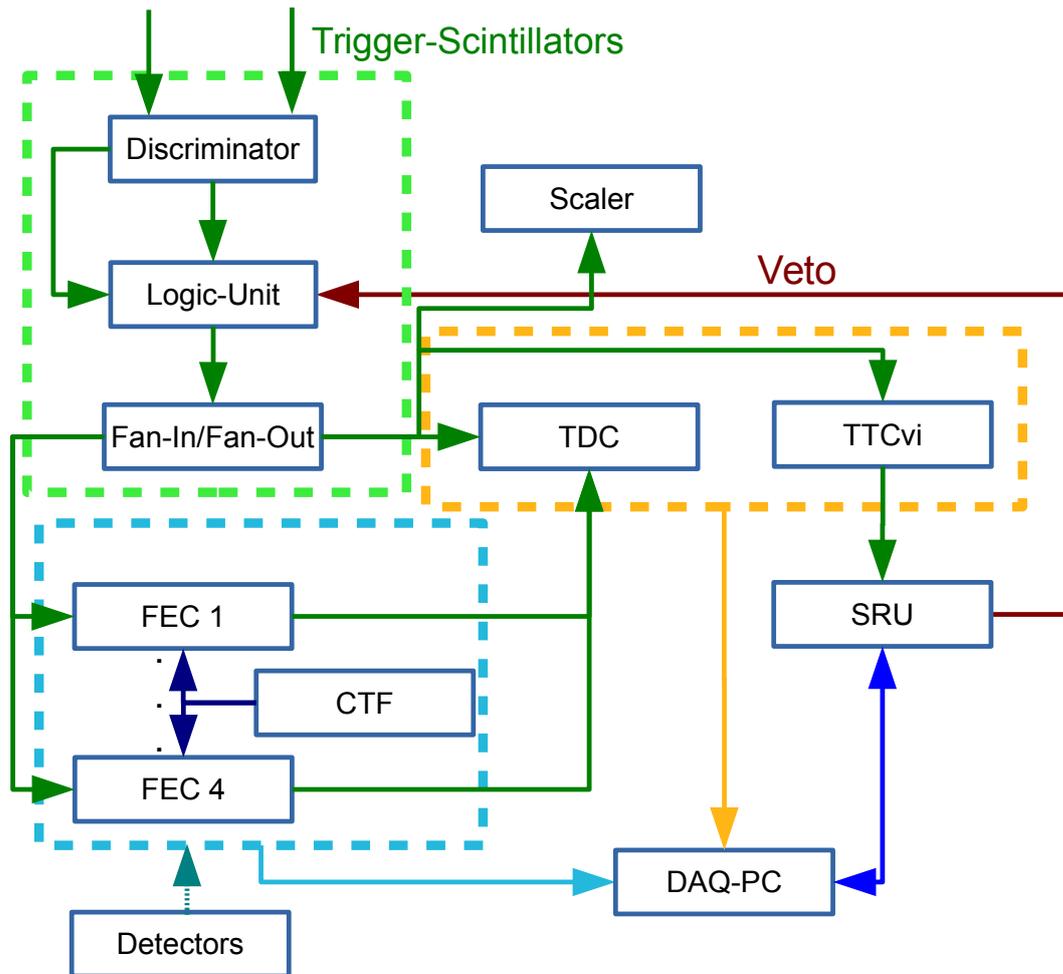
Figure 6.13: Schematic of the read-out chain with all logical elements. The trigger chain and logic is colored in green, the muon data-recording elements and data streams are shown in blue and the jitter recording is shown in yellow.

to start a TDC and to trigger a TTCvi[27] , which was used as event counter and allowed to align the data streams of the TDC with the ones coming from the FEC-cards. In order to do so the TTCvi was read-out together with the measurements from the TDC by a Data-Acquisition PC, but it also communicated every trigger to a SRU via an optical link. After each trigger the SRU raised a veto to further triggers, which was reset if data from all APVs on the connected FEC-cards were received at the Data-Acquisition PC and the trigger counter of the TTCvi was then used to label every event in both streams. This procedure was necessary as the TDC as well as the FEC-cards could skip single triggers. In order to read-out all connected APVs with exactly the same frequency a common external clock for the FEC-cards was provided by a Clock-Trigger-Fan-Out-card (CTF) [Müller, 2011]. For this first full scale test of a SM2-module the full raw ADC-signals of the APVs were recorded without any zero-suppression neither on hardware level on the FEC-cards nor in software. This ensured to record the full event information and also the possibility of off-line correction for common-mode noise. The read-out rate was up to 300 Hz in this mode. In the NSW actually a fully new developed read-out will be used, which will integrate most of the functionality described here in ASIC-based front-end boards [Geronimo et al., 2013]. These boards will be mounted directly on the detectors and also allow triggering on the micromegas signals.

---

[27]The Timing Trigger Counter VME-interface [Farthouat and Gällnö, 2000], which is a part of the ATLAS data-acquisition hardware and allows to distribute LHC-bunch crossing synchronous triggers do different read-out electronic systems

6.4 General Performance at Perpendicularly Incident Muon Beam

The prototype detector was tested at this beam-time for the first time under operational conditions, therefore some calibration runs in order to find a well defined working point in terms of necessary amplification voltages were done in an upright position. As small deviations in the pillar height, the thickness of the resistive strips, and also thickness variations in the panels can influence the nominal distance of 128 μm between the anode and the micromesh and as the gain increases exponentially with the applied electric field even small deviations can lead to a tremendous difference in the pulse height. In order to mitigate local differences between the different panels and layers every anode pcb-board is divided in two high-voltage sectors, which allows to sustain a relatively homogeneous gas amplification over a whole module. A calibration revealed that the optimal amplification voltage for the different layers of this quadruplet showed some significant deviations. With the beam centered in the middle of the module similar amplification for both layers of each read-out panel could be achieved within ±15 % with identical amplification voltage. The gain difference between the two panels was around 25 % for identical voltages, which is shown over a range of different amplification voltages between 560–615 V in figure 6.14. The amplification was determined by a fit of a Landau-function to the cluster charge distributions of the different layers, and the most-probable value of each distribution is plotted here. The voltages were chosen such, that at the data-point with the highest amplification less than 10 % of all events exhibited a strip in a cluster, whose charge was exceeding the dynamical range of the ADC. The
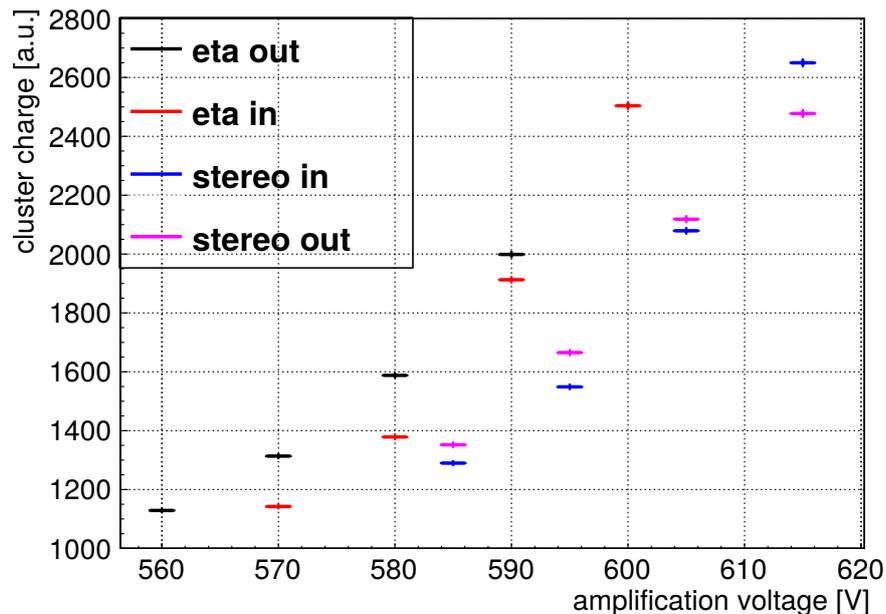
Figure 6.14: Cluster charge, determined by the most probable value of a Landau-function fitted to the cluster charge distributions, plotted against the amplification voltage for all layers. The two sides of a panel show comparable pulse heights at equal voltages,but there is a significant deviation between eta and stereo boards.

amplification differences, albeit hinting on production imperfections, did not directly lead to performance differences in the layers as e.g. for perpendicularly incident these differences had hardly any influence on the position resolution determined by the centroid method, as it can be seen in figure 6.15(a) for the two eta-layers for $E_{drift} = 600\,\mathrm{V\,cm^{-1}}$. A similar behavior was also found in terms of reconstruction efficiency (see section 6.7). Both layers displayed an excellent spatial resolution of below $\sigma_{weighted} = 90\,\mu\mathrm{m}$, which has been determined by a fit of a double Gaussian function to the respective residual distributions, by deconvolution of the track prediction accuracy and by calculating the integral weighted mean of both widths (compare equations (5.2) and (5.3)). An example of this for an amplification voltage of 585 V and $E_{drift} = 600\,\mathrm{V\,cm^{-1}}$ applied to the eta_out-layer is shown in figure 6.15(b), where a spatial resolution of $\sigma_{weighted} = (86 \pm 5)\,\mu\mathrm{m}$ could be

achieved.
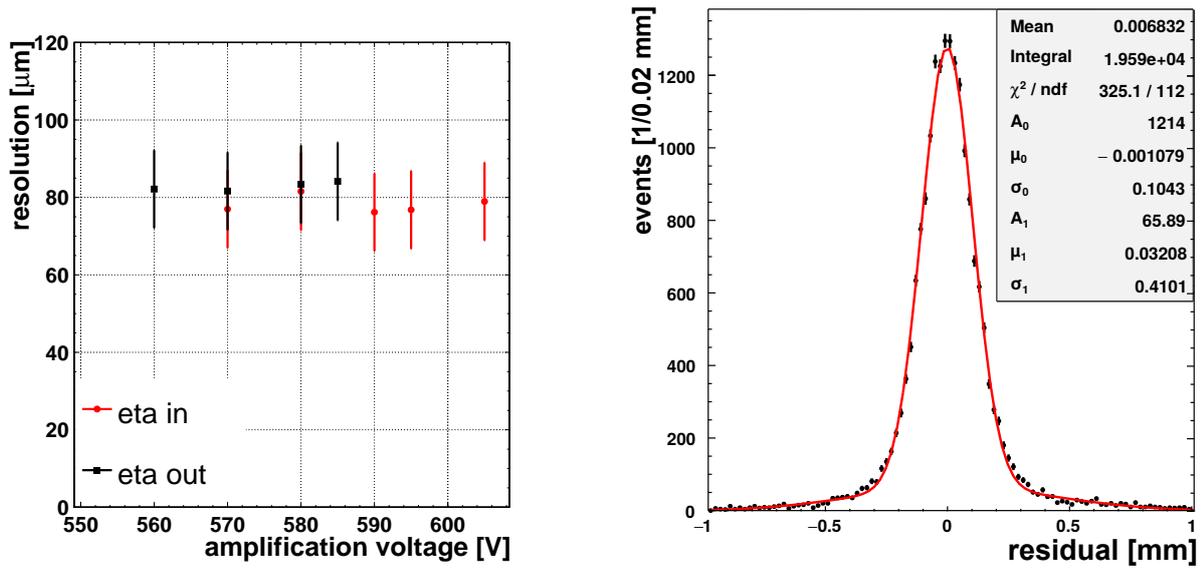
(a) Resolution determined by perpendicularly incident muons for both eta-layers plotted against the amplification voltage for E_{drift} =600 V cm^{-1}. Neither a significant difference between both layers, nor a dependence on the amplification voltage is visible.

(b) Residual distribution determined by the centroid method of the eta$_{out}$ taken with perpendicularly incident muons at an amplification voltage of 585 V and E_{drift} =600 V cm^{-1}. A fit with a double Gaussian reveals an excellent spatial resolution of $\sigma_{weighted}$ =(86 ± 5) μm from the weighted contributions of both Gaussians after subtraction of the track prediction uncertainty of 65 μm.

Figure 6.15

Similar results were found in the combination of the two stereo-layers, described by equations (6.5) and (6.6), with a position resolution in the precision direction of $\sigm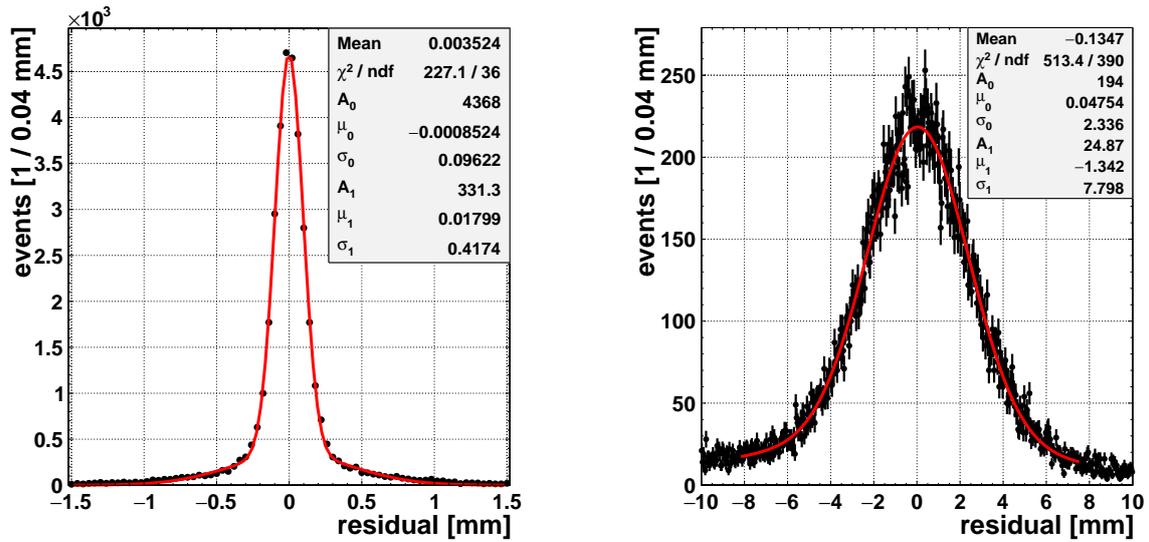a_{weighted}$=(100 ± 10) μm and a resolution of $\sigma_{weighted}$=(3.9 ± 0.1) mm in the perpendicular direction, which is shown in figures 6.16(a) and 6.16(b) for E_{drift} =600 V cm^{-1}. The slightly reduced spatial resolution in the precision direction compared to a single eta-layer can be attributed to the increased influence of the long tails in the double Gaussian fit. These were caused by the mismatch of clusters from both layers, which did not belong to the same particle. On the other side the narrow core of this distribution is due to the case of good resolution in both detectors and has actually a smaller width of only σ_{core}=(70 ± 5) μm. Another reason for the broad tails is visible in the overlay of the hit position distribution for different beam positions in the whole detector, when reconstructed by both stereo-layers, in figure 6.17. Mostly well defined beam-spots were reproduced, but visible are also the underlying patterns along the strips of these panels. These lines represent mis-reconstruction of an event in one of the two layers caused by strips with a high noise level, which were falsely matched with a hit from the other layer. Strips with a high noise level occurred here frequently at the junctions of two read-out boards, which was most likely caused by interrupted or pairwise connected strips due to imperfect trimming of the anode printed-circuit-boards before joining them to a full panel. In the NSW these falsely reconstructed charge clusters will be eliminated by tracking with multiple detector layers, which also yielded in section 6.6 an increased reconstruction performance of the full quadruplet. Despite of production imperfections the amount of badly or non-connected strips, which led to an elevated noise level, was rather low for this prototype, as it can be seen in figure 6.18. The reconstructed cluster positions for a trigger on the whole area of the SM2 with cosmic muons are shown for the eta$_{out}$-layer[28]. The joints between boards at 1024 and 2048 strips can be directly identified by the two dominant peaks on an otherwise relative uniform hit distribution. In total 3 % of strips were found to be dead and 1.6 % to be noisy.

---

[28]The data shown here was taken in the Cosmic Ray Facility in Garching ([Biebel et al., 2003])

Mean	0.003524
χ^2 / ndf	227.1 / 36
A_0	4368
μ_0	-0.0008524
σ_0	0.09622
A_1	331.3
μ_1	0.01799
σ_1	0.4174

(a) Residual of the combined position information of the stereo-layers in eta direction determined for perpendicularly particle incident, $E_{drift} = 300\,\text{V cm}^{-1}$ and $U_A = 615\,\text{V}$. The wide tails come from mis-combination of hits in the two stereo layers. A spatial resolution of $\sigma_{weighted} = (100 \pm 10)\,\mu\text{m}$ was achieved.

Mean	-0.1347
χ^2 / ndf	513.4 / 390
A_0	194
μ_0	0.04754
σ_0	2.336
A_1	24.87
μ_1	-1.342
σ_1	7.798

(b) The coarser spatial information perpendicular to the eta-direction also showed a resolution within the expectations for the same set-up with $\sigma_{weighted} = (3.9 \pm 0.1)\,\text{mm}$.
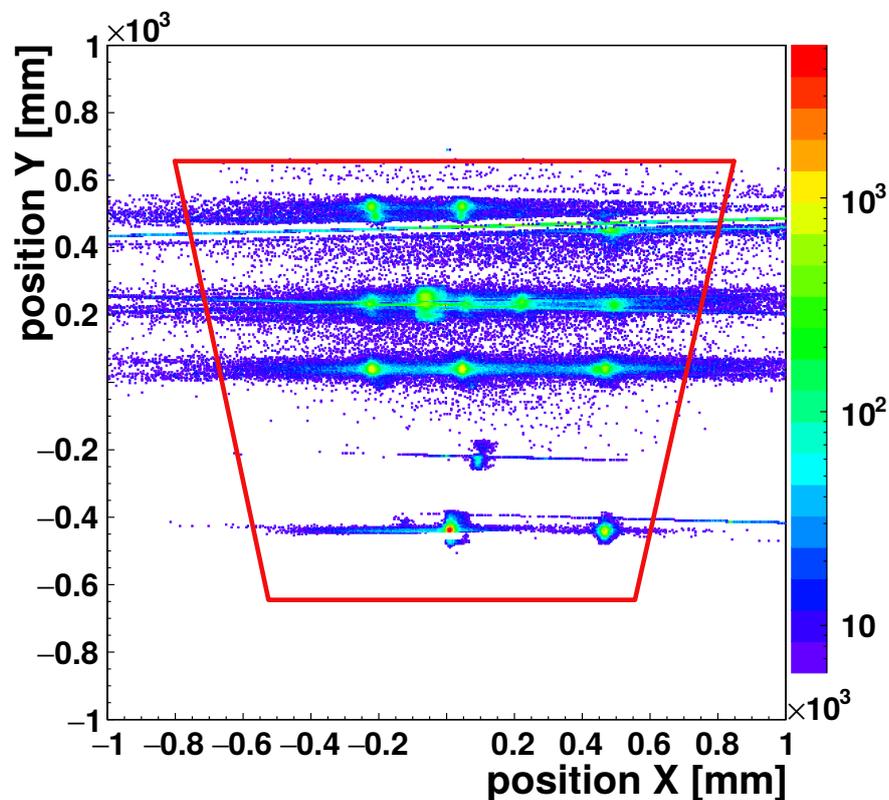
Figure 6.16

Figure 6.17: Hit distribution for all beam positions reconstructed by the two stereo layers with the envelope of the active area.
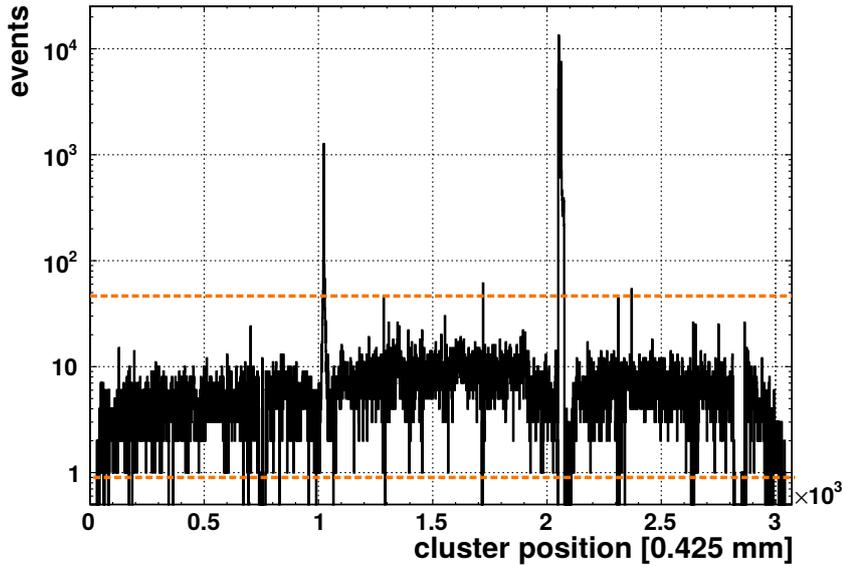
Figure 6.18: Position of clusters reconstructed in the eta$_{out}$-layer taken with cosmic muons in the Cosmic Ray Facility in Garching. The dominant peaks at the junction of two read-boards at the position of the strips 1024 and 2048 are most likely caused by cut and electrically shortened read-out strip due to a production fault. Missing strips, most likely cut close to the read-out electronics, are also visible around strip position 2800.

6.5 Performance under inclined tracks and μTPC results

The detectors of the NSW will be hit by muons from the interaction point with track inclinations in the range between 8–30°. The performance of this large module under inclined muon tracks hence was one of the main aims of this beam-time campaign. This was achieved by tilting the module by 20° and 30° in the far direction of the telescope. For better comparison the results shown in this section represent measurements at the same position close to the center of the read-out planes although the quadruplet was also moved to multiple positions at both inclinations. For the performance tests the amplification voltages were kept constant at the highest values tested in section 6.4, as the amount of primary electrons per strip recedes with increasing track inclination. A first check for the performance was the determination of the number of strips in a cluster compared to the expected amount. Under inclination the number of strips should increase, which is also shown in figure 6.19 at the example of the eta$_{in}$-layer, from a minimal number of strips n_0 perpendicularly incident depending on the width of the drift gap ΔZ according to equation (6.11):

$$n = \sqrt{n_0^2 + \left(\frac{\tan\theta \Delta Z}{\text{pitch}}\right)^2} \qquad (6.11)$$

Consistently the mean amount of strips in a cluster for all four layers was found to be slightly lower than expected, as it can be seen in table 6.1. Here the measured and expected number of strips for different track inclinations for all layers is listed, whereas the stated expected values are derived from the measured mean number of strips for perpendicularly incident muons. $E_{drift} = 600\,\text{V}\,\text{cm}^{-1}$ was used and the highest amplification voltages for each layer, which are shown in figure 6.14, were applied. A systematic deviation from the expected values is observed, which most likely is caused by a non perfect selection of hit-strips with low signal, which did not pass the noise suppression, leading for 20° inclination to on average 0.6 too few selected strips and for 30° even 1.2 strips. The implications of this will be discussed in more detail in section 6.5.2.

The spatial resolution determined by the centroid method without any corrections exhibited

Table 6.1: Expected and measured mean number of strips in a cluster for all layers. Measured values, which differ by more than one strip from the expectation are colored red. In the expected values enter the actual amplification and diffusion, which are not identical for all layers.

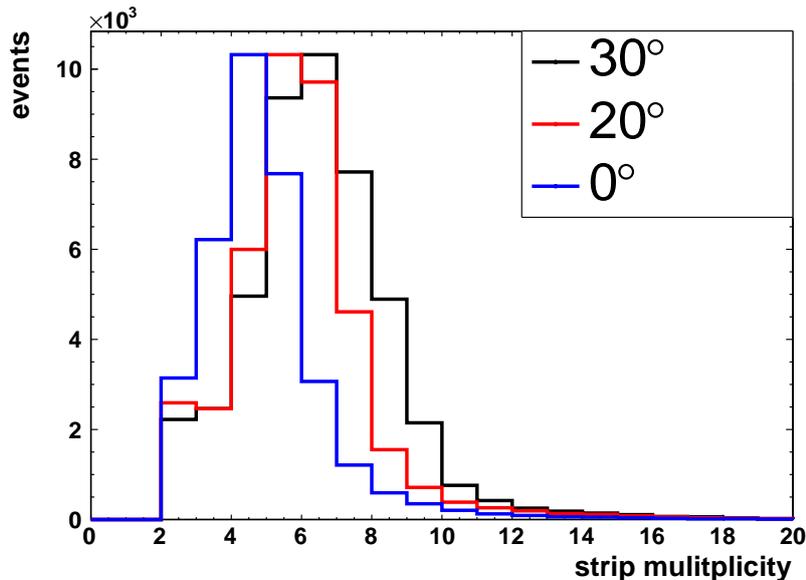| inclination	n expected				n measured			
	eta$_{out}$	eta$_{in}$	stereo$_{in}$	stereo$_{out}$	eta$_{out}$	eta$_{in}$	stereo$_{in}$	stereo$_{out}$
0°	-	-	-	-	4.10	4.00	3.10	4.40
20°	5.9	5.8	5.3	6.1	6.13	5.12	4.15	5.25
30°	8.5	7.9	7.5	8.1	6.75	7.27	6.50	6.87

Figure 6.19: Strip multiplicity of clusters for different inclination angles at $E_{drift} = 600\,\mathrm{V\,cm^{-1}}$ and $U_A = 600\,\mathrm{V}$ at the center of the eta$_{in}$-layer

results, which were comparable to the spatial resolution for similar measurements with much smaller micromegas detectors described by [Ntekas, 2016], as it is shown in 6.20(a) for both eta-layers and the combination of both stereo-layers in eta-direction. Here $\sigma_{weighted}$ is plotted, which shows identical performance of both eta-layers, but also the better performances of the combination of both stereo-layers, which is compatible with the expected $1/(\sqrt{2}\cos\varphi)$ times higher resolution due to this combination. Furthermore a variation of E_{drift} had no significant influence on the centroid resolution, which is shown at the example of the eta$_{in}$-layer in figure 6.20(b).

6.5.1 μTPC-Reconstruction and Position Determination by the Centroid Corrected by Timing Information

Proceeding from this the reconstruction by means of the μTPC-method was probed, in order to reach the required spatial resolution. It immediately showed from the reconstruction of the track inclination the necessity of the previously described refinement methods. This was rather obvious from the unsatisfactory quality of the reconstructed angle without charge correction, which is shown in figure 6.21. The angle distribution obtained from the μTPC-fit is plotted for $E_{drift} = 600\,\mathrm{V\,cm^{-1}}$ at an inclination of 20°. Without correction it could not be reconstructed. This presented quite pictorially the necessity of a charge correction also for resistive strip micromegas similar to the correction described in section 2.4.2. In contrast to the read-out described earlier the coupling of charge to neighboring strips is not only caused by the overlap of the weighting fields of neighboring strips, but by direct capacitive coupling of the strips, which has already been studied by [Bortfeldt, 2014] and [Lösel, 2017]. Simulations by [Lösel, 2017] predicted a coupling between 23 % to 32 % for chambers with a strip length between 9–150 cm. The charge sharing of
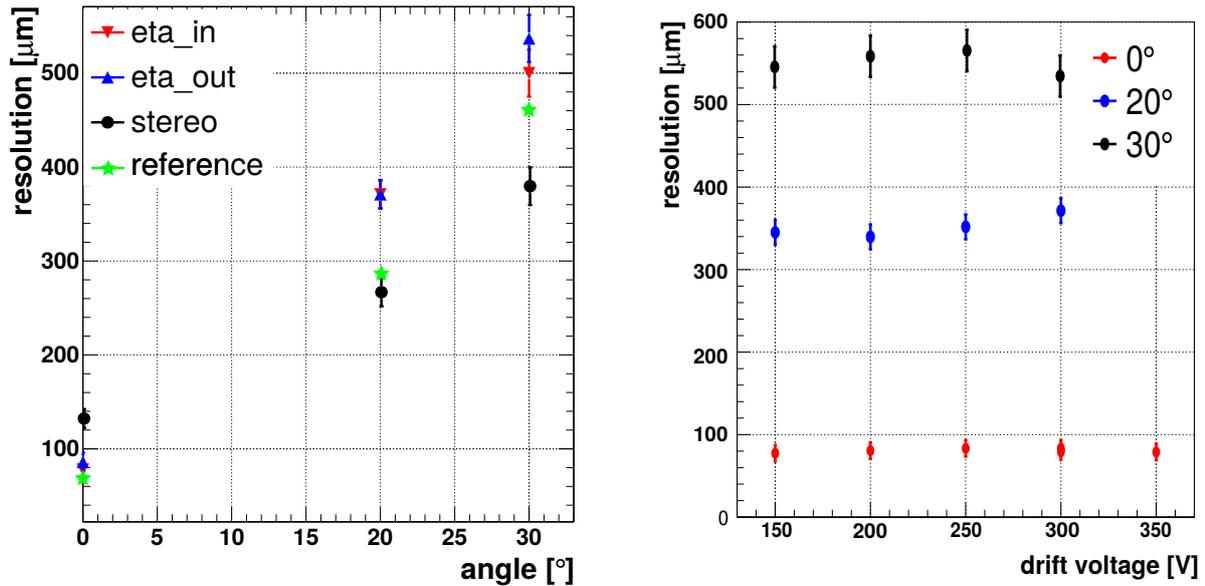
(a) The spatial resolution determined by the centroid method degrades with inclined tracks in the expected way for all layers, whereas the combination from the two stereo-layers shows also within the expectations slightly better results. For reference also the achieved resolutions for smaller micromegas detectors taken from [Ntekas, 2016] are shown. Nonetheless the pure centroid would not allow to meet the spatial resolution requirements of the NSW for inclined muon tracks.

(b) No significant dependence of the spatial resolution to the applied drift voltage for different track inclinations was observed, which is shown for the eta_{in}-layer and U_A =615 V.

Figure 6.20
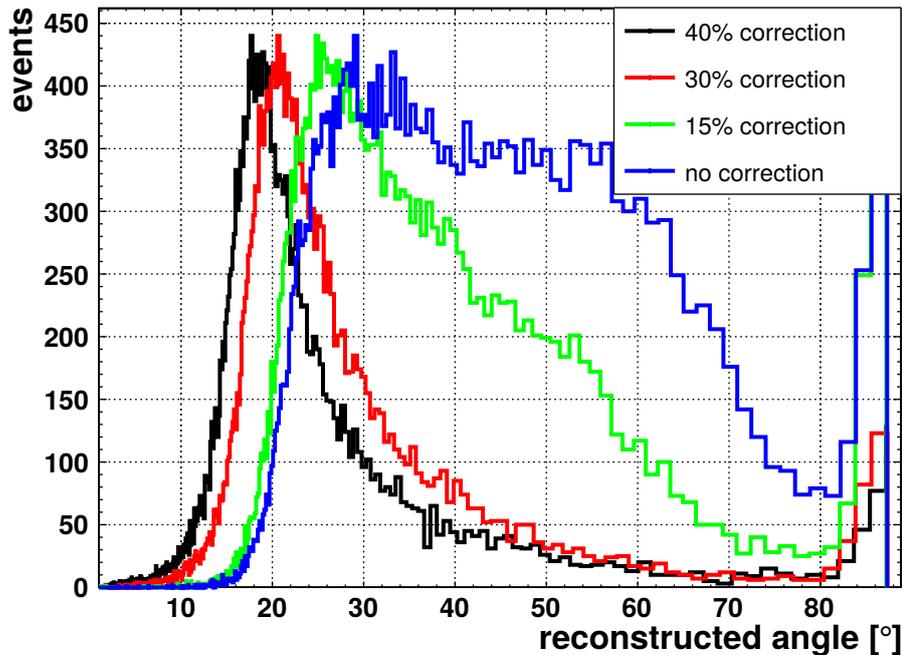
Figure 6.21: Shape, mean value and width of the reconstructed angular distribution with and without charge correction show clearly how necessary this correction is for large scale resistive detectors. Here a run with a nominal inclination of 20° and E_{drift} =600 V cm^{-1} is shown for different assumed fractions of considered charge coupling. The correct angle was reconstructed at an correction of 30 %, for higher values an overcompensation started to appear.
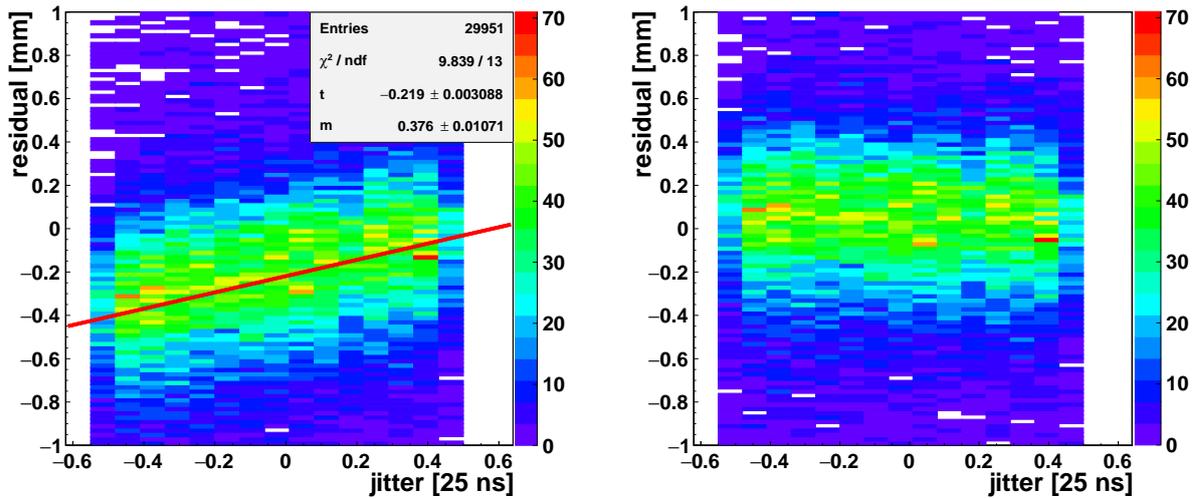
(a) µTPC-residual plotted against the recorded jitter for the inner eta-layer of the quadruplet at an inclination of 30° and E_{drift} =300 V cm^{-1}. As expected, there is a linear dependence of the reconstructed position with the jitter.

(b) After subtraction of the jitter from the strip timings the dependence vanished completely and a much better spatial resolution was obtained.

Figure 6.22

this magnitude has obviously drastic implications for the timing information on the strips, which raised an immense blurring and a shift of the reconstructed angle. A remarkable improvement in resolution and a shift of the most probable reconstructed angle to $(20.0 \pm 0.1)°$ was observed after application of a 30 % charge correction, which also reduces the width of the peak of the distribution to $(4.0 \pm 0.4)°$, determined by a fit of the sum of a Gaussian and a Landau-distribution as shown in section 5.3. An empirical optimization of the fraction of charge sharing in steps of 5 % between 0–40 % revealed experimentally the best reconstruction of the mean angle at a charge coupling of 30 %. Although the distribution shown peaked even sharper for corrections above 30 %, the shift of the peak values below the nominal angle of 20° suggested an overcompensation for these values. This has also been observed later by the determination of the spatial resolution, which reaches its best value for a correction of 30 %. For a nominal angle of 30° an angle resolution of $(3.1 \pm 0.2)°$ was found. Although this compensation considerably increased the performance, the reached angle resolution was still manifestly inferior to the ones achieved with smaller chambers. This is illustrated in a broader peak of the reconstructed angle and the long tail of the distribution towards large angles. The large tail is a hint that the charge coupling could not be resolved perfectly, whereas a broad peak is a sign for reduced timing resolution compared to smaller chambers and also would implicate a reduced spatial resolution.

For the determination of the spatial resolution the absolute timing t_{mid} and therefore also the influence of the time-jitter has been surveyed. The direct impact of the time-jitter on the measurement of $t_{µTPC}$ led to a jitter depending position reconstruction, which due to the measurement of the jitter could be directly compensated on an event-by-event basis. Without any correction the residual distribution displayed exactly the predicted jitter dependence, as it is shown in figure 6.22(a) for the inner eta-Layer at an inclination angle of 30° and E_{drift} =300 V cm^{-1}. Keeping in mind equation (2.33) a linear dependence of the reconstructed position was expected with a slope of $m = v_D \tan\theta$, which in this case would lead to m =15.3 µm ns^{-1}, which is in good agreement with the corresponding value from a linear fit to the distribution of (15.0 ± 2.5) µm ns^{-1}. The correction of all timings with the recorded jitter prior to the µTPC fit allowed to fully resolve this dependence, as it is shown in figure 6.22(b).

Using the jitter correction the spatial resolution determined by the µTPC-method improved from $\sigma_{weighted}$ =(394 ± 30) µm to $\sigma_{weighted}$ =(275 ± 30) µm. For a track inclination of 20°, which is shown

in figure 6.23(a) for the same E_{drift}, even $\sigma_{weighted} = (220 \pm 30)$ µm was achieved. Albeit the position information gained from this procedure is much better than using the centroid reconstruction, the µTPC-fit for the large detectors showed considerably worse results than for small chambers and the position resolution shown could only be achieved by a cut on the quality of the fit on $\chi^2/\text{NDF}<5$, which reduced the reconstruction efficiency distinctly (see section 6.7).

The timing corrected centroid reconstruction (see section 5.4), which does not share this flaw of the µTPC-reconstruction also gained from the jitter compensation. Slightly better results were achieved compared to the µTPC-method, as it can be seen in the corresponding residual distributions in figure 6.23(d) for an inclination of 30° and in figure 6.23(c) for an inclination of 20° at an $E_{drift} = 300\,\text{V cm}^{-1}$. The spatial resolution could be determined to $\sigma_{weighted} = (200 \pm 15)$ µm for 20° and $\sigma_{weighted} = (215 \pm 20)$ µm for 30°, which especially in the direct contrast of the corresponding uncorrected centroid resolution of $\sigma_{weighted} = (550 \pm 35)$ µm shows the capability of this method. The remaining slight angular dependence in both cases hinted again at a similar timing-resolution dependence as observed with the smaller detectors, which also led to a similar E_{drift} drift dependence shown in figures 6.24(a)-6.24(d). Best results were obtained for both angles and methods at the lowest applied $E_{drift} = 300\,\text{V cm}^{-1}$, where a 20 % better spatial resolution was obtained than at the highest $E_{drift} = 600\,\text{V cm}^{-1}$.
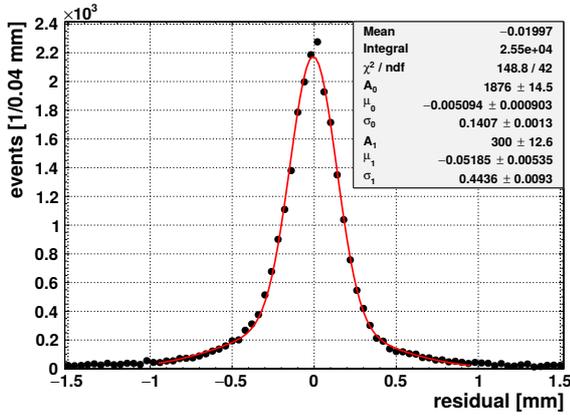
(a) Residual distribution determined by the µTPC method for an inclination angle of 20°
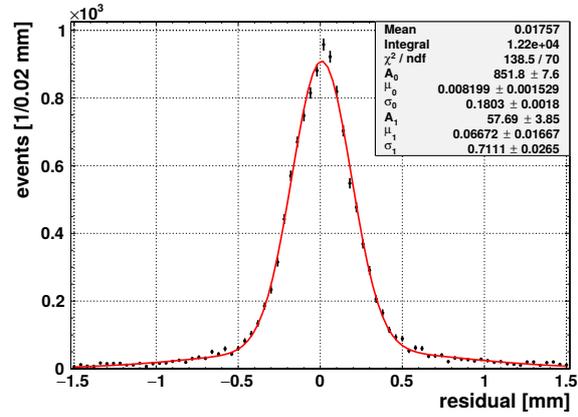
(b) Residual distribution determined by the µTPC method for an inclination angle of 30° and
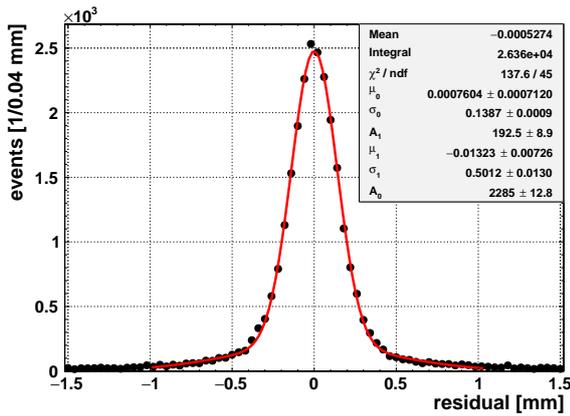
(c) Residual distribution determined by the timing corrected centroid method for an inclination angle of 20°
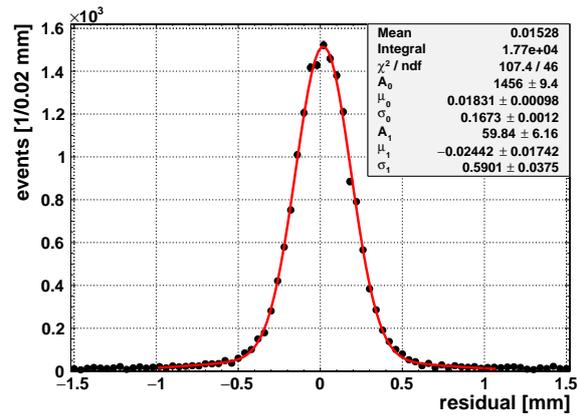
(d) Residual distribution determined by the timing corrected centroid method for an inclination angle of 30°

Figure 6.23: Residual distributions for 20° and 30° and $E_{drift} = 300\,\text{V cm}^{-1}$ at a central position in the eta$_{in}$ layer

As it already was seen for small chambers, this is a manifestation of the intrinsic timing resolution of the detector. For both position reconstruction methods shown the spatial resolution for inclined tracks is nearly identical, and is in fact again strongly correlated as it can be seen in
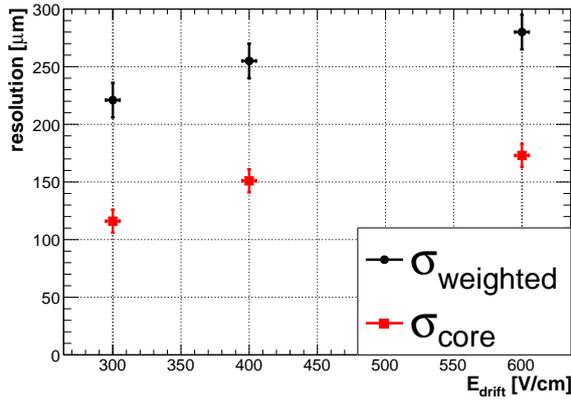
(a) Spatial resolution for the μTPC-method at 20° inclination.
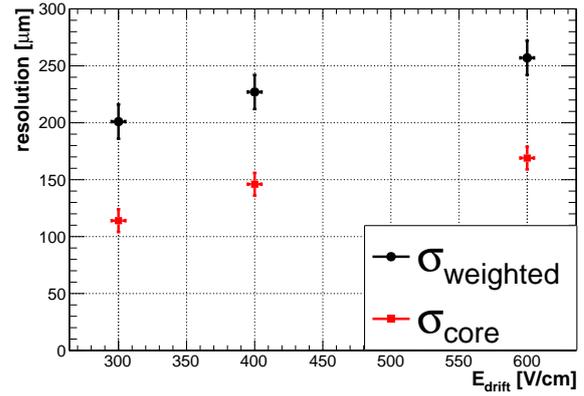
(b) Spatial resolution for the timing corrected centroid at 20° inclination.
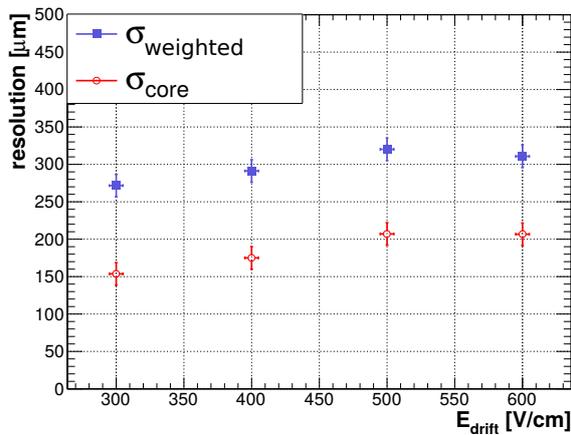
(c) Spatial resolution for the μTPC-method at 30° inclination.
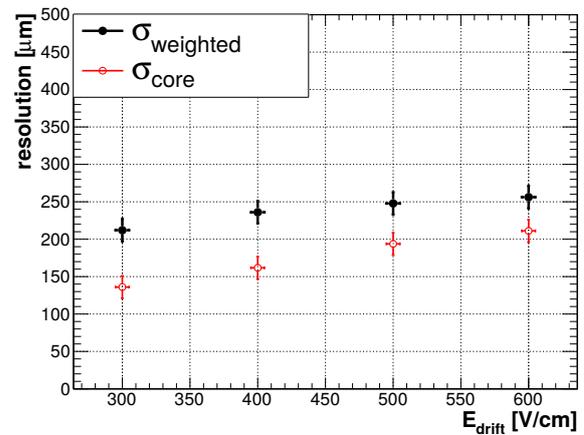
(d) Spatial resolution for the timing corrected centroid at 30° inclination.

Figure 6.24: Spatial resolution determined by μTPC-method and centroid-method with timing correction of the eta$_{in}$-layer for different E_{drift} and U_A =615 V. Although the jitter dependence has already been corrected a remaining influence of E_{drift} can be seen.

figure 6.25. The results of the best case with the lowest examined electric field is shown at 30° inclination.

6.5.2 Timing Resolution and Triggering Capabilities

So far a low value of E_{drift} seemed favorable in terms of spatial resolution. The lowered electron drift velocity in this case however should also have a potentially adverse influence on the triggering capabilities. Reducing the drift velocity comes at the cost of slower timing of the signals. The ability to trigger on the micromegas detectors of the NSW can only be achieved, if a signal can be attributed to a single 25 ns time window, which is dictated by the bunch crossing frequency of the LHC. Triggering on one of the detectors would be done by the fastest responding strip, which would see the charge produced closest to the mesh.

Comparison with the values already determined by [Lösel, 2017] and [Ntekas, 2016] for small resistive micromegas with a size of 9 cm^2 × 9 cm^2 showed that the timing resolution of the large SM2-module is actually considerably worse. As measure for this, the timing distribution of the fastest responding strip in a cluster has been used, which is shown in figure 6.26 for an inclination of 30° with data for the small micromegas taken from [Lösel, 2017] for a very similar set-up: Notably the particle type, energy, inclination angle and E_{drift} =600 V cm^{-1} were identical. Also drift gas, drift gap and the overall detector scheme were sufficiently similar to compare both detectors directly. The only notable differences between both chambers, apart from the overall size, were
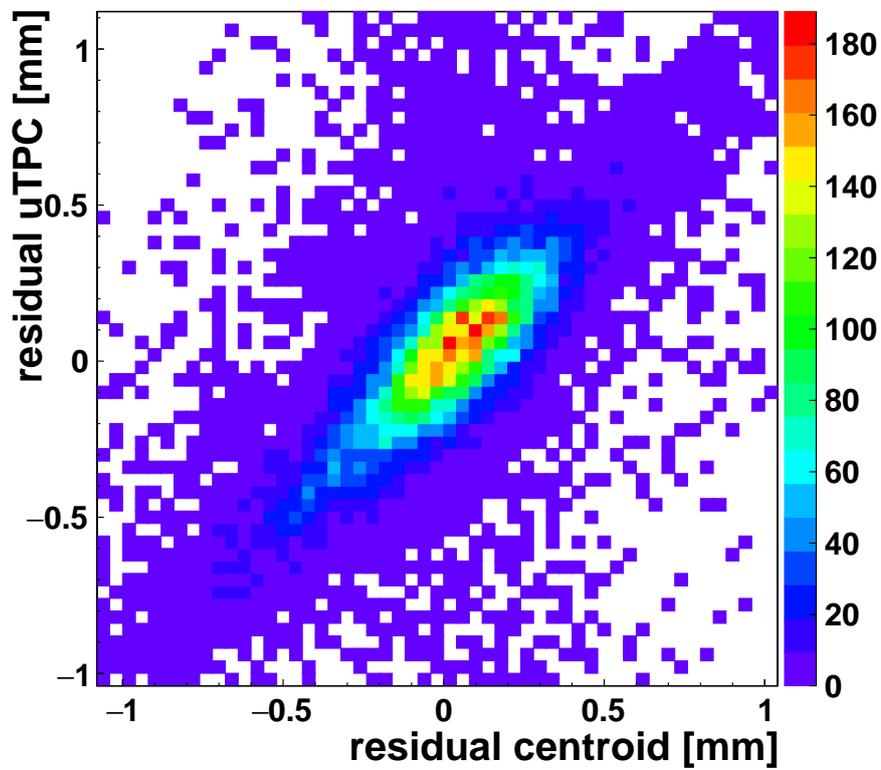
Figure 6.25: Residual determined by the μTPC-method plotted against the residual determined by the timing corrected centroid for the eta$_{in}$-layer at E_{drift} =600 V cm^{-1}, U_A =615 V and an inclination of 30°. The strong correlation is due to the mutual timing dependence of both methods and obstructs a combination of both methods in order to further improve the position resolution.

Figure 6.26: Distribution of the timing of the fastest strip in a cluster for $30°$ track inclination and $E_{drift} = 600\,\mathrm{V\,cm^{-1}}$ for the eta$_{\mathrm{in}}$-layer and a small micromegas detector.

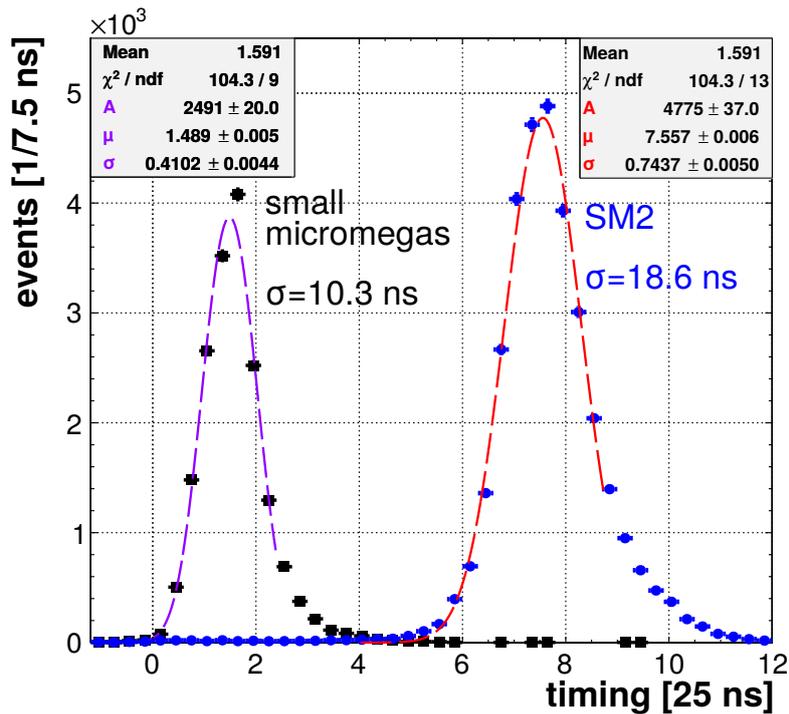the slightly smaller strip pitch of 0.4 mm of the smaller detector compared to 0.425 mm of the SM2-module and the fact that the micromesh of the smaller detectors were laminated onto the pillar structure [29], whereas at the large module the mesh is mounted on the drift panels and is mechanically and by electrostatic force pressed against the pillars. In the measurement with the small detector the time-jitter has not been recorded and the width of the distribution therefore has been determined by a fit of equation (5.7), considering also the 25 ns timing fluctuation, whereas the width of the distribution for the large SM2 module has been determined by a single Gaussian fit, because the influence of the jitter already was subtracted. This led to a timing resolution of (10.3 ± 0.1) ns for the small detector and (18.6 ± 0.1) ns for the large detector. A notable feature of both distributions is the asymmetric shape of the distributions with a tail towards later times, which is caused by the fact, that the fasted strip for inclined tracks should be at the edge of the cluster with relatively small signal height, therefore charge coupling from adjacent strips can shift the timing of this strip towards later times. This effect is much more pronounced for the larger chamber and also a reason for the overall worse timing resolution, albeit not the dominant effect. The applied charge correction did not affect this behavior, as it can be seen from the direct comparison of the timing of the first strip with and without charge correction in figure 6.27 for the eta$_{\mathrm{in}}$-layer. The correction slightly shifted the distribution to earlier times, but as it was designed to minimize the influence of fast responding strips on strips with late signal, it does not reduce the tail of the distribution.

Also the choice of E_{drift} and the drift velocity seemed to have an insignificant effect on the trigger capabilities, which can be seen by determination of the strip with earliest signal in either one of the eta-layers, which is shown in figure 6.28 for both E_{drift} with the highest and lowest v_D measured. The mean value of the fastest responding strip was not affected by the variation of E_{drift} and the lower drift velocity only had an influence of (1.5 ± 0.5) ns on the width of the distribution. One of the reasons for the worse timing resolution was found in the elongated shape of the signals for the large detector compared to smaller chambers, which is shown for different drift fields in figure 6.29. The rise-time, defined by the parameter σ_{rise} of the Fermi-fit to the strip signal of the

---

[29]These so called bulk-micromegas are described in [Giomataris et al., 2006] and allow a better defined distance between micro mesh and read-out anode, but are much more difficult to be built in large scales
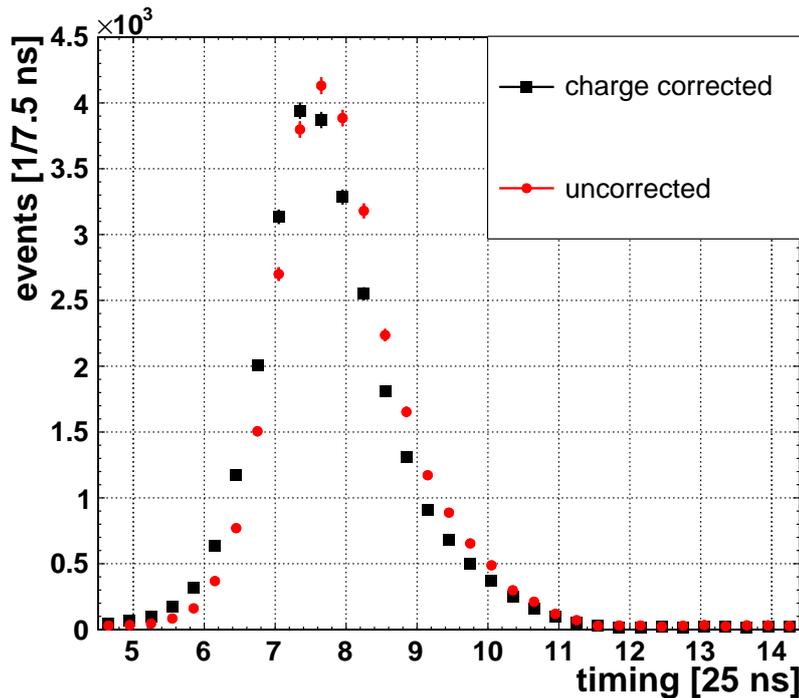
Figure 6.27: Comparison of the timing of the fastest strip in a cluster with and without charge-correction at a track inclination of $30°$ track inclination and $E_{drift} = 600\,\mathrm{V\,cm^{-1}}$ for the eta$_{in}$-layer. As the charge-correction mostly reduces the influence of early strip signal on strips with late signal, the shape of both distributions is nearly identical with the corrected one being slightly shifted towards earlier times.
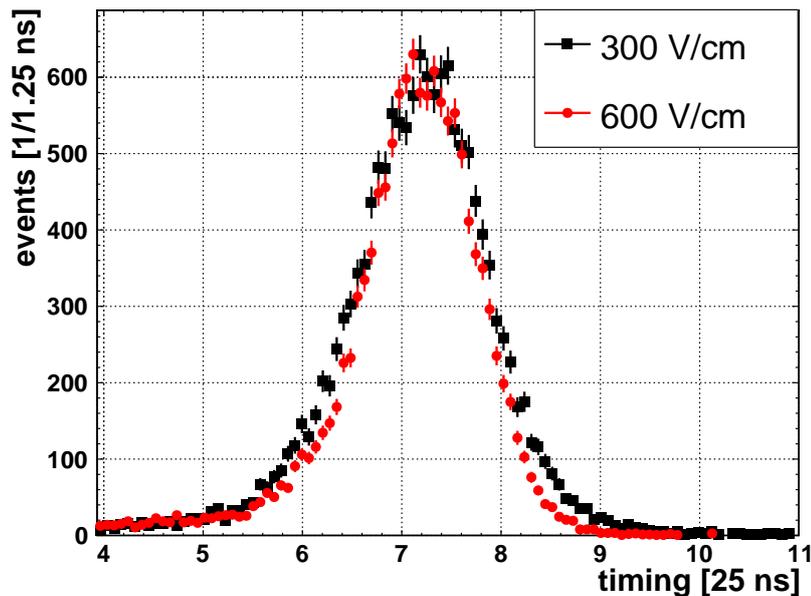
Figure 6.28: Timing t_{start} of the earliest responding strip in a cluster in either of the eta-layers for an angle of $30°$. The difference in the width for a variation of E_{drift}, determined by a Gaussian-fit, is $(1.5 \pm 0.5)\,\mathrm{ns}$.
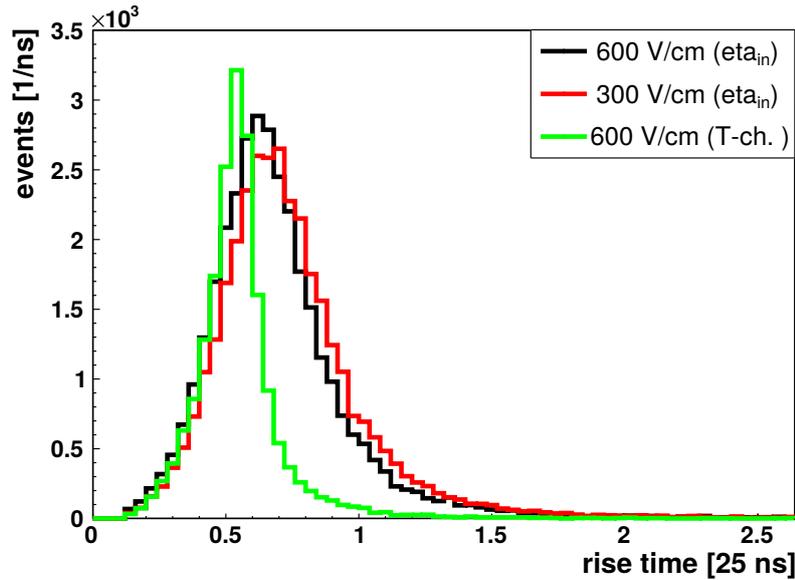
Figure 6.29: The comparison of the rise-time of the fastest responding strip for the large eta_{in}-layer with a small detector shows a significant increase in the width of the distribution. v_D due to different E_{drift}-fields only seems to have a minor influence on this.

fastest strip in a charge cluster, is shown for the eta_{in}-layer. In the strip timing determination implicitly a constant rise-time is assumed which would lead to a common offset in the timing determination of all signals. A broad distribution translates therefore directly to a fluctuation in the reconstructed timing, hence a limited timing resolution. The comparison with the smaller T-chamber at the same inclination with $E_{drift} = 600\,\mathrm{V\,cm^{-1}}$ showed a significant difference in the rise-time. The most probable values of the small and large chamber differ only by $(3 \pm 1)\,\mathrm{ns}$, but the distribution of the large chamber has a full-width-half-maximum of more than $12\,\mathrm{ns}$ compared to only $(4.5 \pm 1.0)\,\mathrm{ns}$ for the small chamber. A variation of E_{drift} at the large chamber on the other hand had only a minor influence on the signal rise-time, which was also expected as the rise-time of the fastest strip in a cluster is dominated by the ion drift in the amplification region (see section 2.4.2). One reason for the increased rise-time is the increased capacitance of the long strips, which leads to a different response-time of the feedback-loop in the pre-amplifiers of the APV25 chip and effectively a different signal-to-noise ratio. The share of the total signal, which is accessible to the pre-amplifier is depending on the relative capacitance of the detector compared to the input-capacitance of the amplifier. This implies also that the noise is depending on this, here described by an equivalent noise charge (ENC), which is equal to a charge resulting in the same signal. The capacitance of the read-out can be optimized in order to minimize to a value ENC_{opt}, which can be described by [Radeka, 1988]:

$$\frac{ENC}{ENC_{opt}} = \frac{1}{2} \left(\sqrt{\frac{C_{det}}{C_{ampl}}} + \sqrt{\frac{C_{ampl}}{C_{det}}} \right) \tag{6.12}$$

Due to the different length, width and design of the read-out the capacitance of the strips in the large chambers is about 15 times higher than in the small chambers with $(500 \pm 50)\,\mathrm{pF}$ for the strips of a SM2 module and $(30 \pm 5)\,\mathrm{pF}$ for a T-chamber and the capacitance of a single read-out channel of an APV25 is $3.7\,\mathrm{pF}$. This shows, that the larger detector in this set-up generally should be more sensitive to noise. The total influence could also be determined. As measure for noise the mean standard deviation per strip of the charge values for all time-bins was used for a random trigger , which is shown in figure 6.30 for the eta_{in}-layer of the SM2 module compared to the small micromegas. A generally higher level of noise for the large chamber can be seen, which on average is $(60 \pm 10)\,\%$ higher than for the small chamber, albeit also fluctuations from the
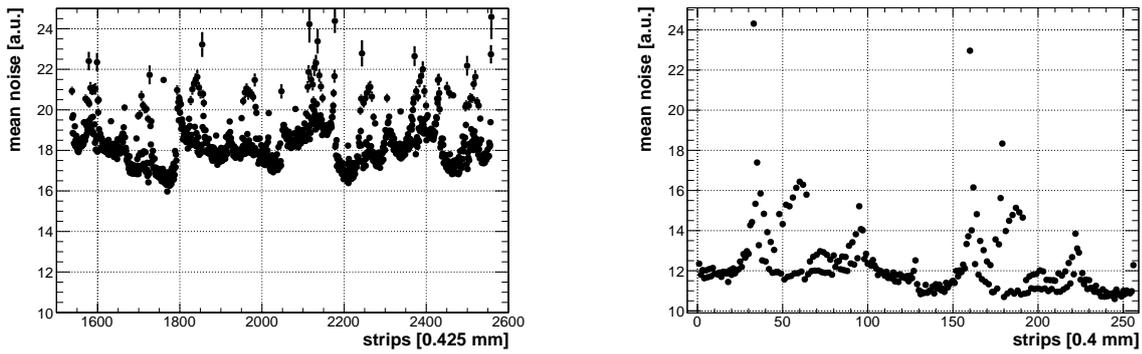
(a) A measure for detector noise is the mean RMS of the strip signal without particles traversing the detector, shown for strips in the eta$_{in}$-layer. Here also some features of the APV25 hybrid board are present, like regular fluctuations due to the channel routing.

(b) Compared to the large module a small resistive micromegas exhibits a much lower mean RMS per strip and therefore also significantly lower noise.

Figure 6.30

different channels are visible. Due to the routing of the channels on the APV25 hybrid-boards and differences in the current supply for the pre-amplifiers some channels on all APV25 board have a higher noise level than others, which is visible for both detectors. Also the different APVs show a slight but distinctive difference in their noise and amplification behavior. For the large module this increased susceptibility for noise especially for low-charge signals led to a decrease in the timing resolution. This can be seen in the width of the rise-time distribution for both detector systems plotted against the charge distribution in figures 6.31(a) and 6.31(b). In both cases, for the large and small detector, a drastic increase in the width of the distribution for low charge events was observed. The actual dependence of this is difficult to measure as adding and reducing noise on the large chambers is difficult to realize in a controlled way. It was, however, possible to simulate this behavior based on single strip signals with random noise added. For this calculation strip signals coming from a Garfield simulation, which was described in chapter 2, for a muon track with 30° inclination were used. For every event 10000 iterations were investigated with random noise of different fractions of the pulse height added time-bin-wise to the signal. In the range of 0–20 % added noise on the ideal signal a clear influence on the width of the rise-time distribution was observed, which is shown in figure 6.31(c). The comparison with the measured values $\sigma_{meas.}$ for the eta$_{in}$-layer, where the noise-to-signal ratio was calculated by dividing the mean noise by the strip charge, shows the same behavior up to a constant offset. This additional constant offset of (1.25 ± 0.20) ns was most likely caused by fluctuations in the distance between the micromesh and the read-out structure. One reason for these fluctuations is the electrostatic sagging of the mesh between pillars, which depending on the mesh tension and the distance and size of the pillars can contribute up to 10 μm (see [Pree, 2015] and [Kuger, 2017]). Single missing pillars on the other hand also can lead to an additional local sagging of the mesh by around 5 μm. Another reason are imperfections in the production, which cause dents or bumps in the modules and in the case of the panels used here are characterized by an unevenness of the surface with a RMS of 12 μm [Müller, 2017]. Simulations of the signal creation (compare 2.7.1) showed that fluctuations of ± 10 μm from the nominal distance of 128 μm would lead to additional fluctuations in the rise-time of $\sigma_{width} = 7$ ns, as it can be seen in figure 6.32. This presumably evenly distributed additional fluctuation in the rise time would account in the limit of a signal without noise to an offset of $\sqrt{\sigma_{meas.}^2 - (\sigma_{width}/\sqrt{12})^2} = (1.75 \pm 0.30)$ ns [30], which is in agreement with the simulated value of $(0.055 \pm 0.001) \cdot 25$ ns $= (1.38 \pm 0.03)$ ns.

For triggering purposes this decrease in timing resolution can be partly overcome by using

---

[30]The division be $\sqrt{12}$ is motivated by the RMS of a rectangular probability distribution
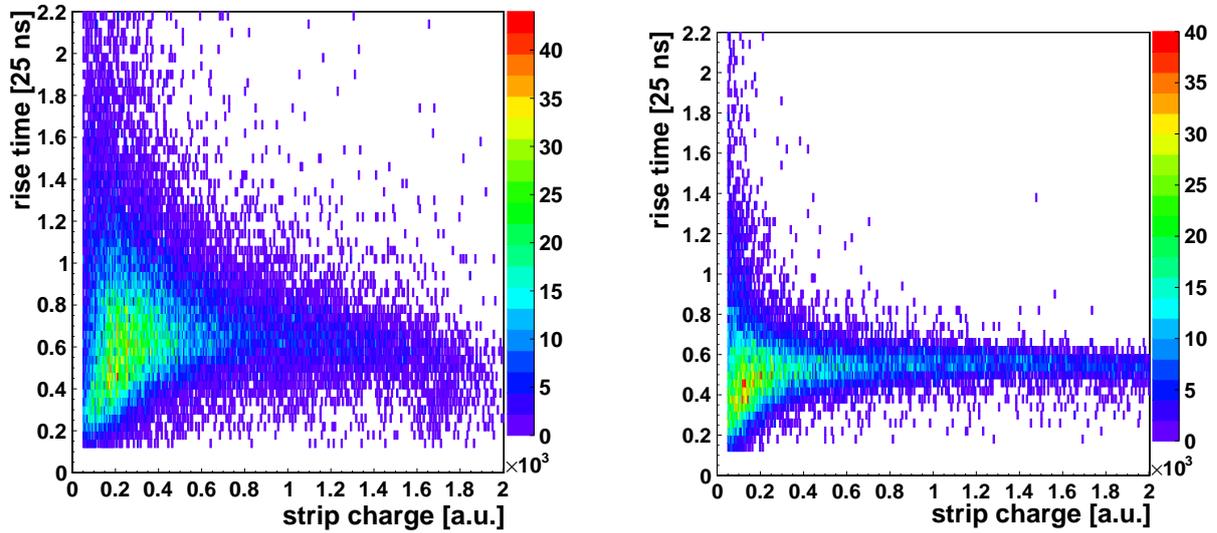
(a) The large width of the signal rise-time for the eta$_{in}$-layer is dominated by the enormous fluctuations for low strip charges.

(b) Compared to the large detector the small T-Chamber shows a similar, but drastically reduced dependence on the strip charge.
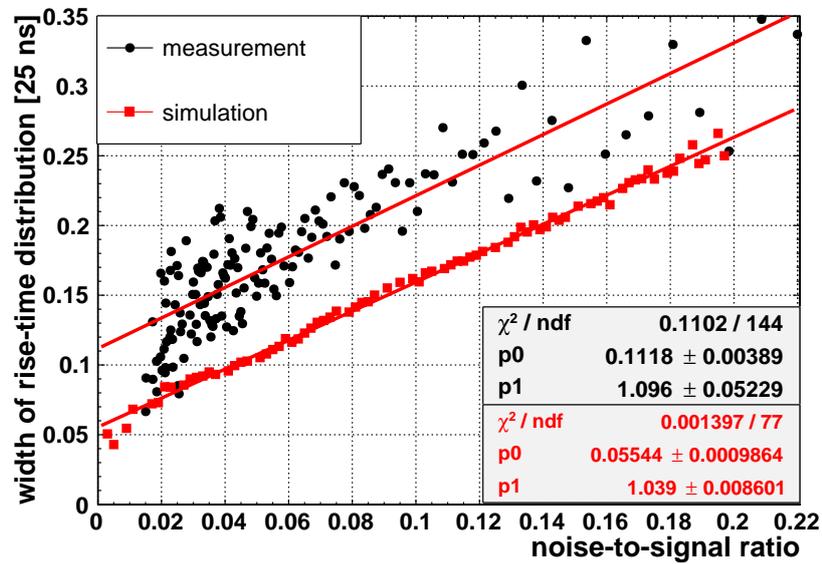
(c) Simulation and measurement with the eta$_{in}$-layer show a high influence of the noise-to-signal ratio on the rise-time and imply a strong correlation between noise and timing resolution.

Figure 6.31
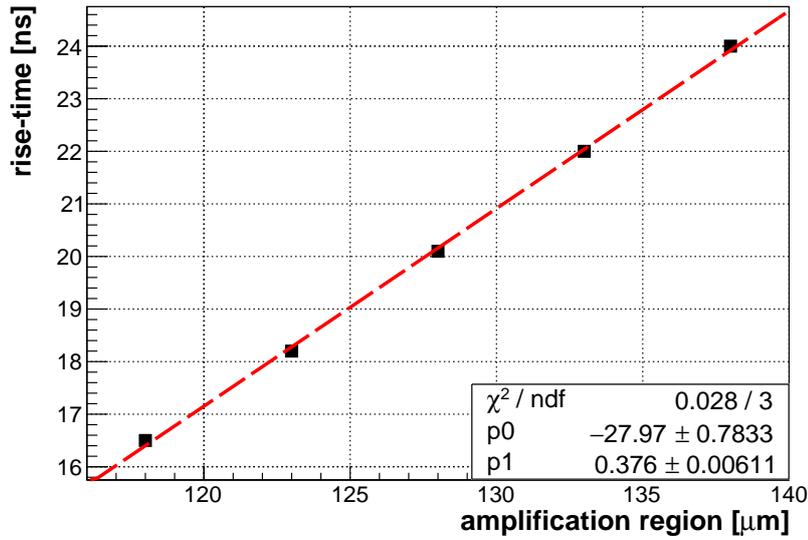
Figure 6.32: Simulation of rise-time for U_A =550 V depending on the width of the amplification region (compare section 2.4.2). The ion drift velocity in this region is nearly constant and the rise-time increases linearly with the distance.

the fastest responding strip from multiple detector planes, which reduced the width of the timing distribution as it can be seen in figure 6.33. The timing distributions of the fastest responding strip for a single eta-layer, the fastest of both eta-layers and the fastest of all layers are shown, for an inclination of $30°$ and E_{drift} =600 V cm^{-1}. As this method systematically discards strips, with a too high reconstructed timing, the distributions are shifted towards faster timings and become sharper. The width decreases significantly from σ =(18.5 ± 0.5) ns for a single layer, determined by a fit of a Gaussian, to σ =(14.0 ± 0.5) ns for all four layers. This would still be only equivalent to a fraction of 63 % of events lying in a window of 25 ns around the mean value, but showed already an improvement over the fraction of 50 %, if only a single detector plane were considered. A further improvement can of course be achieved by an increased amount of layers, but as only a single quadruplet could be tested here the number of detector planes necessary to achieve a fraction of 95 % of events within one bunch-crossing had to be extrapolated. The timing distribution of the fastest responding strip of n detectors with the mean timing of μ and a width of the single distributions of σ can be described by [Ntekas, 2016]:

$$g(t) = \frac{n}{\sqrt{2\pi}\sigma} \left[1 - \frac{1}{2} \left(erf \left(\frac{t - \mu}{\sqrt{2}\sigma} \right) + erf \left(\frac{\mu}{\sqrt{2}\sigma} \right) \right) \right]^{n-1} e^{\frac{-(t-\mu)^2}{2\sigma^2}} \qquad (6.13)$$

Taking the width of the distribution of a single detector as input parameter the fraction of events within 25 ns could be calculated and the extrapolation also fits very well to the data points for two and four layers, which is shown in figure 6.34. Nonetheless the fraction of events in the necessary time window at eight detector planes, which will be used in the NSW, still only reaches 73 %. For 95 % a much higher amount of layers would be needed.
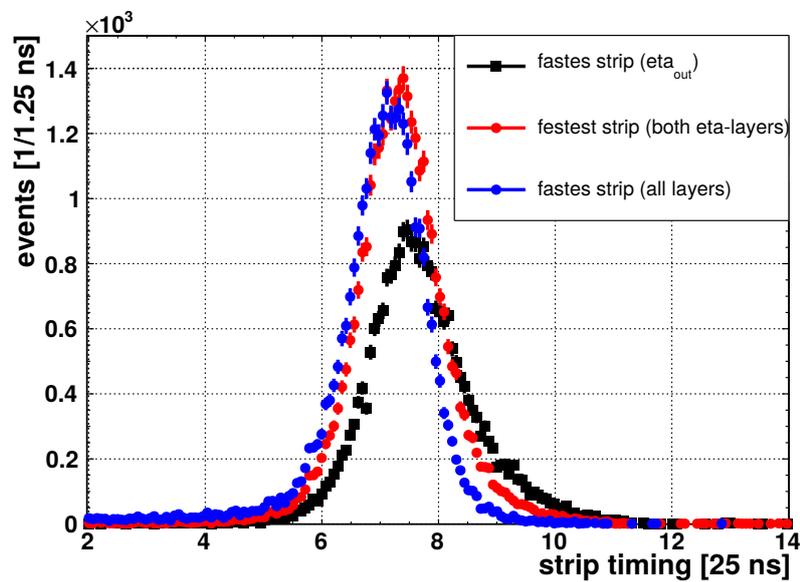
Figure 6.33: Using the fastest responding strip from multiple detector layers the triggering capability can be improved, as it can be seen from the reduced width of the distributions shown for one, two and four detector layers of the SM2 module. Here $E_{drift} = 600\,\mathrm{V\,cm^{-1}}$ was applied and the detector was tilted by $30°$.
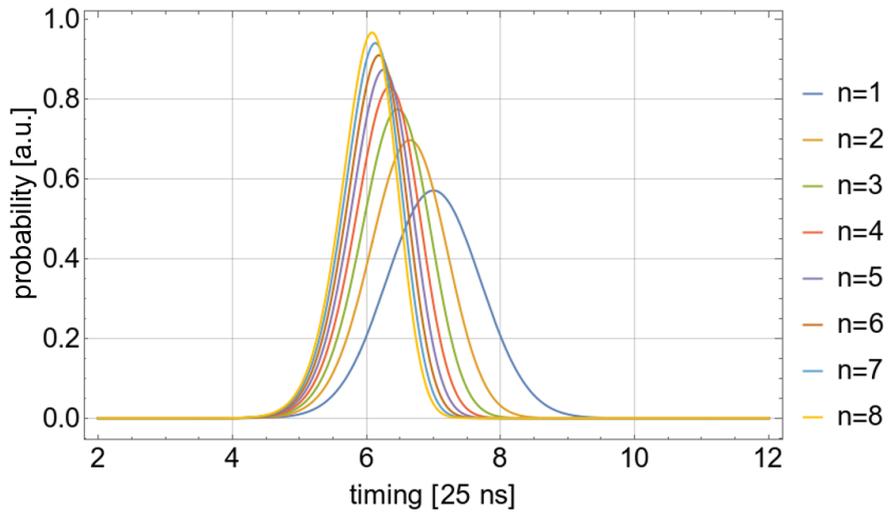
(a) Calculated timing distribution of the fasted strip in a cluster from n detector layers (see equation (6.13)). As input parameters the width and timing of the distribution measured with the eta$_{out}$-layer of the SM2-quadruplet have been used.
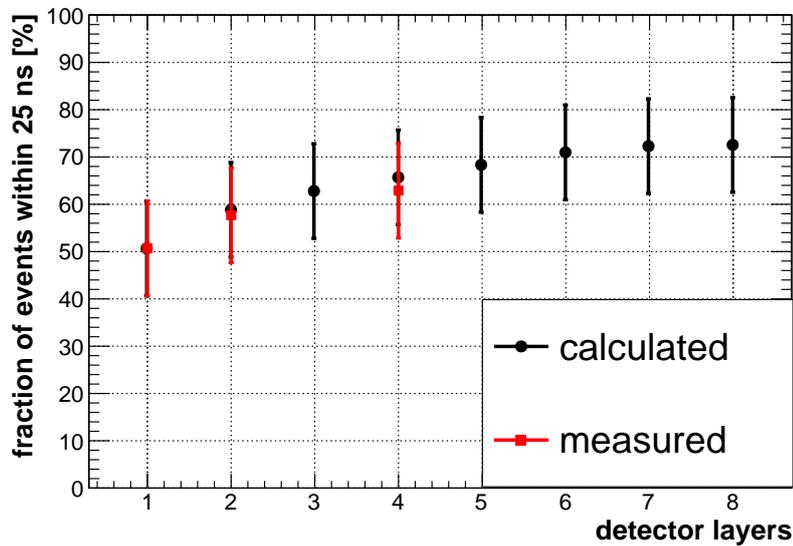
(b) Measured and calculated fractions of events, where the first strip of a cluster of n detector-layers is reconstructed within a time window of 25 ns.

Figure 6.34

6.6 Combined Resolution and Magnetic Field Compensation

In principle the timing correction to the centroid position determination needs an external track inclination information in order to deliver the correct modification to the position. So far in this chapter only a fixed calibration factor for a given angle has been used based on the known tilt of the detector, as in principle the track inclination was fixed by the extreme low divergence of the beam. For an off-line reconstruction this however poses no real obstacle, as in a first iteration the track inclination for every layer can be obtained from the uncorrected positions from the other layers and in a second step the position in every layer can be refined. In this step also the same corrections as for the μTPC-method would have to be applied, which compensate for effects due to the magnetic field. As the NSW will sit entirely in the end-cap toroid system the electrons produced in the drift regions of the detectors will also face Lorentz-force when drifting towards the anode. As the magnetic field reaches values of 0.3 T inside the detectors and will be far from homogeneous, as it can be seen in a magnetic field map of the end-cap toroid at the position of NSW in figure 6.35, this has varying implications for different positions inside the detector, based on the altered electron drift velocity (see also section 2.4.1). This is illustrated in figures 6.36(a) and 6.36(b) for the trajectories of primary electrons originating from muons with track inclination of 30° simulated for two different orientations of a magnetic field with respect to a homogeneous $E_Z = E_{drift} =$600 V cm^{-1}. Here two cases are shown with a magnetic field of $|B| =$0.3 T parallel and anti-parallel to strips pointing in the Y-direction, which alters the trajectory of the electrons, which in the absence of this field would follow the electric field.

This leads to two possible configurations where the angle which is defined by the drift direction of the electrons and the initial particle track is either smaller or larger than the track inclination θ. In the latter case, which is shown in figure 6.36(a) and here referred to as the de-focusing configuration, the apparent track-length on the read-out plane is increased. By application of the μTPC-method a larger apparent angle θ' would be reconstructed, whereas in the focusing configuration in figure 6.36(b) a smaller angle would be reconstructed. Knowing the Lorentz angle α the apparent angle can be described by:

$$\tan \theta' = \cos \alpha \left(\tan \theta + \tan \alpha \right) \tag{6.14}$$

This assumes an unaltered electron drift-velocity of the electrons, which is reasonable as the drift-velocity of the electrons is only slightly affected by the magnetic field as it was already shown in figure 2.13(a). The Lorentz angle on the other hand will be depending on the actual position of a hit within the NSW, as it is depending on the absolute value of the magnetic field perpendicular to the electric field:

$$x'_{\mu TPC} = x_{\mu TPC} + \left(Z - \frac{1}{2} \cos \alpha \right) \left(\tan \theta - \tan \alpha \right) - Z \left(\frac{1}{2} \tan \theta + \tan \alpha \right) \tag{6.15}$$

A similar problem will arise for the application of the timing corrected centroid method, but it can
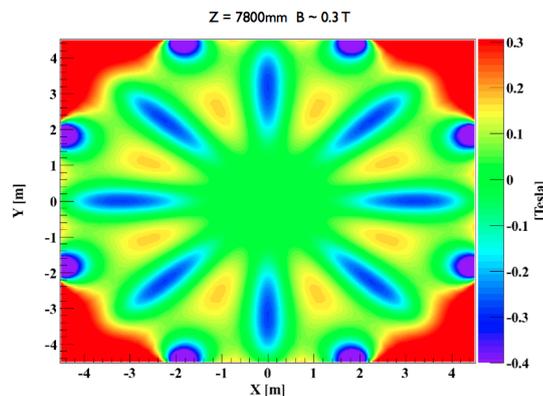

Figure 6.35: Magnetic field map of the ATLAS end-cap toroid at the position of the NSW [Iengo and Alexopoulos, 2014]
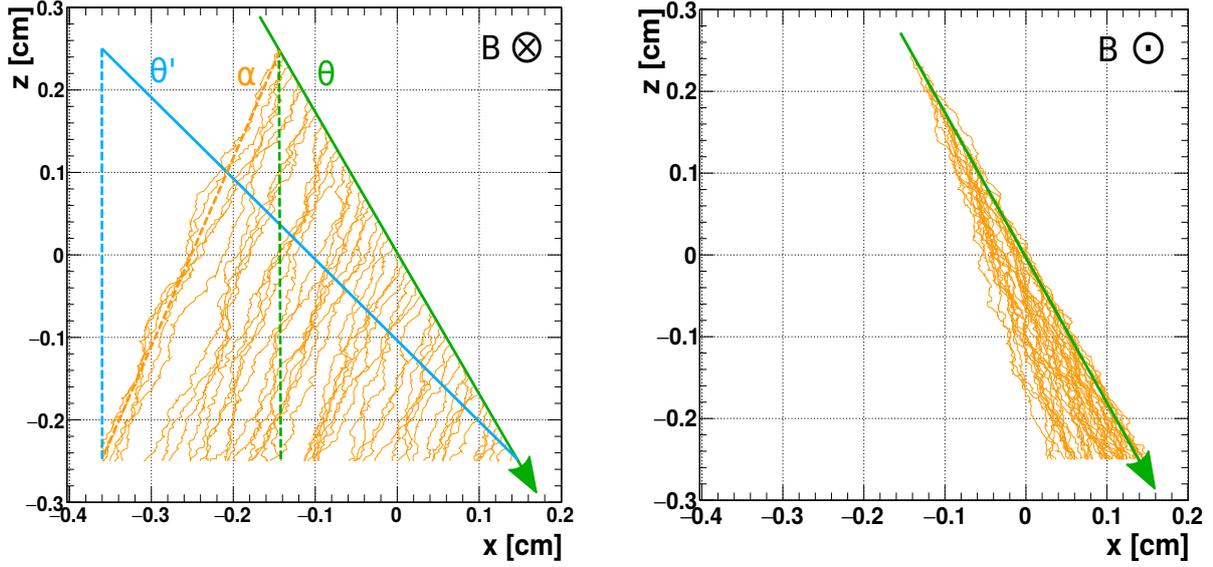
(a) Defocusing magnet field configuration: Due to the Lorentz-force evoked by a magnetic field of 0.3 T perpendicular to an electric field E_{drift} =600 V cm^{-1} the primary electrons originating in a muon track are spread out further on the read-out plane than the projected track length would be.

(b) Focusing magnet field configuration: The effective drift direction of the electrons due to a magnetic field is closer to the direction of the initial traversing particle and the resulting cluster size at the read-out anode is reduced.

Figure 6.36

also be corrected in the same fashion:

$$x'_{timing} = x_{timing} - \tan \alpha \left(\frac{Z}{2 \cos \alpha} + (t - t_{mid}) v_D \right) \tag{6.16}$$

For the µTPC-method it is foreseen to have a look-up table for the corresponding values of α at every detector position, which would also allow the application of the timing correction. Here still the prerequisite of knowing real track inclination θ remains in order to allow for this correction. The range of different effective track inclinations a single quadruplet will see in the NSW is limited to ±5–10° –depending on the magnetic field– around the mean angle of the respective segment. For the longer SM1 and LM1 this will lead to effective inclinations of $(15 \pm 8)°$ and for the shorter but wider SM2 and LM2 to distributions of angles of $(25 \pm 5)°$. Due to the limited possible track angle a fixed track inclination might be assumed if only a single layer is considered and no further track information would be provided. For a real angle of 30° and a correction of the centroid position with an assumed angle of 25°, which for SM2 would geometrically be the worst case scenario, this leads only to a degradation of the position resolution of (19 ± 10) µm, determined by the core and weighted width of a double Gaussian fit, as it can be seen in figure 6.37 for E_{drift} =300 V cm^{-1}.

This shows that already a calibration for a fixed angle within ±5° of the real angle with known electron drift velocity shows a resolution improvement close to the optimum reconstruction quality possible by this method. The multilayer design of the detectors however would allow to utilize an angular dependent reconstruction algorithm, where the information on the track inclination is extracted from the coarse position information determined by the centroid method from the other layers. An example for this approach can be seen in figure 6.38 for the residual distribution of the eta$_{in}$-layer for an inclination of 30° and E_{drift} =300 V cm^{-1}. Using the inclination measured by the other layers a spatial resolution of $\sigma_{weighted}$ =(230 ± 20) µm (σ_{core} =(140 ± 10) µm) was observed, which shows, that this approach in general is useful. The slightly lower resolution and the significant reduction in statistics here compared to the case, where a fixed inclination was assumed, can be explained by mis-match of events in the stereo-layers.
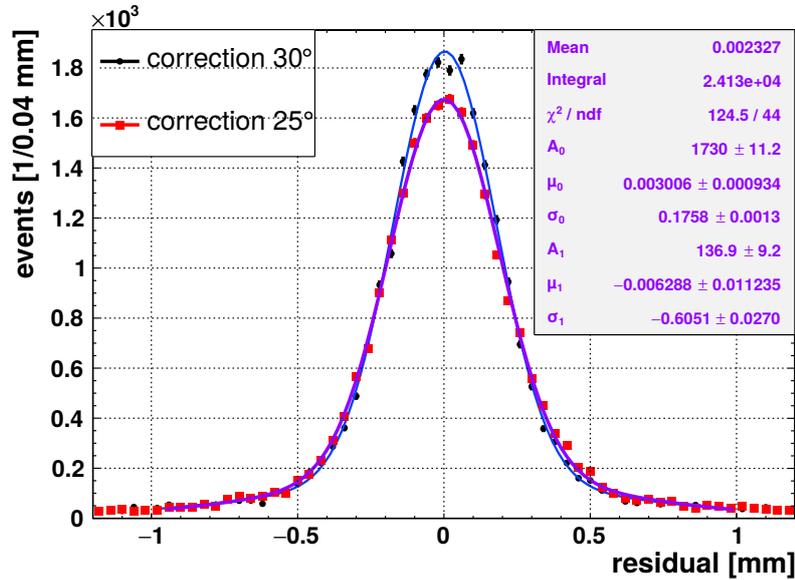
Figure 6.37: Comparison of the residual distributions of the eta_{in}-layer for a nominal inclination of $30°$ and $E_{drift} = 300\,\mathrm{V\,cm^{-1}}$ after timing-correction for the angles of $25°$ and $30°$. A mis-estimation of the inclination angle of $5°$ in this case changes impaired the position resolution by $(19 \pm 10)\,\mu m$.
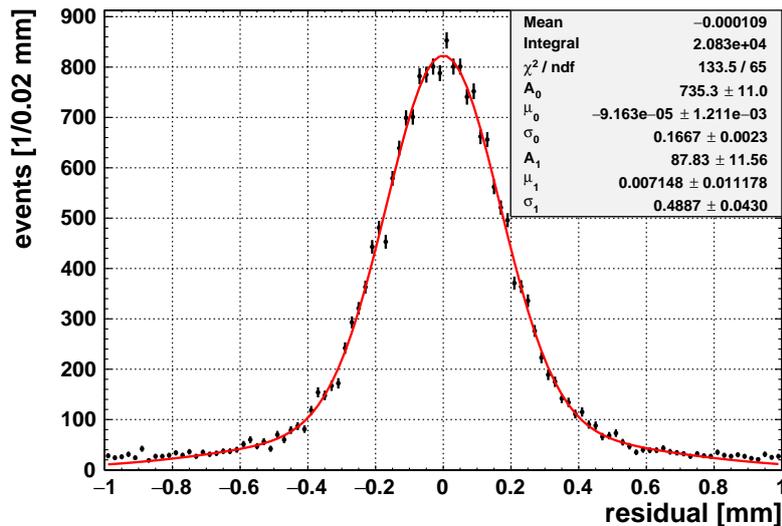

Figure 6.38: Residual distribution in the eta_{in}-layer for a nominal inclination of $30°$ and $E_{drift} = 300\,\mathrm{V\,cm^{-1}}$ after time correction of the centroid by measuring the inclination in three quadruplet-layers. A spatial resolution of $\sigma_{weighted} = (230 \pm 20)\,\mu m$ was observed.

6.7 Reconstruction Efficiency

As described before a high reconstruction efficiency with only very limited areas of reduced performance can be tolerated for the single layers in the NSW. The reconstruction efficiency is mostly depending on two distinct parameters: The quality of the detector, especially the read-out boards, where missing strips or local unevenness might decrease the visibility of particles traversing the detector, and second also the chosen reconstruction method, where also the necessary spatial resolution has to be considered. The reconstruction efficiency hence has been determined by the fraction of clusters found within $\pm 5\,$mm of the track prediction, divided by the total amount of good tracks found by the telescope, which was defined by a $\chi^2/$NDF<1.5 of the linear fit to the refernce track.

As the size of a recorded cluster depends on the track inclination, the diffusion of the electron cloud and lastly also on the amplification a good method to determine the lower limit of the reconstruction efficiency was to minimize the diffusion and to scan through different amplification voltages for the un-tilted detector. At the example of the edge between two read-out boards, where due to the production process for this prototype multiple strips were cut away, this turn-on behavior of the efficiency can be seen. This is shown in figure 6.39(a) for all layers with $E_{drift} = 600\,$V cm^{-1}. The two layers performing best, eta$_{in}$ and stereo$_{in}$, actually had only single strips missing, meaning no two neighboring strips were disconnected, and by exploiting the minimal cluster size due to diffusion achieved a reconstruction efficiency of above 95 %. In both cases these non-connected strips covered space containing more than 8 % of the total number of recorded tracks, which was determined by the track reference. The low reconstruction efficiency at this specific beam position at the eta$_{out}$-layer is caused by a larger amount of missing strips at the junction between two read-out boards corresponding to an acceptance loss of 18 %. The critical point is that a larger gap of in total 7 strips could not be used leading to an effective dead area with 2 mm width along the full breadth of the detector. This can also be seen in the residual distribution for this layer in figure 6.39(b) around x=$-6\,$mm, which is plotted against the position in the detector for this layer at an amplification voltage of 570 V cm^{-1}. A much more serious effect on the reconstruction efficiency however is only faintly visible in this plot. It becomes apparent in figure 6.39(c), as this can only explain a lowered maximum reconstruction efficiency, but not a steeper turn-on curve compared to the other layers. In order to find local spots of low reconstruction efficiency a grid with 1 cm edge length was used for this. A clear drop in the efficiency without the total loss in position information was observed. This locally low efficiency can be caused by production flaws of this prototype detector, for example by unconnected resistive strips, which were already found in the quality-control procedure before the assembly of the detector in one of the stereo-layers and would lead to an undefined electric field at this position. Another cause of inefficient spots would be local thickness variations of the board, which would lead to an increased distance between the mesh and the read-out structure and therefore a lower amplification.

The map in figure 6.39(d), where the mean cluster charge for the same partitions is shown, indicates that this might have happened in this region. A locally decreased pulse-height was observed in the same region, where the efficiency dropped. This was most likely caused by a local deformation in the read-out panel, which led to an increased distance between the micromesh and the anode.

The influence of the reconstruction method on the reconstruction efficiency mainly has to be considered for the application of the µTPC-method, as a faulty reconstruction potentially spoils the spatial information more than the other methods.

This was investigated at a position, where all layers showed a high and homogeneous efficiency at the center of the module. At the same position also all measurements shown in section 6.5 were done. In figure 6.40(a-c) exemplarily the results for layer eta$_{in}$ are shown, but the other layers performed equally well at this position.

As reference the reconstruction efficiency at perpendicularly incident was used, which for this region again is shown in partitions in figure 6.40(a) for $E_{drift} = 300\,$V cm^{-1}, as this allowed the highest spatial resolution. In this region an overall detection efficiency of 94.3 % with a RMS of
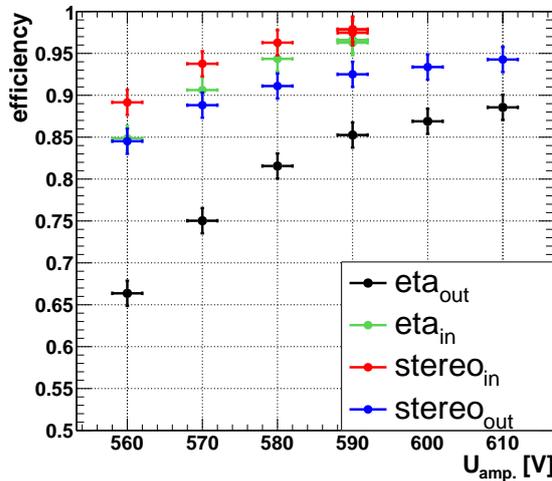
(a) The reconstruction efficiency, which was determined for perpendicularly incident muons with $E_{drift} = 600\,\mathrm{V\,cm}^{-1}$ by means of the centroid method.
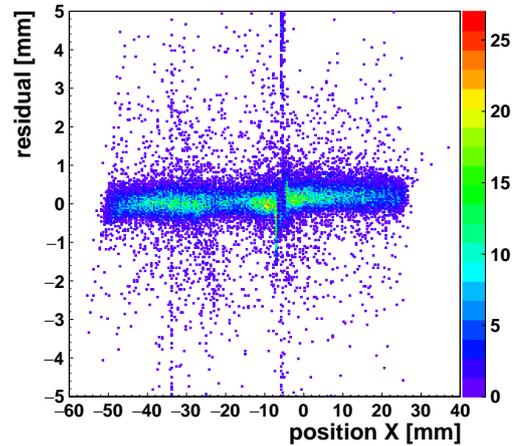
(b) 7 missing strips at the junction between two read-out-boards are visible in the residual distribution plotted against the position in the detector, here shown for the eta$_{\text{out}}$-layer which partly explains the low reconstruction efficiency.
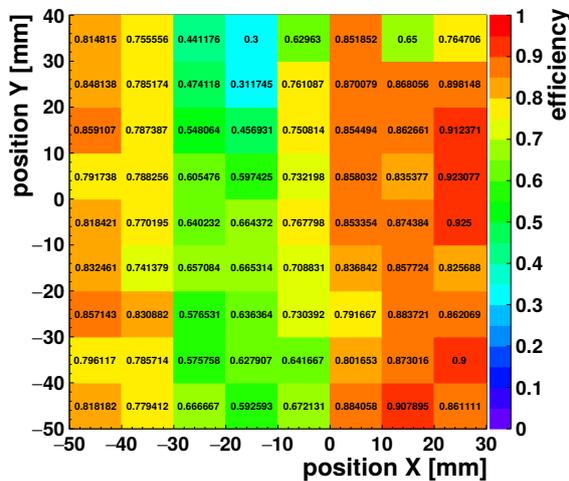
(c) The reconstruction efficiency determined for $1\,\mathrm{cm} \times 1\,\mathrm{cm}$ partitions reveals a band in y at $x \approx -20\,\mathrm{mm}$ of locally lower efficiency, which is not correlated to badly connected or missing strips.
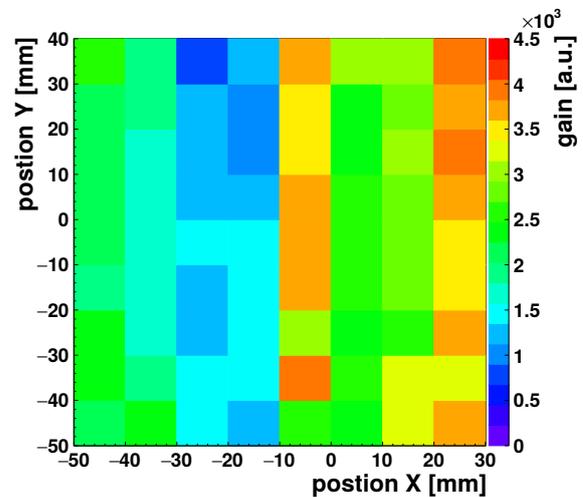
(d) In the same region also the mean pulse-height is significantly lower, which is a strong indicator, that here a local non uniformity of the read-out board causes lower amplification -most likely due to an increased distance between the micromesh and the anode.

Figure 6.39
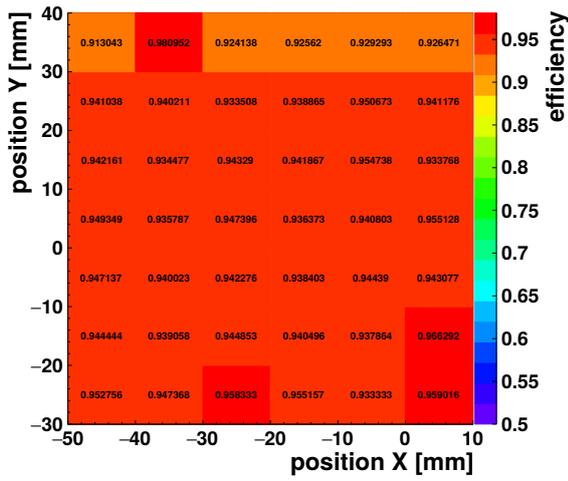
(a) Reconstruction efficiency for perpendicularly incident muons, determined by the centroid method
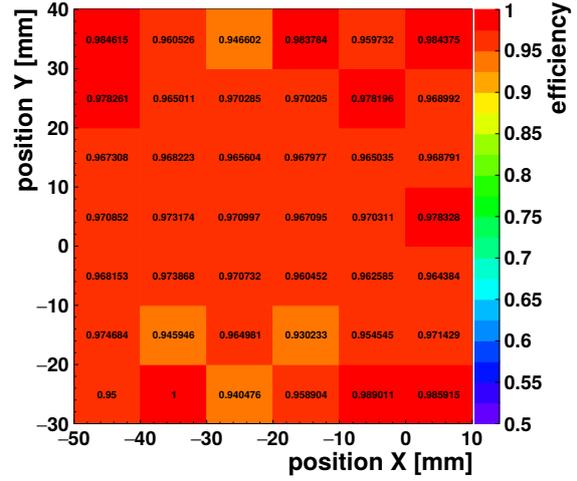
(b) Reconstruction efficiency for an inclination of 30°, determined by the timing corrected centroid-method
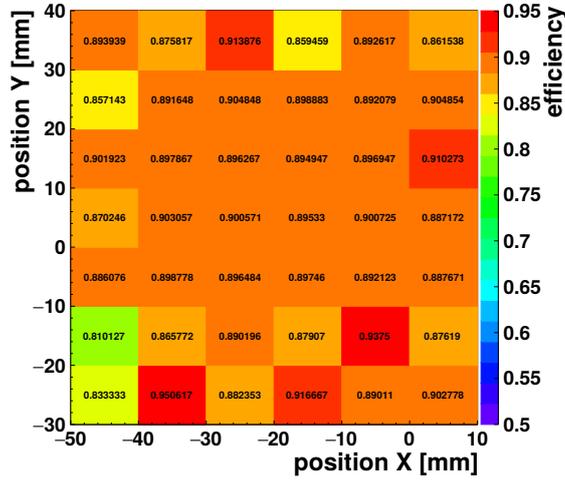
(c) Reconstruction efficiency for an inclination of 30° determined by the μTPC-method

Figure 6.40: Efficiency maps for a $7\,\text{cm} \times 6\,\text{cm}$ section of the center of the eta_in-layer, using U_A=605 V and E_{drift} =300 V cm^{-1}

1.0 % was achieved. The slight difference of the efficiency compared to figure 6.39(a) is due to the selection of the detector region, where every partition has to have at least 100 hits also for the measurements with a tilted detector. Under an inclination of 30° by means of the reconstruction with the timing corrected centroid due to the larger clusters even an increase in the efficiency up to 96.8 % (RMS=1.8 %) could be achieved as it can be seen in figure 6.40(b). The μTPC-method on the other hand showed some non-negligible lower efficiency, due to the necessary cut on the χ^2/NDF for the μTPC-fit. This led to a quasi homogeneous drop in the reconstruction efficiency by about 9 % to only 88.1 % (RMS=3.6 %) for the same measurement, which is shown in figure 6.40(c).

Chapter 7

Performance of a GEM-detector under High Rate Ion Irradiation at the Heidelberg Ion Therapy Center

The Heidelberg Ion Therapy center (HIT) [Haberer et al., 2004] is a cancer treatment facility based at the Heidelberg University Hospital. The concept of cancer treatment with ions is based on the specific energy loss of charged particles in matter depending on their energy. Following the Bethe-Bloch-equation (see section 2.1), the energy loss increases drastically with lower energy. This effect can be used to deposit a high amount of energy in a very confined region in matter, the so called Bragg-peak. The energy loss of ions at higher energy is much lower, which is exploited in cancer treatment to deliver high energy to damage cancer cells but spare the surrounding healthy tissue. The energy of a beam can be tuned to target a tumor with the Bragg-peak, which minimizes the damage to the tissue in front of the tumor. The width of the Bragg-peak itself is depending on the particles used. Often protons with an energy between 40–230 MeV or carbon ions with an energy of 80–440 MeV u^{-1} are used, which correspond to a range of these particles in water of up to 30 cm. The energy depth-dose distributions for these two different particle types in figure 7.1 show the general advantage of heavy ions over protons for this purpose. Here the relative energy loss of ^{12}C-ions of 440 MeV u^{-1} and protons of 230 MeV is shown in water, based on a Geant4 simulation. Although both particle types have roughly the same range the carbon-ions exhibit a much more pronounced peak and a significantly lower relative energy loss in front of this maximum, which allows to spare healthy tissue surrounding a tumor. In both cases this leads to a very well defined range of the particles, with Gaussian shaped range fluctuations of only (1.0 ± 0.1) mm for the carbon ions compared to a width of the peak of (3.3 ± 0.1) mm for the protons. The strong confinement of the maximum of the energy deposition on the other hand requires not only a precise knowledge of the actual dimensions and location of a tumor, but also an extremely well beam handling in order to spare healthy tissue. Thin MPGDs offer the possibility to provide a high resolution in-line beam monitoring and micromegas detectors have already proven to be capable of coping with the high particle fluxes in an irradiation scenario [Bortfeldt, 2014]. In this chapter a triple GEM-detector will be tested in order to determine its suitability to provide a single particle reference even at these high particles rates.
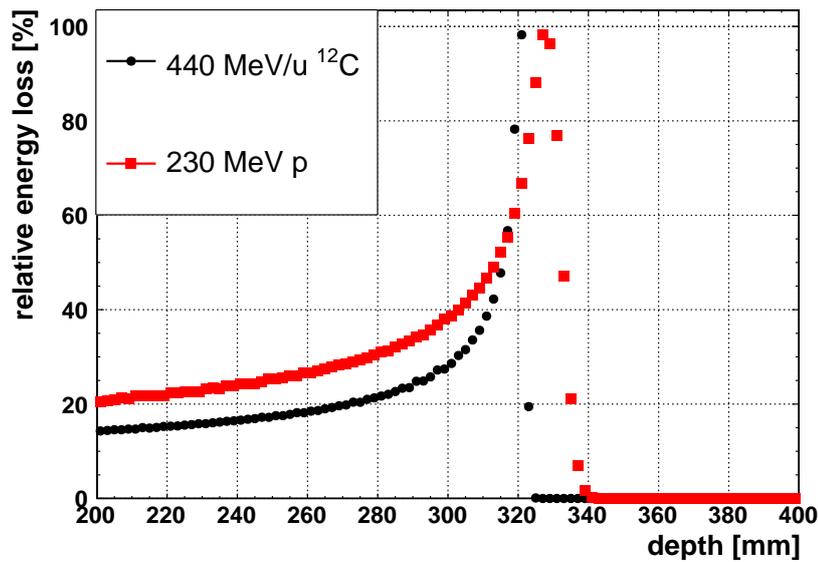
Figure 7.1: Geant4 energy loss simulation of protons with an initial energy of 230 MeV and ^{12}C-ions with an initial energy of 440 MeV u^{-1} in water

7.1 Experimental Set-Up

The HIT irradiation facility is designed for very high particle rates in order to minimize the treatment times for the patients and offered the possibility to test a small GEM-detector under these extreme particle rates. The quality of the position reconstruction was determined by a beam telescope as reference. The setup consisted of a total of six floating strip micromegas detectors[31] and a triple GEM-detector. The micromegas detectors were arranged in low material budget doublets. Two sets equipped with one-dimensional strip read-out were placed in the front of the GEM-detector and a set of two detectors with two-dimensional strip read-out behind it. The active size of the micromegas detectors was 6.4 cm × 6.4 cm with a strip pitch of 0.5 mm. The micromegas detectors used a drift gap of 6 mm width and the GEM detector a drift gap of 5 mm with a drift field E_{drift} =600 V cm^{-1}. In the GEM detector the standard Ar-CO$_2$ 93:7 Vol.% gas mixture was used, whereas the micromegas detectors were filled with a faster counting gas mixture of Ne-CF$_4$ 84:16 Vol.%. A trigger was provided by a coincident signal of two scintillators behind the setup. The full arrangement can be seen in figure 7.2. The micromegas set-up and their performance are also described in [Bortfeldt et al., 2017] and [Magallanes, 2017]. Although the accelerator was capable of tuning the energy of protons in the range between 48–220 MeV and for carbon ions between 88–430 MeV u^{-1}, the measurements shown were limited to the evaluation of the detector performance under irradiation with a carbon beam of 88 MeV u^{-1}. The need of low material budget detectors was driven by the non-negligible multiple scattering of the ions in matter. The overall printed-circuit-board equivalent thickness of the whole system was as low as 3.2 mm with the largest contribution of 2 mm actually coming from the read-out anode of the GEM detector. The nominal energy loss in the whole set-up was simulated for carbon ions to be 42 MeV, which was lower than 4 % of the total energy of the particles. The accelerator provided beam in spills of 5 s length and subsequent pauses of 4–5 s. The spills were subdivided in bunches with a nominal spacing of about 200 ns depending on the beam energy [Schoemers et al., 2015, Bortfeldt, 2014].

---

[31]Floating strip here means a discharge protection scheme for high rate irradiation, the detectors are described in [Bortfeldt, 2014] and [Klitzner, 2016]
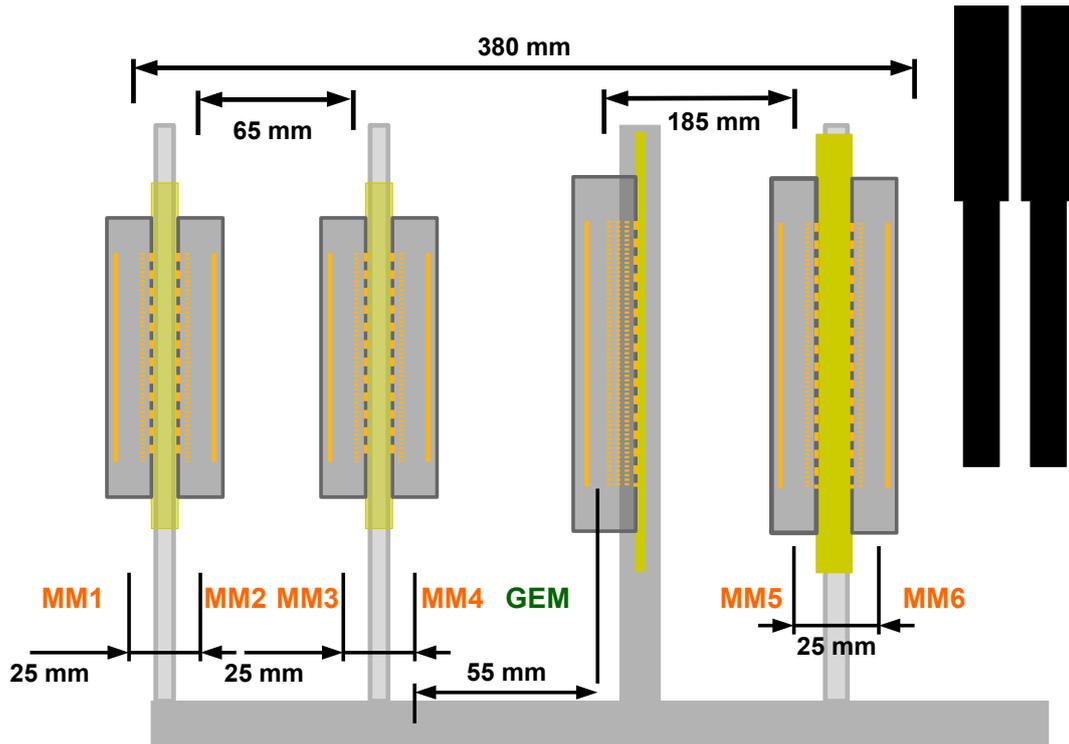
Figure 7.2: Experimental set-up with two doublets of floating strip detectors with 1D-strip read-out in front of the GEM-detector and a doublet of micromegas with 2D strip read-out behind it. The whole set-up was triggered by the coincident signal of two scintillators behind the system.

7.2 High Rate Performance of a GEM detector

Rate tests with carbon ions were carried out in the range of 2–50 MHz spread over a Gaussian shaped beam profile with a Full Width Half Maximum of 13.4 mm. Over the full beam-spot this was equivalent to a mean particle flux of 2.2–54 kHz mm^{-2}.

The high particle flux through the detectors made the use of a track selection algorithm necessary. In all earlier chapters the particle flux through the detectors was sufficiently low, that the probability of having more than one particle at a time could be neglected and tracks could be built from the single clusters in multiple detectors. In the case described a much higher amount of clusters was reconstructed in all detector layers, which had to be matched to actual particle tracks. This can be seen in an event display for a nominal particle flux of 2 MHz in figure 7.3(a) for the GEM-detector and for the hit distribution of the event in figure 7.3(b). Here an event in the GEM-detector is shown, where ten ions hit the detector nearly simultaneously.

Similar to the strip selection described in section 2.7.4 this was done by a Radon-transform, which allowed to find straight tracks through all detectors. This selection led to a reconstruction of up to 12 tracks in all detectors and is explained in more detail in appendix C. A simulation showed that the implementation chosen for the reconstruction was rather stable in terms of reconstruction efficiency and falsely reconstructed tracks. Depending on the number of particles in the detector, tracks, which led to charge clusters in all detectors, should be reconstructed with an efficiency higher than 75 % (also explained in appendix C).

In a first iteration this led to a residual hit distributions for the GEM-detector, as shown in figure 7.4(a). The distance between the position of the cluster closest to the track and the position defined by the reference track is plotted. The narrow centered peak resembles well separated tracks in the GEM-detector, which could be assigned to a track in the reference system, but on the other hand also a large underlying bulge with a width of about 2 mm was observed. Analysis of the events causing this large deviation from the prediction revealed events, where multiple particles were combined to a single charge cluster. The minimal cluster size due to diffusion (see section 2.4.2) meant, that two particles, which traversed the detector within a trigger window of 600 ns
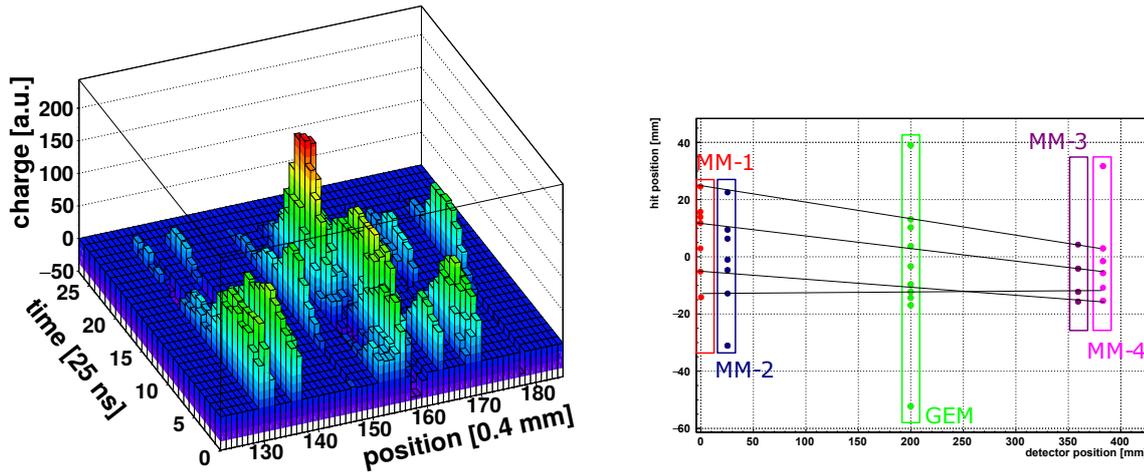
(a) Event display for a spill of 10 particles, which passed the GEM-detector nearly simultaneously

(b) Multiple hits could be assigned to single particles by finding tracks in all detector layers by a Radon-transform, which allowed in the case shown the reconstruction of four tracks in all detectors with a read-out in X-direction.

Figure 7.3

and a distance below 1.4 mm in the read-out direction could not be resolved. This could partly be overcome by an alternative clustering algorithm, which made use of the timing of traversing particles. Proceeding from the time-position-charge distribution local charge maxima were selected and clusters were built from them by the following criteria:

- A local maximum was used as seed, if no other local maximum was found within a distance of $\pm$ ten time-bins along a strip[32] and in the region of $\pm$ four strips and $\pm$ two time-bins around the maximum

- If the two neighboring strips showed also a peak in the region of the local maximum within $\pm$ two time-bins the strips were merged to a cluster

- Gaps in a cluster were not allowed

- If the charge of a local cluster exceeded 100 ADC-counts also single strip clusters were allowed

Local maxima in the time-position-charge distribution of an event were calculated by a peak finding algorithm according to [Morháč, 2015]. The peak finding and the cluster selection is exemplarily show in figure 7.4(c) together with the initial extent of the clusters defined by the recipe from section 2.7.2. In the example shown every initial cluster was subdivided into two new clusters by this selection.

Using this localized clustering algorithm multiple hits within close distance could be well resolved and the residual distribution could be definitively enhanced, as it can be seen in figure 7.4(b). In both cases shown a cut on the quality of the reference tracks was applied by the requirement of $\chi^2/\text{NDF}<1.5$ for the line fit to the clusters in the micromegas detectors.

The residual distributions shown both correspond to a nominal particle rate of 3 MHz and were fitted with a double Gaussian distribution. The micromegas detectors used in this system were tested also for the first time under these conditions and therefore their spatial resolution in this setup was a-priori unknown. An estimation of the spatial resolution for the GEM-detector was therefore done by the method described in [Carnegie et al., 2005], where the spatial resolution of a detector in a system is determined by the residual distributions in the two cases, where the detector under test once is included in the track fit and once excluded from the fit. From the widths of both

---

[32]This was motivated by the electron drift time in the drift region of about 100 ns and the bunch spacing of 200 ns
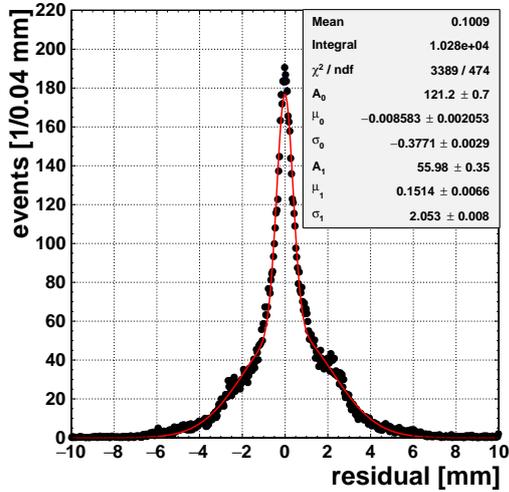
(a) The residual distribution of the GEM-detector for a nominal particle rate of 2 MHz with the standard clustering algorithm shows a dominant underlying contribution of mis-assigned tracks.
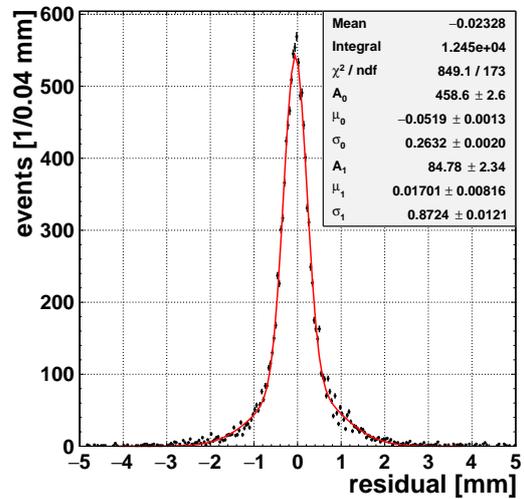
(b) Application of a clustering algorithm taking into account also particle timing reduced mis-reconstruction due to combining particles, which traversed the detector close to each other.
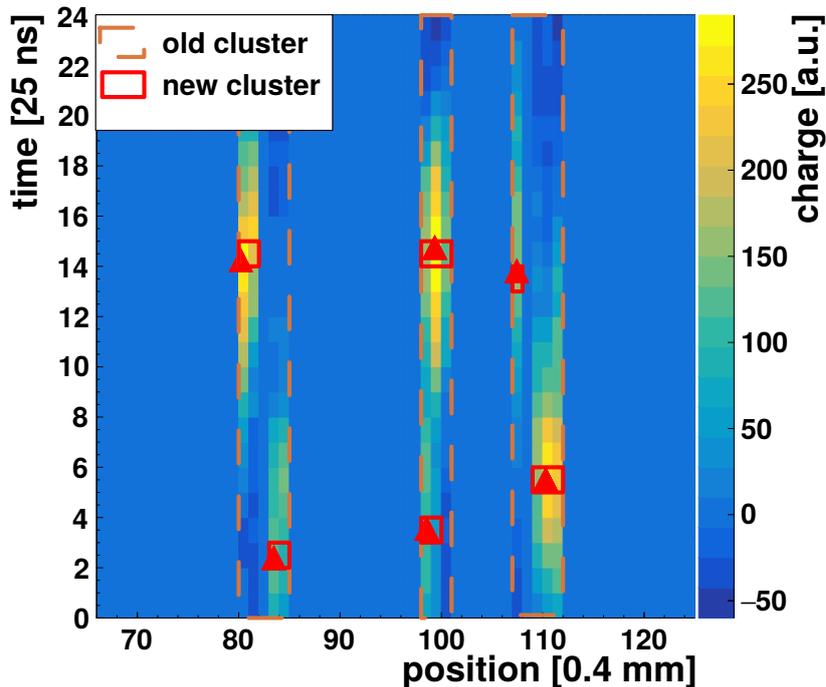
(c) Example of both clustering algorithms: Strips, which were combined to clusters with the standard algorithm are enclosed by dashed orange rectangles. Clusters, determined by the modified algorithm, are enclosed by red rectangles close to local maxima marked by triangles. In this example all three original clusters were split into two new clusters.

Figure 7.4
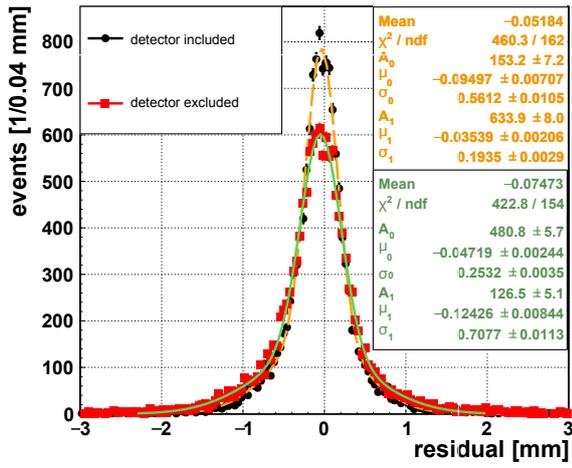
(a) For the determination of the spatial resolution a geometric method was used, which determines the detector resolution from the residual distribution with the detector included in the track fit and excluded from the track fit. Both distributions fitted with a double Gaussian for a particle rate of 3 MHz of ^{12}C-ions are shown.
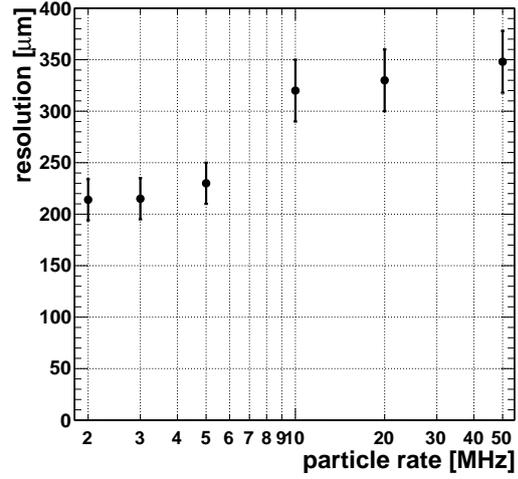
(b) The spatial resolution for ^{12}C-ions of 88.8 MeV u^{-1} degrades with the particle rate. The resolution features two distinct plateaus of $(220 \pm 9)\,\mu m$ for particle rates below 5 MHz and $(332 \pm 14)\,\mu m$ for rates above 10 MHz.

Figure 7.5

distributions the detector intrinsic resolution can be obtained by[33]:

$$\sigma_{det} = \sqrt{\sigma_{incl.} \cdot \sigma_{excl.}} \qquad (7.1)$$

Both residual distribution for the GEM-detector, included and excluded from the track fit, are shown in figure 7.5(a) for a particle rate of 3 MHz together with a fit of a double Gaussian. Considering only the narrow part of the distribution a spatial resolution of $\sigma_{det} = \sqrt{253 \cdot 194}\,\mu m = (220 \pm 20)\,\mu m$ could be achieved. This confinement to the narrow contribution of the fit is justified by the non-negligible multiple scattering of the ions in the read-out anode of the GEM-detector. For higher particle rates the spatial resolution of this GEM-detector degrades, as it can be seen in figure 7.5(b). For the highest rate of 50 MHz a spatial resolution of $(350 \pm 30)\,\mu m$ was still achievable. This degradation in spatial resolution might be caused by an imperfect selection of track due to the higher amount of particles in every cluster.

The number of detected tracks however was not well suited to determine the mean number of particles in a single event, as the size of the GEM and micromegas detectors considerably differed and the overall detection efficiency of the prototype micromegas detectors was rather low. On the other hand also overlap of clusters from single particles due to lateral diffusion had to be considered, which also means that the number of found clusters in a single detector was not well suited to determine the number of particles. Since the energy loss of the particles on the other hand was well defined the total collected charge in the GEM-detector was a good indicator for the actual number of particles in every event, as it can be seen for a measurement with the lowest nominal particle rate in figure 7.6(a). The total charge of all clusters found in the GEM-detector is plotted, and three pronounced equidistant peaks can be observed here. These can be understood as probability distribution of events with one, two or three particles. Assuming a well defined Gaussian energy loss for a single particle this distribution can be parametrized by:

$$f = \sum_{n=1}^{N} A_n \cdot e^{\left(-\frac{1}{2}\left(\frac{q - q_0 \cdot n}{\sqrt{n}\sigma_q}\right)^2\right)} \qquad (7.2)$$

---

[33]Here identical spatial resolution of all detectors is assumed. In fact the spatial resolutions of the micromegas detectors was similar, which justified this (see [Klitzner, 2016]).

Table 7.1: Dependence of mean number of reconstructed tracks in the telescope and mean occupancy $\bar{N}$ in the GEM on the particle rate

particle rate [MHz]	mean number of reconstructed tracks	particles in detector $\bar{N}$
2	2.3	2.4
3	2.4	2.7
5	2.3	3.1
10	2.3	5.4
20	2.3	5.4
50	2.2	7.8

With a mean energy loss of a single particle of q_0, a width of the charge distribution for a single particle of σ_q and a maximum of N particles. The mean particle occupancy of the detector $\bar{N}$ than can be be described by:

$$\bar{N} = \frac{\sum_{n=1}^{N} A_n n}{\sum_{n=1}^{N} A_n} \tag{7.3}$$

In this case a mean number of particles in the detector of 2.4 could be reconstructed. For all different particle rates the number of particles in the detector for every trigger is shown in table 7.1. It is notable that higher particle rates in this context not necessarily meant an increased occupancy of strips for every trigger, as for the lower rates not all bunches were filled. This can be seen from the reconstructed timing of the clusters in figure 7.6(b) for particle rates of 2 MHz and 50 MHz. In both distributions three distinct peaks are visible, which correspond to particles from a single trigger. This shows, that particles of up to three different bunches were recorded within a single trigger. For the lower rate still mostly a single bunch was reconstructed, whereas for the higher rate the contribution from the two later bunches significantly increases. This leads to a distribution in the number of particles in the bunch triggered on depending on the particle rate as shown in figure 7.6(c) and shows a similar behaviour than the mean number of particles in the detector $\bar{N}$. Considering this allows to explain the step-like degradation in spatial resolution as from the minimal cluster size in the detector $d \approx 1.4$ mm it would not be expected to resolve more than 4 particles within the confinement of the beam.

Albeit using X,Y strip read-out is not the best option for high rate applications, this showed that also a GEM-detector, which due to the much larger dimensions of the amplification and transport regions suffers from higher lateral diffusion and a much longer electron life-time in the detector, can be operated at these high fluxes and still delivers good spatial information, which however is slightly degrading with increasing particle rates.
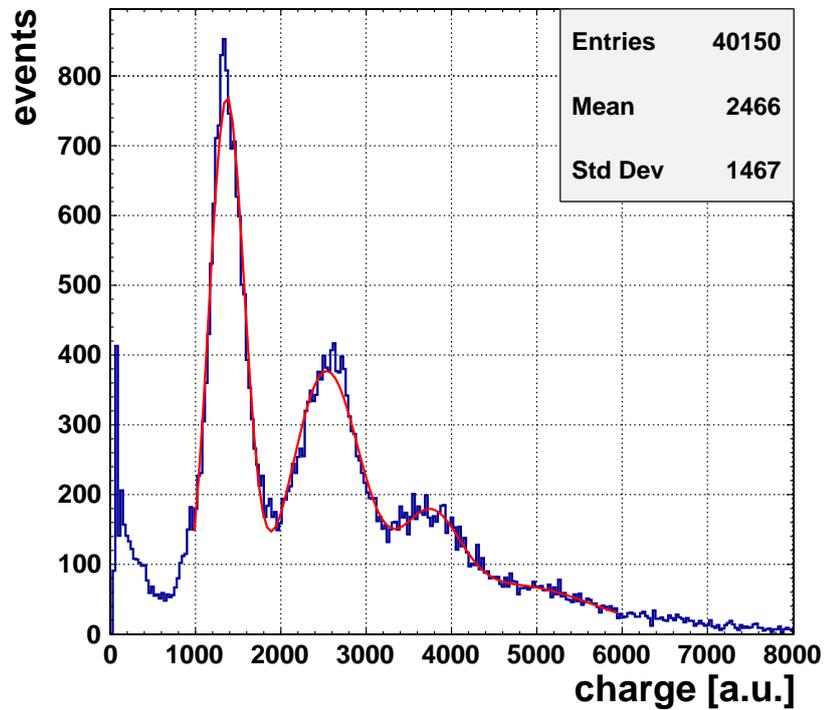
(a) In the total energy spectrum, i.e. the total charge deposited per triggered event, clear peaks are visible for a particle flux of 2 MHz. The peaks correspond to the number of particles being simultaneously in the detector. The evaluation of this spectrum allowed to reconstruct the actual number of particles in the detector for every trigger.
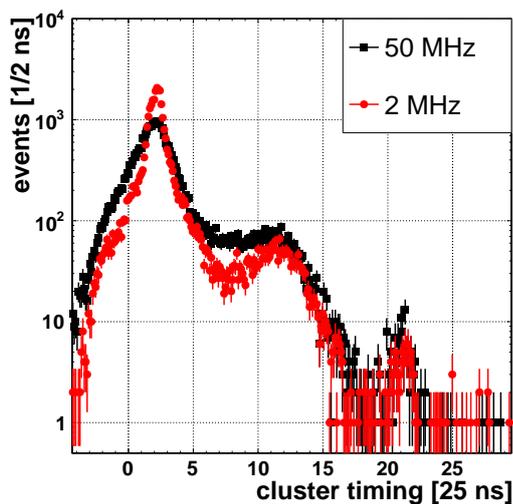
(b) In the cluster timing distributions for 2 MHz and 50 MHz tree peaks, corresponding to different bunches were observed. A distinctive shift with the increase of the particle rate is visible, which can be explained by the higher number of filled bunches.
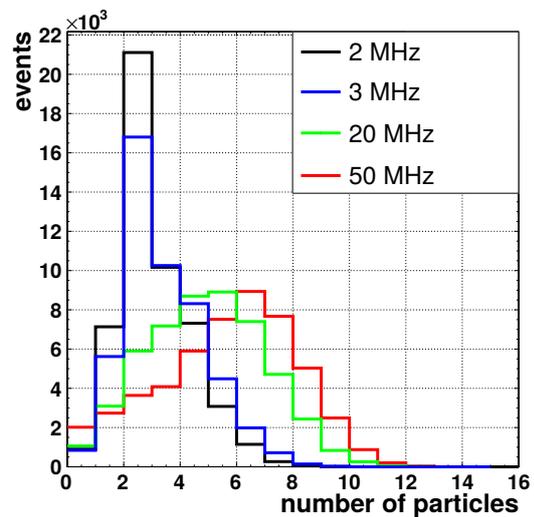
(c) Mean number of particles in triggered bunch for 2 MHz, 3 MHz, 20 MHz and 50 MHz particle rate.

Figure 7.6

Chapter 8

Summary

Tracking of charged particles in Micro-Pattern Gaseous Detectors (MPGDs) allows for a strongly increased position determination compared to standard methods by application of TPC-like reconstruction techniques. In this thesis different methods for position reconstruction are presented, which take into account the energy deposition along the tracks of charged particles in the active volume of planar gaseous detectors. The methods are developed and applied on two different kinds of MPGDs, small size **G**aseous **E**lectron **M**ultiplier detectors (GEM) with an active detector region of $10\,\text{cm} \times 10\,\text{cm}$ and a large scale **Microme**sh **Ga**seous **S**tructure detector (Micromegas) with an active area of $2\,\text{m}^2$. Both detector systems share their general construction with a planar active volume of 5–8 mm width, the electron drift region, a subsequent electron amplification stage and a highly segmented strip read-out. Charged particles ionize the counting gas in the active volume and electrons drift then guided by electric fields towards the amplification region. In the case of the GEM detector this region is made from one or more copper-clad insulating films with etched micro-structured holes. High electric fields in these holes cause amplification of the electrons due to a moderate voltage difference between both sides of these films. For the same purpose in micromegas detectors micromeshes are utilized, which define a region of high electric field together with a read-out anode. Using a time resolving read-out makes it possible to reconstruct the path of a charged particle in the active region. By measuring the drift time differences of electrons their point of creation can be determined similar as in Time-Projection-Chambers (TPCs).

A reconstruction concept for the detection of thermal neutrons based on a GEM detector with a single neutron conversion layer is described. Tests are performed in a thermal neutron beam of 3.7 meV at the Heinz Maier-Leibnitz Zentrum (MLZ) in Garching. Tracking the products of a boron-neutron capture process, namely alpha particles and Lithium-ions, a spatial resolution of $(100 \pm 10)\,\mu\text{m}$ can be reached. This is achieved by exploiting the specific energy loss of the particles along their track, using a highly efficient tracking algorithm, which reconstructs the point of conversion of the neutron in a boron-clad cathode. Calibration of detector and gas-specific parameters for the position calculation increase the performance of this method, even though a spatial resolution of 140 µm is already achieved without any calibration. This exceeds by far the results using standard methods i.e. by determination of the center of energy deposition in the drift region (centroid-method) or by using the track information without accounting for the energy loss along the track (µTPC-method). Typical spatial resolutions are $(1.5 \pm 0.1)\,\text{mm}$ for the centroid-method and $(590 \pm 20)\,\mu\text{m}$ for the µTPC-method. In the set-up a single ^{10}B conversion layer of 2 µm thickness is used and a detection efficiency of 5 % for the thermal neutrons is achieved. The thickness of the conversion layer is found to be optimal in terms of conversion efficiency and range of the ions in the active region of the detector.

Further improvements of the technique in terms of detection efficiency might be achieved by different approaches, which would allow to still use the same reconstruction algorithm:

- Multiple stacked GEM based converter layers – similar to the detector described in [Köhli et al., 2016]– could be used to increase the conversion probability

- The applicability of the described reconstruction method could be tested with structured

converter cathodes (see for example [Stefanescu et al., 2013]), which might increase the detection efficiency by about 50 %

In both cases the reconstruction of the point of interaction should be possible, but the influence of a more complicated cathode and converter structure on the reconstruction capabilities would need to be studied.

The tracking method is also successfully adapted for the usage with a Thick-GEM detector (TGEM). In contrast to standard GEMs, which are made of 50 µm Kapton-films, the TGEM consists of a 0.5 mm printed circuit board and has a much coarser hole distance and size of 0.8 mm and 0.5 mm, compared to 0.14 mm and 0.05 mm for the standard GEM. This granularity limits the spatial resolution by position reconstruction with standard methods. A highly increased spatial resolution of (360 ± 30) µm is achieved by tracking of 5 MeV alpha particles considering also their energy loss.

A third alternative reconstruction method is developed for tracking of minimal ionizing particles, which leave strongly clustered tracks in the active region of MPGDs. In a standard GEM set-up in a 10–150 GeV muon beam at the SPS accelerator at CERN the performance of different reconstruction methods is tested. By extrapolating the muon track from a telescope containing four small micromegas detectors the quality of the position reconstruction in the GEM is determined. For perpendicularly incident muons an excellent spatial resolution of (56 ± 8) µm for the centroid method is observed. Tests with an inclined detector under angles of $15°, 20°, 30°, 36°$ and $40°$ show a nearly linear decline of the spatial resolution. For track inclinations of $40°$ the centroid resolution degrades to 600 µm. Better spatial resolution for inclined tracks is obtained by application of the µTPC-method with spatial resolutions between 230–280 µm for angles in the range 15–$40°$. The best resolution is observed at an angle of $20°$.

An alternative reconstruction allows spatial resolutions of below 150 µm with a high efficiency, which is independent of the track inclination. The method utilizes the determination of the distance of the centroid from the read-out anode by a timing measurement based on the energy deposition and corrects the centroid position depending on the angle. The reconstruction efficiency of the timing corrected centroid method reaches (94 ± 2) %, whereas the µTPC method reaches only (80 ± 2) %. A compensation of cross-talk on read-out strips is developed, which allows to improve the track inclination reconstruction especially for steep inclination angles down to $15°$. This allows to reconstruct the track inclination with a resolution between $\sigma_\theta = 2$–$4°$. The timing resolution of the detector is shown to be dependent on the track inclination, with the best timing resolution of $\sigma_t = (4.8 \pm 0.7)$ ns for a track inclination of $40°$.

A possible application of this alternative method could be the reconstruction of muon tracks in ATLAS micromegas detectors. The increasing luminosity of the Large Hadron Collider (LHC) at CERN will make an upgrade of the forward region of the muon spectrometer of the current ATLAS detector systems necessary, which will be able cope with the background dominated hit rate of up to 15 kHz cm^{-2}. Together with sTGC detectors, small strip Thin Gap Chambers, micromegas detectors have been chosen to replace the existing end-cap Small Wheel detectors, as these will no longer be able to cope with the expected high luminosity of 0.7×10^{35}–1×10^{35} cm^{-2} s^{-1}. The micromegas detectors in the New Small Wheel (NSW) will consist of four detector layers, each with an active area of 2–3 m^2. In this thesis the performance of a first full-scale prototype in a muon test-beam is presented. For perpendicular incident a spatial resolution of (90 ± 10) µm is observed using the centroid method at detection efficiencies above 95 %.

Under inclined tracks a reconstruction efficiency of (97 ± 2) % is reached by the timing corrected centroid method and (88 ± 4) % by means of the µTPC-method. The angle resolution for a single detector layer is $\sigma_\theta = (4.0 \pm 0.4)°$ for an angle of $20°$ and $\sigma_\theta = (3.1 \pm 0.2)°$ for an angle of $30°$.

Tests with an inclined detector and using the µTPC-method show a clear separation of events: the dominant number of events can be reconstructed well with a resolution of (115 ± 10) µm for an angle of $20°$, but there is also a significant amount of events, which are reconstructed with reduced accuracy, leading therefore to a mean spatial resolution of (250 ± 25) µm. By the timing corrected centroid method a similar separation is observed, but the amount of badly reconstructed events is clearly reduced. This leads to a spatial resolution of (115 ± 10) µm for well reconstructed

events and a mean resolution of (200 ± 25) μm. In both cases a drift field dependence of the spatial resolution is observed. Best results are obtained at low electric fields due to the lower drift velocity and the limited timing resolution of the large detector.

The timing resolution of $\sigma_t = (18.6 \pm 0.1)$ ns of the prototype under an inclination of $30°$ shows to have a clear influence on the spatial resolution. Tests with the first series modules in the future will have to show, whether a decrease of E_{drift} from the design value will be necessary and feasible. Three different issues here would have to be addressed:

- Lower drift fields interfere with the rate capabilities, as these cause longer drift times and induce a higher detector occupancy

- The designated gas mixture of Ar-CO_2 exhibits a steep E_{drift} dependence of the electron drift velocity in regions with low velocity. This might lead to an increased susceptibility for variations in the width of the drift region.

- The influence on the trigger capability of these detectors has to be studied, which has especially to be re-evaluated as soon as the series NSW read-out electronics will be available.

Another possible application for MPGDs is the usage in medical physics, for example in beam-monitoring for heavy-ion tumor irradiation or ion radiography. This makes the usage of detectors necessary, which can resolve single particles up to very high rates. The high rate capability of a GEM detector with 2D strip read-out is tested in a high intensity carbon ion beam in the range between 2–50 MHz. The tests at the Heidelberg Ion Therapy Center (HIT) show, that single particles can still be separated at 50 MHz. Due to the occupancy with high rates a degradation of the spatial resolution of (220 ± 20) μm to (350 ± 30) μm is observed. This is caused by up to 8 particles traces simultaneously in the detector.

In this thesis a variety of different approaches is presented, which allows to reconstruct charged particles in MPGDs with increased accuracy. Using the track information together with the energy deposition along this track in all cases the spatial resolution and reconstruction efficiency is ameliorated. The production of NSW micromegas already started and tests with series detectors will show in the near future if the application of one of these methods will allow to fulfill the demanding requirements on spatial resolution and efficiency.

Appendix A

Cluster Size Distributions

The probability to find k electrons in a cluster along a particle track can be described by the distribution $P(k)$, which in general is depending on the counting gas. In table A.1 experimentally by [Fischle et al., 1991] determined values for the corresponding distributions are shown for three different drift gases. In all cases the most probable cluster size is a single electron, but the mean cluster sizes can vary significantly.

Table A.1: Cluster size distributions $P(k)$ in % experimentally determined by [Fischle et al., 1991]

k	Ar	CO_2	He
	65.6	72.5	76.6
2	15.0	14.0	12.5
3	6.4	4.2	4.6
4	3.5	2.2	2.0
5	2.25	1.4	1.2
6	1.55	1.0	0.75
7	1.05	0.75	0.50
8	0.81	0.55	0.36
9	0.61	0.46	0.25
10	0.49	0.38	0.19
11	0.39	0.34	0.14
12	0.30	0.28	0.10
13	0.25	0.24	0.08
14	0.20	0.20	0.0
15	0.16	0.16	0.048
16	0.12	0.12	0.043
17	0.095	0.09	0.038
18	0.075	0.064	0.034
19	0.063	0.048	0.030
>19	$(21.6/k^2)$	$(14.9/k^2)$	$(10.9/k^2)$

Appendix B

Detector Alignment with Tracks

Tracking Accuracy

One way to determine the reconstruction characteristics of a detector is to provide a track information by a reference system consisting of multiple detector layers. Together with a suitable parameterization of the track a fit to the hit positions in the reference detectors the position in the detector at test can be extrapolated.

If a reference system is used the exact positioning of the detector with respect to the reference system has to be known in order to compare the signals from the detector with a track prediction. The difference between this prediction and the reconstructed position will be called residual from now on.

This track prediction is obtained from the measurement stations $\vec{x}_i = (x_i, y_i)$ by a fit – in the assumption of a straight track represented by $y = mx + t$ – is done by calculation of:

$$\chi^2 = \sum_{i=0}^{n} \frac{(y_i - t - mx_i)^2}{\sigma_i^2}, \tag{B.1}$$

which is the sum of the squared distances of the single measurement points to the track weighted by their respective spatial resolution σ_i. The optimal track through the points is found by minimization of χ^2 with the two conditions

$$\frac{\delta\chi^2}{\delta t} = 0$$

$$\frac{\delta\chi^2}{\delta m} = 0,$$

which leads to

$$tS_1 + mS_x = \sum_{i=0}^{n} \frac{y_i}{\sigma_i^2}$$

$$m\left(S_x + S_{xx}\right) = \sum_{i=0}^{n} \frac{x_i y_i}{\sigma_i^2},$$

where:

$$S_1 = \sum_{i=0}^{n} \frac{1}{\sigma_i^2} \qquad\qquad S_{xy} = \sum_{i=0}^{n} \frac{x_i y_i}{\sigma_i^2}$$

$$S_x = \sum_{i=0}^{n} \frac{x_i}{\sigma_i^2} \qquad\qquad S_y = \sum_{i=0}^{n} \frac{y_i}{\sigma_i^2}$$

$$S_{xx} = \sum_{i=0}^{n} \frac{x_i^2}{\sigma_i^2} \qquad\qquad S_{yy} = \sum_{i=0}^{n} \frac{y_i^2}{\sigma_i^2}$$

$$D = S_1 S_{xx} - S_x^2$$
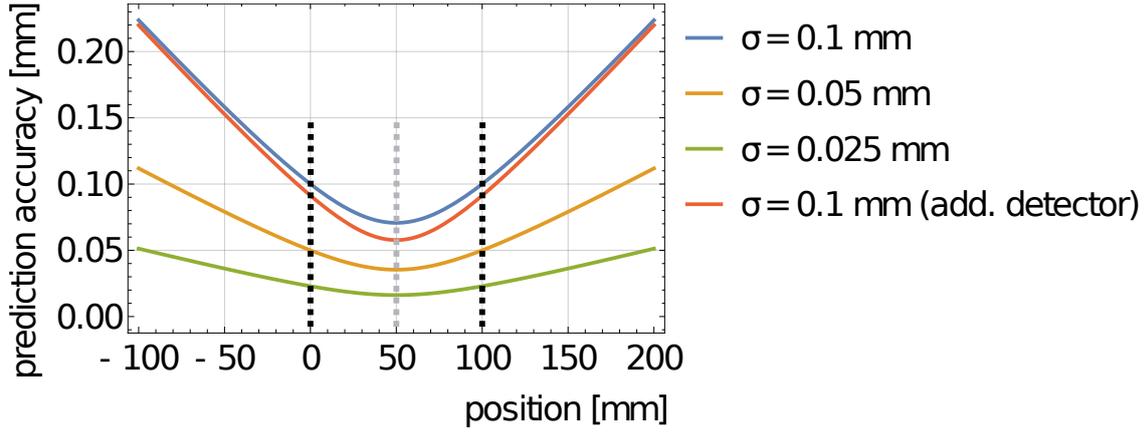
Figure B.1: From equation (B.6) calculated track prediction accuracy for two detectors placed at the positions 0 mm and 100 mm with the same spatial resolution for 0.025 mm, 0.05 mm and 0.1 mm and additionally for σ=0.1 mm if a third detector is added at 50 mm

Solving this for m and t leads to:

$$m = \frac{(S_1 S_{xy} - S_x S_y)}{D}$$

$$t = \frac{(S_y S_{xx} - S_x S_{xy})}{D} \tag{B.2}$$

The uncertainty of m and t due to the uncertainty of y_i characterized by the resolution σ_i can be described by average of the product minus the product of the averages:

$$[y_i y_k] = \langle y_i y_k \rangle - \langle y_i \rangle \langle y_k \rangle \tag{B.3}$$

$$[t^2] = \frac{S_{xx}}{D}$$

$$[m^2] = \frac{S_1}{D} \tag{B.4}$$

$$[mt] = \frac{-S_x}{D}$$

From this the track extrapolation accuracy at the origin is given by:

$$\sigma_{ex.}(0) = \sqrt{[t^2]} \tag{B.5}$$

Which can be generalized to:

$$\sigma_{ex.}(x) = \sqrt{\frac{\sum\limits_{i=0}^{n} \frac{(x_i - x)^2}{\sigma_i^2}}{\sum\limits_{i=0}^{n} \frac{1}{\sigma_i^2} \sum\limits_{i=0}^{n} \frac{(x_i - x)^2}{\sigma_i^2} - \left(\sum\limits_{i=0}^{n} \frac{x_i - x}{\sigma_i^2}\right)^2}} \tag{B.6}$$

The residual distribution is then the convolution of the track prediction accuracy and the track uncertainty due to scattered particles with the spatial resolution of the detector:

$$A(x, a_a, a_s, \mu, \sigma_a, \sigma_s, \sigma_0) = \left[a_0 e^{-\frac{1}{2}\left(\frac{x-\mu}{\sigma_0}\right)^2} \oplus a_s e^{-\frac{1}{2}\left(\frac{x-\mu}{\sigma_s}\right)^2} \right] \oplus \frac{1}{\sqrt{2\pi\sigma_a^2}} e^{-\frac{1}{2}\left(\frac{x}{\sigma_a}\right)^2} \tag{B.7}$$

Here σ_a and σ_s are the widths of the uncertainties due to the track prediction accuracy and multiple scattering of the particles, a_a and a_s are weighting coefficients for these distributions,

μ is the center of the distribution and σ_0 is the spatial resolution. The extraction of σ_0 from the residual can be done by a fit of double Gaussian function with the widths σ_1 and σ_2 and doing the deconvolution by:

$$\sigma_0 = \sqrt{\sigma_1^2 - \sigma_a^2} \tag{B.8}$$

$$\sigma_s = \sqrt{\sigma_2^2 - \sigma_a^2} \tag{B.9}$$

For practical purposes a combined value can be calculated, as these widths might differ depending on the design of the detector and the particle properties. Here this is done by a mean weighted by the integral of the residual distribution:

$$\sigma_{com.} = \frac{\sigma_0 \int\limits_R a_1 e^{-\frac{1}{2}\left(\frac{x-\mu}{\sigma_1}\right)^2} + \sigma_s \int\limits_R a_2 e^{-\frac{1}{2}\left(\frac{x-\mu}{\sigma_2}\right)^2}}{\int\limits_R a_1 e^{-\frac{1}{2}\left(\frac{x-\mu}{\sigma_1}\right)^2} + \int\limits_R a_2 e^{-\frac{1}{2}\left(\frac{x-\mu}{\sigma_2}\right)^2}} \tag{B.10}$$

Alignment of Detectors in a Tracking Telescope

In order to determine the exact intersection of the reference track with the detector at test the exact positioning of this detector has to be known in the reference system. Assuming perfectly known positions and orientations of the reference detectors, the exact values for the test detector can be obtained from tracks through the detector. This also allows to align a set of detectors with respect to each other, without the need to measure their exact alignment externally. A full compensation without the need of an external position determination however is only possible if the test-detector provides more than one position coordinate.

By using a defined coordinate system (X,Y,Z), which is defined by the tracking system, the positions in the system of the test detector can be translated into the reference system by a combination of three translations and rotations. Mis-assumptions in any of these lead to specific deviations of the predicted position in the detector from the measured position and can be used to rule out these errors. The procedure used in this thesis to compensate for mis-alignment of the detector will be discussed at the example of four planar detectors with 2-dimensional strip read-out placed along a Z-coordinate. The positions of the first and the last two detectors are assumed to be well known, and only the second detector has to be corrected in order to match the system defined by the other three detectors. The alignment will be done by straight particle tracks through all detectors, whereas the tracks will be described by two sets of equations of straight lines, one for each read-out direction. A scheme of this is shown in figure B.2.

Translations in the precision coordinate of the detector for example directly translate to shift of the residual distribution and an error in the assumed position can be corrected by the corresponding mean value of the residual distribution.

A translation of the test detector in the Z-direction can be measured and corrected by the dependence of the residual distribution on the measured track inclination m:

$$\frac{\delta x}{m} = \delta z \tag{B.11}$$

Rotations around the X- and Y-axis of the reference system can be obtained from the dependence of the residual in the respective direction on the position measured in the detector (X', Y'):

$$\frac{\delta x}{X'} = \cos\theta \tag{B.12}$$

The last rotation around the Z-axis of the reference system can be calculated from the correlation of the residual distribution in one read-out direction and the position in the other read-out direction.
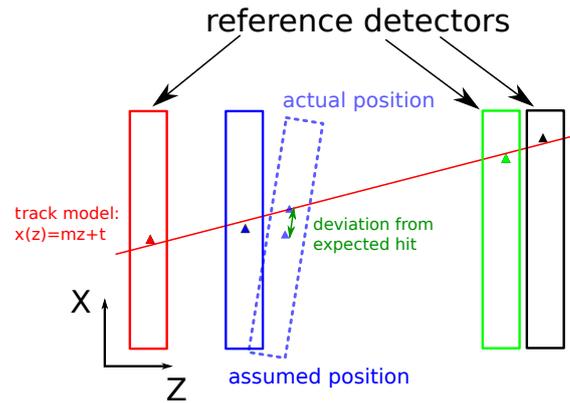
Figure B.2: Concept of the alignment with tracks: A track is defined by a set of measurements with a reference system and compared to the measurements in the tested detector with a-priori non perfect alignment. From systematic deviations of the expected position, defined by the reference system, to the measured position misalignments can be identified and corrected.

$$\frac{\delta x}{Y'} = \sin \phi \tag{B.13}$$

From as good as possible known start conditions small mis-assumption in the reconstruction can be treated as first order perturbations and can be corrected independently of one another in an iterative process.
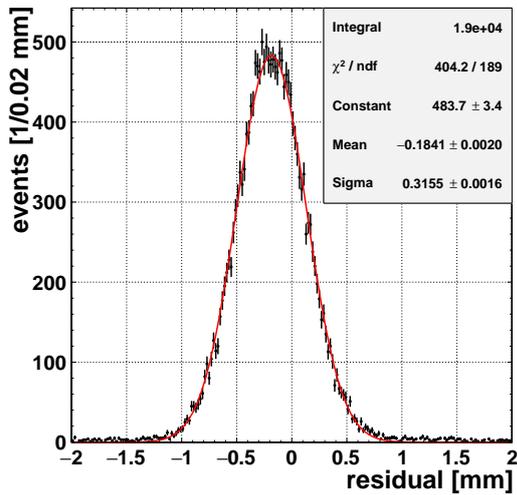
(a) A translation in either read-out direction can be seen directly from the residual distribution in this coordinate
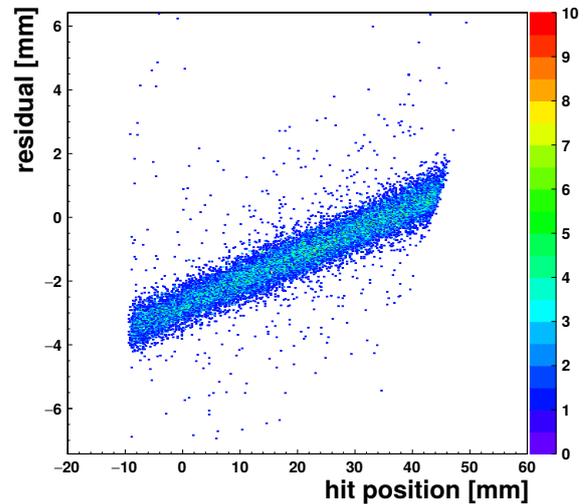
(b) Residual distribution plotted against the position in the same read-out direction for a detector, which is tilted around the axis parallel to the read-out strips for this direction.
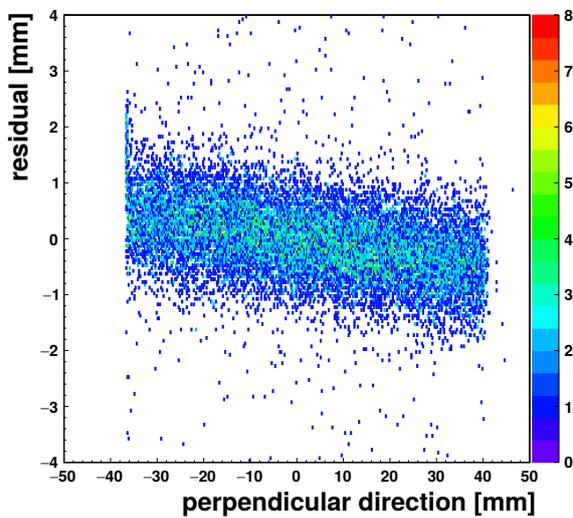
(c) A rotation around the Z-axis of the reference system translates into a correlation between the two read-out directions, and the residual of one direction depends on the position in the other direction
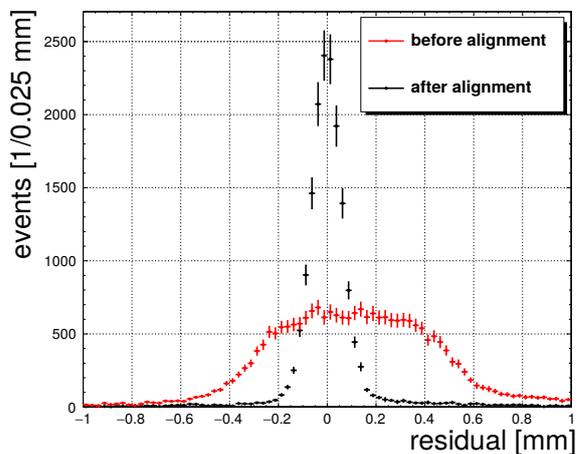
(d) The comparison of the residual distributions in the read-out direction for a non-aligned to a well aligned detector show a sharp improvement.

Figure B.3

Appendix C

Tracking by a Radon-transform

In order to find unbent tracks from multiple particles in a system of detectors a Radon-transform can be used, which allows to identify points laying on a straight line. For this an implementation described in [Bradski, 2000] was chosen, which allowed to reconstruct tracks in two dimensions. For detectors with 2D-read-out the track finding was separated in two steps. The transform translates every point in the detectors according to equation 2.35 into a curve in Radon-space, which is spanned by polar coordinated by an angle and a distance from the center of the initial coordinate origin. Agglomerations in this space describe a line in the initial space. Tracks through all detectors then can be found by finding intersections of lines from all detectors, as it can be seen in figures C.1(a) and C.1(b). Here the points in a set of five detectors are shown in different colors, allowing a better differentiation in the Radon-transform. Intersections of curves of the same color represent the plane of single detectors, whereas real tracks through all detectors are characterized by the intersection of curves with all five colors. In the example here 5 tracks could be reconstructed.

(a) Reconstructed particles in a set of five detectors, together with the tracks found in by the Radon-transform

(b) Radon transform of the left hit distribution, agglomerations which can be attributed to tracks through all detectors are highlighted.
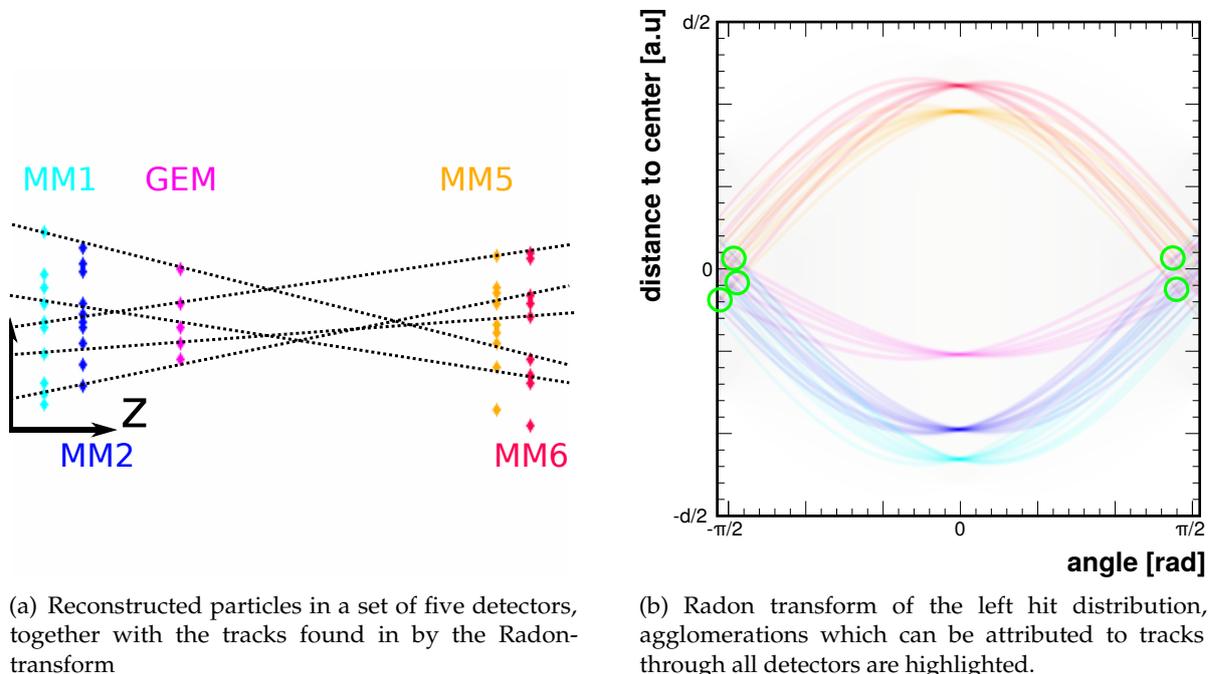
Figure C.1

The efficiency and robustness of this algorithm has been tested by simulation of tracks in a system consisting out of four detectors where hits along a track were placed with random offset according to a resolution of 200 μm. This was done for one and five tracks in the whole system and again with random noise hits added in all the detector layers, where the mean number of additional noise hits per layer was two. In table C.1 it can be seen, that the efficiency to reconstruct

Table C.1: Simulated track reconstruction efficiency for one and five tracks in a system with and without randomly added noise.

	without noise	with noise
1 track	$(99.5 \pm 0.9)\,\%$	$(97.2 \pm 0.9)\,\%$
5 tracks	$(84.4 \pm 1.3)\,\%$	$(76.2 \pm 1.2)\,\%$

a single track is above 97 % with and without noise. For a higher number of tracks the efficiency diminishes considerably.

Appendix D

Position Calculation from Stereo Layers

The position of a point in Cartesian coordinates P(x,y) from an arbitrary coordinate system P(u,v) with the axis U and V, which are rotated from the y axis by the angles φ_1 and $\pi - \varphi_2$, as shown in figure D.1, can be calculated in the following way:

$$x = \frac{u \sin \varphi_2 + v \sin \varphi_1}{\sin (\varphi_1 + \varphi_2)} \tag{D.1}$$

$$y = \frac{u \cos \varphi_2 - v \cos \varphi_1}{\sin (\varphi_1 + \varphi_2)} \tag{D.2}$$

This leads to an unambiguous description of point P, if $\sin (\varphi_1 + \varphi_2) \neq 0$, meaning U and V must not be parallel. If $\varphi_1 = \pi - \varphi_2 = \varphi$ this simplifies to:

$$x = \frac{u + v}{2 \cos \varphi} \tag{D.3}$$

$$y = \frac{u - v}{2 \sin \varphi} \tag{D.4}$$

In a planar detector with strip read-out this can be used to determine the position of a traversing particle in the full plane with two sets of overlapping read-out strips, with the only condition of being not parallel. Here it is implicitly assumed, that both sets of read-out strips are located in the same plane.

The situation if the read-out layers are not in the same plane can be calculated under the assumption of two parallel coordinate systems (U_1,V_1) and (U_2,V_2), which are tilted by an angle $\pm \phi$ with respect to the Y-axis of a Cartesian coordinate system and are placed in the distance ΔZ apart from each other. If a particle traverses both layers at the position (u_1, v_1) and (u_2, v_2), the positions in both layers in the orthogonal system (X,Y) can be calculated as follows:

$$x_1 = \frac{u_1 + v_1}{2 \cos \varphi} \tag{D.5}$$

$$x_2 = \frac{u_2 + v_2}{2 \cos \varphi} \tag{D.6}$$

$$y_1 = \frac{u_1 - v_1}{2 \sin \varphi} \tag{D.7}$$

$$y_2 = \frac{u_2 - v_2}{2 \sin \varphi} \tag{D.8}$$

This is schematically shown in figure D.2 for a track, which is parameterized by the point (x_1, y_1) and the polar and azimuthal angle θ and ϕ, which describe its track in polar coordinates. This allows to describe the distances of both positions in the tilted coordinate systems by:

$$\Delta u = u_1 - u_2 = \tan \theta \Delta Z \sin (\Phi + \varphi) \tag{D.9}$$

$$\Delta v = v_1 - v_2 = \tan \theta \Delta Z \sin (\Phi - \varphi) \tag{D.10}$$
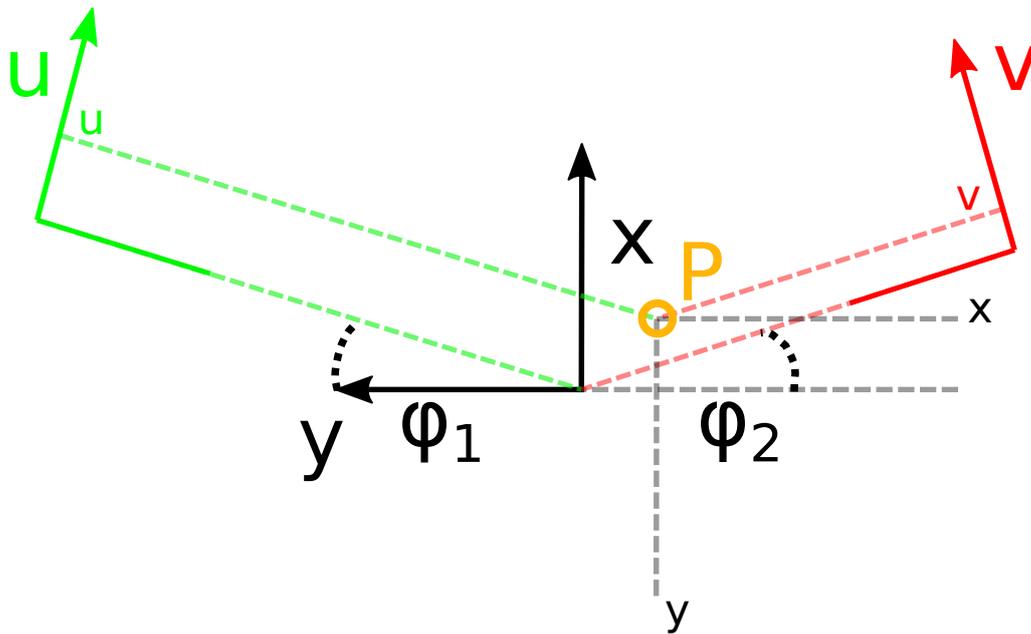
Figure D.1: Schematic of a coordinate system with tow axes (U,V) rotated around the origin of a Cartesian coordinate system by the angles φ_1 and φ_2. An unambiguous description of point P is possible in either coordinate systems as long as $\varphi_1 \neq -\varphi_2$.
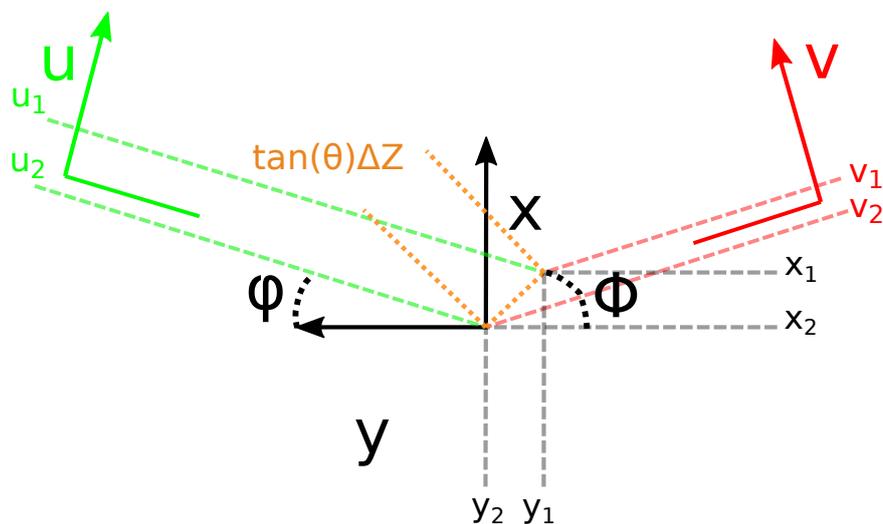
Figure D.2: Schematic of the passage of a particle through two identical read-out layers (U_1, V_1) and (U_2, V_2) with each having two sets of read-out strips being tilted by $\pm\varphi$ to a Cartesian coordinate system (X-Y). Both layers are placed parallel to each other in a distance ΔZ and the particle track is defined by the point (x_1, y_1) in the upper layer and by the two angles θ and Φ of a polar coordinate system.

By defining an auxiliary plane centered between the read-out layers (U_1,V_1) and (U_2,V_2) the intersection of the track with this plane can be described by:

$$x = x_1 - \frac{x_1 - x_2}{2} \tag{D.11}$$

$$y = y_2 + \frac{y_1 - y_2}{2} \tag{D.12}$$

Using now equations D.5-D.8 and solving equation D.9 and D.10 for the values u_2 and v_1 in the following way

$$u_2 = u_1 - \tan\theta\Delta Z \sin(\Phi + \varphi) \tag{D.13}$$

$$v_1 = v_2 + \tan\theta\Delta Z \sin(\Phi - \varphi) \tag{D.14}$$

the positions in the auxiliary plane can be described by only two variables u_1 and u_2:

$$x = \frac{u_1 + v_2}{2\cos\varphi} - \frac{\tan\theta\Delta Z \cos\Phi \tan\varphi}{2} \tag{D.15}$$

$$y = \frac{u_1 - v_2}{2\sin\varphi} - \frac{\tan\theta\Delta Z \sin\Phi}{2\tan\varphi} \tag{D.16}$$

This is equivalent to the case, where both layers consist of strips in a single read-out direction, but are tilted by an angle $+\varphi$ and $-\varphi$ with respect to the system (X,Y).

Appendix E

Detector Parameters for the Presented Measurements

With the exception of chapter 3 all measurements in this thesis were conducted with an Ar-CO$_2$ 93:7 Vol.% gas mixture held at a constant overpressure with respect to ambient conditions of (3 ± 1) mbar and also at ambient temperature. Here all detector parameters, which are not stated in the thesis elsewhere, are listed for completeness.

Measurements in chapter 3

The pressure in the detector was held constant at 1000 mbar at an ambient temperature of 24 °C.

Table E.1: Detector Parameters of the GEM detector

	Electric field or voltage
E_{ind}	3000 V cm^{-1}
ΔU_1	300 V
E_{trans1}	2500 V cm^{-1}
ΔU_2	200 V
E_{trans2}	1000 V cm^{-1}
ΔU_3	200 V
E_{drift}	variable

Measurements in chapter 4

Table E.2: Detector Parameters of the TGEM detector

	Electric field or voltage
E_{ind}	3000 V cm^{-1}
ΔU	1790 V
E_{drift}	600 V cm^{-1}

Measurements in chapter 5

Table E.3: Detector Parameters for all micromegas detectors of the reference system.

	Electric field or voltage
U_A	550 V
E_{drift}	570 V cm^{-1}

Measurements in chapter 6

Table E.4: Detector Parameters for both GEM detectors of the reference system.

	Electric field or voltage
E_{ind}	2000 V cm^{-1}
ΔU_1	300 V
E_{trans1}	2250 V cm^{-1}
ΔU_2	300 V
E_{trans2}	1575 V cm^{-1}
ΔU_3	325 V
E_{drift}	400 V cm^{-1}

Table E.5: Detector Parameters for both micromegas detectors of the reference system.

	Electric field or voltage
U_A	550 V
E_{drift}	430 V cm^{-1}

Measurements in chapter 7

Due to a failure of the power supply no drift voltages were applied at the micromegas reference detectors.

Table E.6: Detector Parameters for the GEM detector.

	Electric field or voltage
E_{ind}	2000 V cm^{-1}
ΔU_1	250 V
E_{trans1}	2250 V cm^{-1}
ΔU_2	250 V
E_{trans2}	2075 V cm^{-1}
ΔU_3	245 V
E_{drift}	590 V cm^{-1}

Table E.7: Detector Parameters for all micromegas detectors of the reference system.

	Electric field or voltage
U_A (MM1)	470 V
U_A (MM2)	490 V
U_A (MM3)	470 V
U_A (MM4)	450–460 V
U_A (MM5)	490 V
U_A (MM6)	460–480 V
E_{drift} (All)	$0\,\mathrm{V\,cm^{-1}}$

Bibliography

[Agostinelli et al., 2003] Agostinelli, S. et al. (2003). GEANT4: A simulation toolkit. *Nucl. Instrum. Meth.*, A506:250–303.

[Airapetian et al., 1999] Airapetian, A., Grabsky, V., Hakopian, H., Vartapetian, A., Dick, B., Fares, F., Guy, L., Moorhead, G., Sevior, M., Taylor, G., Tovey, S., Hashemi-Nezhad, R., Peak, L., Saavedra, A., and Ulrichs, J. (1999). *ATLAS detector and physics performance: Technical Design Report, 2*. Technical Design Report ATLAS. CERN, Geneva.

[Alexopoulos et al., 2011] Alexopoulos, T., Burnens, J., De Oliveira, R., Glonti, G., Pizzirusso, O., Polychronakos, V., Sekhniaidze, G., Tsipolitis, G., and Wotschack, J. (2011). A spark-resistant bulk-micromegas chamber for high-rate applications. *Nuclear Instruments and Methods in Physics Research Section A: Accelerators, Spectrometers, Detectors and Associated Equipment*, 640(1):110–118.

[Alexopoulos et al., 2015] Alexopoulos, T. et al. (2015). Stereo information in micromegas detectors. Technical report, ATL-MUON-PUB-2015-001, CERN, Geneva.

[Allis and Morse, 1931] Allis, W. P. and Morse, P. M. (1931). Theorie der Streuung langsamer Elektronen an Atomen. *Zeitschrift für Physik*, 70(9-10):567–582.

[Alves, 2014] Alves, L. (2014). The IST-LISBON database on LXCat. *Journal of Physics: Conference Series*, 565:012007.

[Amelung et al., 2015] Amelung, C., Bini, C., Giraud, P., Iakovidis, G., Iengo, P., Iodice, M., Lelouch, D., Mikenberg, G., Pontecorvo, L., Schune, P., and Vlachos, S. (2015). *Requirements for the construction precision of any NSW chamber*. https://edms.cern.ch/document/1350308/1 Accessed: 15.02.2018.

[ATLAS Collaboration, 2012] ATLAS Collaboration (2012). Observation of a new particle in the search for the Standard Model Higgs boson with the ATLAS detector at the LHC. *Physics Letters B*, 716(1):1–29.

[ATLAS Collaboration, 2013] ATLAS Collaboration (2013). New Small Wheel Technical Design Report. Technical Report CERN-LHCC-2013-006. ATLAS-TDR-020. ATLAS New Small Wheel Technical Design Report.

[Atlas Collaboration, 2018] Atlas Collaboration (2018). ATLAS Experiment-Public Results. https://twiki.cern.ch/twiki/bin/view/AtlasPublic/LuminosityPublicResultsRun2 Accessed: 16.11.2017.

[Banhart et al., 2010] Banhart, J., Borbely, A., Dzieciol, K., García-Moreno, F., Manke, I., Kardjilov, N., Kaysser-Pyzalla, A., Strobl, M., and Treimer, W. (2010). X-ray and neutron imaging - complementary techniques for materials science and engineering. *International Journal of Materials Research*, 101:1069–1079.

[Beckurts et al., 1964] Beckurts, K., Dresner, L., and Wirtz, K. (1964). *Neutron Physics*. Springer Berlin Heidelberg.

[Berger, 1992] Berger, M. J. (1992). ESTAR, PSTAR, and ASTAR: Computer programs for calculating stopping-power and range tables for electrons, protons, and helium ions. `http://physics.nist.gov/Star`. Accessed: 28.12.2017.

[Berger et al., 1998] Berger, M. J., Coursey, J., Zucker, M., and Chang, J. (1998). *Stopping-power and range tables for electrons, protons, and helium ions*. NIST Physics Laboratory Gaithersburg, MD.

[Berger et al., 2010] Berger, M. J., Hubbell, J. H., Seltzer, S. M., Chang, J., Coursey, J. S., Sukumar, R., Zucker, D. S., and Olsen (2010). XCOM: Photon Cross Sections Database. *NIST Standard Reference Database 8 (XGAM)*.

[Berglund and Wieser, 2011] Berglund, M. and Wieser, M. E. (2011). Isotopic compositions of the elements 2009 (iupac technical report). *Pure and applied chemistry*, 83(2):397–410.

[Biagi, 2000] Biagi, S. (2000). Magboltz-transport of electrons in gas mixtures. *CERN program library*.

[Biebel et al., 2003] Biebel, O., Binder, M., Boutemeur, M., Brandt, A., Dubbert, J., Duckeck, G., Elmsheuser, J., Fiedler, F., Hertenberger, R., Kortner, O., et al. (2003). A cosmic ray measurement facility for ATLAS muon chambers. *arXiv preprint physics/0307147*.

[Binnie, 1985] Binnie, D. (1985). Drift and diffusion of electrons in argon/co2 mixtures. *Nuclear Instruments and Methods in Physics Research Section A: Accelerators, Spectrometers, Detectors and Associated Equipment*, 234(1):54 – 60.

[Blum et al., 2008] Blum, W., Riegler, W., and Rolandi, L. (2008). *Particle Detection with Drift Chambers*. Particle Acceleration and Detection. Springer Berlin Heidelberg.

[Bortfeldt, 2014] Bortfeldt, J. (2014). *Development of floating strip micromegas detectors*. PhD thesis, Ludwig-Maximilians-Universität München.

[Bortfeldt et al., 2017] Bortfeldt, J., Biebel, O., Flierl, B., Hertenberger, R., Klitzner, F., Lösel, P., Magallanes, L., Müller, R., Parodi, K., Schlüter, T., Voss, B., and Zibell, A. (2017). Low material budget floating strip micromegas for ion transmission radiography. *Nuclear Instruments and Methods in Physics Research Section A: Accelerators, Spectrometers, Detectors and Associated Equipment*, 845:210 – 214. Proceedings of the Vienna Conference on Instrumentation 2016.

[Bradski, 2000] Bradski, G. (2000). The OpenCV Library. *Dr. Dobb's Journal of Software Tools*, 25(11):120–126.

[Breskin et al., 2009] Breskin, A., Alon, R., Cortesi, M., Chechik, R., Miyamoto, J., Dangendorf, V., Maia, J., and Santos, J. D. (2009). A concise review on thgem detectors. *Nuclear Instruments and Methods in Physics Research Section A: Accelerators, Spectrometers, Detectors and Associated Equipment*, 598(1):107 – 111. Instrumentation for Collding Beam Physics.

[Breskin et al., 2003] Breskin, A., Balcerzyk, M., Chechik, R., Guedes, G., Maia, J., and Mörmann, D. (2003). Recent advances in gaseous imaging photomultipliers. *Nuclear Instruments and Methods in Physics Research Section A: Accelerators, Spectrometers, Detectors and Associated Equipment*, 513(1):250 – 255. Proceedings of the 6th International Conference on Position-Sensitive Detectors.

[Byszewski, 2012] Byszewski, M. (2012). MMDAQ Q and A-ATLAS micromegas DAQ . `https://indico.cern.ch/event/218341/contributions/1519619/attachments/352429/491014/mmdaq_QA.pdf`. Accessed: 27.12.2017.

[Byszewski and Wotschack, 2012] Byszewski, M. and Wotschack, J. (2012). Resistive-strips micromegas detectors with two-dimensional readout. *Journal of Instrumentation*, 7(02):C02060.

[Carnegie et al., 2005] Carnegie, R., Dixit, M., Dubeau, J., Karlen, D., Martin, J.-P., Mes, H., and Sachs, K. (2005). Resolution studies of cosmic-ray tracks in a TPC with GEM readout. *Nuclear Instruments and Methods in Physics Research Section A: Accelerators, Spectrometers, Detectors and Associated Equipment*, 538(1):372 – 383.

[Charpak, 1969] Charpak, G. (1969). Development of multiwire proportional chambers. *CERN Courier*, 9:174–176.

[Chauchaix et al., 2000] Chauchaix, B., Efthymiopoulos, I., and Fabich, A. (2000). The SPS North Area Beams, Introduction to H8 Beam Line. Technical report, CERN. `http://sba.web.cern.ch/sba/BeamsAndAreas/h8/H8manual.pdf` Accessed: 27.12.2017.

[Farthouat and Gällnö, 2000] Farthouat, P. and Gällnö, P. (2000). TTC-VMEbus INTERFACE TTCvi-MkII. `http://cern.ch/ttc` Accessed: 17.11.2017.

[Fermi, 1940] Fermi, E. (1940). The Ionization Loss of Energy in Gases and in Condensed Materials. *Phys. Rev.*, 57:485–493.

[Firestone and Shirley, 1996] Firestone, R. and Shirley, V. (1996). *Table of Isotopes: A*. Table of Isotopes. John Wiley.

[Fischle et al., 1991] Fischle, H., Heintze, J., and Schmidt, B. (1991). Experimental determination of ionization cluster size distributions in counting gases. *Nuclear Instruments and Methods in Physics Research Section A: Accelerators, Spectrometers, Detectors and Associated Equipment*, 301(2):202–214.

[Flierl et al., 2016a] Flierl, B., Herrmann, M., Hertenberger, R., Lösel, P., Müller, R., Zibell, A., Klitzner, F., and Biebel, O. (2016a). Improvement of spatial resolution by selfconsistent full muon track reconstruction in gaseous detectors. *Proceedings of Science*, page 292.

[Flierl et al., 2016b] Flierl, B., Hertenberger, R., Biebel, O., and Zeitelhack, K. (2016b). TPC-like readout for thermal neutron detection using a GEM-detector. *Nuclear Instruments and Methods in Physics Research Section A: Accelerators, Spectrometers, Detectors and Associated Equipment*, 824:528–531.

[French et al., 2001] French, M., Jones, L., Morrissey, Q., Neviani, A., Turchetta, R., Fulcher, J., Hall, G., Noah, E., Raymond, M., Cervelli, G., et al. (2001). Design and results from the APV25, a deep sub-micron CMOS front-end chip for the CMS tracker. *Nuclear Instruments and Methods in Physics Research Section A: Accelerators, Spectrometers, Detectors and Associated Equipment*, 466(2):359–365.

[Geronimo et al., 2013] Geronimo, G. D., Fried, J., Li, S., Metcalfe, J., Nambiar, N., Vernon, E., and Polychronakos, V. (2013). VMM1—an ASIC for micropattern detectors. *IEEE Transactions on Nuclear Science*, 60(3):2314–2321.

[Giomataris et al., 2006] Giomataris, I., De Oliveira, R., Andriamonje, S., Aune, S., Charpak, G., Colas, P., Fanourakis, G., Ferrer, E., Giganon, A., Rebourgeard, P., et al. (2006). Micromegas in a bulk. *Nuclear Instruments and Methods in Physics Research Section A: Accelerators, Spectrometers, Detectors and Associated Equipment*, 560(2):405–408.

[Giomataris et al., 1996] Giomataris, Y., Rebourgeard, P., Robert, J. P., and Charpak, G. (1996). Micromegas: a high-granularity position-sensitive gaseous detector for high particle-flux environments. *Nuclear Instruments and Methods in Physics Research Section A: Accelerators, Spectrometers, Detectors and Associated Equipment*, 376(1):29–35.

[Haberer et al., 2004] Haberer, T., Debus, J., Eickhoff, H., Jäkel, O., Schulz-Ertner, D., and Weber, U. (2004). The heidelberg ion therapy center. *Radiotherapy and Oncology*, 73:S186–S190.

[Hagelaar and Pitchford, 2005] Hagelaar, G. and Pitchford, L. (2005). Solving the boltzmann equation to obtain electron transport coefficients and rate coefficients for fluid models. *Plasma Sources Science and Technology*, 14(4):722.

[Heinz Maier-Leibnitz Zentrum et al., 2017] Heinz Maier-Leibnitz Zentrum et al. (2017). TREFF: Reflectometer and instrument component test beamline at MLZ. *Journal of large-scale research facilities JLSRF*, 3.

[Hough, 1962] Hough, P. (1962). Method and means for recognizing complex patterns. U.S. Patent 3069654.

[Iengo and Alexopoulos, 2014] Iengo, P. and Alexopoulos, T. (2014). The Micromegas Project for the ATLAS Upgrade. `https://indico.cern.ch/event/348222/contributions/816989/attachments/687160/943755/theoalex_31_10_2014_rd51_MM_nsw_atlas.pdf` Accessed: 15.02.2018.

[Iodice, 2015] Iodice, M. (2015). *Micromegas Construction Manual.* `https://edms.cern.ch/document/1400217/1` Accessed: 15.02.2018.

[Klein and Nishina, 1929] Klein, O. and Nishina, Y. (1929). Über die Streuung von Strahlung durch freie Elektronen nach der neuen relativistischen Quantendynamik von Dirac. *Zeitschrift für Physik*, 52(11-12):853–868.

[Kleinknecht, 1998] Kleinknecht, K. (1998). *Detectors for Particle Radiation*. Cambridge University Press.

[Klitzner, 2016] Klitzner, F. F. (2016). Studies of Floating Strip Micromegas Detectors in Proton and Carbon Ion Beams with a Fast Gas Mixture. Master's thesis, Ludwig-Maximillians-Universitat, Munchen.

[Köhli et al., 2016] Köhli, M., Klein, M., Allmendinger, F., Perrevoort, A., Schröder, T., Martin, N., Schmidt, C., and Schmidt, U. (2016). CASCADE-a multi-layer Boron-10 neutron detection system. *Journal of Physics: Conference Series*, 746(1):012003.

[Kuger, 2017] Kuger, F. (2017). *Signal Formation Processes in Micromegas Detectors and Quality Control for large size Detector Construction for the ATLAS New Small Wheel*. PhD thesis, Julius-Maximilians-Universität Würzburg.

[Lehmann et al., 2017] Lehmann, E., Mannes, D., Kaestner, A., and Grünzweig, C. (2017). Recent applications of neutron imaging methods. *Physics Procedia*, 88(Supplement C):5 – 12.

[Leo, 2012] Leo, W. (2012). *Techniques for Nuclear and Particle Physics Experiments: A How-to Approach*. Springer Berlin Heidelberg.

[Lösel, 2017] Lösel, P. (2017). *Precision Calibration of Large Area Micro Pattern Gaseous Detectors*. PhD thesis, Ludwig-Maximilians-Universität München.

[Lyly et al., 1999] Lyly, M., Ruokolainen, J., and Järvinen, E. (1999). Elmer–a finite element solver for multiphysics. *CSC-report on scientific computing*, 2000:156–159.

[Lösel, 2013] Lösel, P. (2013). Performance Studies of Large Size Micromegas Detectors. Master's thesis, Ludwig-Maximilians-Universität München.

[Lösel and Müller, 2015] Lösel, P. and Müller, R. (2015). Design and Construction of Large Size Micromegas Chambers for the Upgrade of the ATLAS Muon Spectrometer. Technical Report arXiv:1508.02541.

[Magallanes, 2017] Magallanes, L. (2017). *Low-dose ion-based transmission radiography and tomography for optimization of carbon ion-beam therapy*. PhD thesis, Ludwig-Maximilians-Universität München.

[Martin, 1998] Martin, S. P. (1998). A Supersymmetry Primer. In *Perspectives on Supersymmetry*, pages 1–98.

[Martínez et al., 2016] Martínez, A. R. et al. (2016). The Run-2 ATLAS Trigger System. In *Journal of Physics: Conference Series*, volume 762, page 012003.

[Martoiu et al., 2013] Martoiu, S., Muller, H., Tarazona, A., and Toledo, J. (2013). Development of the scalable readout system for micro-pattern gas detectors and other applications. *JINST*, 8(03):C03015.

[Melissinos, 1966] Melissinos, A. (1966). *Experiments in modern physics*. Academic Press.

[Mishima et al., 1999] Mishima, K., Hibiki, T., Saito, Y., Sugimoto, J., and Moriyama, K. (1999). Visualization study of molten metal–water interaction by using neutron radiography. *Nuclear Engineering and Design*, 189(1):391 – 403.

[Morháč, 2015] Morháč, M. (2015). *TSpectrum manual: 6 Release Cycle*. `https://root.cern.ch/root/htmldoc/guides/spectrum/Spectrum.pdf` Accessed: 06.02.2018.

[Mouche, 2014] Mouche, P. (2014). Overall view of the LHC. Vue d'ensemble du LHC. General Photo.

[Müller, 2011] Müller, H. (2011). SRS scalable readout system Status and Outlook. `https://indico.cern.ch/event/158402/contributions/226252/attachments/178355/250865/Scalable_Readout_System__H.M._22112011.pdf`. Accessed: 27.12.2017.

[Müller, 2017] Müller, R. (2017). *Quality control of Micromegas detectors for the ATLAS new small wheel upgrade project and optimization of the spatial resolution of PoSSuMuS detectors in two dimensions*. PhD thesis, Ludwig-Maximilians-Universität München.

[Nakhostin, 2017] Nakhostin, M. (2017). *Signal Processing for Radiation Detectors*. Wiley.

[Ntekas, 2016] Ntekas, K. (2016). *Performance characterization of the Micromegas detector for the New Small Wheel upgrade and Development and improvement of the Muon Spectrometer Detector Control System in the ATLAS experiment*. PhD thesis, Natl. Tech. U., Athens.

[Nygren, 1974] Nygren, D. R. (1974). Proposal to investigate the feasibility of a novel concept in particle detection. Technical report, LBL internal report.

[Olive et al., 2014] Olive, K. A. et al. (2014). Review of Particle Physics. *Chin. Phys.*, C38:090001.

[Penning, 1927] Penning, F. M. (1927). Über ionisation durch metastabile atome. *Naturwissenschaften*, 15(40):818–818.

[Pequenao, 2008] Pequenao, J. (2008). Computer generated image of the whole ATLAS detector.

[Perkins and Seltzer, 1991] Perkins, S. and Seltzer, S. (1991). Tables and graphs of electron-interaction cross-sections from 10 eV to 100 GeV derived from the llnl evaluated electron data library. *Lawrence Livermore National Laboratory Report UCRL*, 31.

[Phelps, 2017] Phelps, A. (2017). Phelps database -A compilation of atomic and molecular data, assembled and evaluated by A.V. phelps and collaborators. `http://jilawww.colorado.edu/~avp/`. Accessed: 27.12.2017.

[Pree, 2015] Pree, E. (2015). Construction of Large Area Micromegas Detectors. Master's thesis, Ludwig-Maximilians-Universität München.

[Radeka, 1988] Radeka, V. (1988). Low-noise techniques in detectors. *Annual Review of Nuclear and Particle Science*, 38(1):217–277.

[Radeka et al., 1996] Radeka, V., Schaknowski, N., Smith, G., and Yu, B. (1996). High precision thermal neutron detectors. In *Neutrons in biology*, pages 57–67. Springer.

[Radon, 1917] Radon, J. (1917). Über die Bestimmung von Funktionen durch ihre Integralwerte längs gewisser Mannigfaltigkeiten. *Akad. Wiss.*, 69:262–277.

[Ramo, 1939] Ramo, S. (1939). Currents induced by electron motion. *Proceedings of the IRE*, 27(9):584–585.

[Ramsauer, 1921] Ramsauer, C. (1921). Über den Wirkungsquerschnitt der Gasmoleküle gegenüber langsamen Elektronen. *Annalen der Physik*, 369(6):513–540.

[Raymond et al., 2000] Raymond, M., French, M., Fulcher, J., Hall, G., Jones, L., Kloukinas, K., Lim, L., Marseguerra, G., Moreira, P., and Morrissey, Q. (2000). The APV25 0.25 µm CMOS readout chip for the CMS tracker. *IEEE Nucl. Sci. Symp. Conf. Rec.*, 2:9/113.

[RD51-collaboration, 2010] RD51-collaboration (2010). Scalable Readout System (SRS). `http://rd51-public.web.cern.ch/RD51-Public/Activities/Documents/WG5SRS.pdf`. Accessed: 28.12.2017.

[Rose and Korff, 1941] Rose, M. E. and Korff, S. A. (1941). An investigation of the properties of proportional counters. i. *Phys. Rev.*, 59:850–859.

[Rossi, 2011] Rossi, L. (2011). LHC Upgrade Plans: Options and Strategy. (CERN-ATS-2011-257):6.

[Sauli, 1997] Sauli, F. (1997). GEM: A new concept for electron amplification in gas detectors. *Nucl. Instrum. Meth.*, A386:531–534.

[Schoemers et al., 2015] Schoemers, C., Feldmeier, E., Naumann, J., Panse, R., Peters, A., and Haberer, T. (2015). The intensity feedback system at heidelberg ion-beam therapy centre. *Nuclear Instruments and Methods in Physics Research Section A: Accelerators, Spectrometers, Detectors and Associated Equipment*, 795:92 – 99.

[Schune, 2015] Schune, P. (2015). ATLAS-Muon Spectrometer. `http://irfu.cea.fr/Images/astImg/2243_4.png`. Accessed: 27.12.2017.

[Shea and Morgan, 2010] Shea, D. A. and Morgan, D. (2010). The helium-3 shortage: Supply, demand, and options for congress. Congressional Research Service, Library of Congress.

[Smirnov, 1997] Smirnov, I. (1997). Heed: Interactions of particles with gases. *CERN Program Library Writeup W*, 5060.

[Stefanescu et al., 2013] Stefanescu, I., Abdullahi, Y., Birch, J., Defendi, I., Hall-Wilton, R., Höglund, C., Hultman, L., Zee, M., and Zeitelhack, K. (2013). A 10b-based neutron detector with stacked multiwire proportional counters and macrostructured cathodes. *Journal of Instrumentation*, 8(12):P12003.

[Stefanescu et al., 2017] Stefanescu, I., Christensen, M., Fenske, J., Hall-Wilton, R., Henry, P., Kirstein, O., Müller, M., Nowak, G., Pooley, D., Raspino, D., et al. (2017). Neutron detectors for the *ess* diffractometers. *Journal of Instrumentation*, 12(01):P01019.

[Takahashi et al., 2013] Takahashi, H., Mitsuya, Y., Fujiwara, T., and Fushie, T. (2013). Development of a glass GEM. *Nuclear Instruments and Methods in Physics Research Section A: Accelerators, Spectrometers, Detectors and Associated Equipment*, 724(Supplement C):1 – 4.

[Thompson and Vaughan, 2001] Thompson, A. and Vaughan, D. (2001). *X-ray Data Booklet*. Lawrence Berkeley Laboratory.

[Veenhof, 1998] Veenhof, R. (1998). Garfield, recent developments. *Nuclear Instruments and Methods in Physics Research Section A: Accelerators, Spectrometers, Detectors and Associated Equipment*, 419(2):726–730.

[Zeitelhack, 2012] Zeitelhack, K. (2012). Search for alternative techniques to helium-3 based detectors for neutron scattering applications. *Neutron News*, 23(4):10–13.

[Zibell, 2014a] Zibell, A. (2014a). Development of a read out driver for ATLAS micromegas based on the Scalable Readout System. *Journal of Instrumentation*, 9(01):C01038.

[Zibell, 2014b] Zibell, A. (2014b). *High-rate irradiation of 15mm muon drift tubes and development of an ATLAS compatible readout driver for micromegas detectors*. PhD thesis, Ludwig-Maximilians-Universität München.

[Ziegler et al., 2010] Ziegler, J. F., Ziegler, M. D., and Biersack, J. P. (2010). SRIM - The stopping and range of ions in matter (2010). *Nuclear Instruments and Methods in Physics Research B*, 268:1818–1823.

List of Abbreviations

ADC	-	Analogue-to-Digital Converter
APV25	-	Analogue Pipeline ASIC, designed for read-out of silicone strip detectors, but also widely used for gaseous detectors
ASIC	-	Application-Specific Integrated Circuit
ATLAS	-	A Toroidal LHC ApparatuS, one of four main detectors located at LHC
CERN	-	European Organization for Nuclear Research (Conseil européen pour la recherche nucléaire)
CSC	-	Cathode Strip Chamber, multi-wire based high precision muon tracker system in ATLAS
FEC	-	Front-end-Concentrator card
GEM	-	Gaseous Electron Multiplier
HIT	-	Heidelberger Ionenstrahl-Therapiezentrum
IP	-	Interaction Point of beams in LHC
LHC	-	Large Hadron Collider, proton accelerator located at CERN
MDT	-	Monitored Drift Tube, high precision muon tracking system used by ATLAS
MLZ	-	Heinz Maier-Leibnitz Zentrum
Micromegas (MM)	-	Micromesh Gaseous Structure
MPGD	-	Micro-Pattern Gaseous Detector
NSW	-	New Small Wheel, replacement of forward muon spectrometer of ATLAS
PCB	-	Printed-Circuit-Board
RPC	-	Resitive Plate Chamber
SPS	-	Super Proton Synchroton, proton accelerator located at CERN
SRS	-	Scalable Readout System
SRU	-	Scalable Readout Unit
sTGC	-	small Strip Thin Gap Chamber
TDC	-	Time-to-Digital Converter
TGEM	-	Thick-GEM, GEM base on standard PCB-material
TPC	-	Time-Projection-Chamber
μTPC	-	micro-TPC, TPC-like reconstruction method foreseen for muon reconstruction in NSW micromegas

Danksagungen

An dieser Stelle möchte ich mich bei allen bedanken, die mich im Kleinen wie im Großen in den letzten Jahren unterstützt haben und ohne die ich diese Arbeit nicht hätte schreiben können:

- Mein besonderer Dank gilt Herrn Prof. Dr. Otmar Biebel und Frau Prof. Dr. Dorothee Schaile für die Betreuung und die Möglichkeit diese Arbeit in einem so konstruktiven Umfeld verfassen zu können.

- Dr. Ralf Hertenberger für die intensive Betreuung über die letzten sechs Jahre. Besonders aber auch für die vielen Korrekturen und Denkanstöße zum Ende der Arbeit.

- Ich möchte auch Prof. Dr. Wolfgang Dünnweber dafür danken, dass er sich zum Verfassen des Zweitgutachtens bereit erklärt hat.

- Prof. Dr. Jochen Weller für den Vorsitz über die Prüfungskommission und selbstverständlich auch Prof. Dr. Thomas Kuhr, Prof. Dr. Katia Parodi und Prof. Dr. Christian Kiesling als Mitglieder der Kommission.

- Prof. Katia Parodi und Dr. Lorena Magallanes für die Möglichkeit Messungen am HIT im Rahmen des DFG Forschungsprojekts "A novel imaging technique for ion beam therapy: Ion Computed Tomography" durchzuführen. Hier seien auch alle Mitarbeiter des HITs erwähnt die den reibungslosen Ablauf ermöglichten, insbesondere Dr. Stephan Brons wegen seiner Vorbereitungen und Unterstützung vor Ort.

- Dr. Karl Zeitlhack für die unglaubliche Untersützung in allen Belangen im Zusammenhang mit den Neutronen-Messungen und die Möglichkeit diese am Heinz Maier-Leibnitz Zentrum durchführen zu können.

- Dr. Jonathan Bortfeldt für die Unterstützung während der Messungen am CERN und am HIT und auch während seiner Zeit am Lehrstuhl Schaile.

- Natürlich gilt mein Dank auch dem gesamten Lehrstuhl und insbesondere: Maximillian Herrmann, Dr. Friedrich Hönig, Felix Fidelio Klitzner, Dr. Ralph Müller, Dr. Philipp Lösel, Dr. Chrysostomos Valderanis, Atila Varga und Dr. Andre Zibell.

- Bei den Mitarbeitern der mechanischen Werkstatt und deren Leiter Rolf Oehm.

- Meiner ganzen Familie, besonders aber meiner Mutter für den vielen Kuchen.

- Und zuletzt natürlich meiner Freundin Andrea Matić die mich in den letzten Wochen und Monaten noch mehr als sonst unterstützt hat.